Distributed Fiber Optic Sensor for On-Line Monitoring of Coal Gasifier Refractory Health

Final Report

Reporting Period Start Date: May 1, 2011
Reporting Period End Date: October 31, 2015

Principal Authors: Anbo Wang and Zhihao Yu

Report Issued: November 30, 2015

DOE Award Number: DE-FE0005703

Submitted by: Center for Photonics Technology
Bradley Department of Electrical Engineering
Virginia Polytechnic Institute & State University
Blacksburg, VA 24061-0111

CPT
CENTER FOR PHOTONICS TECHNOLOGY

Disclaimer

Abstract

This report summarizes technical progress on the program "Distributed Fiber Optic Sensor for On-Line Monitoring of Coal Gasifier Refractory Health," funded by the National Energy Technology Laboratory of the U.S. Department of Energy, and performed by the Center for Photonics Technology of the Bradley Department of Electrical and Computer Engineering at Virginia Tech.

The scope of work entails analyses of traveling grating generation technologies in an optical fiber, as well as the interrogation of the gratings to infer a distributed temperature along the fiber, for the purpose of developing a real-time refractory health condition monitoring technology for coal gasifiers. During the project period, which is from 2011-2015, three different sensing principles were studied, including four-wave mixing (FWM), coherent optical time-domain reflectometer (C-OTDR) and Brillouin optical time-domain analysis (BOTDA). By comparing the three methods, the BOTDA was selected for further development into a complete bench-top sensing system for the proposed high-temperature sensing application.

Based on the input from Eastman Chemical, the industrial collaborator on this project, a cylindrical furnace was designed and constructed to simulate typical gasifier refractory temperature conditions in the laboratory, and verify the sensor's capability to fully monitor refractory conditions on the back-side at temperatures up to 1000 ℃. In the later stages of the project, the sensing system was tested in the simulated environment for its sensing performance and high-temperature survivability. Through theoretical analyses and experimental research on the different factors affecting the sensor performance, a sensor field deployment strategy was proposed for possible future sensor field implementations.

Table of Contents

List of Figures and Tables

1 Introduction

Recent advances in fossil fuel energy production technologies have shown tremendous potential to efficiently create clean, sustainable electricity using a variety of carbonaceous fuels. Techniques such as the integrated coal-gasification combined cycle (IGCC) have been demonstrated as feasible next-generation energy sources, but commercial operation of these facilities poses significant challenges [1, 2]. Foremost among these difficulties is the issue of refractory wear. The high-temperature reducing environment in the gasifier causes rapid corrosion of even the toughest refractory materials, limiting their typical useful lifetime to 6-18 months [3]. Furthermore, the complexity and uncertainty of the gasification process makes remaining refractory life difficult to predict in working gasifiers [4]. Non-uniform degradation of the refractory brick, occurring in the form of localized thinning, cracking, or spalling, can generate weak points that determine the effective overall lifetime of the gasifier liner [4-7].

To date, the most widely adopted solution to refractory wear is the adoption of scheduled inspection and replacement of gasifier liners. Driven by the unpredictable nature and tremendous risk of refractory failure, maintenance is often scheduled at conservatively short intervals, at great financial penalty. Unplanned outages are potentially even more costly, as they are often accompanied by collateral equipment failure or the need to co-opt additional resources at short notice. Re-bricking a large scale gasifier refractory typically takes up to three weeks and costs $1-2 million. These financial concerns are compounded by the fact that the rate of refractory wear is highly dependent on the properties of the coal feedstock and the effects of thermal cycling. In addition to reducing plant availability, frequent inspection and maintenance also accelerate refractory wear. Unfortunately, existing external sensing technology is unable to generate useful refractory health data, and as such, external sensors are mainly used to monitor the integrity of the outer gasifier shell as a safety precaution.

The development of a technology capable of monitoring refractory health and predicting remaining lifetime could help reduce the cost of IGCC, through improved efficiency and reliability, to below the threshold for wide-scale commercialization [3]. Recognizing this potential, researchers have begun to apply numerical modeling to help achieve a better understanding of refractory degradation [6]. Theoretical analysis of the refractory wear problem provides half of the required solution; to fully realize the potential of coal gasification, these models must be accompanied by a sensor technology capable of on-line refractory health monitoring to achieve greater confidence in determining the remaining lifetime of the refractory.

In this four-year program, three different sensing schemes were thoroughly investigated, which are four-wave mixing (FWM, Chapter 5), coherent optical time-domain reflectometry (COTDR, Chapter 6), and stimulated Brillouin scattering (SBS, Chapter 7). Based on comparative evaluation and analysis of the experimental results, the SBS sensing scheme was determined to be the optimal approach for online, real-time, and reliable monitoring of coal gasification refractory walls. The sensing scheme was realized as a bench-top system, and fully optimized and evaluated with the use of a cylindrical furnace, which was designed and constructed for the simulation of typical coal gasifier refractory walls. This direct measurement technology will enable early detection of hot spots in the refractory walls and measurement of their remaining

lifetime, and therefore allow gasifier operators to adopt a conditions-based maintenance model, which could reduce the frequency of facility shut-downs.

2 Background of this proposed research

Coal is the most abundant natural resource for industrial heating and power production applications. Coal gasification represents the next generation of coal-based energy production as a means to generate extremely clean electricity and other high-value energy products. Real-time health monitoring of the coal gasifier refractory wall requires a distributed sensing technology that can withstand the harsh environment posed by the high working temperature. This research, supported by the National Energy Technology Laboratory (NETL) of the U.S. Department of Energy, was designed to address the critical harsh environment sensing need. This work was performed in collaboration with Eastman Chemical Company, which operates coal gasifiers in Kingsport, Tennessee.

2.1 Existing gasifier monitoring techniques

Operators of existing coal gasifiers rely largely on indirect measurements, obtained externally, to provide vital information on operating conditions and component health in the gasifier. By monitoring the syngas composition in the cooling stages, engineers are able to estimate process conditions with reasonable accuracy, enabling real-time optimization of slurry and oxygen feed rates [7]. However, output gas composition measures the cumulative effect of a variety of process parameters and provides, at best, an indication of the average conditions in the gasifier. Local anomalies, which may provide early warning of refractive failure, are impossible to detect using this technique.

Thermal imaging devices are often used to provide external assessment of gasifier health. Optical pyrometers, mounted outside the gasifier, can provide a distributed temperature measurement of the outer gasifier shell. This measurement is insulated by multiple layers of refractory material and is therefore incapable of detecting the early stages of local refractory degradation. As such, external thermal imaging devices or temperature sensor networks are used primarily for detection and prevention of catastrophic refractory failure and are not suitable early detection and location of refractory degradation [7].

Single-point temperature measurements, made using precious metal thermocouples or high-temperature optical components, can provide a direct measurement of gasifier temperature [7-9]. Although they provide valuable information, these sensors are impractical for refractory health monitoring. The stochastic, localized nature of refractory wear necessitates a network of measurement points. Therefore, refractory condition assessment based on point sensors would require installation of hundreds of devises over the entire outer wall of the vessel. Installation of such a complex single-point network would likely compromise the outer refractory layer at many points and require the installation of multiple ports in the outer gasifier shell.

2.2 Distributed fiber optic sensing technologies review

Optical fiber provides an ideal platform for distributed, *in situ* refractory health monitoring with limited disturbance to the refractory wall. There exists a variety of optical fiber-based technologies for distributed sensing, but to date, no single technology provides the necessary monitoring capabilities for extended exposures at high temperatures. Existing fully-distributed measurement technologies are based on two nonlinear effects in optical fibers, namely simulated Brillouin scattering (SBS) and stimulated Raman scattering (SRS). In the past decades, we have witnessed a great commercial success of these sensor systems and their rapidly growing applications in structural health monitoring, oil and gas exploration, and industrial process control. However, none of these technologies has been successfully demonstrated in very high-temperature sensing applications.

Another existing alternative is the fiber Bragg grating (FBG), which provides a means of quasi-distributed temperature measurement through the permanent writing of inline sensing structures, spaced along an optical fiber. FBG-based sensors can be classified in two categories: Type-I gratings are based on the artificially-induced grouping of charge in the silica fiber material and are quickly bleached at temperatures exceeding 500 ℃ [10, 11]; Type-II gratings are constructed by inducing micro-structured damage to the fiber in a periodic pattern [10]. These Type-II FBGs, often written with femtosecond laser radiation, have been investigated for high-temperature sensing applications [12, 13]. Although these structures have been shown to retain their grating strength, they may display irregular resonant wavelength drift with time at temperatures of 1000 ℃ and above, making useful measurements difficult to achieve [12]. The primary cause of the grating instability is the presence of dopants, which are used to define the light-guiding core from the surrounding cladding in conventional optical fibers [12]. At temperatures greater than 650 ℃, these dopants begin to diffuse throughout the glass, permanently changing the characteristics of the fiber and any FBG inscribed inside [14]. Under long-term exposure to high temperatures, dopant diffusion changes the effective refractive index in the core, leading to a slow drift of the grating.

One possible solution to the dopant diffusion problem is the use of photonics crystal fiber (PCF), which can be made entirely of pure fused silica [15]. Type-II FBG structures written in single-mode PCF are proven to be more stable than those in conventional fibers [16]. However, due to their reliance on permanent damage to the glass microstructure, Type-II FBGs have high transmission loss [10], making it impractical to multiplex the hundreds of gratings as needed for full-scale refractory monitoring. Ultimately, these drawbacks make FBG sensors less attractive for the proposed application.

2.3 Distributed sensing system developed in this research

In this research, we investigated several sensing technologies, both new and existing, to find the most capable one for further development into a long range distributed sensing system for the high temperature application of coal gasifier refractory health monitoring. The detailed technical requirements of the sensing system were development based on the inputs from our industrial partner, Eastman Chemicals, which will be described in the following chapter.

3 Determination of sensor technical requirements

In the early stage of the project, the specifications of the sensor were determined by working with Eastman Chemicals, as to provide sufficient and accurate information upon which the structural health condition of the gasifier refractory can be inferred. The technical specs are listed in Table 3-1.

Table 3-1. Technical requirements of the sensing system.

Parameter	Value
Temperature Range	Room temperature to 1000°C
Temperature Resolution	5-10°C
Frequency Response	5-10 minutes
Spatial Resolution	2-5 meters
Wrapping Density (Vertical)	1 meter

4 Comparison of distributed temperature sensing schemes

4.1 Available distributed sensing schemes

To date, several different methods have been developed for reliable applications in industry for distributed sensing. The distributed fiber-optic sensing needs to deal with two major issues: the origin of the detected signal and the method to locate the measurand. For the former, there are four main source of the signal: elastic scattering (Rayleigh scattering), inelastic scattering (Raman scattering, Brillouin scattering and fluorescence), nonlinear optical effect (Stimulated Raman scattering, Kerr effect, Stimulated Brillouin scattering) and mode conversion. For the latter, there are also four methods: optical time domain reflectometry (OTDR), optical frequency domain reflectometry (OFDR), sub-carrier frequency domain reflectometry (SCFDR) and pseudo-random encoded source modulation.

In terms of experiment setup, there are three basic detecting schemes, as shown in Figure 4-1.

Backscattering

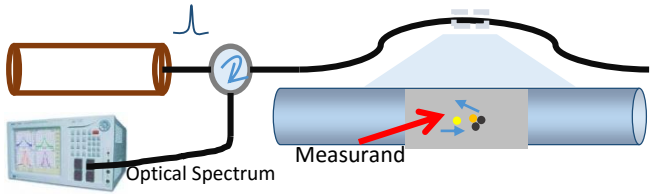

Forward detection

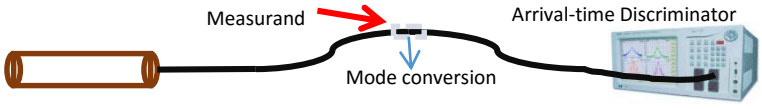

Pulse collision

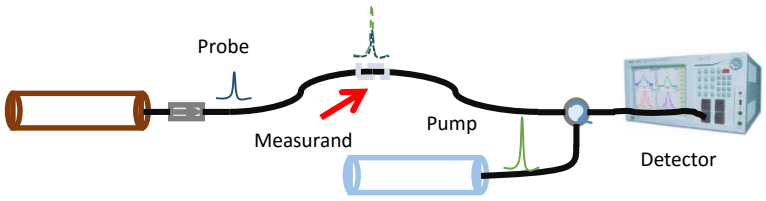

Figure 4-1. The basic detection schematics for distributed sensing technology.

The key parameters of the most advanced distributed sensing techniques and their features as for the time when the project begins are shown in Table 4-1 and Table 4-2. We can see that the resolution of these systems is very high and their applicable distance is quite long. However, none of them has been reported for very high temperature (>500 ℃) measurement. The goal of this project is to develop a distributed fiber sensor technology that is capable of operation at temperatures up to 1,000 ℃.

Table 4-1. State of the art in the laboratory.

Year	Spatial resolution (m)	Spatial range (km)	Measurand resolution	Measurand range(℃)	Basic principle
2011[17]		19	1.5 ℃	-10~50 ℃	Anti-stokes
2011[18]	2.5	50	1 ℃	20~50 ℃	BOTDA
2011[19]	3	0.3	1 ℃	25~55 ℃	Rayleigh-BOTDA
2010[20]	0.02	0.5	73 με	800 N/50 mm	Rayleigh & PM
2011[21]	2	120	45με/2.1°C	25~50 ℃	Raman-BOTDA

Table 4-2. Key parameters of commercial products.

Type	Company	Spatial resolution (m)	Spatial range (km)	Measurand resolution	Basic principle
NBX6020[22]	Neubrex	0.02	5	25με	Brillouin-OTDA
NBX6050[22]		0.1	5	4με/0.2℃	
OBR4600	Luna	10^{-5}	0.03	1με/0.1 ℃	Rayleigh-OFDR
		$2*10^{-5}$	0.07		
		10^{-3}	2		

4.2 Analysis and comparison of the different approaches

(1) Scattering:

There are three major types of back scattering when light propagates in an optical fiber, which include Rayleigh scattering, Raman scattering and Brillouin scattering, which are distinct from each other by their strengths and wavelengths (shown in Figure 4-2). Rayleigh scattering remains at the same wavelength as the source light and the other two scatterings shift for a certain wavelength. All these three have been utilized for distributed sensing.

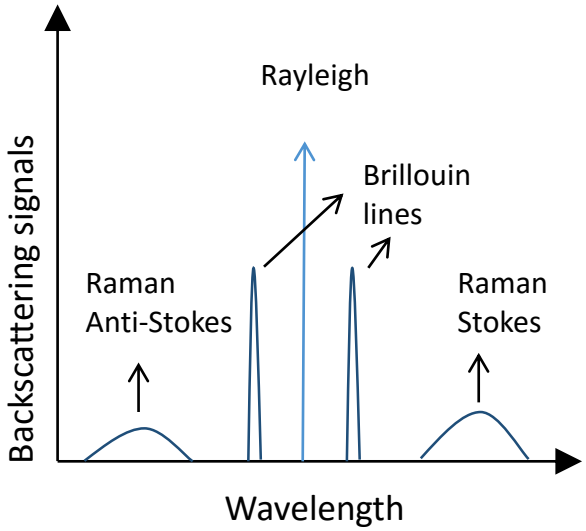

Figure 4-2. The spectra of the back scatterings.

a. Rayleigh scattering:

Rayleigh scattering is the result of elastic collision between the photons and atoms. Since there is no energy exchange in the collision, the backscattering wavelength is the same as the incident beam. This phenomenon has been utilized for distributed temperature or strain sensing via the optical frequency domain reflectometry [23].

b. Raman scattering:

Raman scattering is generated by inelastic collisions between photons and atoms. The specific relation between the intensities of Stokes and anti-Stokes lines are dependent on temperature, as shown in the following formula[24]

$$R(T) = \frac{I_{anti-Stokes}}{I_{Stokes}} = \left(\frac{\lambda_s}{\lambda_{a-s}}\right)^4 \exp\left(-\frac{hc\Delta\nu}{kT}\right) \qquad \text{Eq. 4.1}$$

where $\Delta\nu$ is the frequency shift from the incident light wavelength, λ_s is the central wavelength of Stokes line, λ_{a-s} is the central wavelength of anti-Stokes line, *k* and *h* are Boltzmann's and Plank's constants, respectively. Hence, we can measure the temperature by this phenomenon.

c. Brillouin scattering [25, 26]:

Brillouin scattering is the result of the inelastic collision between photons and the thermally excited acoustic phonons (not the vibration of the atom) which are induced by the light through electrostriction. Therefore, the scattered light undergoes the Doppler frequency shift, which can be used to measure the external factors [26]. Since the frequency shift is always very small (~11GHz at 1.5μm of optical wavelength), heterodyne detection methods are usually used to select the Brillouin lines from the Rayleigh scattering. Since the intensity of Brillouin lines is at least one order of magnitude higher than that of Raman lines, and the measurand affects the frequency of the backscattering signal [27] rather than the intensity as in the Raman scattering, Brillouin scattering has been extensively investigated in the past decade and has been applied to many fields.

(2) Nonlinear Effects

a. Stimulated scattering:

In pulse collision schemes, if the probe laser pulse can be amplified by the pump pulse due to the Raman or the Brillouin effect, and if the amplification properties such as intensity and frequency are influenced by the external factors, these factors could be measured indirectly.

b. Kerr effect:

Also if a pulse collision scheme is employed, the phase of the probe light is modulated by the pump pulse induced changes in the refractive index. However, the sensitivity of the Kerr effect to external parameters is in general rather weak. Some prior work has been conducted to investigate Kerr effect sensitivity to external parameters and their use for potential distributed sensing (See, e.g., [28]). Kerr effect describes the refractive index change because of the light travelling in the material. Since light is also electromagnetic wave, it can affect the polarization of the molecules, and hence change the dielectric constant of the material. This process is reported however not sensitive to the temperature [29].

(3) Mode conversion

In the forward probe light scheme, the mode conversion effect is often applied to determine the quantity of the measurand. The polarization modes (PMs) are most widely investigated due to their sensitivity to various external factors and the fact that PMs are easily separable. The conversion between different spatial modes such as LP_{01} and LP_{11} has also been investigated [30]. This is based on the linear dependence of fiber beat length on temperature [31]. In a pulse collision scheme [32], the strong pump pulse acts as a moving grating because of the beat between two polarization modes. Then the two modes of the probe pulse couple to each other when the beat length of the two spatial modes is equal to the pump-pulse-induced grating period.

(4) Optical Time-Domain Reflectometry (OTDR)

A high-intensity optical pulse is launched into a fiber under-test. Because of the distributed backscattering effect, a continuous signal can be detected in the backward direction. The signal properties, such as intensity, frequency or state of polarization are related to fiber parameters which may be influenced by external stimuli such as temperature or strain. Hence, the external measurand can be detected by the measurement of changes in the signal properties and the location can be determined by the arrival time of the signal.

(5) Optical Frequency-Domain Reflectometry (OFDR)

In order to overcome the low-duty-cycle drawback of OTDR, OFDR is proposed. Taking advantage of the high resolution of frequency detection compared with intensity detection, the OFDR method transfers the signal arrival time used in OTDR to signal frequency difference. For example, the frequency of a continuous wave laser is modulated by a saw-tooth shape signal. Then, by detecting the frequency of the backscattering signal, the corresponding delay time can be calculated, so does the corresponding location of the backscattering point. Usually, the interferometry method is applied to measure the frequency difference. OFDR can also be used in transmission schemes.

(6) Two-photon absorption

The two-photon absorption is one of the third-order nonlinear optical processes. It is basically the simultaneous absorption of two photons in order to excite a molecule from one state to a higher energy electronic state. It is generated if the phases are different between the generated polarization and the original electric field, which means the material cannot respond immediately to the applied electric field. The imaginary part of the third-order nonlinear susceptibility describes this kind of property of the material while the real part of the third-order nonlinear susceptibility describes the Kerr effect. Two-photon absorption can exhibit minimum interference depending on the location of the intermediate states and on the electro-magnetic field applied, which can be used to control the two-photon absorption efficiency [33]. Two-photon absorption also imposes limitations on the light intensity in a waveguide [34].

(7) Thermal nonlinear optical effects [35]

When a laser beam is travelling in a fiber, the fiber will absorb the light and transfer the energy of the light to thermal energy. The temperature variation will result in the change of refractive index. This phenomenon can be written as

$$\mathrm{n} = \mathrm{n}_0 + n_2^{th} I^{max} \qquad \text{Eq. 4.2}$$

where $n_2^{th} \approx 10^{-11} cm^2 / W$ for a continuous wave laser beam and $n_2^{th} \approx 10^{-16} cm^2 / W$ for a pulse laser beam. For a common laser and typical single mode fiber, $I \approx \frac{1W}{10\mu m^2} = 10^3 W / cm^2$, so the change of refractive index $\Delta n \approx 10^{-8}$, which is extremely difficult to measure.

(8) Parametric amplification [36]

Temperature variations can affect the group velocity dispersion in a fiber, thus leading to the parametric sidebands tunability. The experiment result shows there is 17 THz spectral shift with the temperature variation from 20 ℃ to 500 ℃.

(9) Specialty fibers

For an Erbium-doped fiber, the depth of the spectral hole burning depends on the temperature [37]. For an Ytterbium-doped fiber, the temperature dependence of photo-darkening is [38]

$$\text{absoption\_920nm}[dB/m] = -0.25T/°C + 245[dB/m] \qquad \text{Eq. 4.3}$$

For a crystal fiber, there will be time-correlated two-photon excited fluorescence. And the temperature variation results in a spectral shift, intensity change and decay time variation [39].

5 Four-wave mixing based sensing scheme

5.1 Theoretical analysis

In this section, a traveling long period grating (TLPG) generated through four-wave mixing (FWM) was evaluated for distributed temperature sensing. The TLPG is promoted with two optical waves which beat upon spatial overlap to yield an intensity modulation. The modulation is converted to a periodic refractive index modulation via the nonlinear Kerr effect. The induced TLPG will serve as an optical pump to initiate the core-to-cladding conversion of a third wave (as the probe), with a frequency shift defined by the energy conservation requirement of the process. The whole process can be studied in the context of an FWM process.

5.1.1 Governing Equations:

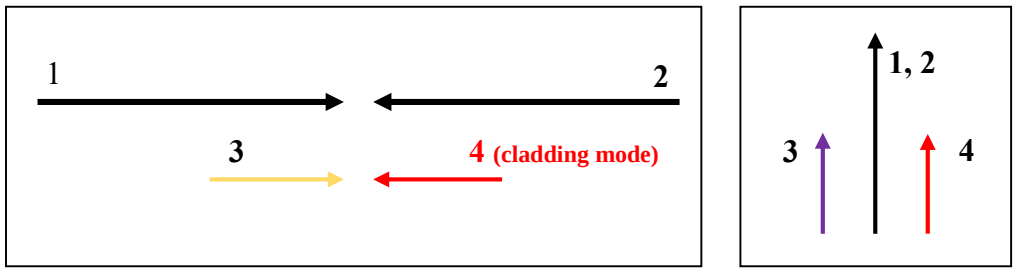

Figure 5-1. (a) Pump (1,2), signal (3) and idler(4) directions. (b) Energy diagram.

The system configuration and the frequency diagram of the proposed sensing scheme are provided in Figure 5-1, in which the two beating pump waves are counter-propagating, the probe is co-propagating with one of the pumps, and the generated cladding-mode wave (idler) will be counter-propagating with the probe. The governing equation for the process can be written as [40]

$$\begin{aligned}
\frac{dA_1}{dz} &= i\gamma\left[\left(|A_1|^2+2\left(|A_2|^2+|A_3|^2+f_2|A_4|^2\right)\right)A_1+2f_1A_2^*A_3A_4e^{i\Delta\beta z}\right]\\
\frac{dA_2}{dz} &= -i\gamma\left[\left(|A_2|^2+2\left(|A_1|^2+|A_3|^2+f_2|A_4|^2\right)\right)A_2+2f_1A_1^*A_3A_4e^{i\Delta\beta z}\right]\\
\frac{dA_3}{dz} &= i\gamma\left[\left(|A_3|^2+2\left(|A_1|^2+|A_2|^2+f_2|A_4|^2\right)\right)A_3+2f_1A_1A_2A_4^*e^{-i\Delta\beta z}\right]\\
\frac{dA_4}{dz} &= -i\gamma\left[\left(|A_4|^2+2f_2\left(|A_1|^2+|A_2|^2+|A_3|^2\right)\right)A_4+2f_1A_1A_2A_3^*e^{-i\Delta\beta z}\right]
\end{aligned} \qquad \text{Eq. 5.1}$$

In these equations, γ is the nonlinear coefficient of the optical fiber (the effect of effective mode field diameter will be accounted for by $f_{1,2}$) and

$$f_1 = \frac{\left\langle \varphi_s^* \varphi_i^* {\varphi_p}^2 \right\rangle}{\left[\left\langle \left|\varphi_s\right|^2 \right\rangle \left\langle \left|\varphi_i\right|^2 \right\rangle \left\langle \left|\varphi_p\right|^2 \right\rangle \left\langle \left|\varphi_p\right|^2 \right\rangle \right]^{1/2}} \quad \text{Eq. 5.2}$$

$$f_2 = \frac{\left\langle \left|\varphi_p\right|^2 \left|\varphi_i\right|^2 \right\rangle}{\left\langle \left|\varphi_i\right|^2 \right\rangle \left\langle \left|\varphi_p\right|^2 \right\rangle} \quad \text{Eq. 5.3}$$

$$\Delta\beta = \beta(\omega_3) - \beta(\omega_4) \quad \text{Eq. 5.4}$$

or

$$\Delta\beta = \beta(\omega_2) + \beta(\omega_3) - \beta(\omega_1) - \beta(\omega_4) \quad \text{Eq. 5.5}$$

for the scenario where the two pumps possess different wavelengths.

The above equations are a set of ordinary differential equations, traditional 'ode45' function in Matlab cannot be used for solving them, because the boundary conditions are not given at z=0. More advanced functions such as 'bvp4c' can be used. For more physical insights, the equations will be solved analytically after proper assumptions and approximations are made.

5.1.2 Analytical Solution

5.1.2.1 Simplified Coupled-Mode Equations

Assume that the pumps are very strong and are undepleted, Eq. 5.1 can be simplified to

$$\begin{aligned} \frac{dA_s}{dz} &= i\kappa_3 A_s + i\kappa A_i^* e^{-i\Delta\beta z} \\ \frac{dA_i}{dz} &= -if_2\kappa_3 A_i - i\kappa A_s^* e^{-i\Delta\beta z} \end{aligned} \quad \text{Eq. 5.6}$$

in which $\kappa_3 = 2\gamma\left|A_p\right|^2$, and $\kappa = f_1\gamma A_p^2$ are constants (proof of κ being constant is provided in Boyd, 3rd Ed., on p.350).

5.1.2.2 Solve Eq. 5.6 for Analytical Solution

Substituting $A_s = A_s' e^{i\kappa_3 z}$ and $A_i = A_i' e^{-if_2\kappa_3 z}$ into Eq. 5.6, we get:

$$\begin{aligned} \frac{dA_s'}{dz} &= i\kappa A_i'^* e^{-i\Theta z} \\ \frac{dA_i'^*}{dz} &= i\kappa^* A_s' e^{i\Theta z} \end{aligned} \quad \text{Eq. 5.7}$$

Note that A_s and A_s' only differ by a phase term. In the above equations,

$$\Theta = \kappa_3(1 - f_2) + \Delta\beta \quad \text{Eq. 5.8}$$

is the "generalized phase mismatch", consisting of the pure phase mismatch and the nonlinear phase mismatch caused by cross-phase modulation (XPM). The difference between the signal and idler in their overlapping with the pump waves produce the unbalanced XPM-induced phase delay, as manifested by the term f_2.

In order to solve Eq. 5.7, we perform the following substitution: $A_s' = a_s e^{-i\frac{\Theta}{2}z}$, $A_i'^{*} = a_i^{*} e^{i\frac{\Theta}{2}z}$, and we end up with a linear homogeneous differential equation set:

$$\begin{bmatrix} \frac{da_s}{dz} \\ \frac{da_i^*}{dz} \end{bmatrix} = \begin{bmatrix} i\frac{\theta}{2} & i\kappa \\ i\kappa^* & -i\frac{\theta}{2} \end{bmatrix} \begin{bmatrix} a_s \\ a_i^* \end{bmatrix} \qquad \text{Eq. 5.9}$$

Solving Eq. 5.9, the expression for the fields are obtained with B and C as constant factors to be determined by boundary conditions:

$$A_i' = \left(B\sin(\xi z) + C\cos(\xi z)\right) e^{-i\frac{\Theta}{2}z} \qquad \text{Eq. 5.10}$$

$$A_s' = -\frac{i}{\kappa^*}\left[\left(i\frac{\Theta}{2}B^* - \xi C^*\right)\sin(\xi z) + \left(i\frac{\Theta}{2}C^* + \xi B^*\right)\cos(\xi z)\right] e^{-i\frac{\Theta}{2}z} \qquad \text{Eq. 5.11}$$

In the above equations,

$$\xi = \left(\frac{\Theta^2}{4} + |\kappa|^2\right)^{1/2} \qquad \text{Eq. 5.12}$$

is the gain factor. Applying the boundary conditions yields

$$A_s'^{*}(0) = \frac{i}{\kappa}\left[\xi B - i\frac{\Theta}{2}C\right] \qquad \text{Eq. 5.13}$$

$$A_i'(L) = \left(B\sin(\xi L) + C\cos(\xi L)\right) e^{-i\frac{\Theta}{2}L} = 0 \qquad \text{Eq. 5.14}$$

The output intensity of the idler can be calculated as

$$\left|A_i'(0)\right|^2 = \frac{4|\kappa|^2 \sin^2(\xi L)}{\Theta^2 \sin^2(\xi L) + 4\xi^2 \cos^2(\xi L)} \left|A_s'(0)\right|^2 \qquad \text{Eq. 5.15}$$

Because the FWM process will simultaneously create a pair of signal and idler photons, the power increment of the signal should be equal to the value in Eq. 5.15, so the total gain of the signal will be:

$$G_s = \left(1 + \frac{4|\kappa|^2 \sin^2(\xi L)}{\Theta^2 \sin^2(\xi L) + 4\xi^2 \cos^2(\xi L)}\right) \qquad \text{Eq. 5.16}$$

5.1.2.3 Phase Matching

a. Degenerated Pump (Pump Wavelengths Are Identical)

For the case of degenerated pump, the pure phase mismatch is described by Eq. 5.4, and the generalized phase mismatch is obtained by substituting Eq. 5.4 into Eq. 5.8. The equation for phase matching is thus expressed as:

$$\omega_s n_s - \omega_i n_i = c\kappa_3 \left(f_2 - 1 \right) \qquad \text{Eq. 5.17}$$

where n_s and n_i are the effective refractive indices of the signal (fundamental core mode) and cladding (a particular cladding mode). Solving the above equation involves calculating the propagation constants of the fiber modes, and can be quite complex for analytical solutions. The software *OptiGrating* was used to yield numerical solutions.

a.1 Neglect the XPM Induced Phase Mismatch

Under this assumption, the phase matching condition is reduced to

$$\frac{1}{c}\left(\omega_s n_s - \omega_i n_i \right) = 0 \qquad \text{Eq. 5.18}$$

Nine lowest cladding modes were calculated to seek solution to the above equation, and the results are plotted below (the figure shows the numerical values for the left-hand-side of Eq. 5.18 versus wavelength). The calculation considers material dispersion, inter-modal dispersion and intra-modal dispersion.

In Figure **5-2**, the solution for the core mode is also plotted for comparison. As shown in the figure, for the core mode, the only solution overlaps with the pump wavelength, which means that all the wavelengths (including signal, pumps, and idler) are degenerated. This renders the signal and idler inseparable from the pumps, and prevents using the core mode for all the interacting waves. This can be intuitively understood by linearization of Eq. 5.18 around the pump wavelength. Both ω and n_{eff} decrease as wavelength increases. This means the sole solution is the wavelength where signal and idler coincide (this is not true if the pumps are non-degenerated, as will be discussed in the next subsection). However, if the idler is in the cladding, its refractive index is significantly smaller, this offset value will counteract the effect from ω, and guarantee a solution deviating from the pump wavelength.

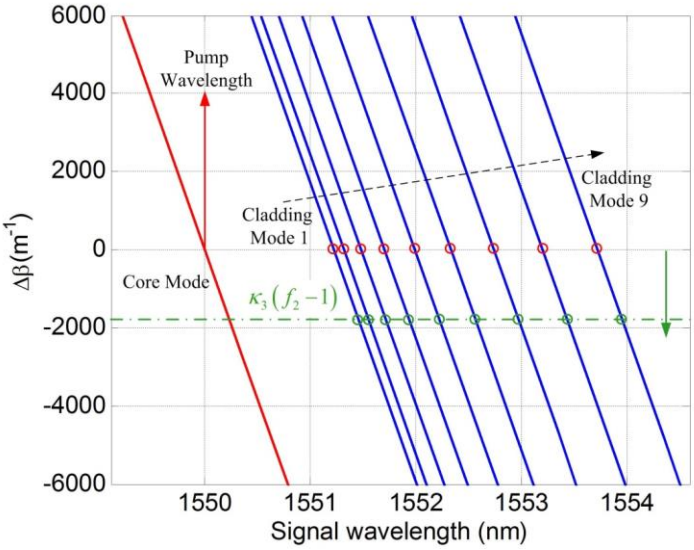

Figure 5-2. Solution of Eq. 5.18 for the nine lowest cladding modes; solution for the fundamental core mode is also provided for comparison. The red circles on the x-axis represent the solutions. The horizontal green line is the right-hand-side of Eq. 5.17, which considers the influence of the XPM-induced phase mismatch. This effect, as shown in the figure, will slightly shift the solution to longer wavelengths, but not significant. The position of the green line in the figure is for pump power ~1MW. The wavelength shift at such a high pump level is only less than 0.5nm.

a.2 <u>Influence of the XPM Induced Phase Mismatch</u>

Under this assumption, the phase matching condition is

$$\frac{1}{c}\left(\omega_s n_s - \omega_i n_i\right) = \kappa_3\left(f_2 - 1\right) \qquad \text{Eq. 5.19}$$

Note that the right-hand-side of Eq. 5.18 is always negative. This means in Figure **5-2**, instead of seeking a solution on the x-axis, solutions will be sought on a horizontal line at y= $k_3\left(f_2 - 1\right)$, which is below the y=0 line. As shown in the figure, all the solutions will be shifted to longer wavelength side, but not by much. The green line shown in the figure represents the case where the pump power is ~1MW, and clearly the wavelength shifts are less than half a nanometer. This leads to the conclusion that for the rest of the analysis we can neglect the influence of the XPM induced phase mismatch to simplify the following analysis. However, due to the extremely sharp gain profile (section 2.4), the stabilization of the pump power is very important to minimize XPM-induced spectral shifts.

b. <u>Non-Degenerated Pump</u>

For the case of non-degenerated pump, the condition for phase matching is expressed as:

$$\frac{1}{c}\left(\omega_s n_s - \omega_i n_i\right) = -\left[\kappa_3\left(1 - f_2\right) + \frac{1}{c}\left(\omega_{p2} n_{p2} - \omega_{p1} n_{p1}\right)\right] \qquad \text{Eq. 5.20}$$

Compared to Eq. 5.19, the above equation will further "offset" the horizontal line in Figure **5-2**, and the solutions will accordingly shift toward longer wavelengths, if $\omega_{p2} n_{p2} - \omega_{p1} n_{p1}$ is greater

than zero (this condition is satisfied if $\lambda_{p1} > \lambda_{p2}$, it should be noted that the labeling of subscripts follows the tradition in Figure 5-1).

5.1.2.4 Bandwidth and Gain

a. Resonance Behavior

If the phase matching condition is satisfied ($\Theta = \kappa_3(1 - f_2) + \Delta\beta = 0$), the expression for the parametric gain (Eq. 5.16) will be simplified to:

$$G \approx 1 + \tan^2(|\kappa| L) \qquad \text{Eq. 5.21}$$

Visible in Eq. 5.21 is the fact that the parametric process exhibits a series of "resonance points" when the following condition is satisfied:

$$|\kappa| L = \frac{\pi}{2} + N\pi, N = 0,1,2,3... \qquad \text{Eq. 5.22}$$

It is observed that the gain will approach infinity at these resonance points, which is unrealistic to happen. This is due to the undepleted pump assumption, which assumes the pumps to be "infinitely strong". In reality, pump depletion will prevent the gain from being infinite. However, there do exist such resonance points for maximal gain if the pump power and interaction lengths are adjusted for optimization according to Eq. 5.22.

b. Minimum Pump Power for Resonant Operation

Recall the expression for $|\kappa|$: $|\kappa| = \gamma f_1 P_p$, in Eq. 5.22, L can be regarded as the spatial resolution (L_{res}). This requires the following equation to hold for the minimum pump power required to reach the resonance operation:

$$\gamma f_1 P_p \cdot L_{res} = \frac{\pi}{2} \Rightarrow P_p = \frac{\pi}{2\gamma f_1 L_{res}} \qquad \text{Eq. 5.23}$$

If L_{res} =1 m, γ = 0.001W^{-1}m^{-1}, f_1=0.1, we have P_p= 15708W.

c. Off-Resonance Bandwidth

As discussed above, it is impossible to calculate the gain profile at resonance points due to the limitation imposed by the analytical model. In this subsection, we will calculate the gain profile at off-resonance points. By the use of the following operation condition: L_{res} =1 m, γ = 0.001W^{-1}m^{-1}, f_1=0.1, P_p= 500W, the system is adjusted to off-resonance, and we plot the gain profile using Eq. 5.16, where phase mismatch is calculated using Eq. 5.4 numerically. Unlike the co-propagation configuration used for parametric amplifier, the model predicts the gain bandwidth of the counter-propagation configuration to be very narrow, in the sub-pm range (100MHz).

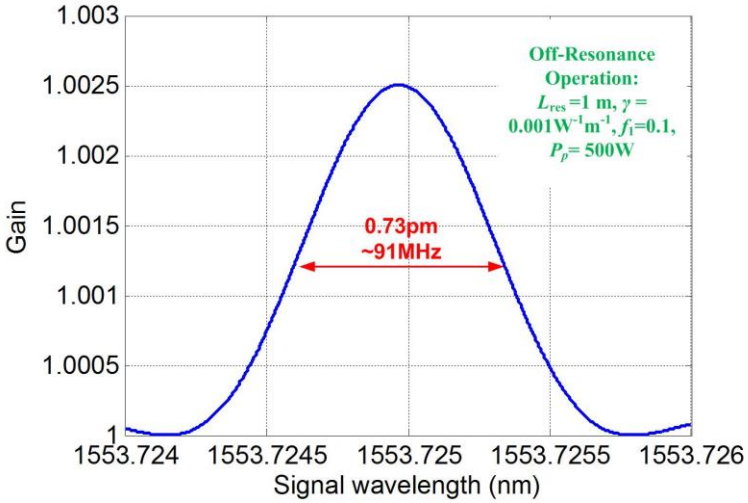

Figure 5-3. Calculated gain profile using Eq. 5.16, operation condition was set to off-resonance by L_{res} =1 m, γ = 0.001W^{-1}m^{-1}, f_1=0.1, P_p= 500W.

5.1.2.5 Summary of the Analytical Model

The limitations imposed by the applied analytical model are summarized in this subsection as follows:

a. Undepleted pump assumption is not justified if significant energy conversion from the pump to the signal and idler exists, e.g., resonant operation;

b. The model does not account for the dynamic shape of the pulses, which renders the model a "static" approximation;

c. The model does not consider the depletion of the idler, i.e., the idler will be re-coupled back into the pump given sufficient interaction length. In reality, this is not true: once the idler is generated (in the cladding), it will be depleted (absorbed by the fiber coating, or scattered/absorbed by the outer environment in direct contact with the bare fiber, etc.).

5.1.3 Temperature Dependence of the Gain Profile

If the core and cladding have the same thermo-optic coefficients (here defined as $\sigma = dn/(ndT)$), and if the thermal expansion of the fiber is neglected, this would lead to the fact that the effective refractive indices of the modes (including core and cladding modes) will be dependent on the temperature change at the same ratio, as expressed by:

$$n_{eff,i}\left(1+\sigma\Delta T\right), i \text{ is the mode index} \qquad \text{Eq. 5.24}$$

By applying Eq. 5.24 to Eq. 5.19, we can find that the phase matching point will be independent on temperature changes. However, the condition that "refractive indices of different modes have the same thermo-optic coefficients" is not true in reality, factors such as different compositions of the core and cladding, thermal expansion, and the influence of higher-order dispersions, will subsequently lead to different thermo-optic coefficients for different fiber modes. For example, if a photonic crystal fiber or a ClearCurve fiber is used, the large proportion of air in the cladding region would result in very different thermo-optic coefficients between the core and cladding

modes. In the following simulation, we assume the core and cladding to have slightly different thermo-optic coefficients (TOC) (0.1% difference), such as the TOC of the core mode is 1×10^{-5}, and the cladding mode TOC is 0.999×10^{-5}. This slight difference will lead to a clear spectral shift in the parametric gain profile if temperature change is merely 10°C, as shown in Figure 5-4 (thermal-expansion effect is neglected), the condition for the simulation is L_{res} = 1 m, γ = $0.001W^{-1}m^{-1}$, f_1 = 0.1, P_p = 500W. This also implies a system design merit: if temperature is to be measured, the selected fiber should exhibit large difference between the core and cladding TOC; in opposite, if the application requires temperature-independency, the fiber chosen should have a TOC difference between the core and cladding as small as possible.

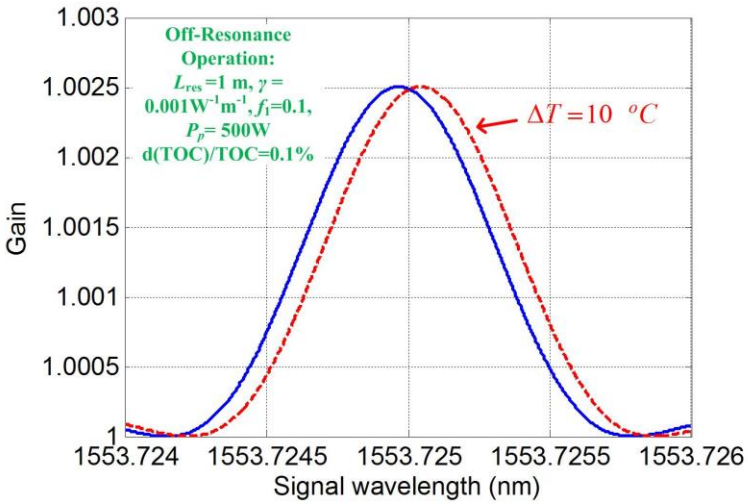

Figure 5-4. Spectral shift of the parametric gain profile caused by 10 ℃ temperature change, is L_{res} =1 m, γ = $0.001W^{-1}m^{-1}$, f_1=0.1, P_p= 500W, and the TOC of the core and the ninth cladding modes are set to 1×10^{-5} and 0.999×10^{-5} respectively.

5.2 System design

5.2.1 Design of system using Kerr effect and requirements estimation

A preliminary design using Kerr effect to generate T-LPG is shown in Figure 5-5. A continuous wave at about 1550 nm is modulated by a $LiNbO_3$ modulator driven by a microwave signal. The microwave signal is generated by a 40 GHz resonator and amplified by an amplifier. After the high speed modulator, another low speed modulator, which is driven by a waveform generator, is used to shape the LPGs. At the output of the second modulator, the optical power is relatively low to be directly amplified by a booster optical amplifier due to the insertion loss of modulators and loss introduced by modulation, so the 40 GHz optical is first amplified by a pre-amplifier to a suitable level, and then amplified by a booster to a high level. The sequences of pulses with high peak power are then launched into a section of sensing fiber via a circulator, generating a travelling LPG by the Kerr effect. At the other end of the sensing fiber, a broadband source, which acts as a probe, is injected into the fiber, propagating in the opposite direction. An isolator is inserted between the broadband source and the sensing fiber to avoid damage. The broadband light will be collected at Port 3 of the circulator and then analyzed using an optical spectrum analyzer (OSA).

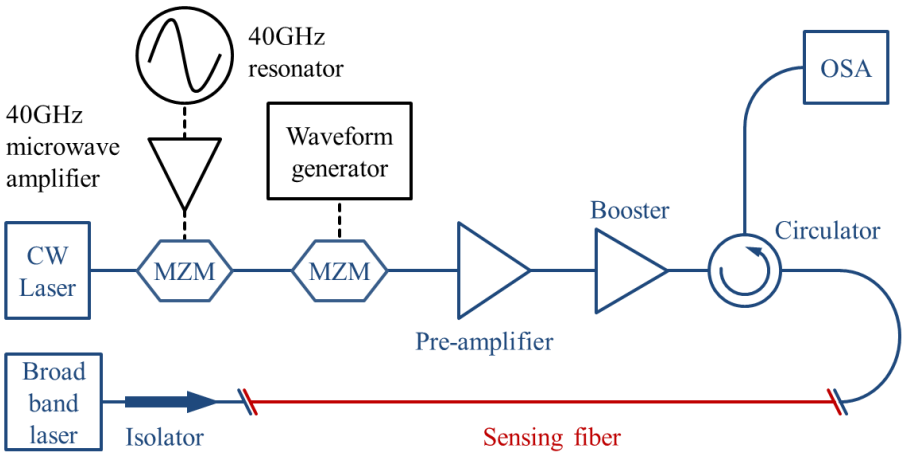

Figure 5-5. System using Kerr effect to generate T-LPG

The key issue in this system is the saturate power of erbium-doped fiber amplifiers (EDFAs), which directly affect the refractive index difference of the LPG. To produce a refractive index difference of 10^{-7}, the required peak power is about 290W or about 55dBm ($n_2 = 2.7 \times 10^{-16} cm^2/W$, field diameter = 5 μm).

Assuming each T-LPG includes 200 periods (corresponding to a length of 1 m), and the repetition rate of gratings is 200 kHz (corresponding to a distance of 1,000m between two adjacent LPGs), then the peak power will be 33dB higher than the average power, as a result the required average power will be 22dBm. This is much lower than needed, because we did not consider the second modulation before. Therefore if we have an EDFA which has a saturation output power of 40dBm, the peak power can be more than 5000W and the generated refractive index difference will be in the order of 10^{-6}.

There are other issues about the system design. The LPG is travelling so fast that we have to collect information fast enough to guarantee a reasonable spatial resolution. Obviously the typical speed of an OSA is not enough to do this. Thus other data collection methods should be used, for example, using a tunable laser as probe and oscilloscope with a high sampling rate to collect the data.

5.2.2 Survey of available commercial products

The previous design requires a variety of special optical or optoelectronic devices. Work was carried out to find the availability of such desired components.

a. Laser at 1550 with high output power:

IPG Photonics offers a series of CW lasers at 1550 nm with high output power. ELR series has different models whose output power ranges from 10 W to 100 W. Of those models, ELR-50-1550 has output power of 50 W and its price is $41,300.

Manlight also provides series fiber lasers at 1550 with different output power. Their ML**-CW-TKS-1550 series have output power ranging from 1W to 30W. Price for a 1W version is €4,117.

b. 40GHz modulators:

High speed modulators are easier to get. A number of companies provide $LiNbO_3$ modulators at the speed of 40GHz, or even higher. Oclaro, Fujitsu, Thorlabs, Versawave, and Eospace have 40G modulators and price ranges from $4350 to $7500, depending on the bandwidth. Fujitsu has 100GHz modulators. Maximum input power of these modulators is usually 100mW. In this case, we don't need CW laser with high power, 1W will be enough.

c. EDFA with high saturate output power:

EDFA is a key component in the system, the higher its output power, the better the performance. Most of commercial EDFAs provide a saturation output power less than 30dBm, but few companies do have EDFAs with very high output power. Manlight has an EDFA with 43dBm output power. The price for PM version is $35295 and $29411 for non-PM version. It is assured that this EDFA can work well when input signal has a frequency of 40GHz. IPG Photonics' EAR series and EAR-LP series EDFAs can provide output power as high as 100W (50dBm).

d. Relative microwave components:

A 40GHz microwave source is required to generate an LPG with a period of 5mm. Miteq has a dielectric resonator oscillator (PLDRO40000) with output frequency ranging from 26.8GHz to 40GHz. Its output power is 10dBm (2V). Considering connection loss, this will not be high enough to drive a $LiNbO_3$ modulator. Miteq provides several amplifiers with narrow bandwidth and high speed. Their output powers range from 25dBm to 30dBm and prices range from $2830 to $3475.

5.3 Calculation and experimental investigation of LPG coupling

Traditional LPGs usually have periods of a few hundreds of microns. But in order to reduce the requirement of microwave's frequency, LPG with a period of about 5mm is preferred, corresponding to a driving microwave frequency of 40GHz. Computational simulation and experimental investigation have been conducted to investigate the possibility of coupling between core-mode and cladding-modes under such conditions.

5.3.1 Simulation using OptiGrating software

When the refractive index difference is 2×10^{-4}, the transmission spectrum of the LPG is calculated when the period Λ is 0.75mm, 3mm and 5mm, as shown in Figure 5-6 (a),(b) and (c), respectively.

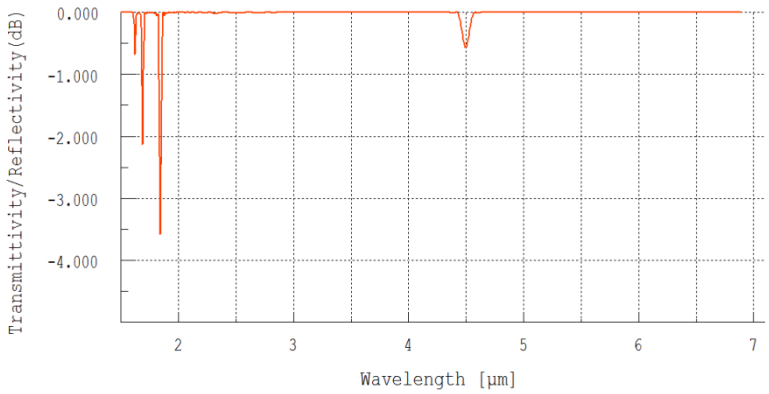

(a) Λ=0.75mm

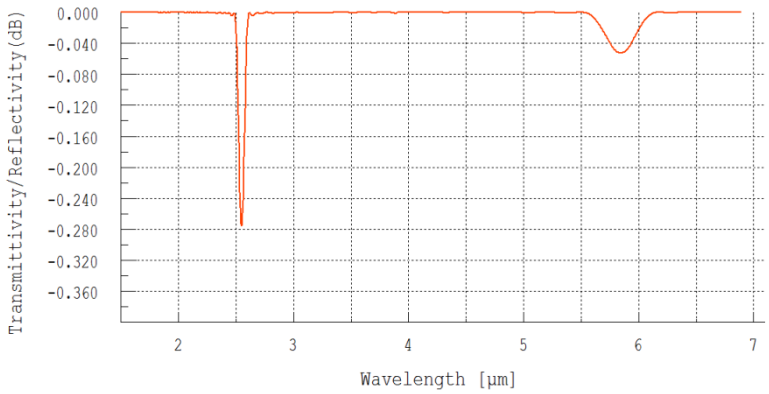

(b)Λ=3mm

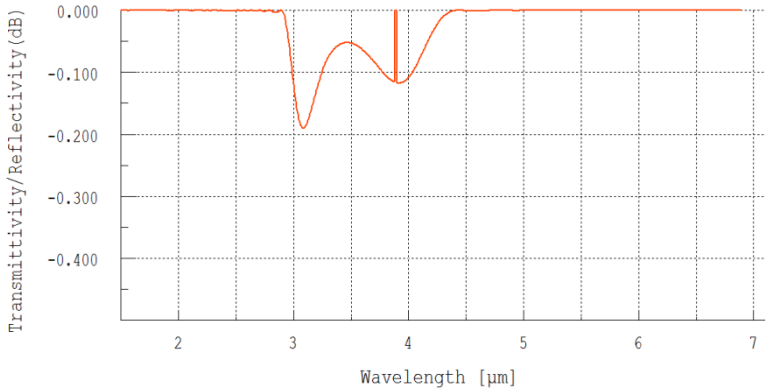

(c)Λ=5mm

Figure 5-6. Transmission spectra of LPG with different periods.

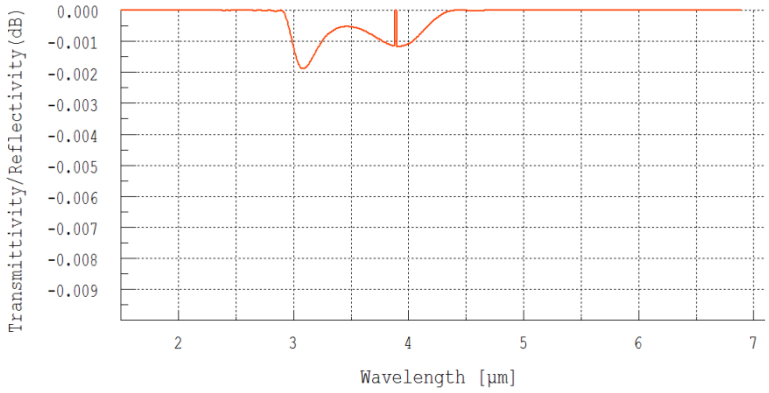

Figure 5-7. Transmission spectrum of LPG with Λ=5mm and Δ=2×10^{-5}.

Simulation results show that when the LPG period increases, the position of the spectral dip shifts toward longer wavelength, with a decreasing depth. When Λ=3mm, the wavelength of dip is shifted to 2.5μm and the depth is about 0.3dB. When Λ=5mm, the wavelength of dip is shifted

to more than 3μm and depth is less than 0.2dB. When the refractive index difference is reduced to 2×10^{-5}, the depth of dip is less than 0.002dB, as shown in Figure 5-7. In this case, the signal will be too weak to be detected.

5.4 Demonstration of static ultra-long period grating

5.4.1 Mechanically induced LPG

LPGs were generated by pressing objects with periodical grooves onto the fiber. LPGs with 3 different periods were tested. A supercontinuum laser was used as the light source, and an OSA was used to record the transmission spectrum. The spectral range of the OSA covers from 350nm to 1750nm.

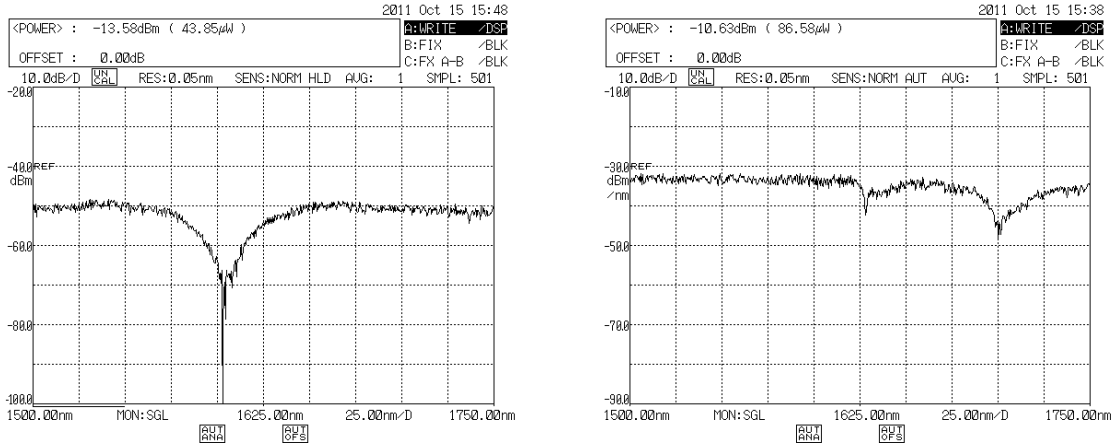

(a)Λ≈750μm (b) Λ ≈550μm

Figure 5-8. Transmission spectra obtained on LPGs with different periods.

Figure 5-8 (a) and (b) show the transmission spectra when the periods of the LPG are 550 μm and 750 μm. The wavelengths of the strongest dips are about 1600 nm and 1700 nm respectively. It shows that the dips are still in the range of detection.

When the period of LPG is increased to about 3mm, a dip can still be measured within the range of our OSA, and its wavelength is about 1690 nm. Comparing with the previous two cases, this dip is very wide and shallow. A possible reason for the large bandwidth may be the tool used to generate the LPG, which has square shape teeth whereas the previous two pressing tools have triangle teeth.

When the period is changed, the cladding mode to which the core mode is coupled may also change, so the wavelength and the coupling coefficient will change as well. When the LPG period is 3mm, the mode coupling occurred between the LP_{01} mode and a cladding mode whose lateral field distribution has a low overlap with that of the LP_{01} mode, so the coupling efficiency is low and the dip is shallow.

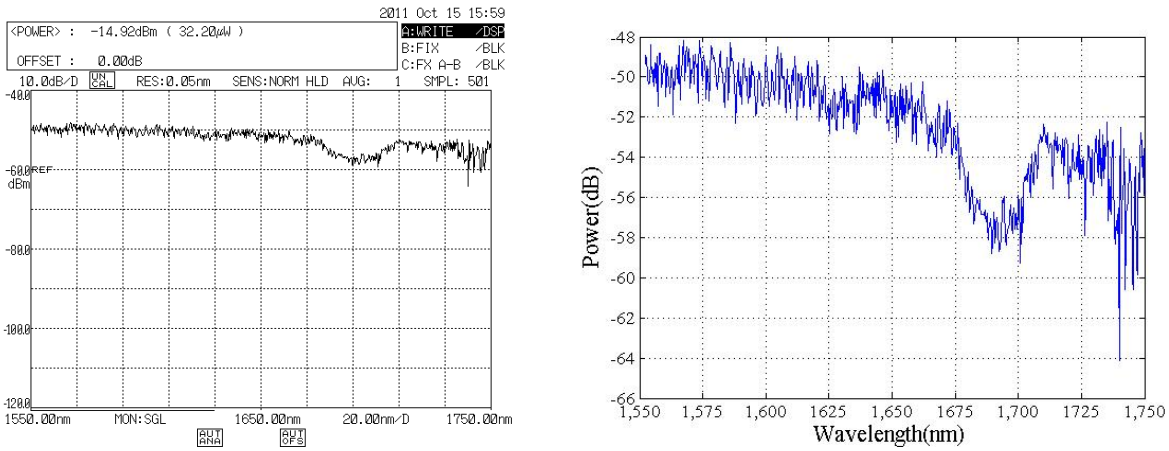

(a) Spectrum of transmission (b) Details of spectrum

Figure 5-9. Transmission spectra when Λ≈3mm.

Experimental results are quite different from the results of simulation. Also, when the order of the grating is changed to be more than 1, the calculated spectrum using OptiGrating has no variation. The results show that there are spectrum variations when the LPG period is large (3mm). Besides, there are two factors that should be noted. Firstly, the dip is fairly wide, which could affect the detection accuracy. A slight wavelength shift won't be detectable in this case. Secondly, in the experiment, the fiber was pressed very hard using a screw. It is questionable whether the optical Kerr effect can provide index modulation with a similar strength.

5.4.2 Electric arc induced LPG

The experimental setup of the static LPG measurement is shown in Figure 5-10. A splicer is used to introduce refractive index difference through electric arc, and refractive index difference can be changed by changing the arc duration and arc power. A step motor is used to move the fiber step by step to control the grating period. Limited by the resolution of the step motor, which is about 3mm, gratings with periods of 3mm and 6mm were made.

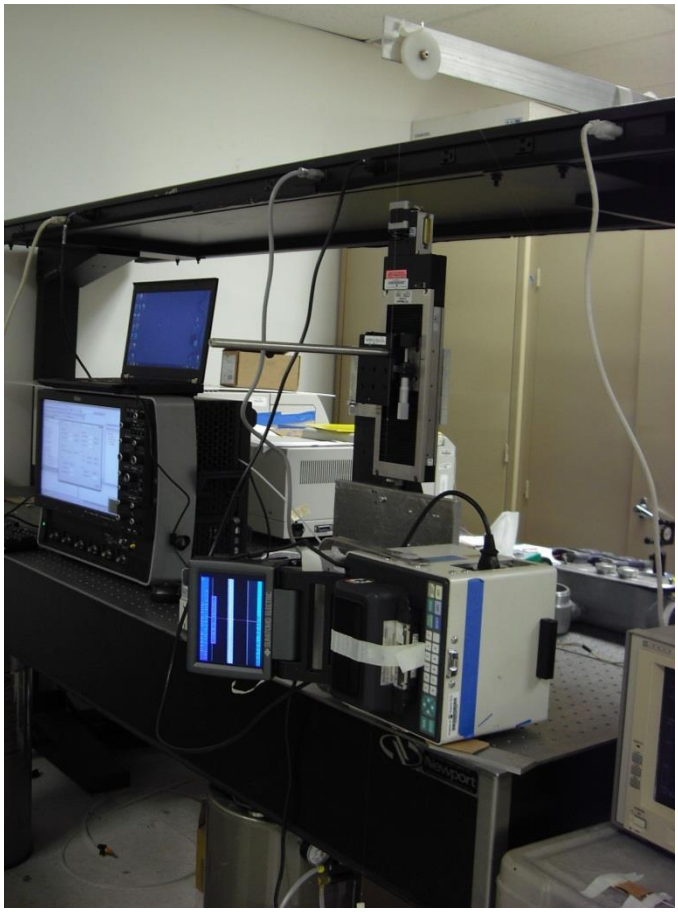

Figure 5-10. Setup of grating demonstration

To find the best splicing condition, an LPG with 500um was made first. Meanwhile, the transmission spectrum was monitored by the use of a supercontinuum source and an OSA. When significant dips were observed, the condition was recorded.

When demonstrating 3mm grating, the transmission spectra were also monitored simultaneously. It is noticed that under the same condition of the 500um LPG, no significant changes in spectrum were observed when the number of period is 26. So the arc power and arc duration were both increased a little. After another 20 arcs, spectral dips became obvious. The transmission spectra were taken under different numbers of periods are shown in Figure 5-11. Dips were observed when N was increased to 47 and became deeper when N was increased to 66.

When N=125, five dips were observed in the range of 1150 nm to 1750 nm and the depths of them were all greater than 1 dB, as shown in Figure 5-12. The wavelength of the deepest dip was about 1685 nm, and the other four were about 1450 nm, 1490 nm, 1570 nm and 1607 nm.

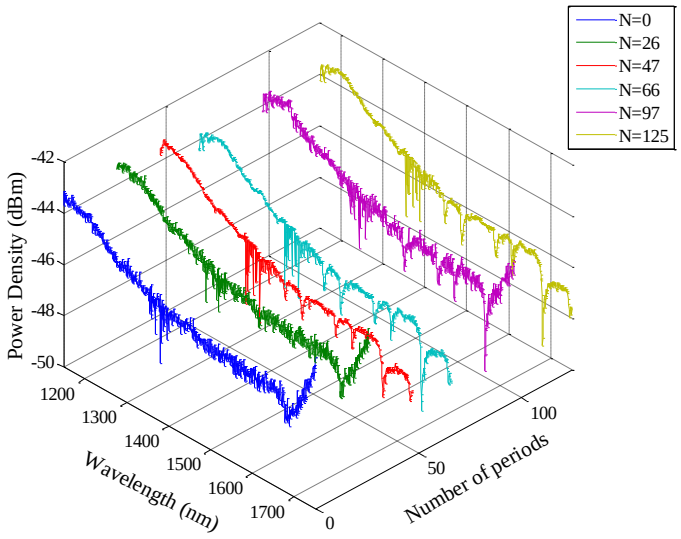

Figure 5-11. Transmission spectra of 3 mm LPG with different number of periods.

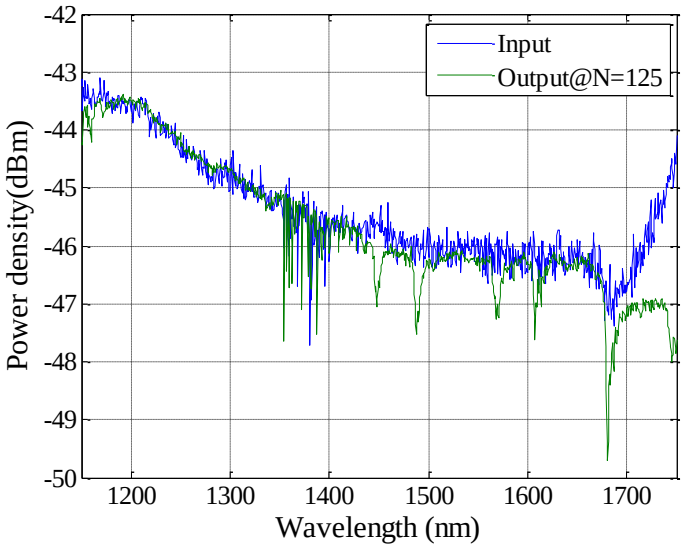

Figure 5-12. Transmission spectrum of 3 mm LPG with 125 periods.

Similarly, transmission spectra of LPG with period of 6 mm were also taken, shown in Figure 5-13. As N increases, changes in spectrum became more notable. When N reaches 110, several dips appeared in the range of OSA's detection but they were shallow and almost covered by noise. When N reached 200, more than 10 dips could be observed.

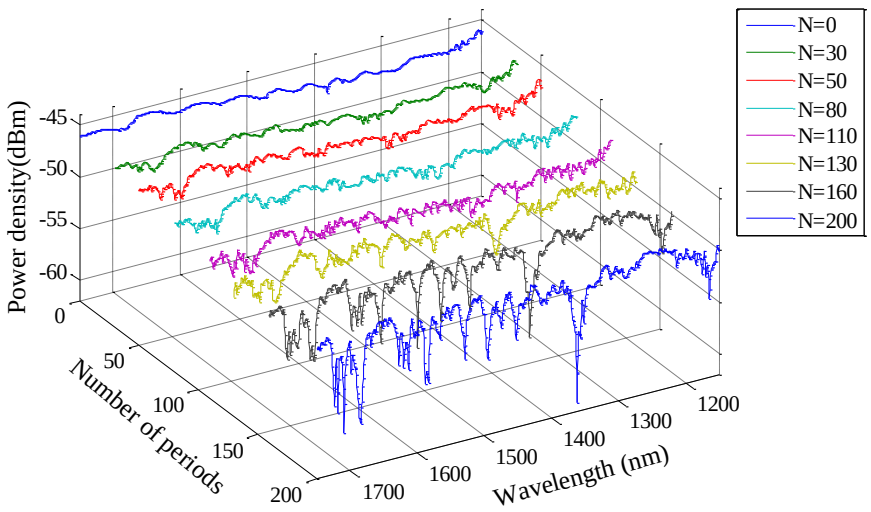

Figure 5-13. Transmission spectra of 6 mm grating with different numbers of periods.

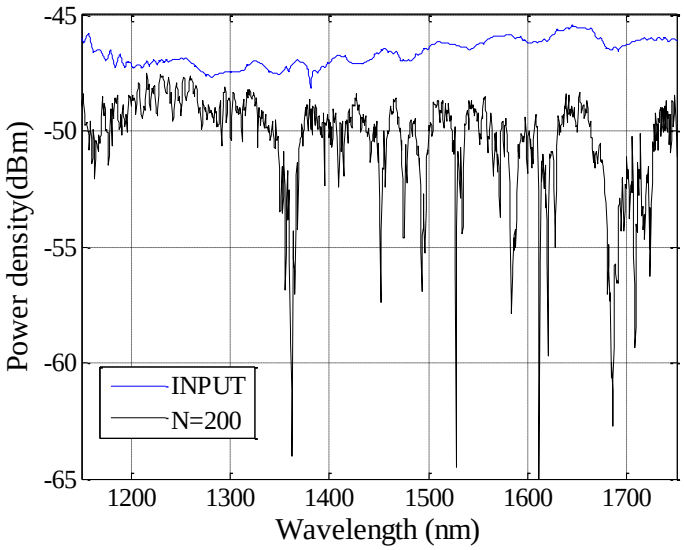

Figure 5-14. Transmission spectrum of 6 mm grating with 200 periods.

Transmission spectrum of the LPG when N = 200 is shown in Figure 5-14. It is noticed that the depths of most peaks were greater than 5 dB. Four of them had depth greater than 10 dB. The central wavelengths are about 1365 nm, 1530 nm, 1610 nm and 1690 nm.

Compared with the spectrum from the LPG with 3mm period, the one with 6 mm period shows more dips with greater depths. This result is well expected since the latter one has more periods (200) compared to former one (125). It is also noticed that transmission spectrum of the 6 mm LPG is not as clear as the one of 3 mm LPG, which is due to a poorer uniformity. Also, more periods will result in more insertion loss and instability.

The goal of this experiment is to verify if an LPG with a period of about 5 mm can lead to observable mode coupling in the range of the OSA's detection spectral range, and according to

the results, the answer is positive. However, when the Kerr effect is applied to generate the LPG, the refractive index modulation is expected to be weaker than the static LPG, which will be further investigated.

5.5 Analysis of influence of index variation on LPG

Limited by the modulation speed, we have to use an LPG with a period of 5mm to demonstrate mode coupling between the core mode and cladding modes. In order to have significant core-cladding mode coupling, the phase matching condition between the core mode and a certain cladding mode should be met:

$$\Delta\beta = \beta_{core} - \beta_{clad} = m\frac{2\pi}{\Lambda} \qquad \text{Eq. 5.25}$$

When m is a large integer, even when Λ is much greater than conventional periods of LPGs, such as 500μm, the phase matching condition can also be met. This is also the explanation to previous experiment based on an LPG with periods of 3mm and 6mm made by a thermal fusion splicer.

For a fiber grating, the mode coupling equations are:

$$\begin{aligned}\frac{dA_\mu}{dz} &= i\sum_\nu A_\nu (K_{\nu\mu}^t + K_{\nu\mu}^z) exp[i(\beta_\nu - \beta_\mu)z] \\ &\quad + i\sum_\nu B_\nu (K_{\nu\mu}^t - K_{\nu\mu}^z) exp[-i(\beta_\nu + \beta_\mu)z] \\ \frac{dB_\mu}{dz} &= -i\sum_\nu A_\nu (K_{\nu\mu}^t - K_{\nu\mu}^z) exp[i(\beta_\nu + \beta_\mu)z] \\ &\quad - i\sum_\nu B_\nu (K_{\nu\mu}^t + K_{\nu\mu}^z) exp[-i(\beta_\nu - \beta_\mu)z]\end{aligned} \qquad \text{Eq. 5.26}$$

where A and B are the amplitudes of the transverse mode fields travelling in z and –z directions, respectively. $K_{\nu\mu}^t$ and $K_{\nu\mu}^z$ are the transverse and longitudinal coupling coefficients between modes ν and μ. Longitudinal mode coupling coefficient is always few order of magnitude lower than transverse mode coupling coefficient, so it can be ignored in the analysis. $K_{\nu\mu}^t$ then becomes:

$$\begin{aligned}\Delta n(z) &= \Delta n_{max}(z)\left[1 + m \cdot f_\Lambda(z)\right] \\ K_{\nu\mu}^z(z) &= \kappa_{\nu\mu}(z)\left[1 + m \cdot f_\Lambda(z)\right]\end{aligned} \qquad \text{Eq. 5.27}$$

in which $\kappa_{\nu\mu}(z)$ is the coupling constant calculated from the mode field distribution and the envelop of the grating, m is the modulation depth, and $f_\Lambda(z)$ is a periodical function which represents the index variation of the LPG, having maximum and minimum value of 1 and 0, respectively. When the grating is sinusoidal, $K_{\nu\mu}^t$ can be written as:

$$K_{\nu\mu}^{z}(z)=\kappa_{\nu\mu}(z)\left[1+m\cos\left(\frac{2\pi}{\Lambda}z\right)\right] \qquad \text{Eq. 5.28}$$

Substituting $K_{\nu\mu}^{t}$ in the coupling equations and neglect the terms with rapid oscillation (phase matching condition is not met in these terms), we have the mode coupling equations for a long period grating as

$$\frac{A^{co}}{dz}=iA^{co}\kappa_{01-01}^{co-co}+i\sum_{\nu}\frac{m}{2}A_{1\nu}^{cl}\kappa_{1\nu-01}^{cl-co}e^{-j(\beta_{01}^{co}-\beta_{1\nu}^{cl}-\frac{2\pi}{\Lambda})z}$$
$$\sum_{\nu}\left[\frac{dA_{1\nu}^{cl}}{dz}=i\frac{m}{2}A^{co}\kappa_{1\nu-01}^{cl-co}e^{j(\beta_{01}^{co}-\beta_{1\nu}^{cl}-\frac{2\pi}{\Lambda})z}\right] \qquad \text{Eq. 5.29}$$

In this case, for strict phase matching, the power of the exponential should be $2m\pi$, which means

$$(\beta_{01}^{co}-\beta_{1\nu}^{cl}-\frac{2\pi}{\Lambda})z=(\Delta\beta-\frac{2\pi}{\Lambda})z=2m\pi \qquad \text{Eq. 5.30}$$

When the waves propagate, z increases, so the only case that phase matching is met for an ideal sinusoidal grating is m=0 and $\Delta\beta=\frac{2\pi}{\Lambda}$.

For an LPG whose index variation follows periodical function $f_{\Lambda}(z)$, a general mode coupling equation can be obtained in a similar way. Since $f_{\Lambda}(z)$ is a periodic function, it can be written by the following expression:

$$f_{\Lambda}(z)=\sum_{n=-\infty}^{\infty}F_{n}e^{jn\frac{2\pi}{\Lambda}z} \qquad \text{Eq. 5.31}$$

where $F_{n}=\frac{1}{\Lambda}\int_{-\frac{\Lambda}{2}}^{\frac{\Lambda}{2}}f_{\Lambda}(z)e^{-jn\frac{2\pi}{\Lambda}z}dz$, representing the amplitude of the *n*-th order harmonic.

By inserting the expression of $f_{\Lambda}(z)$ above into the original coupled mode equations and neglecting the rapid oscillating terms, we can get equations for the LPG as follows:

$$\frac{dA^{co}}{dz}=iA^{co}\kappa_{01-01}^{co-co}+i\sum_{\nu}\left[mA_{1\nu}^{cl}\kappa_{1\nu-01}^{cl-co}\sum_{n=1}^{\infty}\left(F_{n}e^{j(\beta_{1\nu}^{cl}-\beta_{01}^{co}+n\frac{2\pi}{\Lambda})z}\right)\right]$$
$$\sum_{\nu}\left[\frac{dA_{1\nu}^{cl}}{dz}=imA^{co}\kappa_{1\nu-01}^{cl-co}\sum_{n=1}^{\infty}\left(F_{n}e^{j(\beta_{01}^{co}-\beta_{1\nu}^{cl}-n\frac{2\pi}{\Lambda})}\right)\right] \qquad \text{Eq. 5.32}$$

From the equations above we know that when $f_{\Lambda}(z)$ is not sinusoidal, there are more than one frequency, and these high order components can meet phase matching condition even when Λ is large:

$$\beta_{01}^{co} - \beta_{1\nu}^{cl} = n\frac{2\pi}{\Lambda} \qquad \text{Eq. 5.33}$$

Mode coupling strength depends on not only the refractive index difference but also F_n.

In the previous experiment, $f_\Lambda(z)$ can be described by a Gaussian function or a super Gaussian function in one period. Assuming the full width at half maximum (FWHM) is 4%, amplitudes of each harmonics when $f_\Lambda(z)$ is a Gaussian or super Gaussian function are shown in Figure 5-15. It is obvious that a number of high order harmonics have relatively high amplitude, which help to satisfy the phase matching condition when the period of LPG is very long. When Λ = 6mm, the 10th order harmonic component will present as an LPG with period of 600μm. Therefore, the observed dips in the experiment are the high order components of the grating.

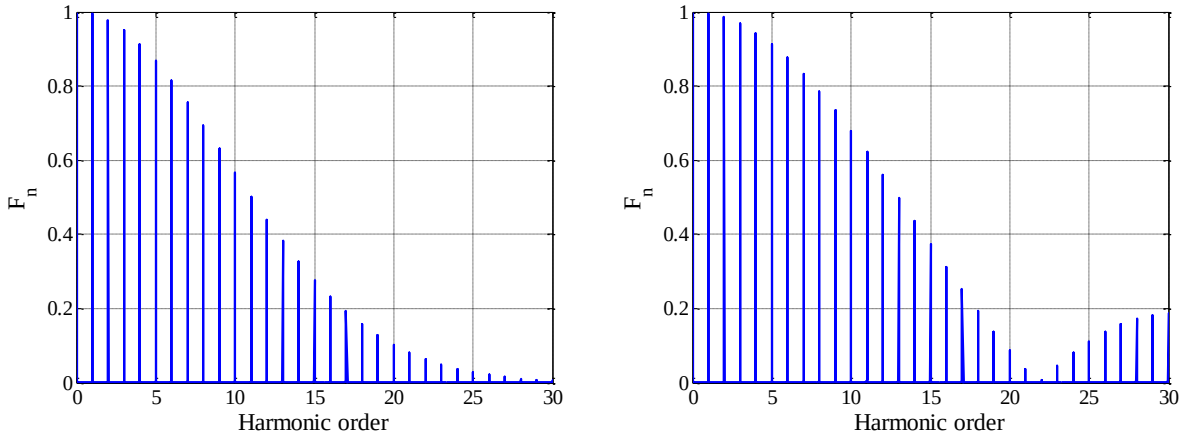

(a) Gaussian (b) Super Gaussian (n=10)

Figure 5-15. Spectra of Gaussian and super Gaussian gratings.

As a result, the phase matching condition $\beta_{01}^{co} - \beta_{1\nu}^{cl} = n\frac{2\pi}{\Lambda}$ can only be applied to gratings that are non-sinusoidal and have relatively strong high order harmonics. In our current experimental design, the pump is modulated by a sinusoidal microwave signal. Without consideration of other effects that can cause pulse distortions, the induced index difference of the core (Δn) will be proportional to the intensity of the pump. When modulation depth is 1, the normalized index variation and its spectrum are shown in Figure 5-16.

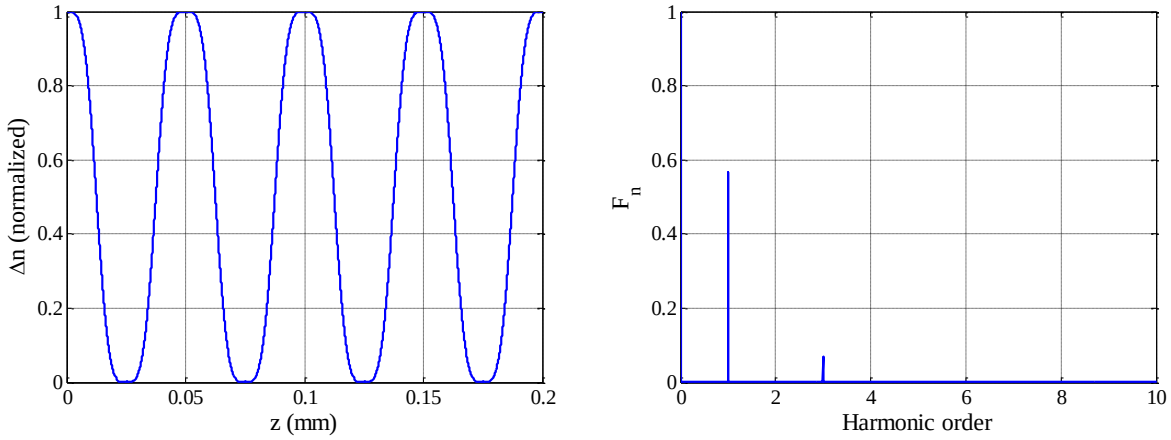

(a) Index variation (b) Spectrum

Figure 5-16. Index variation and its spectrum.

From Figure 5-16 (b) it can be seen that even when the modulation depth is as high as 1, only 3rd order harmonic can be observed, which is about 9dB weaker than the first order. To generate more harmonics, the amplitude of the microwave signal is required to be very high. Even if they are generated, the bandwidth of the modulator is required to be larger for the high order harmonics to be observable. Also, the tolerance on the fiber dispersion will be significantly stronger.

5.6 Analysis of the influence of the fiber NA on LPG

At a certain wavelength, the core and cladding modes in a single mode fiber can be calculated by assuming the waveguide has double layer and three-layer structures respectively. When the propagation constants βs and field distributions of all the modes are obtained, the mode coupling coefficient ($\kappa_{1\nu-01}^{cl-co}$) between the core mode and a cladding mode can be calculated. The required period of LPG to meet the phase matching condition is then given by $2\pi/\Delta\beta$.

It is known that for a single mode fiber, when its numerical aperture (NA) is reduced, the required LPG to meet the phase matching condition can have a larger period. The NA will affect an LPG with a period of few millimeters by modulating the strength of the mode coupling between the core mode and some cladding modes.

Given a fixed V number (1.623) and index of cladding (n_2=1.45), we can reduce the core index and radius to decrease the NA. At the wavelength of 1.55 μm, when NA = 0.15, the LPG periods required to couple the core mode to each cladding mode are shown in Figure 5-17 (a), and the corresponding coupling constant is shown in Figure 5-17 (b). In this case, the largest Λ is about 700 μm and the strongest mode coupling happens when Λ is about 200 μm.

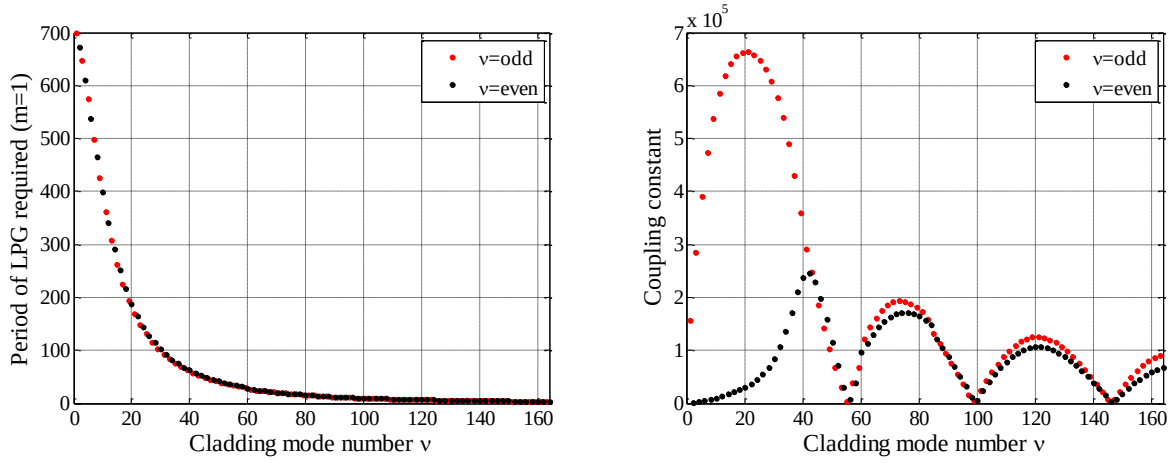

(a) Λ (μm) (b) κ

Figure 5-17. (a) Number of LPG periods required and (b) corresponding coupling constant for a single mode fiber with NA = 0.15.

When the NA is reduced to 0.1 and 0.05, Λ and κ in each case are calculated and shown in Figure 5-18 and Figure 5-19, respectively. When NA = 0.1, the largest period required is about 1.5 mm and the strongest mode coupling happens when Λ is about 400 μm. If the NA is reduced to 0.05, the periods required are 4.89 mm and 1.76 mm, respectively.

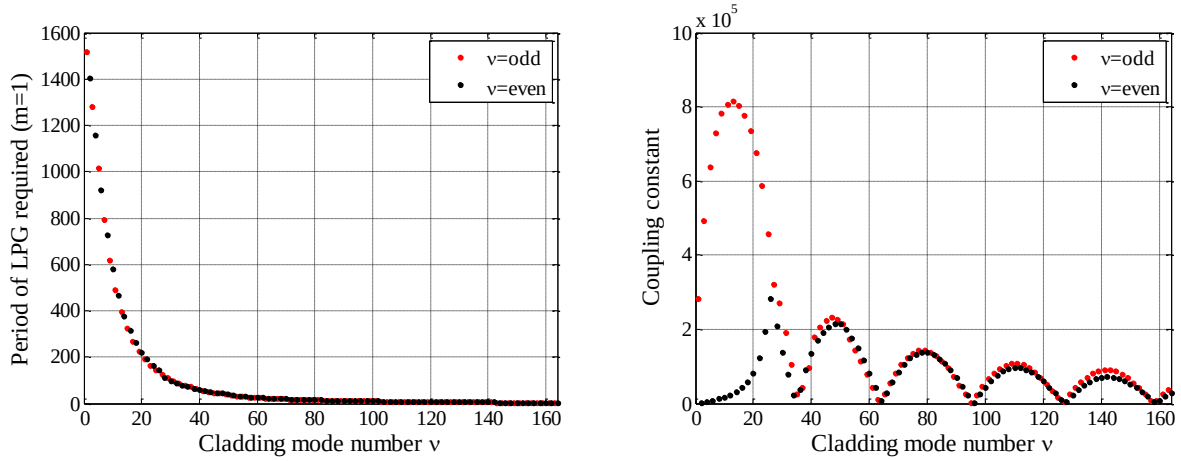

(a) Λ (μm) (b) κ

Figure 5-18. (a) Number of LPG periods required and (b) corresponding coupling constant for a single mode fiber with NA = 0.1.

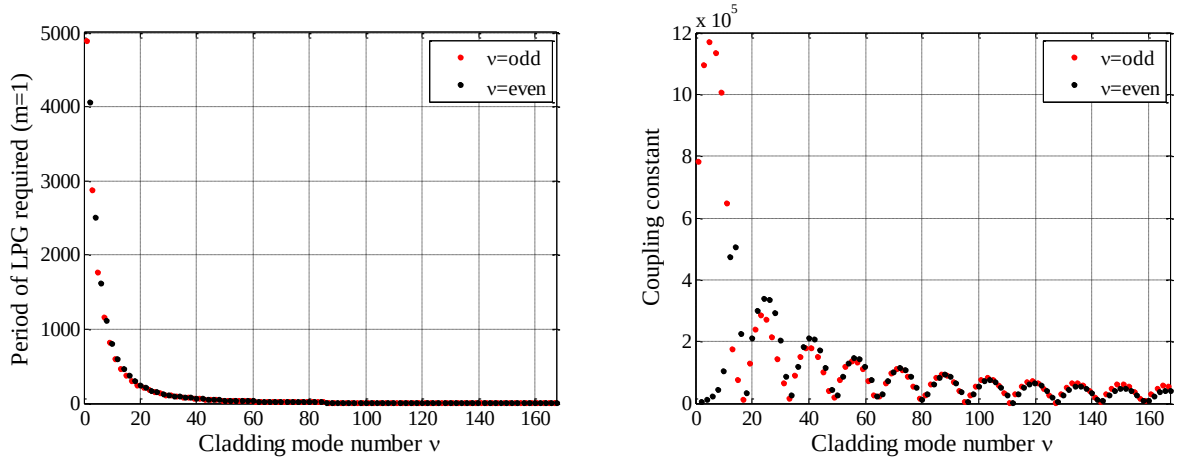

(a) Λ (μm) (b) κ

Figure 5-19. (a) Number of LPG periods required and (b) corresponding coupling constant for a single mode fiber with NA = 0.1.

For an LPG with a sinusoidal index variation, in order to increase the period to a few millimeters, NA should be reduced to below 0.1 and the LPG should have index variation with steep edges.

5.7 Conclusion

In this part of work, we investigated the potential of using the four-wave mixing effect in a singlemode fiber to generate traveling an LPG for the purpose of fully-distributed temperature sensing. Through comprehensive studies, both theoretical and experimental, we conclude that realizing such a sensing scheme is not practical given the laser and modulation devices currently available in market. In the following chapters, more sensing mechanisms will be investigated to meet the project goal.

6 Coherent OTDR sensing scheme

Rayleigh scattering is an intrinsic property of all optical fibers. It is generated by 'scattering centers' due to fiber material small-scale discontinuities. The optical interference between the scattered lights is temperature dependent and may be employed to measure the ambient temperature.

6.1 Sensing principle

Rayleigh scattering in a fiber can be modeled by assuming randomly distributed scattering centers in the fiber and considering their reflected fields as a function of time. Assuming that the input light pulse inducing the scattering to bear a top-hat shape with temporal width *W*, each scattering center contributes to the back-scattered signal a coherent sub-wave, the arrival time of

which is determined by the spatial location of the scattering event. The total electric field, detected at the same input port, can be written as a coherent superposition of the sub-waves:

$$I = \left(\sum_i E(i) \right) \left(\sum_k E^*(k) \right) = I_s + I_X \qquad \text{Eq. 6.1}$$

in which the term I_s is the power term contributed by the product of each sub-wave and its own conjugate, and I_x denotes the cross-terms as a manifestation of interference among different scattering centers:

$$I_X = \sum_{i \neq k} a_i a_k \cos\left[2\pi\nu\left(\Delta\tau_{ik}\right)\right] \left\{ \text{rect}\left[\left(t-\tau_i\right)/W\right] \text{rect}\left[\left(t-\tau_k\right)/W\right] \right\} \qquad \text{Eq. 6.2}$$

where a_i and a_k denote the electric field amplitudes of the *i*'th and *k*'th back-reflected sub-waves, ν is the frequency of the carrier optical wave, $\Delta\tau_{ik}$ is the time delay between the two sub-waves, τ_i and τ_k denote the time of the scattering events, and *rect*[] is the top-hat function. The expression describes a temperature-sensitive signature embedded in the Rayleigh signal, and it may be possible that by quantitatively correlating the signature with the local temperature to realize distributed sensing.

6.2 Design of an interferometric OTDR system

In order to record and analyze the sharp and high-frequency features in the OTDR trace to deduce the local temperature information, a customized intra-pulse interference system was built. In such a system, a light source with long coherent length (narrow linewidth) must be used. At the same time, in order to acquire temperature information quantitatively, it is required that the laser source is wavelength-tunable.

6.2.1 Laser modulation and wavelength tuning

a. Distributed feedback (DFB) laser – Lucent D2526

The features of this 1550 nm laser module include: (1) narrow linewidth (3dB bandwidth = 0.1 nm); (2) high intensity modulation speed (2.488 Gbits/s); (3) temperature tunable for precise wavelength selection. The narrow linewidth makes it possible to use a narrow bandpass optical filter to block the blackbody radiation background in the sensing fiber at high temperatures. The high modulation rate permits a high spatial resolution as dictated by the laser pulse width. Wavelength tuning is essential to extract temperature information.

b. Laser driver – Maxim Max3736

This laser driver matches well with the above DFB laser in the following aspects: (1) the modulation rate can be as high as 3.2 Gbits/s; (2) adjustable bias current from 1 mA to 100 mA and modulation current from 5 mA to 65 mA (for the laser requirement: I_{th} is 30 mA and I_{max} = 150 mA). (3) 14-pin butterfly interface (required by the laser module).

c. Experiment result

The laser assembly is shown in Figure 6-1, including the DFB laser and the evaluation board for its driver. Only the power for the circuit and the modulation signal are needed to generate light

pulses. A photodetector (PD) and an oscilloscope are employed to measure the light signal and the result is shown in Figure 6-2.

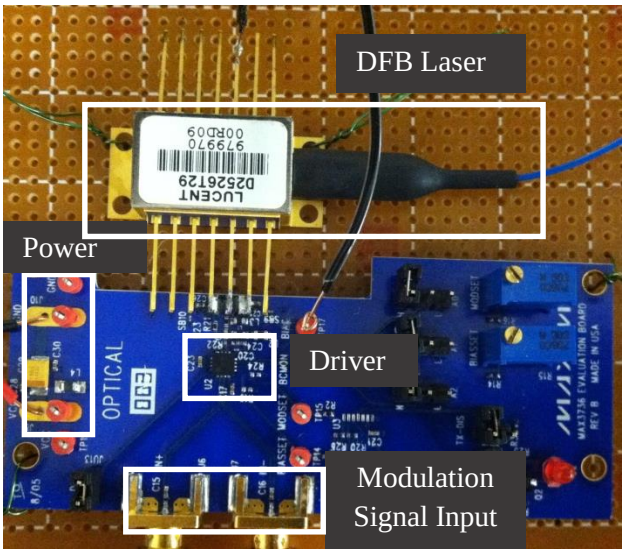

Figure 6-1. DFB laser and its driver.

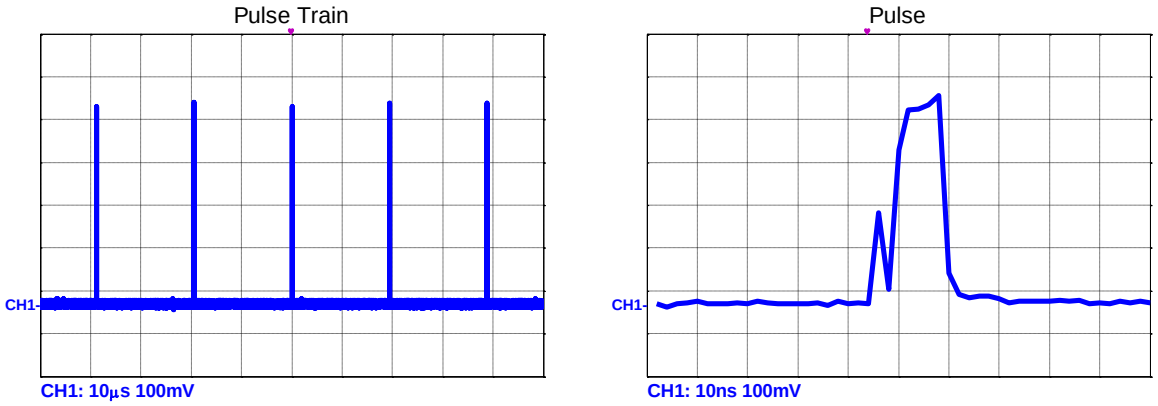

Figure 6-2. Measured signal. (Overview of the pulse train in the left figure and enlarged detail of a pulse in the right figure)

Adequate peak power is crucial in providing sufficient signal-to-noise ratio (SNR), since the Rayleigh scattering is very weak. Two methods have been used to characterize its peak power.

Method 1: Peak power characterization using the oscilloscope. From the signal properties read from Figure 6-2: Pulse width = 10ns, Pulse repetition period = 20 µs. It is straightforward to get: Peak power = $\frac{0.45V}{300V/W}$ = 1.5 mW (using the efficiency of the PD: 300V/W).

Method 2: Peak power characterization using power meter. The direct output from the power meter is: 1.06µW. Peak power = $\frac{1.06\mu W}{10ns/20\mu s}$ = 2.12 mW, which is similar to the value measured

by the oscilloscope. This number will be used in the choice of the photodetector for the system later.

d. Laser wavelength tuning

By introducing the temperature controller (HTC1500) to the laser, we can change the wavelength of the laser by adjusting the rheostat in Figure 6-3 (left). The result is shown in Figure 6-3 (right).

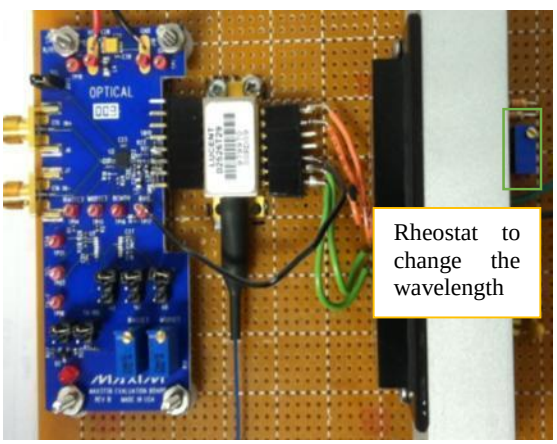

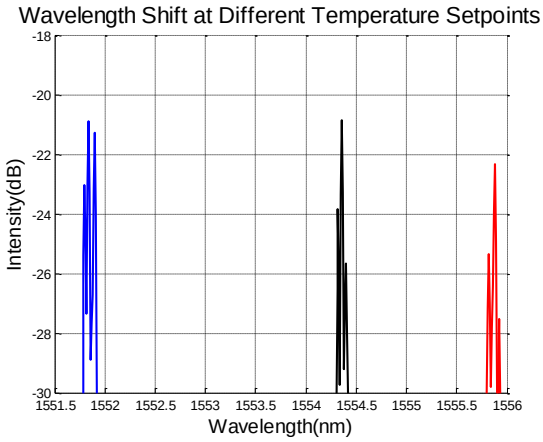

Figure 6-3. Wavelength shift generated by a temperature controller.

From the figure, we can see there is not much intensity change if the wavelength shifts from 1551.7 nm to 1554.4 nm. But there is about 4dB drop if the wavelength shifts to 1555.7 nm. This shows the adjustable wavelength range to be larger than 2.7 nm and less than 4 nm.

6.2.2 Selection of the photodetector

a. Intensity of the Rayleigh scattering

It is important to estimate the signal power using a standard fiber to determine the sensitivity of the photodetector. Assuming the attenuation of the fiber is α (dB/m) and the spatial resolution of the OTDR is L (m), the lost power is

$$\frac{P_{loss}}{P_i} = 1 - 10^{-\frac{\alpha L}{10}} \qquad \text{Eq. 6.3}$$

Transfer the above number to dB:

$$10\log_{10}(1-10^{-\frac{\alpha L}{10}}) \approx 10\log_{10}\frac{\alpha L * ln10}{10}, \text{when } \alpha L \ll 1 \qquad \text{Eq. 6.4}$$

According to Tajima *et al.* [41], about 90% of the intrinsic attenuation in the fiber is due to Rayleigh scattering, and the total attenuation of SMF28 at 1550 nm is 0.2 dB/km. For a 1 ns pulse, the travelling length is L = c ×t = 0.3m. Then we can calculate that

$$P_{loss}(dBm) - P_i(dBm) = 10\log_{10}\frac{0.2\times10^{-3}\times0.3\times ln10}{10} = -48.6\text{dB} \qquad \text{Eq. 6.5}$$

If we use a simplified scattering model by assuming the incident wave is scattered into all directions with equal probability, the probability of the scattered light accepted by the fiber is

$$P = \frac{\pi\left(R \times \frac{NA}{n_1}\right)^2}{4\pi R^2} = \frac{\left(\frac{0.14}{1.48}\right)^2}{4} = 0.024 \qquad \text{Eq. 6.6}$$

So the Rayleigh scattering intensity (P_r) which can be detected at the start point of the fiber is only 2.4% of the attenuation power, which gives

$$P_r\left(dBm\right) - P_i\left(dBm\right) = -48.6 + 10 \times \log_{10} 0.024 = -64.8dB \qquad \text{Eq. 6.7}$$

Note: this result is corresponding to the fact that optical reflection loss < -60 dB [42].

b. The comparison between the PIN and the APD

Since the photomultiplier (PMT) is as expensive as $10,000, P-I-N photodiode (PIN) and the avalanche photodiode (APD) are better practical choices as shown in Table 6-1.

Table 6-1. The comparison between different PINs and APDs.

Parameter	Silicon		Germanium		InGaAs	
	PIN	APD	PIN	APD	PIN	APD
Wavelength range (nm)	400 – 1100		800 – 1800		900 – 1700	
Peak (nm)	900	830	1550	1300	1300 (1550)	1300 (1550)
Responsivity ρ (A/W)	0.6	77-130	0.65-0.7	3-28	0.63-0.8 (0.75-0.97)	
Quantum Efficiency (%)	65 – 90	77	50-55	55-75	60-70	60-70
Gain (M)**	1	150-250	1	5-40	1	10-30
Excess Noise Factor (x)	-	0.3-0.5	-	0.95-1	-	0.7
Bias Voltage (-V)	45-100	220	6-10	20-35	5	<30
Dark Current (nA)	1-10	0.1-1.0	50-500	10-500	1-20	1-5
Capacitance (pF)	1.2-3	1.3-2	2-5	2-5	0.5-2	0.5
Rise Time (ns)	0.5-1	0.1-2	0.1-0.5	0.5-0.8	0.06-0.5	0.1-0.5

Since the wavelength of the laser source is 1550 nm, according to Table 6-1, silicon-based detector could not be used. Furthermore, considering the low signal intensity, APD, which has higher sensitivity, is preferred. In order to achieve an acceptable temperature resolution for the system, a high signal-to-noise (SNR) is required. The SNR calculation is provided below [43]:

(1) PIN photodiode:

Shot noise: $\mathrm{I_N} = \left(2qBI_D\right)^{\frac{1}{2}}$, where q is the electron charge, B is the bandwidth, I_D is the dark current.

Thermal noise: $N_{th} = \frac{4kTB}{R_{sh}}$, where k is the Boltzmann constant, T is the absolute temperature, B is the bandwidth, R_{sh} is the shunt resistance (~$10^8\Omega$).

$$\mathrm{SNR} = \frac{\left(\mathrm{P_s}R\eta\right)^2}{I_N^2 + N_{th}} \qquad \text{Eq. 6.8}$$

Example: FGA04

In its data sheet, it gives the noise equivalent power = 1.5 × 10^{-15} W/$\sqrt{Hz}$ (NEP) directly, $\mathrm{t_{rise}} = 0.1ns \rightarrow B = \frac{0.35}{t_{rise}} = 3.5GHz$

$$\mathrm{SNR} = \frac{\mathrm{P_s}}{NEP * \sqrt{B}} \qquad \text{Eq. 6.9}$$

If we want to achieve 3 dB SNR, the required input power P_s > 0.17 nW

(2) APD detectors:

Shot noise: $\mathrm{I_N} = \left(2qB\left(I_D + I_{DM}\right)\right)^{\frac{1}{2}}$, where q is the electron charge, B is the bandwidth, I_D is the dark current, I_{DM} is the multiplied dark current.

Thermal noise: the same as that for PIN.

$$\mathrm{SNR} = \frac{\left(\mathrm{P_s}R\eta M\right)^2}{I_N^2 + N_{th}} \qquad \text{Eq. 6.10}$$

where R is the responsibility and η is the quantum efficiency.

Example: NR8300FC (typically used for OTDR)

I_D = 5 nA, I_{DM} = 1 nA, η=80%, R = 0.96, B = 2.5 GHz, M = 10. T = 298 K

We can obtain: I_N^2 = 4.8 × 10^{-18}, N_{th} = 4.18 × 10^{-19}, $R\eta M$ = 7.68.

If we want to achieve a SNR no less than 3dB, the required input power $\mathrm{P_s}$ > 0.59 nW.

Comparison and conclusion:

Considering the output power of the laser is ~2 mW and the backscattered reflection is -65 dB, Rayleigh backscattering intensity is 0.63 nW. Therefore, both two detectors can satisfy the system requirement.

6.3 Commercial OTDR instrument (OFM130)

In this section, a commercial OTDR system (OFM130) was used for a coherent optical time-domain reflectometer (COTDR) measurement.

6.3.1 The Signal Amplitude

6.3.1.1 The schematic design for intensity calibration:

The schematic is shown in Figure 6-4.

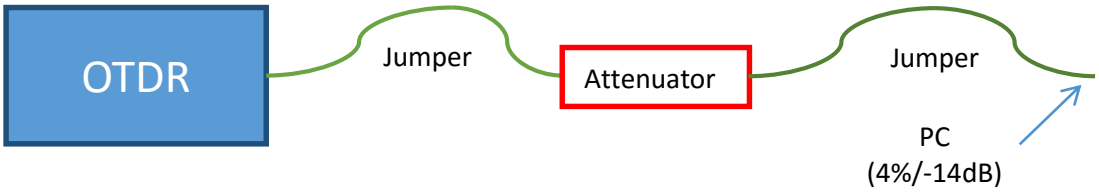

Figure 6-4. Experimental schematic to calibrate the displayed signal intensity.

Two methods are used in the measurements:

a. First, adjust the sensitivity on the OTDR to let the signal be 2 divisions high and record the corresponding sensitivity. Then, change the attenuator by 1 dB and repeat the previous step to record the corresponding sensitivity again. Repeat the procedure for ten times and evaluate the accuracy of this measuring method.

b. Remain the OTDR at a certain sensitivity level, change the attenuator in 1 dB step and measure the signal strengths on the screen of the OTDR.

Typical results of the two measurement methods are shown in Figure 6-5. The first method, as indicated by the user's manual, is more reliable.

6.3.1.2 Measurement of the reflection from a SMF-MMF splice

The measured reflection of the splicing point was -44.11 dB. Theoretically, assume n_1 = 1.47, $NA_{MMF} = 0.275 \pm 0.015$, we can calculate

$$R = \left(\frac{n_1 - n_2}{n_1 + n_2} \right)^2 \approx -41.5 \pm 0.5 dB \qquad \text{Eq. 6.11}$$

The difference between the theoretical and the measured value is 3dB, which may be due to the inaccuracy of the calibration and the imperfection of the reflection surface.

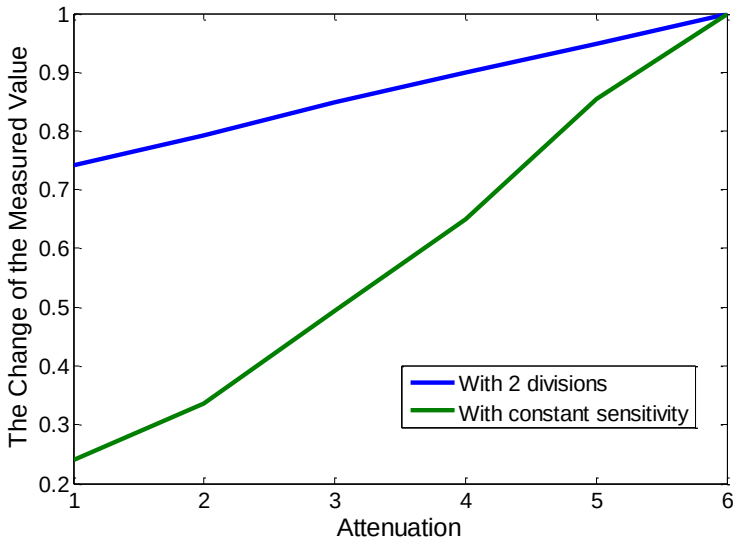

Figure 6-5. Test result for comparison of the two measurement methods.

6.3.2 Comparison of data averaging in instrument and post-processing

Average is a routine method to increase SNR of a measurement system. Here two average methods were used: within the OTDR itself and in the post-processing in computer.

With different average time set in the OTDR, we measured the signal along a section of regular SMF28 fiber and the result is shown in Figure 6-6.

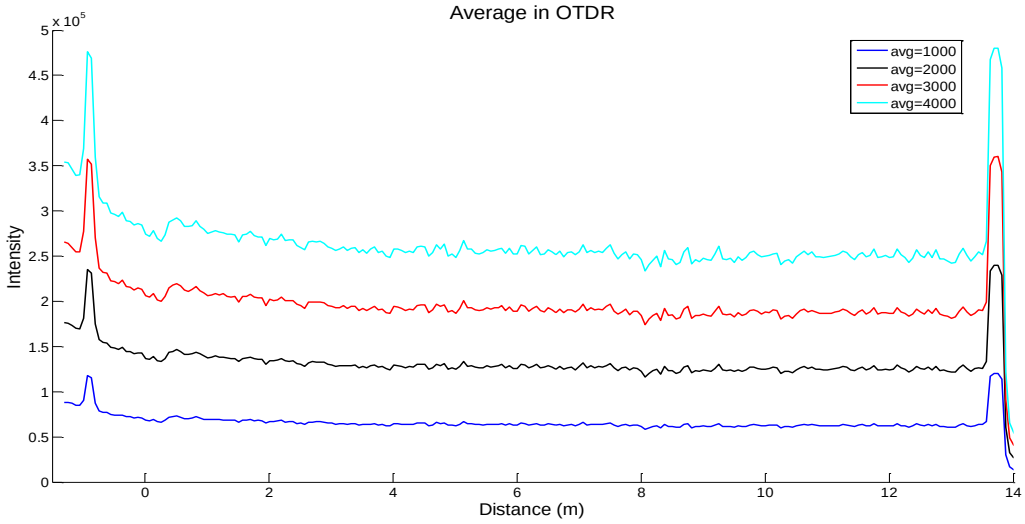

Figure 6-6. The measurement results with difference data averaging time in the OTDR.

As shown in the figure, the data with more averaging better exposes the details along the fiber, which is desired for sensitive pattern recognition for temperature characterization. According to this result, the largest average time (i.e., N_{ave} = 16,383) was used in order to reach the detection limitation of the OTDR.

Post-processing is another common method to improve SNR. Usually, averaging the data of multiple test results can cancel some random noise and thus increase the SNR. So, ten rounds of tests were conducted with the average time set to be 2000 in the OTDR. The result before and after the data averaging are depicted and compared in Figure 6-7.

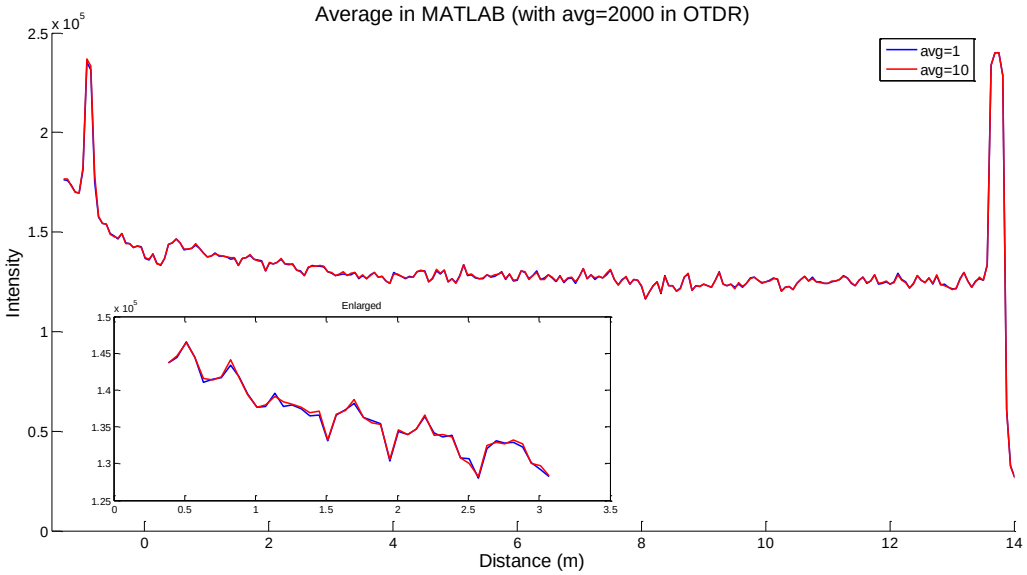

Figure 6-7. The comparison of the result averaged in MATLAB and the result without averaging in MATLAB.

The figure shows little difference between the averaged result and non-averaged result, indicating good repeatability of the system.

6.4 Measurement of the Rayleigh scattering pattern

6.4.1 Basic measurement

A section of SMF28 has been tested three times with the OTDR system at room temperature under optimized parameters (average times = 16383, sensitivity = -60 dB). The result is shown in Figure 6-8.

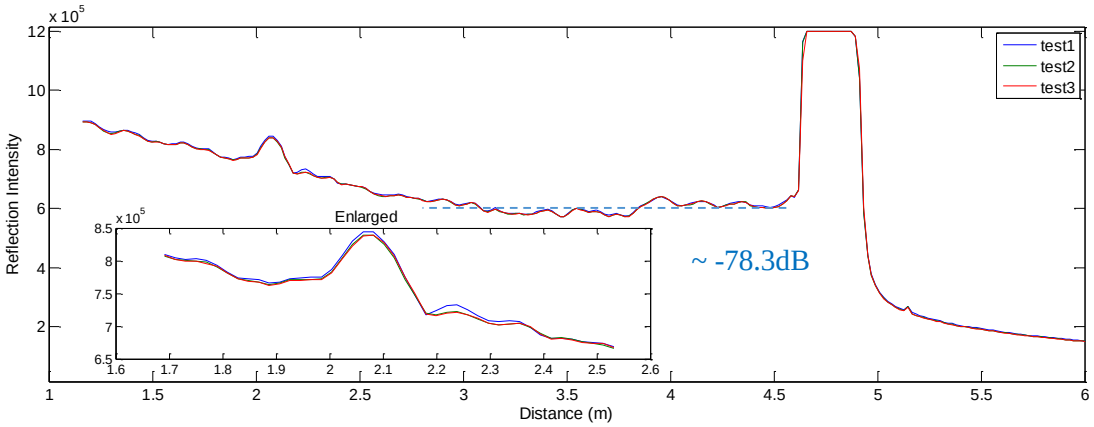

Figure 6-8. The results of repeated tests of a section of SMF28 fiber.

Assuming the Rayleigh scattering coefficient is α (dB/m) and the spatial resolution of the OTDR is *L* (m), the reflected power can be expressed as

$$\frac{P_r}{P_i} = 1 - 10^{-\frac{\alpha L}{10}} \qquad \text{Eq. 6.12}$$

Transfer this value to logarithmic scale (dB):

$$10\log_{10}(1-10^{-\frac{\alpha L}{10}}) \approx 10\log_{10}\frac{\alpha L}{10}, \text{when } \alpha L \ll 1 \qquad \text{Eq. 6.13}$$

According to Tajima *et al.* [41], about 90% of the intrinsic attenuation in the fiber is due to Rayleigh scattering, and the total attenuation of SMF28 at 1310nm is 0.35dB/km. At the same time, the spatial resolution is 1cm. Therefore, the calculated Rayleigh scattering intensity is -75dB, which is also 3dB different from the measured value (-78.3dB). (The difference is the same as that in the previous SMF-MMF splice experiment).

According to the Corning SMF28 specifications, the Rayleigh scattering intensity is -77dB at 1310nm. This number further confirms that our measurement is right.

6.4.2 Pattern repeatability of the Rayleigh scattering

a. Polarization effect:

To further confirm the fine features in the signal obtained were truly the coherent Rayleigh scattering induced rather than the result of polarization interference, a simple experiment was conducted as follows. By adjusting the polarization controller and comparing the result with different states of polarization, we can easily see the polarization dependence of the signal. The experiment setup is shown in Figure 6-9.

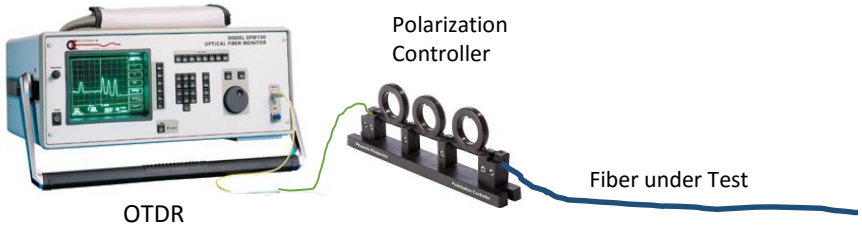

Figure 6-9. Experimental setup for verifying polarization dependence of the Rayleigh signal.

During the test, two tests were taken in each state of polarization to ensure the reliability of the signal. The measured results of the signal under three different polarization states are shown in Figure 6-10.

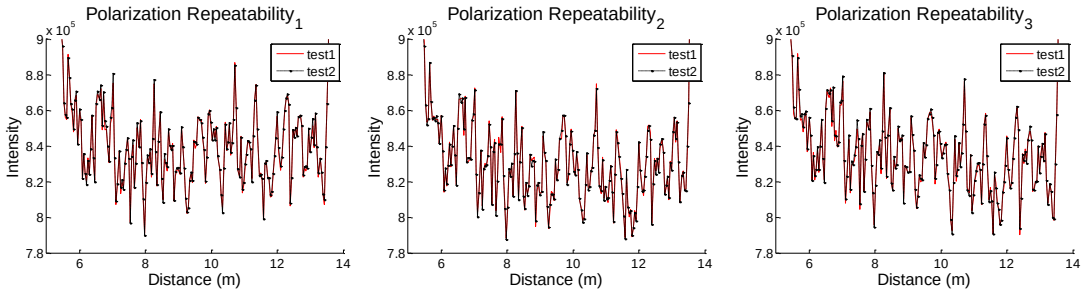

Figure 6-10. Signals obtained at three different polarization states.

The results in Figure 6-10 indicate that the signal was stable at each polarization state. Comparing the signals at these three different polarization states (Figure 6-11), the pattern and intensity of these curves were basically identical, which indicates that the signature is not very sensitive to the polarization although it can be affected by the polarization to some extent.

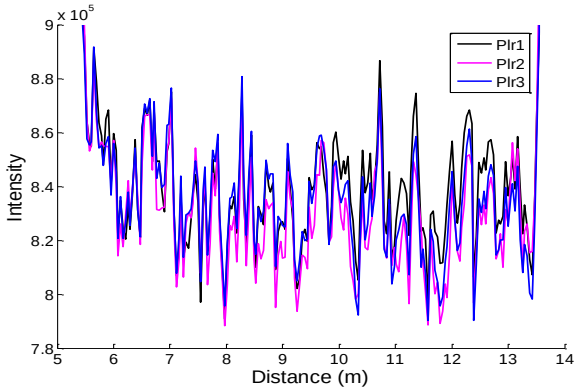

Figure 6-11. Comparison of the signals at three different polarization states.

b. Influence of fiber bending:

Fiber bending can generate stresses in the fiber, which may change the state of polarization of the light in the fiber via the fiber material photoelasticity. The pattern of signal from a 500m long

fiber was measured while the end section of the fiber was bended. The bending effect to the signal pattern is presented in Figure 6-12. Three measurements were made under each situation, and the signals repeat quite well while the pattern changes a little bit in different situations. In this case, bending is not an issue for the pattern measurement.

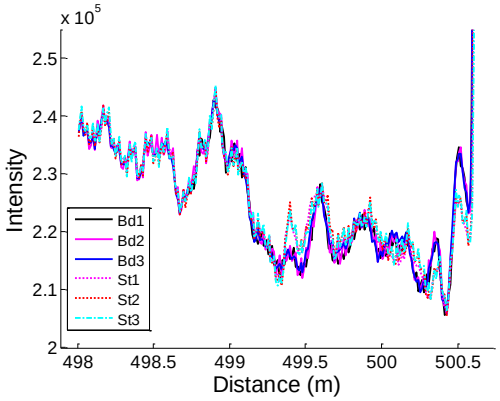

Figure 6-12. Results of the bending repeatability tests.

c. Temperature repeatability:

The pattern repeatability with respect to temperature is crucial to ensure the accuracy of the temperature measurement. Four measurements with a time interval of 4 hours under room temperature (Figure 6-13 (a)) show very good repeatability. The fiber was then measured four times under elevated temperature of 54 ℃ (test 11-14 in Figure 6-13 (b)). Then the fiber was cooled down and heated to 54 ℃ again before another four measurements were made (test 21-24 in Figure 6-13 (b)). Again, the results show good repeatability.

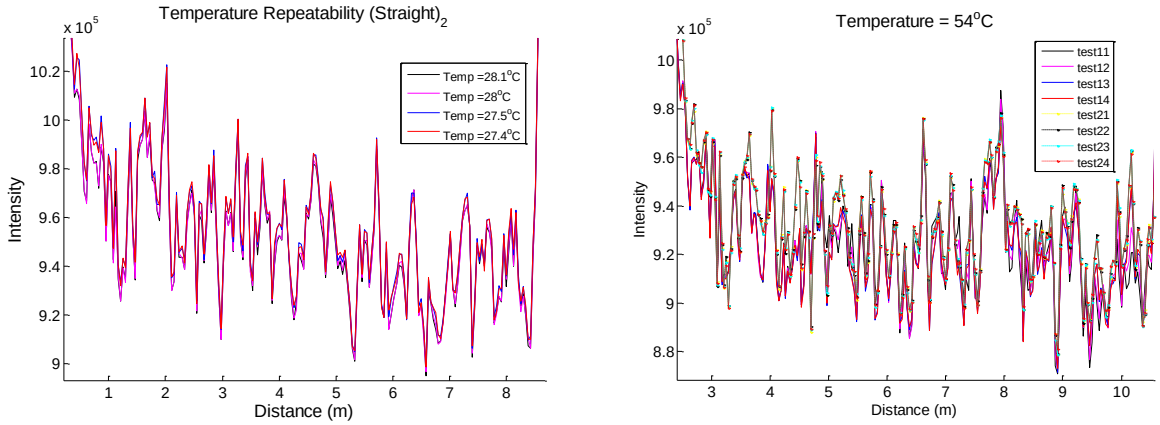

(a) (b)

Figure 6-13. Pattern stability test at (a) room temperature and (b) 54 ℃.

6.5 Temperature dependence of Rayleigh scattering

6.5.1 Qualitative measurement of the temperature dependence

a. Temperature test with 50 ℃ interval

A section of SMF28 fiber was placed in a furnace and heated from room temperature to 250 ℃. With 50 ℃ interval, the temperature was maintained at each level until equilibrium was reached before each measurement. The experiment schematic is shown in the upper part of Figure 6-14 and the result is shown in the lower part of the same figure. The unheated section remains quite similar for the ten times of measurement (which is consistent with the previous experiment results) while the heated section shows a lot of variations. It is encouraging to see that the pattern is dependent on temperature.

b. Measurements with 1 ℃ temperature interval:

In order to see more detailed dependence of the Rayleigh scattering on temperature, a temperature chamber was employed to heat the fiber, which can provide more stable and accurate temperature tuning. The pattern was measured at each temperature with interval of 1 ℃ from 45 ℃ to 54 ℃ and the result is shown in Figure 6-15. The pattern doesn't change much for small temperature changes. The difference at some peaks are due to the low sampling frequency (only 256 points for the pattern). A potential drawback of using the temperature chamber is that the air circulation may introduce strain on the fiber to introduce noise in the pattern.

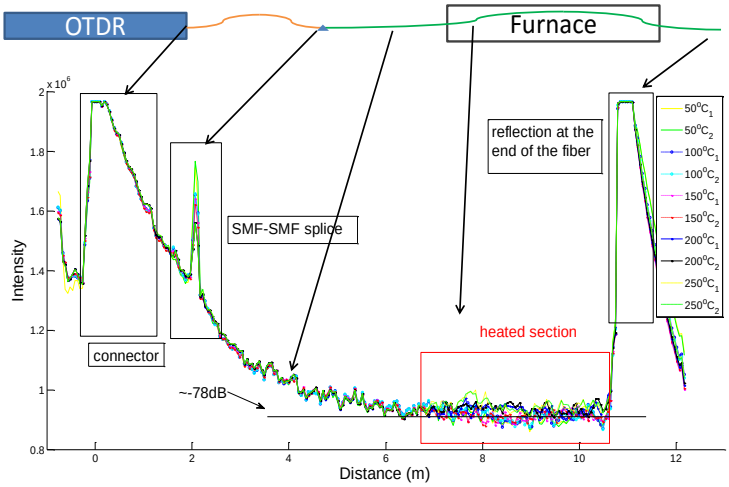

Figure 6-14. Experiment schematics (upper part) and the results (lower part).

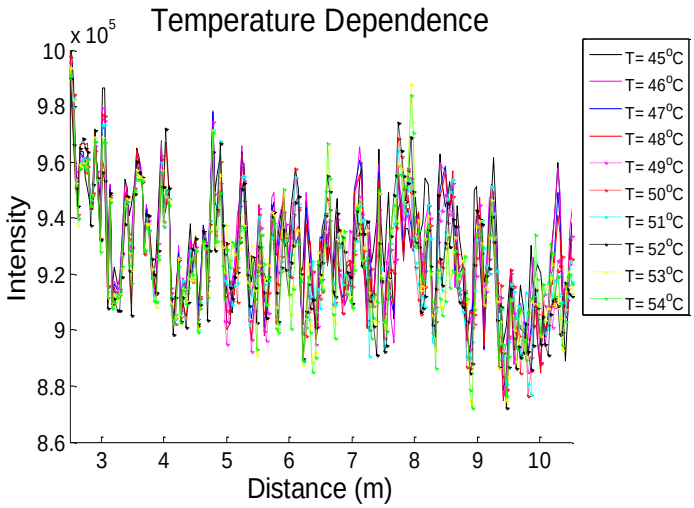

Figure 6-15. Result of Rayleigh scattering patterns at each temperature with 1 ℃ increment.

6.5.2 Temperature characterization

a. Without an optical filter

For more thorough investigation on the temperature dependence, especially under high temperature, further experiment was conducted. The end section of a 500m long SMF28 fiber was heated from 400 ℃ to 1000 ℃ and the patterns were recorded with a 5 ℃ interval. Some of these patterns are plotted and shown in Figure 6-16. The intensity increases during the heating process. The relation between the signal intensity and the temperature was measured (Figure 6-17), which could be a result of thermal radiation.

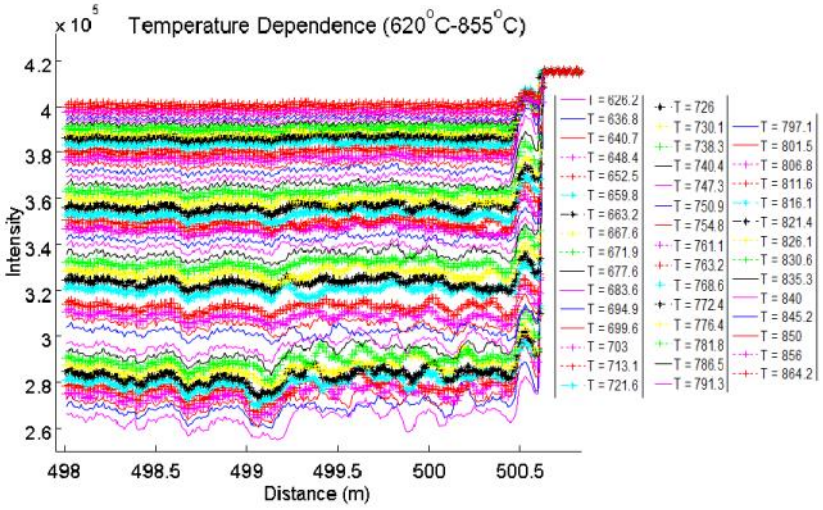

Figure 6-16. Patterns recorded during the heating process.

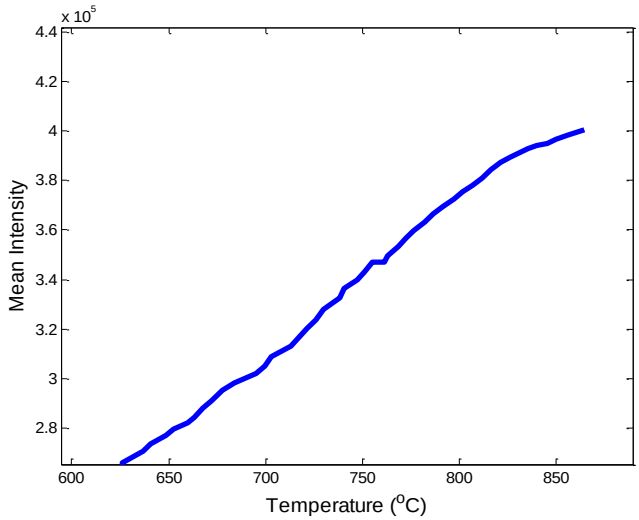

Figure 6-17. Temperature dependence of signal intensity.

Cross-correlation was used to characterize the temperature-dependent pattern by comparing the pattern acquired at a certain temperature with patterns obtained under other conditions. A correlation coefficient is defined to quantitatively describe the similarity between two patterns as

$$r_{X,Y} = \frac{E\left((X-\mu_X)(Y-\mu_Y)\right)}{\sigma_X \sigma_Y} = \frac{\mathrm{E}(XY) - \mathrm{E}(X)\mathrm{E}(Y)}{\sqrt{E(X^2) - E^2(X)}\sqrt{E(Y^2) - E^2(Y)}} \qquad \text{Eq. 6.14}$$

where μ_X and μ_Y are the expectation values of X and Y (two sets of data) and σ_X and σ_Y are the standard deviations of X and Y, respectively.

Using this method, we can calculate the similarity between a pattern at an arbitrary temperature and the patterns at other temperatures. The results of the patterns at 612.5, 584.2, 840 and 835.3 ℃ are shown in Figure 6-18. It is interesting to see the periodicity of the similarity. The period can be easily calculated by reading the data in the figures. For the 612.5 ℃ figure, the peaks are at x = [423, 458, 522, 551, 584, 614], the intervals are [35, 64, 29, 33, 30]. For 840 ℃ figure, the peaks are at x = [687, 720, 752, 781, 812, 840], the intervals are [33, 32, 29, 31, 28]. For 835.3 ℃ figure, the peaks are at x = [663, 747, 777, 805, 835], the intervals are [84, 30, 28, 30]. The intervals are similar and the average value was roughly 30 ℃. (There may be some peaks missing due to the lack of data at that temperature, so the intervals become two or three times of the period.) According to this result, the temperature dependence of the Rayleigh scattering pattern is periodic and the period is about 30 ℃.

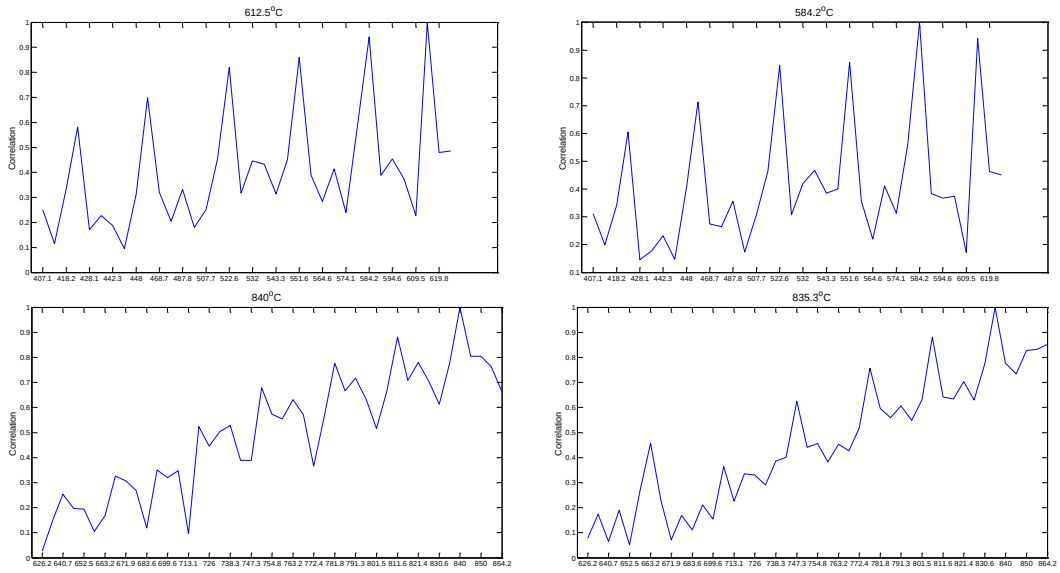

Figure 6-18. Correlation coefficient between the pattern at the temperature indicated by the title in each figure and the patterns at other temperatures indicated by the X axis.

b. With an optical filter

Since the detector in the OTDR system is a photon multiplier with an effective optical bandwidth of ~100nm, an optical filter can eliminate the noise outside the signal band and thus help increase the SNR and improve the signal quality.

First, the optical properties of the OTDR light source were measured. A 10 Gbit/s photodetector and a 20 Gbits/s oscilloscope were employed to measure the optical signal from the OTDR. The result is shown in Figure 6-19. The repetition rate is 1/6 μs ≈ 167 kHz and the pulse width is 1 ns. Meanwhile, an OSA is employed to measure the spectrum of the light source and the result is shown in Figure 6-20, which indicates that the OTDR light source is a multimode laser with a spectral bandwidth of about 10 nm.

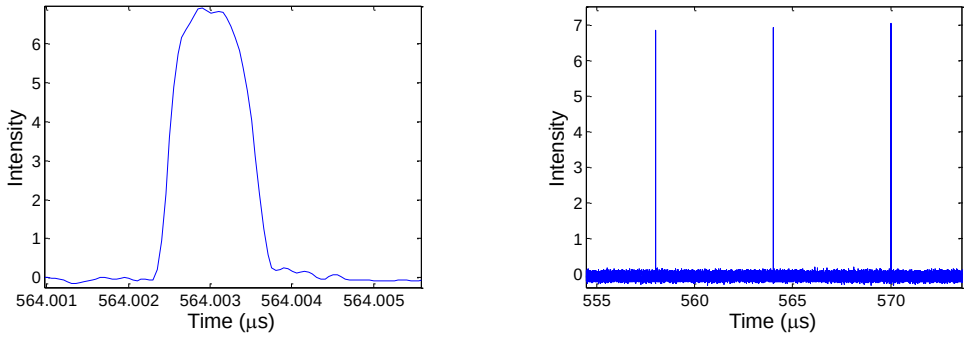

Figure 6-19. The optical signal of the light source in the OTDR measured by an oscilloscope (no filter).

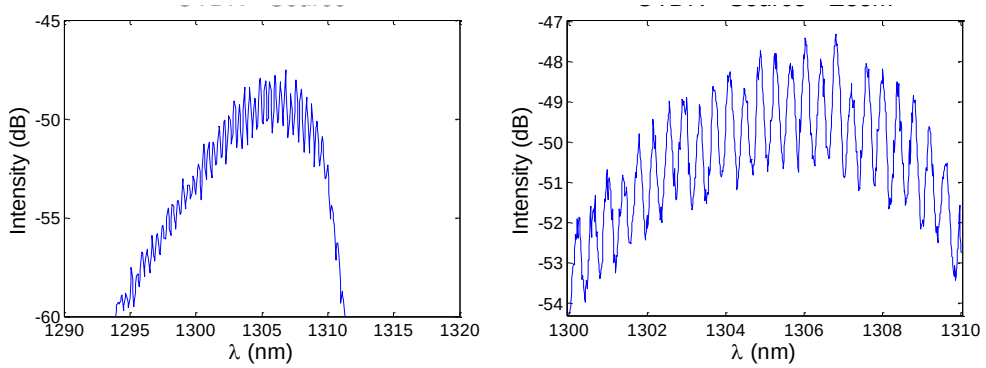

Figure 6-20. The optical property of the light source in the OTDR measured by an OSA (no filter).

An optical filter with 1 nm bandwidth was used. After applying the filter, the pulse is distorted and the pulse train is not uniform any more (Figure 6-21). Both of these negative effects are due to the cutoff in frequency domain by the filter. Also, the intensity of the signal drops to 1/10 of the original one due to the insertion loss of the optical filter, which is 10 dB as indicated by its datasheet. This makes it impossible to detect the weak Rayleigh scattering signal.

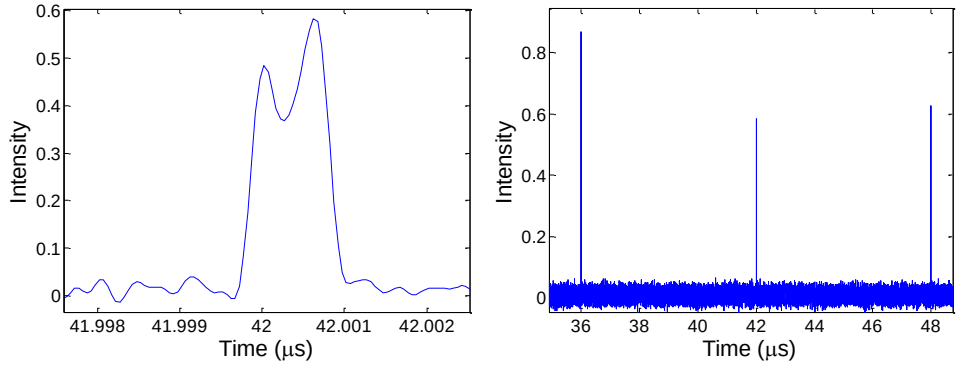

Figure 6-21. Signal filtered by a 1nm bandpass optical filter.

6.6 Temperature repeatability tests

In order to verify that the pattern of Rayleigh scattering can reliably reflect the local temperature in which the sensing cable resides, several tests at high temperature were conducted to evaluate the repeatability of the pattern.

6.6.1 Pattern repeatability at high temperature

A ClearCurve (Corning Inc.) fiber was heated from 900 ℃ to 1000 ℃ and the Rayleigh scattering patterns were recorded with a 5 ℃ interval (Test 1). After the temperature was kept at 1000 ℃ for two days, the fiber was cooled down to 900 ℃ and the same thermal procedure was repeated (Test 2). The results are shown in Figure 6-22 and Figure 6-23. 'T1' and 'T2' indicate data for 'Test 1' and 'Test 2' respectively. The number such as '929.9' stands for the measured temperature by thermocouple is 929.9 ℃. A low pass digital filter was employed to eliminate the high frequency noise, especially the sampling noise introduced by the OTDR data acquisition board. At the same time, the DC component in the signal was eliminated.

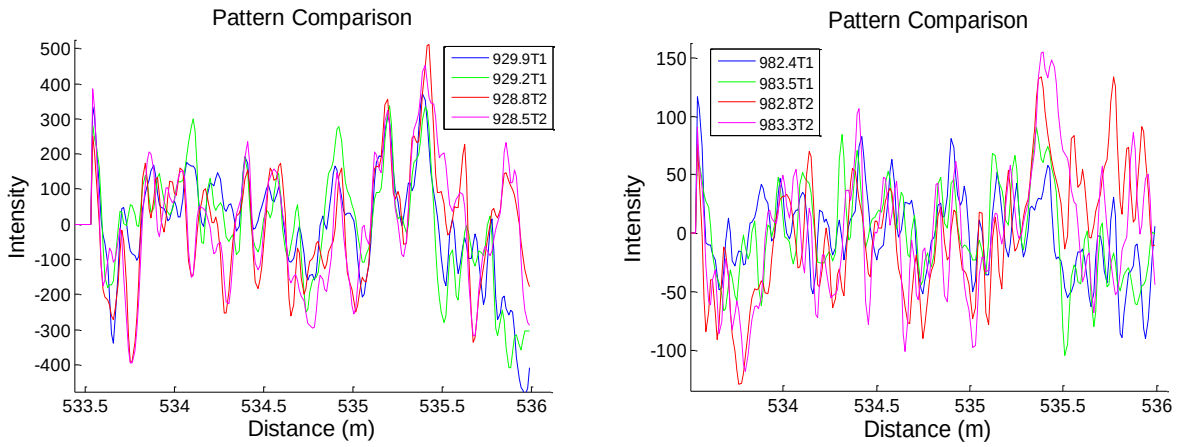

(a) (b)

Figure 6-22. Fringe repeatability tests at the temperature of (a) 930 ℃ and (b) 985 ℃.

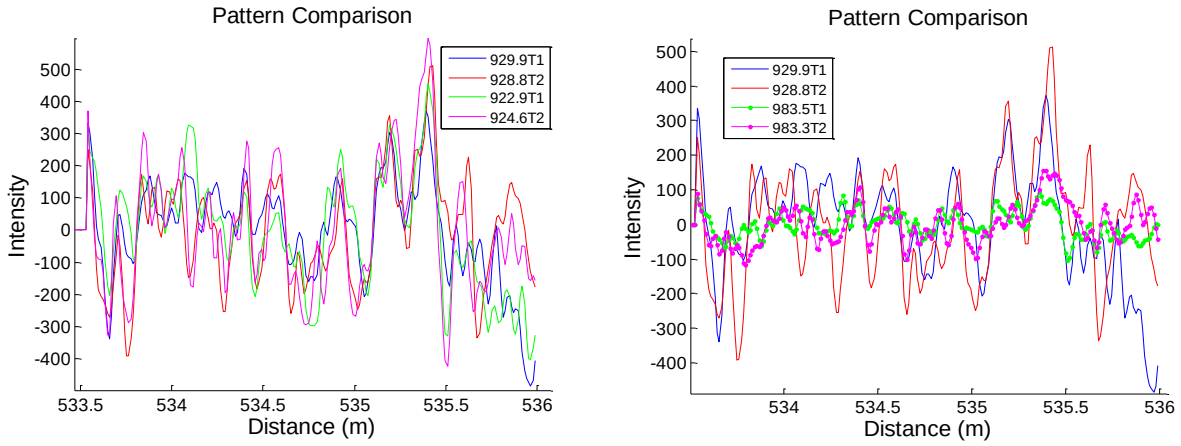

(a) (b)

Figure 6-23. Patterns recorded at slightly different temperatures.

From Figure 6-22 (a), it is clear that at the same temperature, patterns are repeatable even after the annealing process. But from Figure 6-22 (b), the repeatability is not as obvious at higher temperature. In Figure 6-23 (a), comparing the pattern at slightly different temperature, we can find the pattern variation is almost as large as the variation at the same temperature, which means the temperature resolution is larger than 5 ℃. Last, according to Figure 6-23 (b), the pattern changes a lot at very different temperature. In conclusion, the repeatability of the patterns is not good enough to be used as an indicator of temperature to measure the high temperature.

6.6.2 Pattern repeatability at room temperature

Since the SNR at high temperature is relatively high, further experiment about the pattern repeatability was conducted at room temperature. Three tests were taken with two annealing processes, each including the heating of the ClearCurve fiber to 1000 ℃, keeping for one day and then cooling down to room temperature. Three measurements were conducted in each test, as shown by the legends in Figure 6-24.

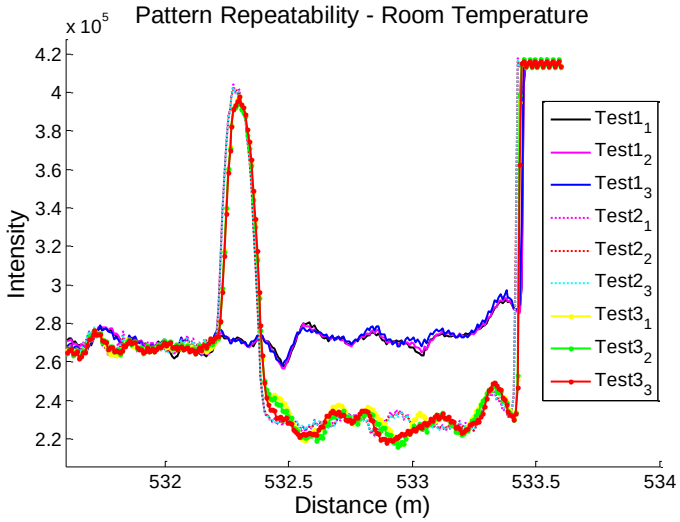

Figure 6-24. Results of the pattern repeatability experiment at room temperature.

Comparing the pattern of Tests 1 and 2, we can see a peak appeared after the fiber was heated for the first time. It seems that the high temperature made the fiber to form micro cracks and created a significant reflection in the fiber. Comparing the pattern from Tests 2 and 3, we can see the large peak remained the same while other small features kept changing. The cracks could be a result of unreleased internal stresses, which will be discussed further in Chapter 9.

6.7 Conclusion

In conclusion, an interferometric coherent OTDR system with a ClearCurve fiber is tested in detail and determined not to be suitable for high temperature sensing due to its poor thermal stability at high temperatures. The temporal features of the interferometric OTDR relies on the optical-path difference (OPD) among the spatially distributed and "frozen-in" scattering centers in the fiber, and the relative positions as well as the refractive indices contributing to the OPDs. It seems the scattering centers, the fiber indices or both exhibit permanent changes under high temperature for extended period of time. This method is thus deemed not to be the choice for distributed high temperature sensing.

7 Brillouin scattering based distributed temperature sensing

7.1 Principle

7.1.1 Fundamentals

When light travels in media, it interacts with phonons in the media and could gain or lose energy. For the material, the vibration and rotation of the molecules correspond to the phonons of Raman scattering, while other low frequency vibrations dominates in Brillouin scattering. This frequency is called Brillouin frequency, which is an inherent property of the material, and

changes with the environmental temperature. The phonons in the Brillouin scattering process are generated by the optical radiation via electrostriction effect. When two beams counter-propagate and meet each other and the frequency difference between them coincides with the material's Brillouin frequency, one beam will generate phonons and lose energy, while the other beam will interact with the phonon and gain energy. This physical phenomenon is referred to as the Stimulated Brillouin scattering (SBS). The propagating phonons in this phenomenon behave as a travelling grating, which could be adopted for distributed sensing. In the sensing scheme, one light pulse propagates along the fiber and meets another counter-propagating light, with a frequency difference matched to the fiber's Brilluoin frequency. Any location along the fiber could be pinpointed by controlling the relative delay between the two light beams.

In a Brillouin scattering based distributed fiber sensor, the frequency shift of Brillouin scattered light is proportional to the local velocity of the acoustic phonons, which depends on the local density and tension of the glass, and thus on the material temperature and strain [44]. The Brillouin frequency shift can be given approximately by:

$$v_B(z) = \frac{2n_{eff}(z)V_a}{\lambda} \qquad \text{Eq. 7.1}$$

where $n_{eff}(z)$ is the effective mode refractive index of the fiber as a function of distance z. V_a is the velocity of sound wave in the fiber glass and λ is the free-space wavelength. The sensing capability is based on the measurement of the distributed Brillouin frequency shift dependence on either strain or temperature.

Brillouin optical time domain analysis (BOTDA) used in this technique is proposed as a pump-probe detecting approach. The scheme involved launching a short pump pulse into one end of the test fiber and a continuous wave (CW) probe beam into the other end. When the CW wave is at the Stokes frequency of the pulse light, energy transfers from pulse to CW wave, generating Brillouin gain to this CW wave. Conversely, if the pulse light was set at the Stokes frequency of CW light, the CW light transfers energy to the pulse, and the detected CW signal will contain a Brillouin loss.

When the frequency difference between the pulse and CW lasers are tuned to the Brillouin frequency of the sensing fiber, the CW wave would experience varying gain/loss along the fiber. As a function of position along the fiber, the gain/loss of CW light shows in the time domain. The Brillouin frequency at every location on the fiber can be determined by performing a frequency scan on the CW beam and detect the gain/loss signal at corresponding time delay.

7.1.2 Stimulated Brillouin scattering (SBS) in a single mode optical fiber

Brillouin frequency shift is determined by the material's local thermodynamic properties, including sound velocity and refractive index. Over quite a large range of temperature and strain, the Brillouin frequency shifts of single mode fibers are proportional to local changes in temperature[45] and strain[46]:

$$\begin{aligned} v_B(\epsilon) &= v_B(0)\left[1 + C_s\epsilon\right] \\ v_B(t) &= v_B(t_r)\left[1 + C_t(t - t_r)\right] \end{aligned} \qquad \text{Eq. 7.2}$$

where ϵ is tensile strain, t is temperature and t_r is reference temperature. The coefficients C_s and C_t varies with wavelength, while the dependences mainly originate from the change in the acoustic velocity rather than the change in the refractive index in fibers [47, 48].

For Stimulated Brillouin Scattering (SBS) applications in optical fiber, the frequency difference between the pulse and CW waves equals to the acoustic wave frequency, which is the Brillouin Frequency. At Brillouin Frequency, the CW and pulse beams produce a beat signal, which induces a density wave enhancing the acoustic wave, and increases the number of phonons as a result [44]. This enhancing effects in the SBS leads to a better efficiency of the scattering process characterized as operating in the stimulated regime.

In our experiment, the SBS is generated by launching a pulse and a counterpropagating CW wave into the two fiber ends. The Maxwell equations describing the beat signal induced nonlinear polarization contribution via the electrostriction effect associated with the mass density change $\Delta\rho$ writes as follows [49]:

$$P_{NL} = \varepsilon_0 \Delta E = \varepsilon_0 \rho_0 \left(\frac{\Delta \varepsilon}{\Delta \rho} \right) \frac{\Delta \rho}{\rho_0} E = \frac{\varepsilon_0 \gamma_E}{\rho_0} \Delta \rho E$$

$$\frac{\partial^2 E}{\partial z^2} - \frac{1}{\left(\frac{c}{n} \right)^2} \frac{\partial^2 E}{\partial t^2} = \frac{\gamma_E}{c^2 \rho_0} \frac{\partial^2 \left[\Delta \rho E \right]}{\partial t^2} \qquad \text{Eq. 7.3}$$

Where ρ_0 denotes the mean mass density of the material, and $\Delta\rho$ is the mass density variation associated with the acoustic waves. These equations form the theoretical foundation for the SBS gain and loss calculation and static condition of Brillouin gratings in optical fibers.

7.1.3 Minimum detectable change

The Brillouin spectrum could be approximated to a Lorentzian function with a resonance frequency of υ_B when the pulse width is larger than 10 ns. The detectable change in υ_B is determined by the linewidth and electrical SNR:

$$\delta \nu_B = \left(\Delta \nu_L + \Delta \nu_B \right) / \sqrt{2} \left(SNR \right)^{1/4} \qquad \text{Eq. 7.4}$$

When the laser linewidth $\Delta\upsilon_L$ is much smaller comparing to $\Delta\upsilon_B$, it can be neglected and $\Delta\upsilon_L + \Delta\upsilon_B$ turns into $\Delta\upsilon_B$ in the above equation. The minimum detectable change in strain and temperature is given by:

$$\delta \epsilon = \frac{\delta \nu_B}{C_\epsilon \nu_B (0)}$$

$$\delta t = \frac{\delta \nu_B}{C_t \nu_B (t_r)} \qquad \text{Eq. 7.5}$$

It is also reported that the Brillouin linewidth in fibers is slightly larger than in fused-silica glass due to the non-uniform core profiles and variations in dopant concentration along the fiber [50].

7.1.4 Spatial resolution

For a BOTDA system with pulse width W, the spatial resolution is determined by

$$\delta z = vW / 2 \qquad \text{Eq. 7.6}$$

where v is the light velocity in the fiber. It can be calculated from the equation that for a 1 μs pulse, a 100m spatial resolution can be obtained [50].

The factor that limits the spatial resolution is the phonon lifetime. For maximum SBS efficiency, the optical pulse width should match the lifetime of the phonons generated. In typical fibers, the phonon lifetime is on the order of 10 ns, which leads to a spatial resolution limit of 1m in a general SBS distributive measurement.

The relations between the normalized pump (E_p), Stokes(E_s) and phonon (E_A) in Brillouin scattering can be described with the following coupled partial differential equations[51, 52]:

$$\begin{aligned}
&\frac{\partial E_p}{\partial t} + \frac{\partial E_p}{\partial z} + \frac{\gamma_p}{\gamma_A} E_p = -E_s E_A \\
&\frac{\partial E_S}{\partial t} + \frac{\partial E_S}{\partial z} + \frac{\gamma_s}{\gamma_A} E_s = E_p E_A^* \qquad \text{Eq. 7.7} \\
&\frac{\partial E_A}{\partial t} + \left[1 + j\Delta(z)\right] E_A = E_p E_s^*
\end{aligned}$$

where Δ(z) is the normalized resonance-detuning parameter given by

$$\Delta(z) = \frac{2\pi}{\gamma_A}\left[\nu_p - \nu_s - \nu_B(z)\right] \qquad \text{Eq. 7.8}$$

and γ_p, γ_s and γ_A are the field-damping constants.

In BOTDA sensors using positive pulses, the acoustic field takes around 10 ns to build up in the presence of pulse light. According to the equations, the increase in pump power that to be measured is limited by acoustic the field E_A, therefore, interaction increases as the acoustic wave builds up. In a high spatial resolution measurements (i.e. Stokes pulse shorter than 10 ns), there's not enough time for E_A to reach its maximum, leading to a low efficiency of interaction between two light waves. Furthermore, pulse with duration shorter than the acoustic lifetime (typically 10 ns) will generate spectral broadening in υ_s. Since the retrieving of strain of temperature is based on spectrum peak assigning, such broadening will result in additional inaccuracy in the temperature demodulation.

7.1.5 Polarization

In BOTDA experiments, polarization needs to be strictly controlled for better signal quality. The interaction strength between the counter-propagating light depends on their polarization. No interaction would take place between two perpendicularly polarized light beams. At first, people assumed that the birefringence in the fiber will result in the variation of Brillouin intensity along fiber. However, according to Bao's work in 1995 [53], it is possible to achieve the maximum Brillouin gain along the whole fiber, but still, polarization should be carefully controlled in order to observe the Brillouin scattering effect. It was proved afterwards that by scrambling the polarization states of the interacting light, the system can become polarization-insensitive. [54].

7.1.6 Brillouin gain vs Brillouin loss

In a Brillouin gain scheme, the pulsed light transfers its power to the CW light, leading to a continuous decrease in the pulse's power as it propagates along the sensing fiber. As a result, the gain/loss signal decreases all the way along the sensing fiber, as shown in Figure 7-1. To overcome this disadvantage, Brillouin loss scheme was proposed.

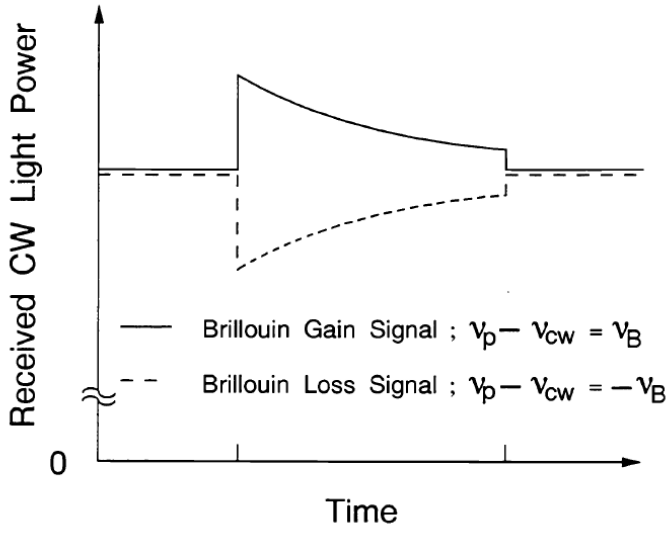

Figure 7-1. Signal of Brillouin Gain and Brillouin Loss [55].

In the Brillouin loss scheme, the frequency of the probe light (pulsed beam) is higher than the pump light (continuous wave). By overcoming the pump loss problem, we can obtain a longer sensing length and a higher SNR than that of the Brillouin gain method.

7.1.7 Dual Brillouin interaction technique for SBS signal enhancement

Another sensing scheme in BOTDA uses both sidebands in the probe light to interact with the pump pulse to maintain the intensity of the pump pulse. [56] The schematic of this scheme is shown in Figure 7-2.

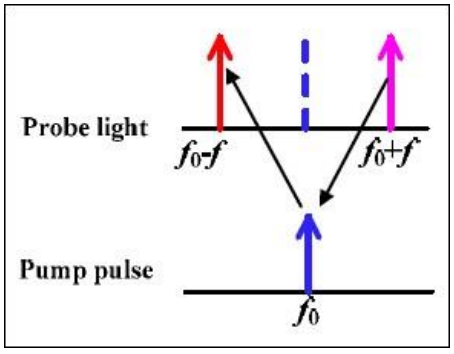

Figure 7-2. Schematic of energy transfer in dual gain-loss Brillouin interaction.

In a single Brillouin detection scheme, a filter is applied after the frequency shifting electro-optical modulator (EOM) on the probe light arm to select the Stokes light. In a dual gain-loss Brillouin interaction scheme, both Stokes and anti-Stokes light passes through and get amplified by the following EDFA. In the sensing fiber, when the Stokes light gains energy from the pump pulse, the anti-Stokes light transfers energy to the pump pulse at the same time, compensating the pump pulse along its propagation. Through this effect, the power intensity of the pump pulse can be maintained.

7.2 Three-wave interaction modelling using FDTD method

The finite-difference time-domain (FDTD) modeling of SBS is a powerful tool for evaluating the three field evolution along the fiber. It provides a deeper understanding of the internal dynamics of SBS generation, offering an approach of optimizing parameters for higher system performance.

The generation of SBS can be described by the three-wave interaction (3WI) model which can be expressed by the following equations [57]:

$$\begin{aligned}
&\frac{\partial a_p}{\partial t}+\frac{c}{n}\frac{\partial a_p}{\partial z}+\gamma_p a_p=-Ka_s a_a e^{-j\delta(z)t}\\
&\frac{\partial a_s}{\partial t}-\frac{c}{n}\frac{\partial a_s}{\partial z}+\gamma_s a_s=K^* a_p a_a^* e^{-j\delta(z)t}\\
&\frac{\partial a_a}{\partial t}+u\frac{\partial a_a}{\partial z}+\gamma_a a_a=K^* a_p a_s^* e^{-j\delta(z)t}
\end{aligned} \qquad \text{Eq. 7.9}$$

where a_p, a_s and a_a represent the pump, Stokes and acoustic fields, respectively. γ_p, γ_s and γ_a represent each field's damping constant. K stands for the Brillouin coupling constant. c is the speed of light. n is the refractive index of the fiber and u is the speed of sound along the fiber. $\delta(z)$ is the resonance detuning parameter which depends on the temperature and strain of the fiber with an expression

$$\delta(z)=2\pi\left[\nu_p-\nu_s-\delta\nu^{\mathrm{Res}}(z)\right] \qquad \text{Eq. 7.10}$$

In an optical fiber, optical losses are relatively low, thus γ_s and γ_p can be neglected. By normalizing the time and spatial variables according to $\gamma_a t\to t$, $z\gamma_a(n/c)\to z$, $\Delta(z)=\delta(z)/\gamma_a$, $E_p=a_pK/\gamma_a$, $E_s=a_sK/\gamma_a$ and $E_a=(a_aK/\gamma_a)e^{-j\Delta(z)t}$, Eq. 7.9 becomes

$$\begin{aligned}
&\frac{\partial E_p}{\partial t}+\frac{\partial E_p}{\partial z}=-E_s E_a\\
&\frac{\partial E_s}{\partial t}-\frac{\partial E_s}{\partial z}=E_p E_a^*\\
&\frac{\partial E_a}{\partial t}+\left[1+j\Delta(z)\right]E_a=E_p E_s^*
\end{aligned} \qquad \text{Eq. 7.11}$$

In a CW pump and pulsed Stokes light scheme, the boundary conditions can be expressed as

$$E_p\big|_{z=0} = C$$
$$E_s\big|_{z=l} = p(t) + A \qquad \text{Eq. 7.12}$$

where C is the CW constant amplitude, $p(t)$ describes the pulse profile and A is the background of the pulse related to the extinction ratio ε as

$$A = 10^{\varepsilon(dB)/10} \qquad \text{Eq. 7.13}$$

To solve Eq. 7.11, FDTD method [58] is applied through discretizing the domain over an M by N grid with $z = m\Delta z, t = n\Delta t,\ m = 0,1,...M-1, n = 0,1,...N-1$ and rewriting the derivatives, yielding

$$\begin{aligned}
&\frac{E_p(m,n) - E_p(m,n-1)}{\Delta t} + \frac{E_p(m,n) - E_p(m-1,n)}{\Delta z} = -E_s(m,n-1)E_a(m,n-1) \\
&\frac{E_s(m,n) - E_s(m,n-1)}{\Delta t} - \frac{E_s(m+1,n) - E_s(m-1,n)}{\Delta z} = E_p(m,n)E_a^*(m,n) \qquad \text{Eq. 7.14} \\
&\frac{E_a(m,n) - E_a(m,n-1)}{\Delta t} + \left[1 + j\Delta(z)\right]E_a(m,n) = E_p(m,n-1)E_s^*(m,n-1)
\end{aligned}$$

With these equations, we can simulate the SBS signal acquired from a specific sensing system. Take an example of a 30 m long fiber with Brillouin frequency $\delta\nu^{\mathrm{Res}}(z) = 12.78\,\mathrm{GHz}$. A 5 m section in the center with a frequency 12.50 GHz is set to simulate a high temperature section. 3 mW CW power and 30 mW Stokes light power are set as the experiment condition. A pulse of 16.5 ns width and 100 ps rise time is used, with an extinction ratio of 20 dB and $\Delta t = \Delta z = 0.05$. The acoustic damping constant is set to be 110 MHz according to a standard SMF28 fiber. The simulation results are shown in Figure 7-3, which agrees well with the results in [58].

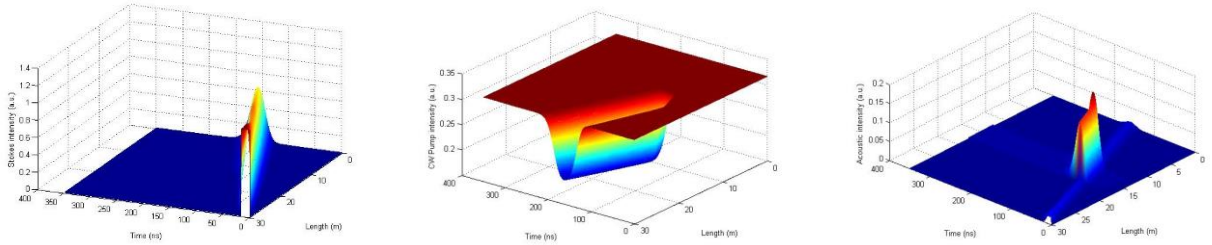

(a) (b) (c)

Figure 7-3. Evolution profile for (a) Stokes, (b) CW and (c) acoustic wave in a 30m long fiber. The frequency difference is set to be on resonance with a 5 m section at the center of the fiber.

7.3 Single-sideband BOTDA experiments

7.3.1 Schematics

The experimental schematic is shown in Figure 7-4. The laser (NP Photonics) was operating at 1550.072 nm with power output of 56.6 mW. A coupler was employed to divide the light into two beams, creating the counter-propagating situation.

For the upper branch, light was shifted (both up and down) by Δv in frequency by an EOM (JDS Uniphase, OC192 modulator). Δv was controlled by a microwave generator (Agilent N5183A). At this point, a polarization controller was placed in front of the EOM to adjust polarization state of the input light and obtain the best modulation efficiency. A spectrum analyzer (HP 8566B) was used to monitor the modulated spectrum. A sharp tunable filter (Santec OTF350) was used to choose only the downshifted frequency component in the spectrum. Since the bandwidth of the filter was very broad, only the sharp edge was used to suppress the unwanted spectrum of the light. Two EDFAs (AFL Telecommunications EDFA –MW-BA-40-18-19) were used due to the large attenuation caused by both EOM and filter. A polarization scrambler (General Photonics PCD-104) changed the light polarization state quickly to eliminate the polarization dependence of Brillouin scattering in the fiber. An isolator was used to prevent the light back-reflection.

On the lower branch, light was modulated into pulses by another EOM (JDS Uniphase, OC192 modulator). A pulse generator (Tektronix AFG3252) provided a pulsed modulation signal with 100 KHz repetition rate and the pulse width was adjusted from 100 ns to 1ms. A polarization controller was used to optimize the pulse shape. One tunable EDFA (NORTEL NETWORKS) was sufficient to achieve sufficient gain for the signal.

The two beams counter-propagated in the fiber under test (FUT) and the pulsed light transferred energy to the frequency-downshifted light through SBS. The output signal went to the circulator and was then detected by the photodetector (HP 11982A). A preamplifier (Preamble Instruments 1822 Differential amplifier) was used to optimize the signal intensity for the oscilloscope (Agilent DSO90254A).

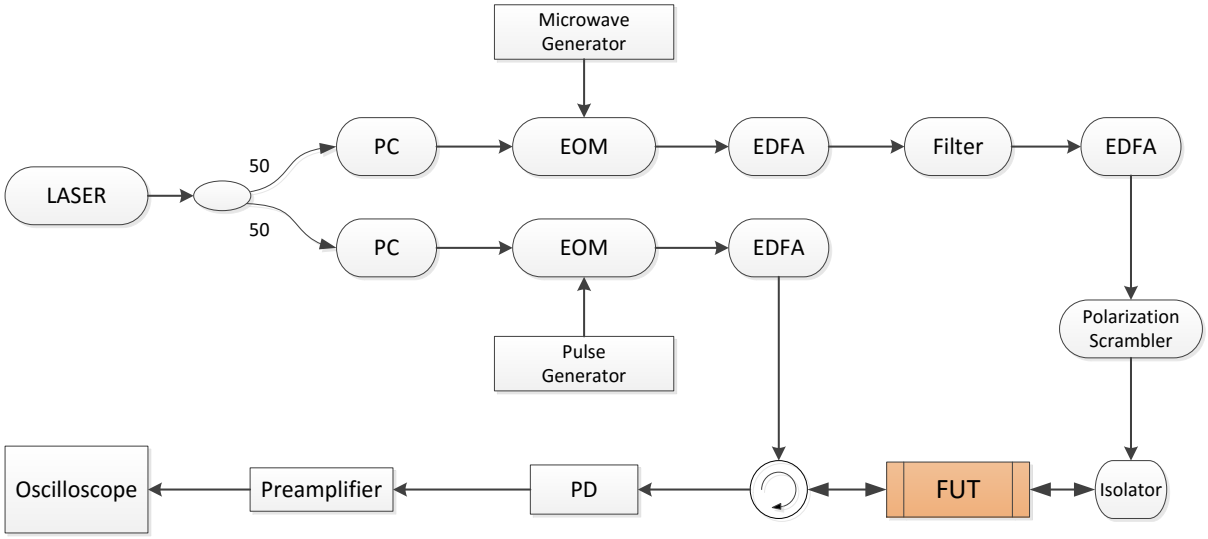

Figure 7-4. Experimental schematics for the single-sideband BOTDA measurement.

The completed bench-top system is shown in Figure 7-5.

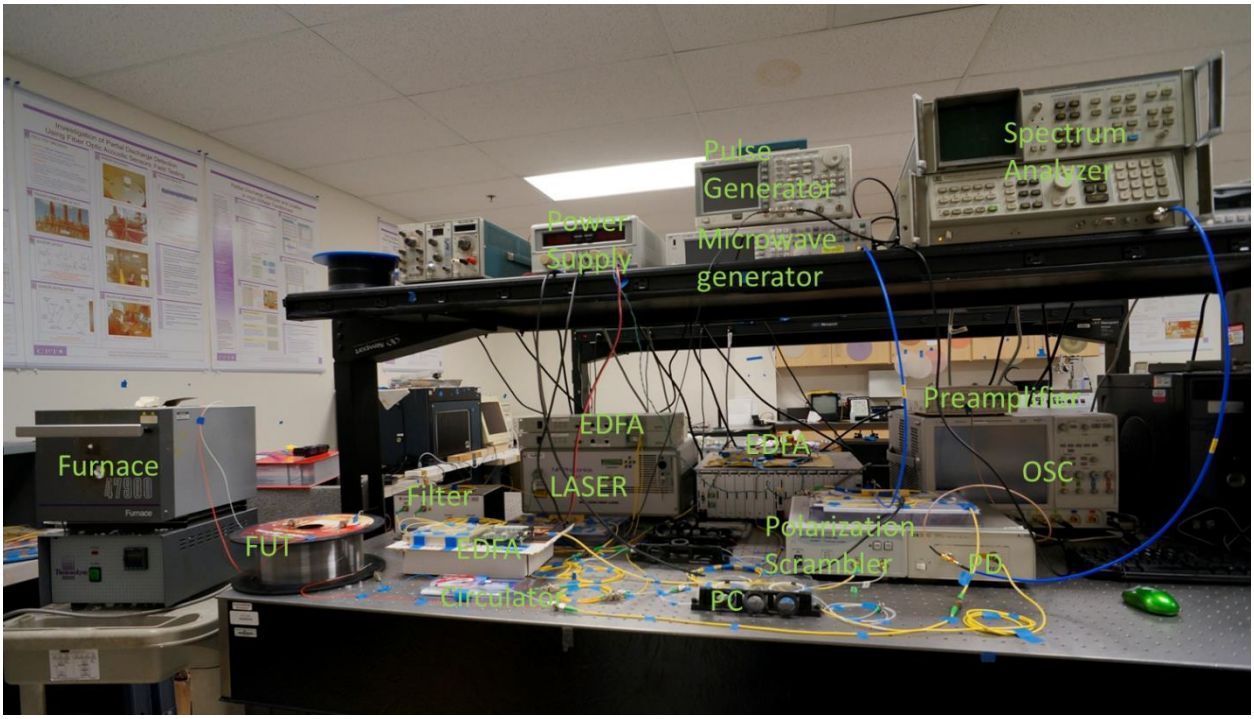

Figure 7-5. Photo of the experiment setup of the bench-top BOTDA system.

7.3.2 First experimental test

7.3.2.1 Twenty meter fiber heating test

The experimental setup in the first test is shown in Figure 7-6. A 20 m section of a 450m single mode fiber (SMF28) was put in the furnace and heated from room temperature up to 1000 ℃. The measurement results for 500 ℃ and 1000 ℃ are shown in Figure 7-7 and Figure 7-8 respectively. We can see that for the fiber at room temperature, the Brillouin frequency is around 10.9 GHz, while for the heated section (located at 100 m), the Brillouin frequency shifts to 11.31 GHz at 500 ℃ and to 11.67 GHz at 1000 ℃. This result, in principle, proves that the Brillouin frequency and the temperature are correlated, and it can be applied up to 1000 ℃ for distributed sensing.

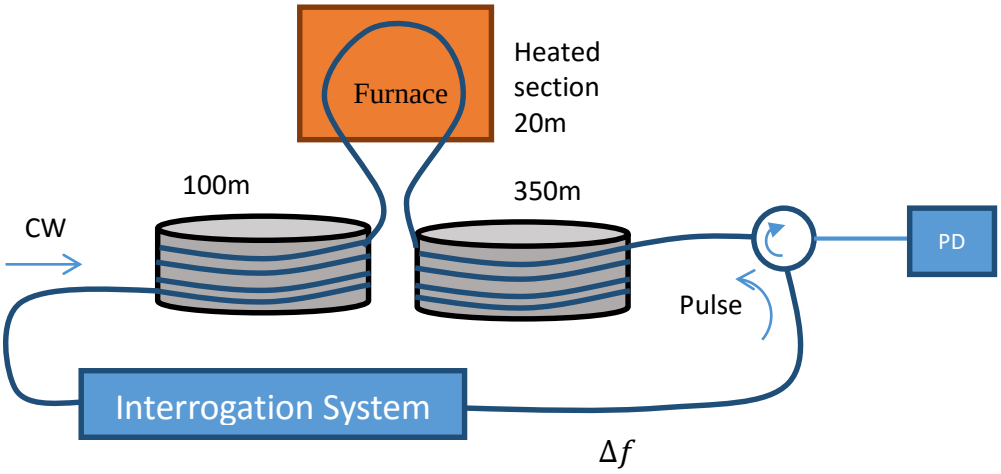

Figure 7-6. Experiment setup for distributed temperature measurement.

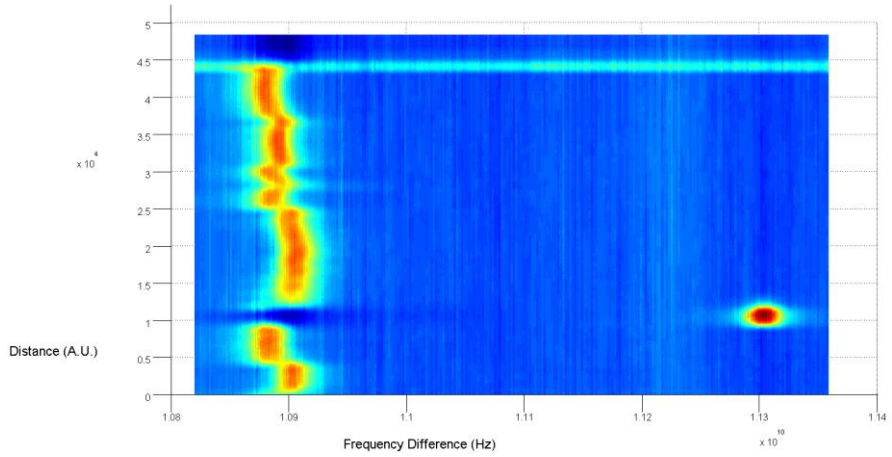

Figure 7-7. Brillouin signal measured at 500 ℃, color corresponds to temperature.

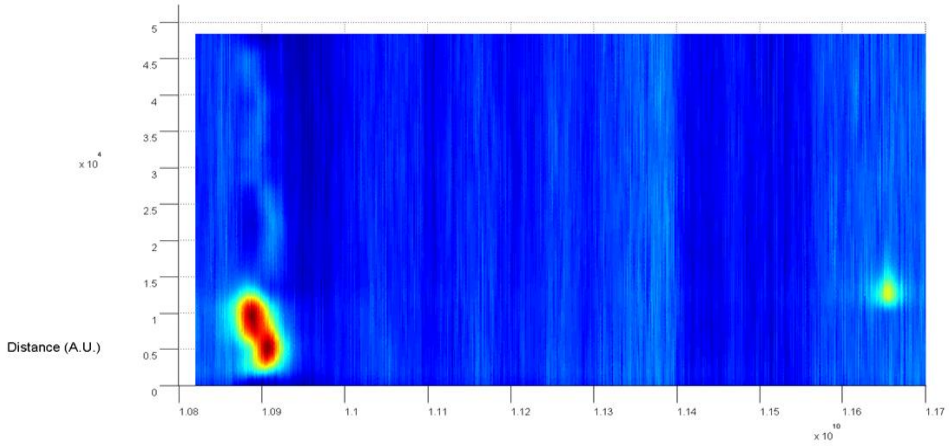

Figure 7-8. Brillouin signal measured at 1000 ℃.

The non-uniform background frequency shown in Figure 7-7 is attributed to the strain along the fiber. Since the fiber kept in room temperature was wrapped on spools, strain along the fiber could vary from section to section. The pattern for any section of the fiber was repeatable (as shown in Figure 7-9). Since the temperature information is only encoded in the frequency change, this background fluctuation will not affect the measurement if baseline correction is performed, which is shown in Figure 7-10.

In Figure 7-8, it can be observed that the Brillouin signal in the fiber section following the heated section became significantly weaker. This is due to the high loss in the heated section. This phenomenon is further investigated in Chapter 9.

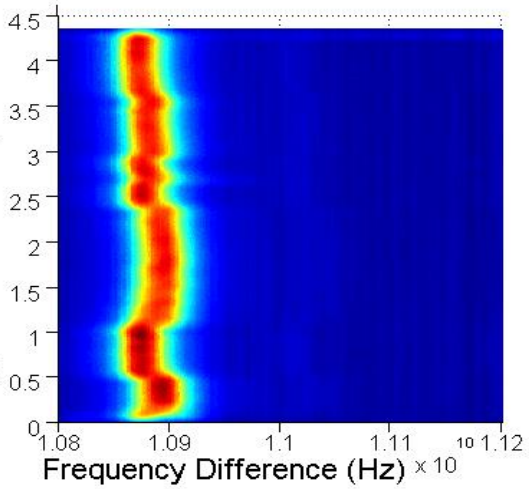

Figure 7-9. Raw data of the unheated section obtained in second measurement.

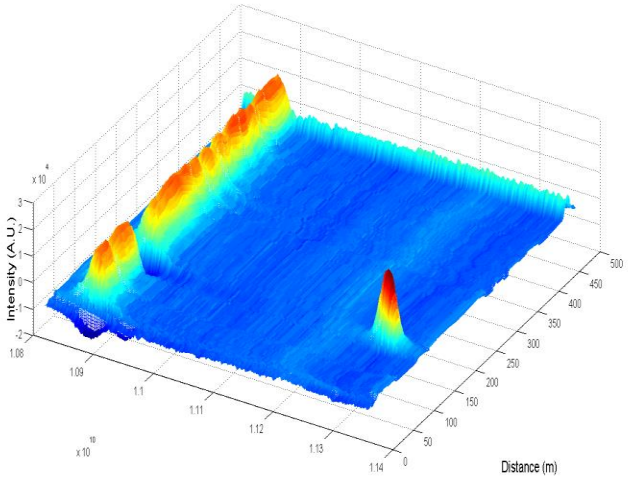

Figure 7-10. Brillouin data with background corrected.

The relationship between the Brillouin frequency shift and temperature is plotted in Figure 7-11. The relation is linear, while the error is relatively high for this setup.

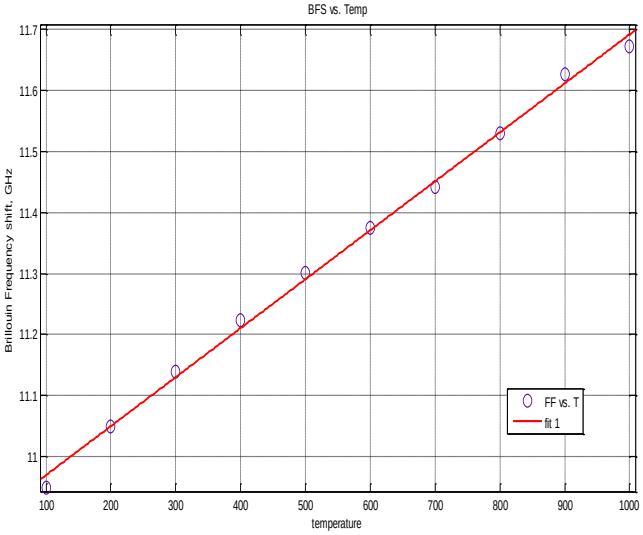

Figure 7-11. Temperature dependence of the Brillouin frequency.

7.3.2.2 Five meter fiber heating test

Using the same interrogation system in the former section, the fiber in the furnace is changed to a new 5m SMF28. At the same time, the pulse width was decreases to 50 ns to achieve 5 m spatial resolution. Measurements were taken at the temperature of 980 ℃, 990 ℃ and 1000 ℃. At each temperature, the frequency difference between the two light beams was swept from 11.6 GHz to 11.72 GHz, and the corresponding intensity of the DC light was recorded (shown in Figure 7-12). The spectral shift as a function of temperature can be clearly observed. This preliminary result demonstrates the feasibility that the spatial resolution can be as short as 5m and the temperature resolution can be on the level of 10 ℃, with the measurement range up to 1000 ℃.

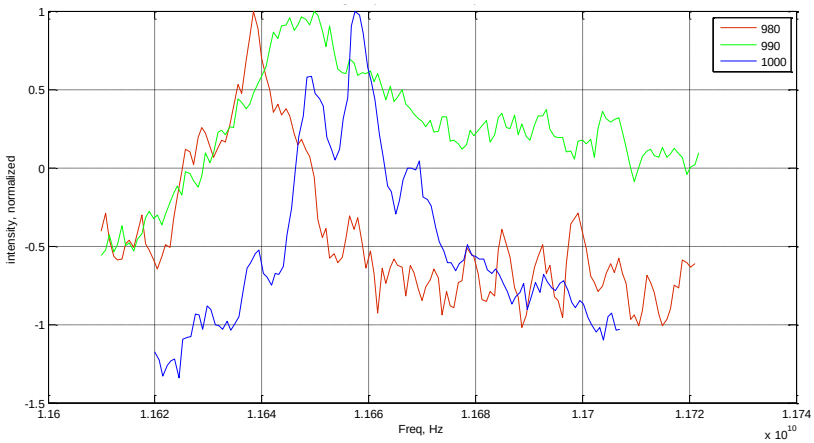

Figure 7-12. Spectra of a 5m long fiber heated up to 980 ℃ (red), 990 ℃ (green) and 1000 ℃ (blue) respectively.

7.3.3 Second experimental test

In the second test, the strain on the sensing fiber was released, and the interrogation system was optimized. A single-mode fiber with total length of 230m was tested. In the middle of it, a 1 m

section went through a furnace heated up to 500℃， while the other part was kept in room temperature. A 10 ns pulse beam was used for the pulse to achieve a spatial resolution of 1m.

The result is shown in Figure 7-13. A sharp peak can be observed at the position of ~165m, corresponding to the heated section. By zooming into the peak (Figure 7-14), we can see that at the heated position, 1m spatial resolution was well achieved, where the Brillouin frequency shifted from 10.87GHz (room temperature) to 11.3GHz (500℃).

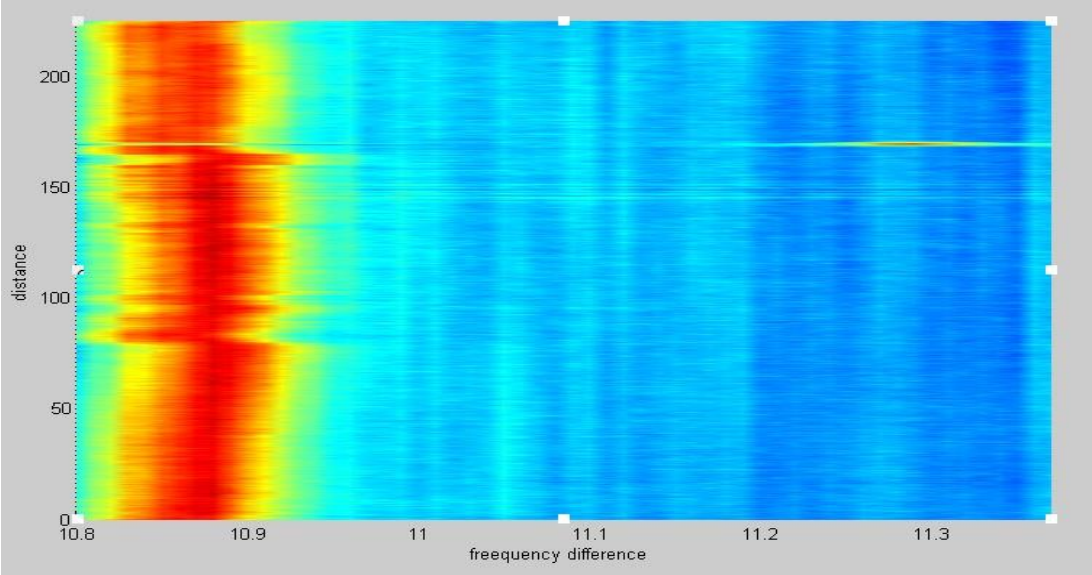

Figure 7-13. SBS distributed temperature measurement at 500℃ with spatial resolution 1m over 230m span.

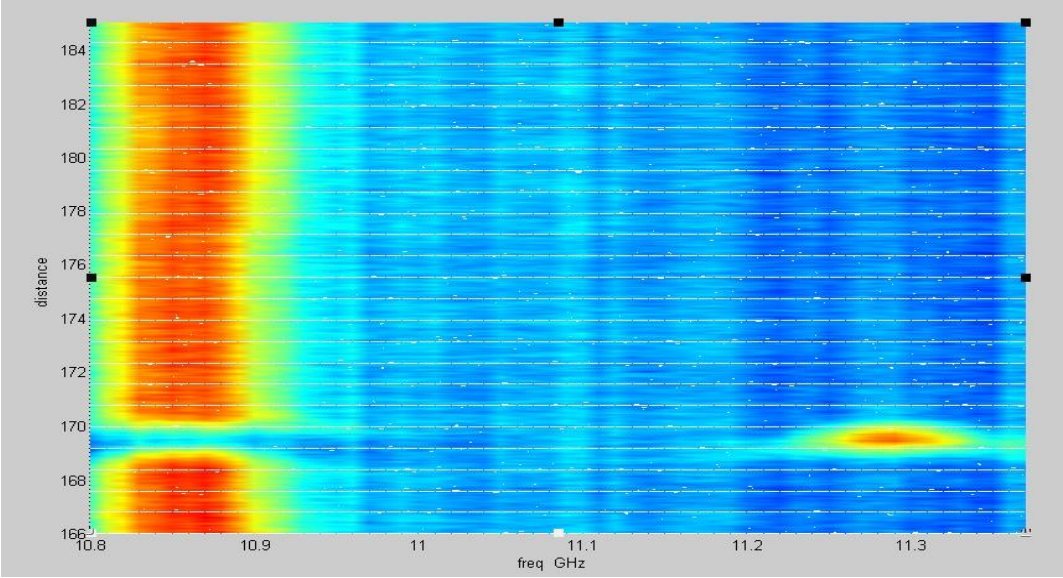

Figure 7-14. Intensity distribution zoomed in the heated fiber region. A spatial resolution of 1 m is well demonstrated.

Figure 7-15 shows the SBS intensity distribution along the fiber at 10.87 GHz, which is the Brillouin shift frequency of single mode fibers at room temperature and 1550 nm wavelength. The heated part is shown as a peak on the SBS intensity background at this frequency, which is sharp and clean, well achieving 1m spatial resolution. The background is not flat due to non-uniform strain distribution, which can be flattened by background subtracting.

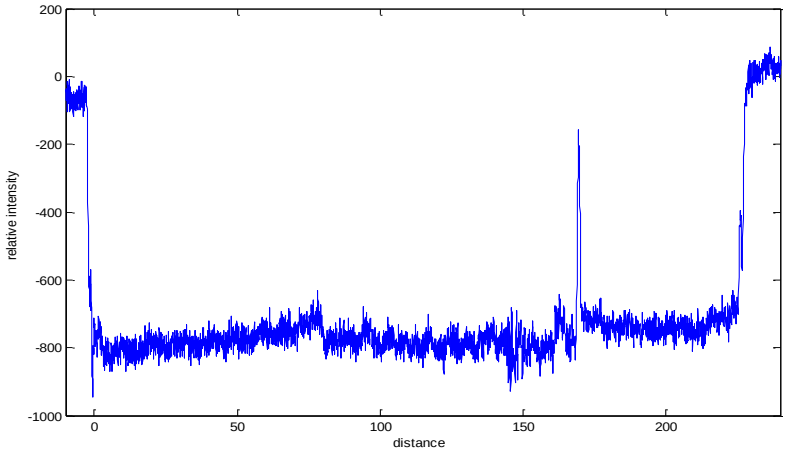

Figure 7-15. Brillouin gain signal observed at 10.87GHz, 500 ℃.

By looking at the Brillouin loss signal at 11.30GHz, we can see that the signal peak on a cleaner background (Figure 7-16). Observing at this frequency could help obtain better signal in single temperature demodulation compared with the Brillouin gain method.

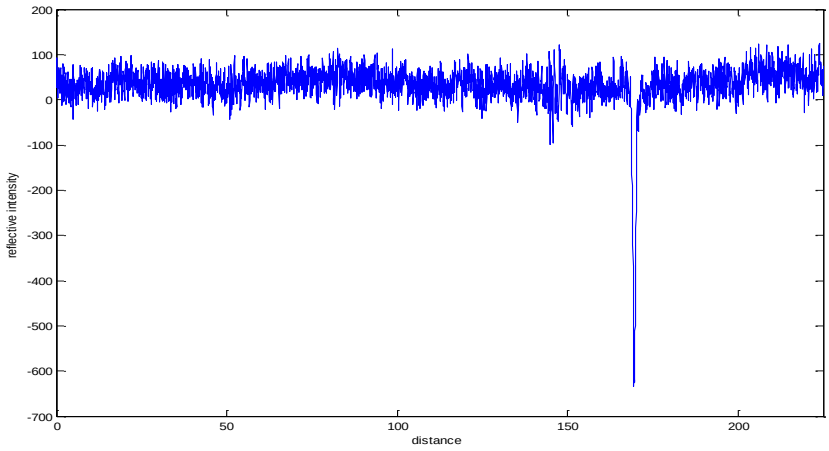

Figure 7-16. Brillouin loss signal observed at 11.30GHz, 500 ℃.

Then, the test continues and the fiber was heated up to 1000 ℃. At 1000 ℃, the system also showed good performance. As we can see in Figure 7-17 and Figure 7-18, the system achieved 1m spatial resolution over 230 m fiber, which is the same as the systems used for the 500 ℃ test. The Brillouin frequency shift of the heated part is 11.67 GHz instead of 11.3 GHz at 500 ℃, indicating the additional 500 ℃ temperature difference. The frequency shift of 11.67 GHz also agrees with the experiment results recorded in the 1000 ℃ test.

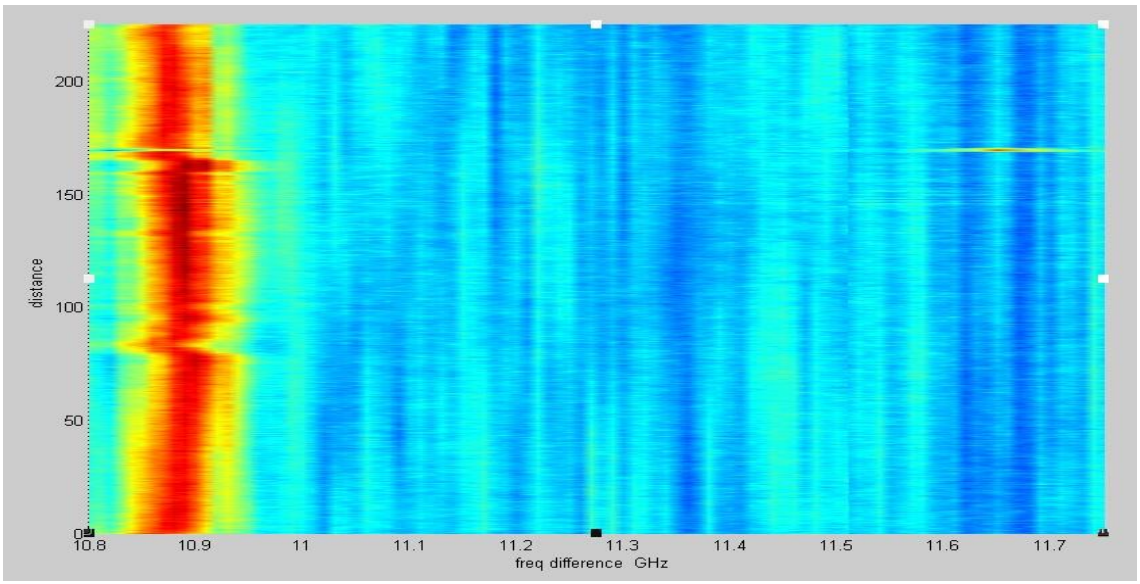

Figure 7-17. SBS distributed temperature measurement in 1000 ℃ with spatial resolution 1m over 230m fiber.

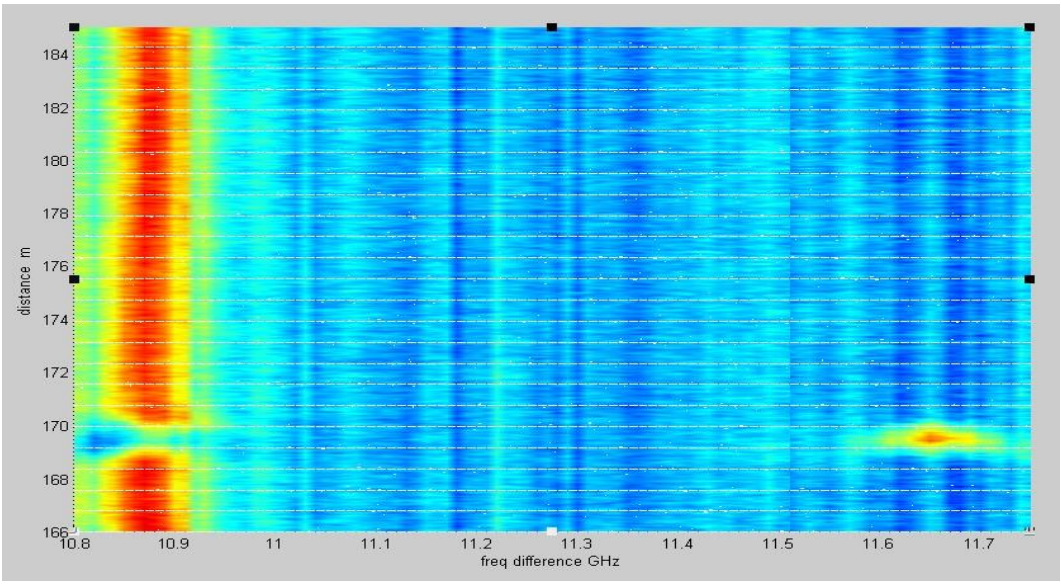

Figure 7-18. Zoomed intensity distribution at the heated part. One-meter spatial resolution well achieved.

By comparing the Brillouin gain intensity distribution at 10.87GHz (Figure 7-19 and Figure 7-15), we can see the system SNR at 1000 ℃ is much lower due to a notably increased random background noise. Nonetheless, the peak in the heated region can still be clearly identified and 1m spatial resolution can be still guaranteed. The Brillouin loss signal also suffers from the increased background noise, but the influence is obviously smaller than in the Brillouin gain data (Figure 7-20).

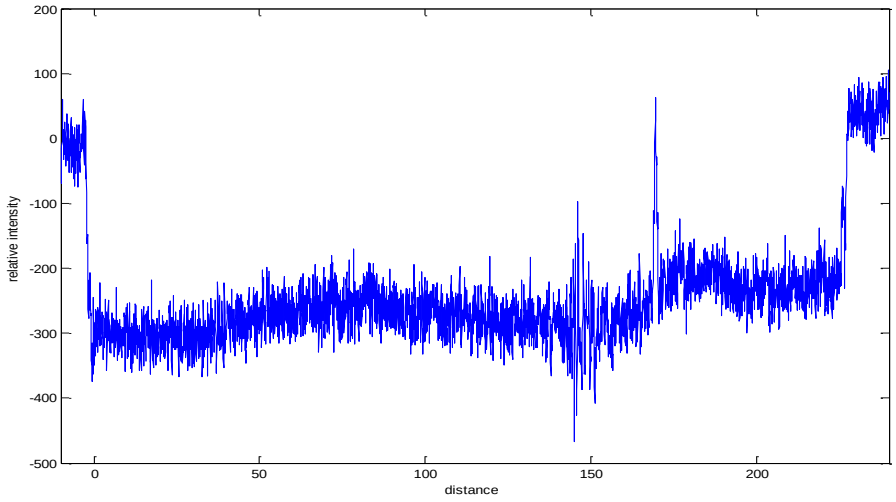

Figure 7-19. Brillouin gain signal observed at 10.87GHz, 1000 ℃.

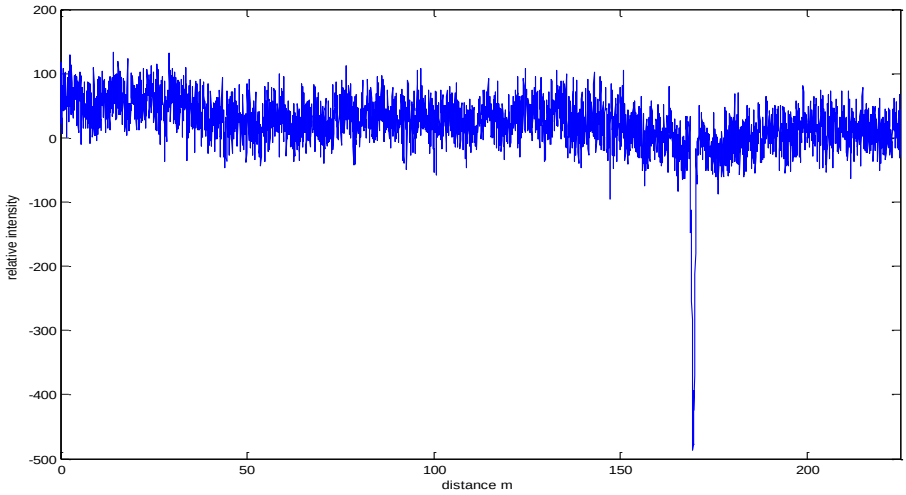

Figure 7-20. Brillouin loss signal observed at 11.30GHz, 1000 ℃.

To measure the temperature resolution of the system, tests were conducted near 1000 ℃ where the noise level is highest over the entire sensing range. Three measurements were made at 990 ℃, 995 ℃ and 1000 ℃ respectively, and the Brillouin loss method was used with a frequency scan range of 11.6 GHz to 11.76 GHz. The intensity peaks are shown in Figure 7-21.

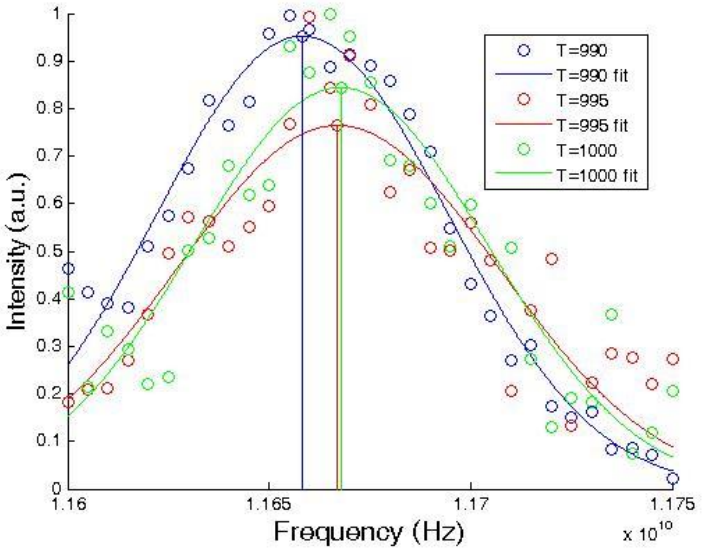

Figure 7-21. Measured (dots) and fitted (curve) spectra of 1m fiber under 990 ℃ (blue), 995 ℃ (red) and 1000 ℃ (green).

By fitting the data with Gaussian functions, the 990 ℃ peak (11.6582GHz) can be clearly distinguished from the 1000 ℃ peak (11.6678GHz), while 995 ℃ peak (11.66705GHz) is quite close to the 1000 ℃ peak. The variation in the spacing between the three peaks comes from the influence of the system noise and other errors. By improving the system SNR and the demodulation algorithm, the temperature resolution could be further improved.

7.4 Dual-sideband BOTDA scheme

As discussed in Section 7.1.7, allowing both sidebands generated by the EOM to propagate in the FUT in a BOTDA will allow continuous energy transfer from the higher frequency probe light into the pump pulse, resulting in longer sensing range and better signal quality. In this section, the system was modified to realize the dual-sideband BOTDA sensing scheme.

The experimental setup is shown in Figure 7-22. The system is basically similar to the one described in section 7.3.1, but with the tunable filter moved before the photo diode. This allows both sidebands generated in the probe light interact with the pump light, and the measured side band only got selected after the probe light was circulated into the detection arm. By this means, dual-sideband BOTDA measurements could be performed.

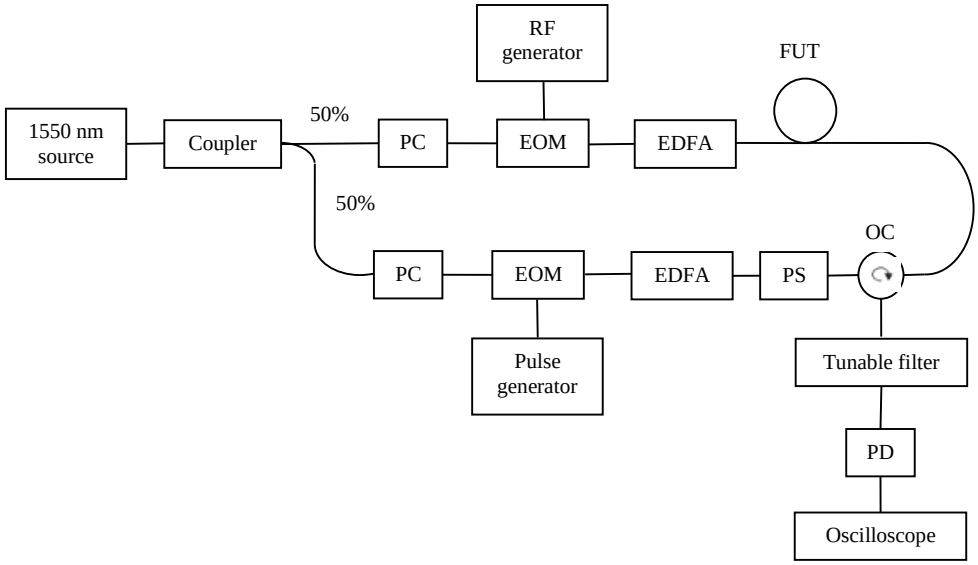

Figure 7-22. Experimental setup of the dual gain-loss SBS measurement scheme. The optical tunable filter which was previously on the probe light arm is now placed at the output of optical circulator.

The new scheme was tested with a 100 m heated FUT and 100 ns pump pulse. Compared with single band scheme, the signal intensity increased by a factor of 3, as shown in Figure 7-23.

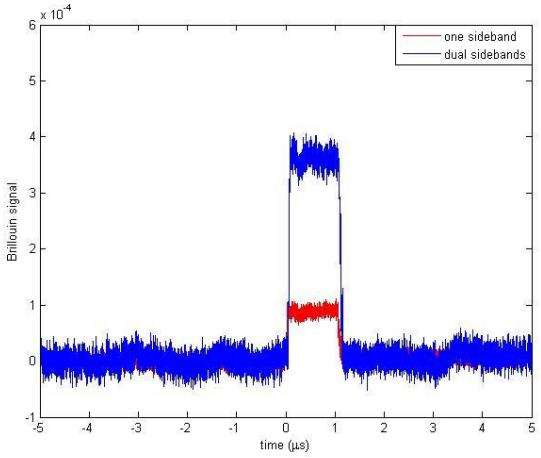

Figure 7-23. Measured Brillouin signals using single sideband (red) and dual sidebands (blue) of EOM frequency.

With the higher signal using a dual gain-loss setup, improvement on system temperature resolution and data acquisition speed is possible.

At 1000 ℃, temperature resolution of the system is challenged by the noise from the thermal radiation background. At the same time, the temperature vibration of the testing environment also introduces error during the system resolution characterization. To minimize the influence of furnace temperature fluctuation, long stabilizing time, tight sealing and improved thermocouple positioning were applied in this test.

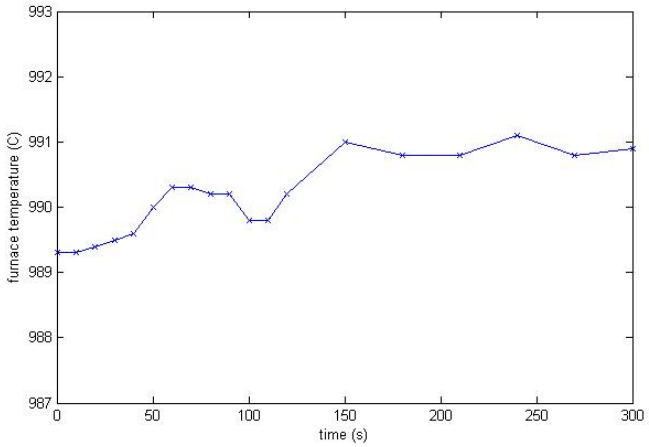

Figure 7-24. Furnace temperature reading over 6min (furnace temperature set to 990 ℃).

A temperature stability test of the furnace was done, as shown in Figure 7-24. A 2 ℃ temperature variation was observed during the 6 min test. In the current SBS system, the acquisition time for each frequency point is ~30 s, which means ~10 min acquisition time for each temperature measurement. As a result, it can be estimated that ~2 ℃ temperature uncertainty can be introduced by the furnace.

In the second test, a one meter section of the 100 m sensing fiber was heated in the furnace, and 10 ns pump pulses guaranteed a spatial resolution of <1 m. The SBS gain signals are shown in Figure 7-25.

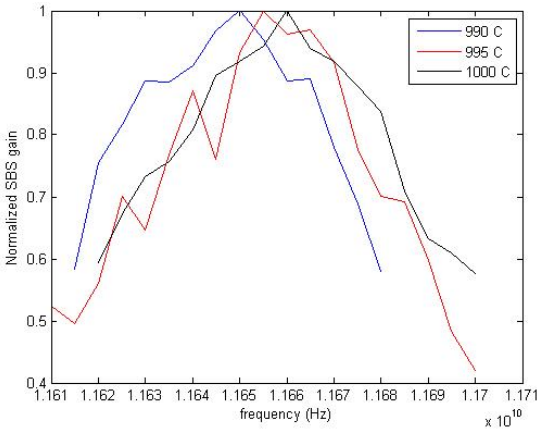

Figure 7-25. Measured SBS gain within the 1m heated fiber as a function of frequency at the temperature T = 990 ℃ (Blue), 995 ℃ (Red) and 1000 ℃ (Black), respectively.

To demodulate the central Brillouin frequency, Gaussian fittings are applied to these three data sets, as shown in Figure 7-26. The fitted peak frequencies of 990 ℃, 995 ℃ and 1000 ℃ are 11.650, 11.655 and 11.660 GHz, respectively. The 0.005 GHz frequency difference for 5 ℃ agrees well with former results. The error introduced by furnace temperature drift shows clearly as data point shift, which indicates that the actual system resolution can be higher than the measured value.

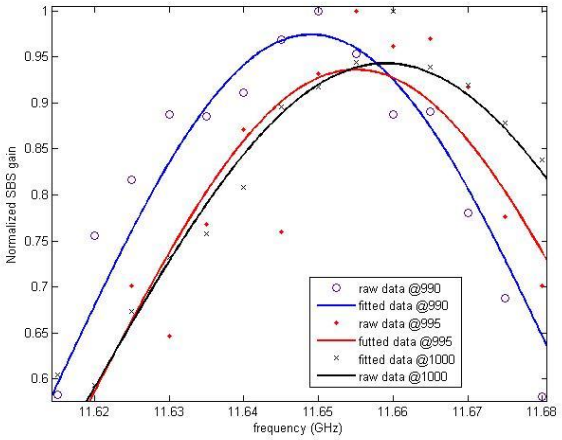

Figure 7-26. Gaussian fitted data at T = 990 ℃, 995 ℃ and 1000 ℃.

7.5 Further system optimizations

7.5.1 Optimization of optical tunable filter settings

The performance of the optical tunable filter (OTF) in the sensing system is one of the key factors that affect the acquired SNR. In the current system (Figure 7-27 (a)), the OTF is used to filter all lights expect the sideband carrying Brillouin signal. Since the pump light is very close to the wanted sideband (~87 pm for 10.875 GHz shift), the OTF is required to have a very narrow filtering bandwidth. For OTF, setting at a narrow bandwidth leads to a high insertion loss. Balance has to be found between these two factors to achieve best SNR.

By monitoring the spectrum on a component test system (CTS), fine adjustment of the OTF was performed for system optimization. The optimized OTF setting is shown in Figure 7-27 (b), with a transmission loss of -8 dB, and a filtering efficiency of -12 dB at the pump light wavelength.

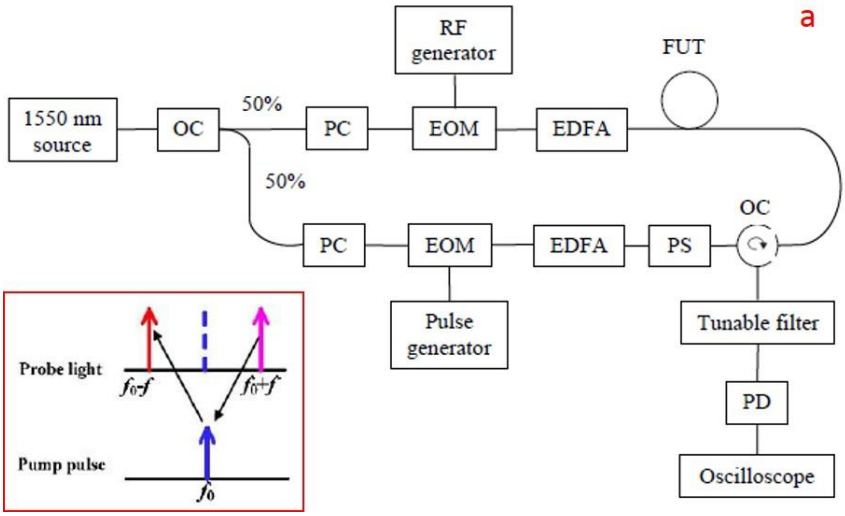

(a)

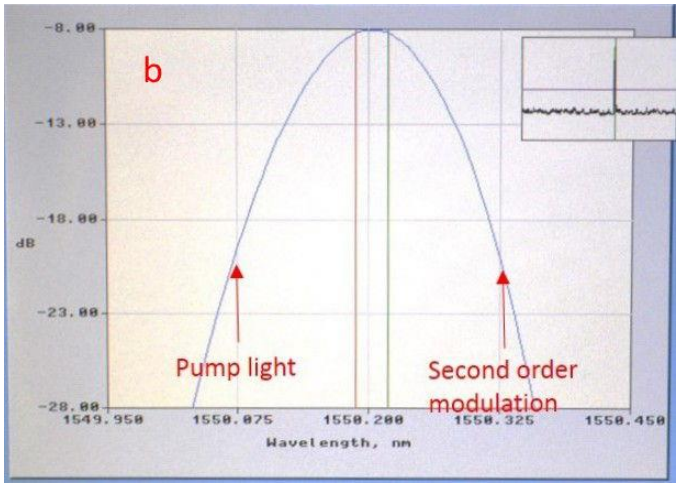

(b)

Figure 7-27. (a) Distributed sensing system setup. (b) Optimized OTF setting.

Figure 7-28 shows the Brillouin loss (left) and Brillouin gain (right) signals acquired with the OTF settings presented above. The unit on the y-axis is the voltage reading on the oscilloscope without temperature calibration. The blue lines are signals recorded from one scan, while the red lines presents the signals after 100 averages. The total signal intensity was enhanced ~8 times with the OTF optimized comparing to the former results, and similar SNR could be achieved with only 100 averages instead of the former 1000 averages.

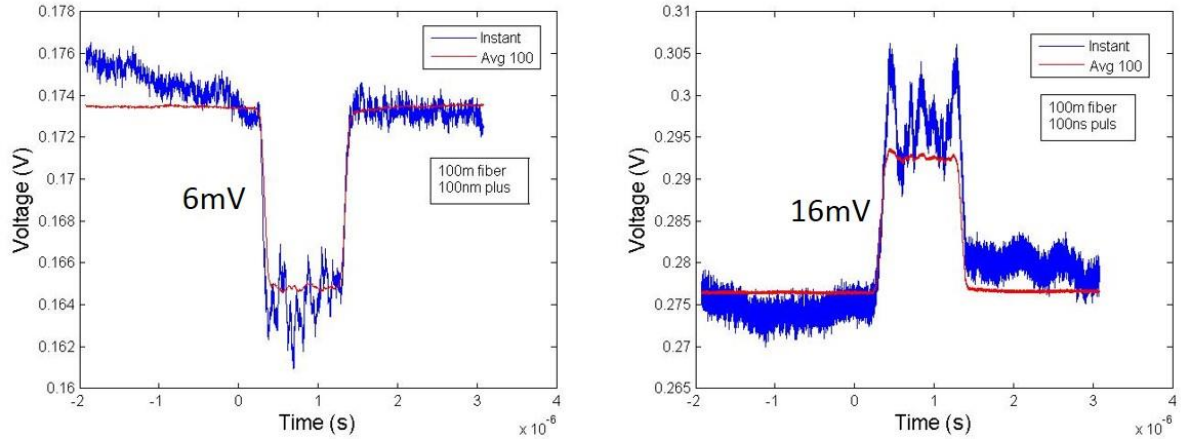

(a) (b)

Figure 7-28. Signal acquired with Brillouin loss (a) and Brillouin gain (b) schemes.

7.5.2 Optimization of data acquisition

The most notable drawback of the former sensing system is the relatively long data acquisition time. In the former reports, a complete scan from room temperature to 1000 ℃ takes about 70 minutes, which is too slow for real-time monitoring. To increase the data acquisition speed, a new continuous data acquisition scheme was developed.

In the former scheme, the synchronization between the microwave generator and the oscilloscope was controlled by the master computer, which takes extra time waiting and reading data in each scanning cycle. In the new data acquisition scheme, as the RF signal scans periodically within the frequency sweeping range, the high-speed oscilloscope records all data continuously and outputs the data as a completed packet, as shown in Figure 7-29. By directly synchronizing the two instruments, the idle time between the acquisitions could be eliminated, greatly boosting the data acquisition speed.

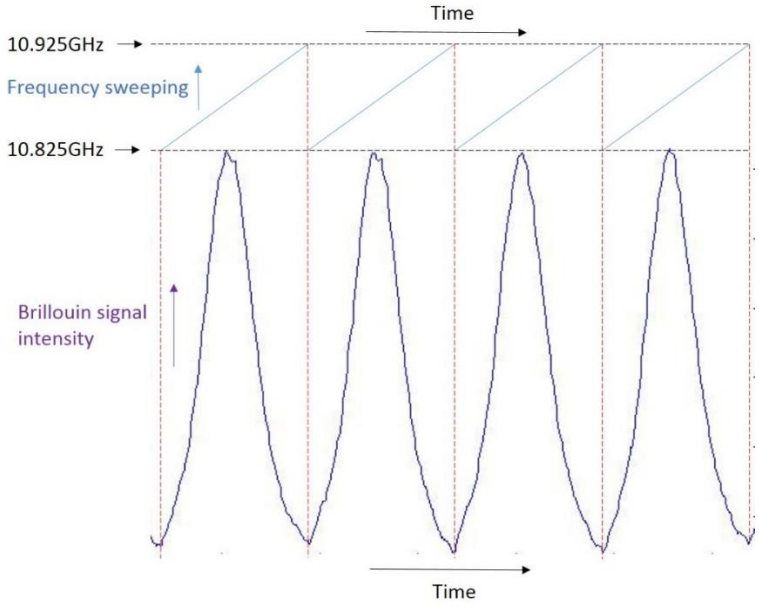

Figure 7-29. New continuous data acquisition scheme.

Figure 7-30 shows the Brillouin spectrum obtained using 100 ns pulses with 10 averages at room temperature. The scanning and averaging over the 10.825 GHz to 10.925 GHz range took less than 1 s to finish in a 1000 m long fiber (without data processing). Figure 7-30 (a) shows the Lorentz fitting of one of the acquired spectrum. The complete set of spectra over the 1000 m fiber is shown in Figure 7-30 (b).

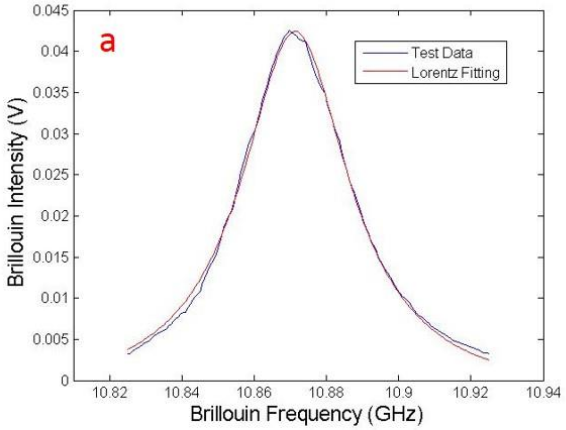

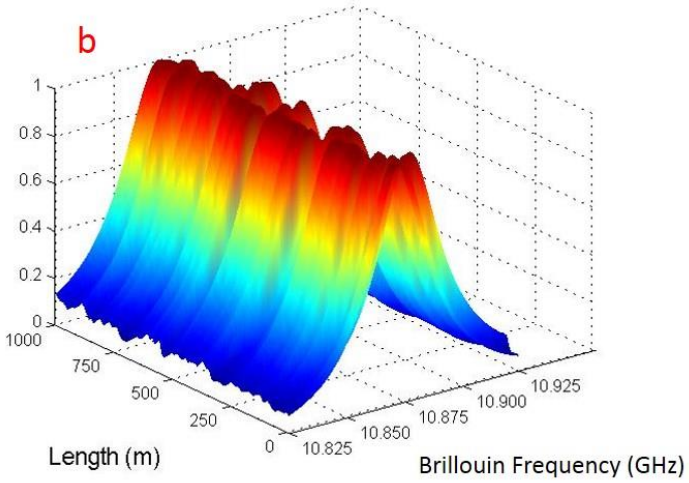

Figure 7-30. Brillouin signal scanned with the new data acquisition scheme, with 100 ns pulses over a 1000 m long fiber. (a) Acquired Brillouin spectrum. (b) 3D plot of complete data set.

Figure 7-31 shows the scanning data with 10 ns pulse width, which corresponds to the high spatial resolution mode (<1 m). The SNR in this mode is relatively low compared to the low resolution mode. To acquire clean data, 100 averages were taken for each data set. Figure 7-31 (a) and Figure 7-31 (b) show the signal acquired with 10 and 100 averages respectively. The complete averaged data acquired in a 1000 m fiber is shown in Figure 7-31 (c). The scanning and averaging took less than 5 s to finish without data processing.

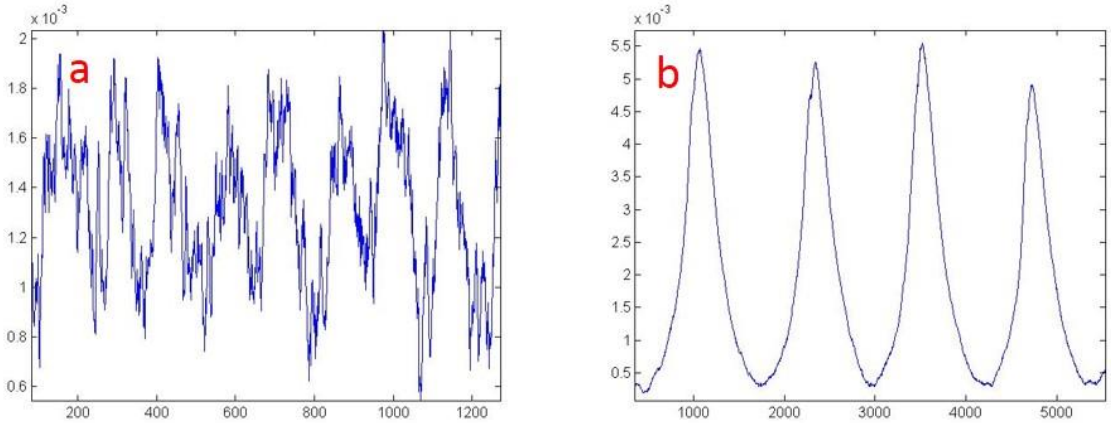

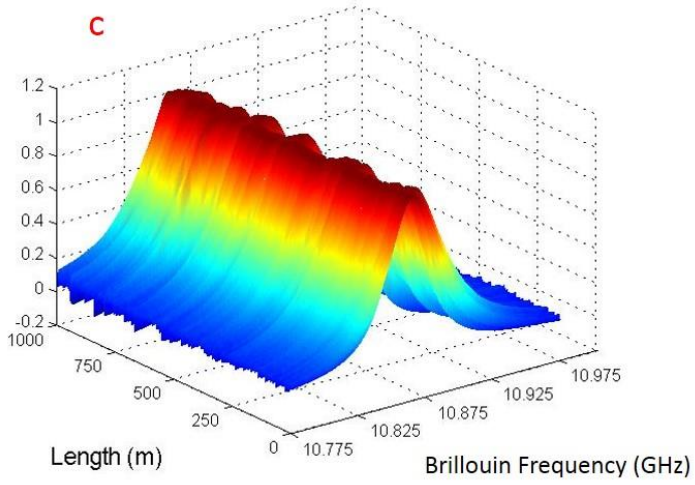

Figure 7-31. Brillouin signal scanned with 10 ns pulses over a 1000 m long fiber. (a) Brillouin spectrum with 10 averages. (b) Brillouin spectrum with 100 averages. (c) 3D plot of the complete data set.

A comparison between the 100 ns and 10 ns scan results is shown in Figure 7-32. It is clearly shown that more details in the stress-induced Brillouin shifts could be recognized from the high resolution data (Figure 7-32(b)).

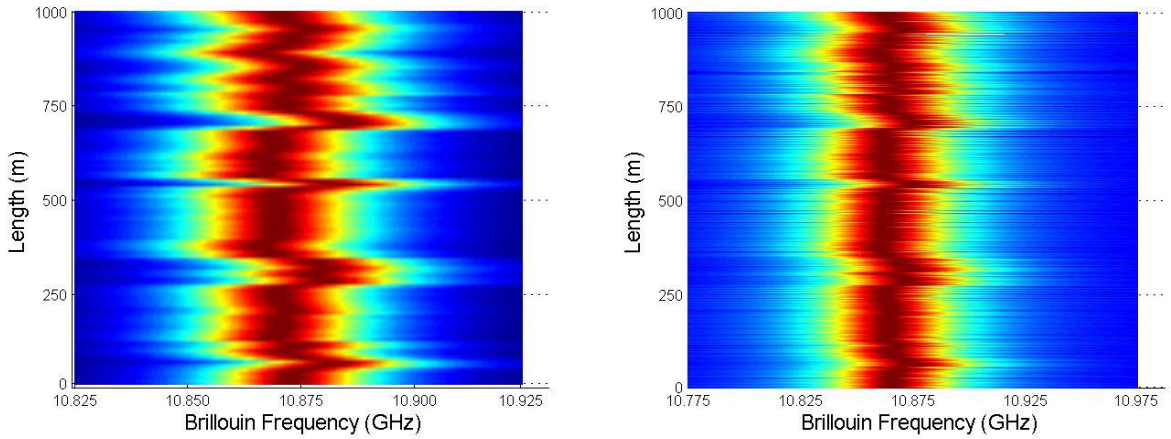

(a) (b)

Figure 7-32. Comparison of stress-induced Brillouin shifts using (a) low resolution (100 ns) and (b) high resolution (10 ns) scanning modes.

Comparing to the former acquisition scheme, the time consumption of a complete room temperature to 1000 ℃ scan and the following data processing using the new scheme was reduced to ~3 min from the former ~70 min, which is a speed boost of a factor of 20.

7.6 Temperature and spatial resolution tests

7.6.1 Temperature repeatability and accuracy test

The system setup for the temperature measurement accuracy and repeatability test is shown in Figure 7-33 (a). Two segments of the sensing fiber were looped in a box furnace and heated up to 1000 ℃. The length of the two segments were 1m and 3m respectively, separated by a 3m long segment, which was kept in room temperature. The heated fiber segments were coiled and placed at the bottom of a box furnace. As the temperature reference, a thermocouple was collocated with the fiber loops to record the temperature near the sensing fiber, as shown in Figure 7-33 (b).

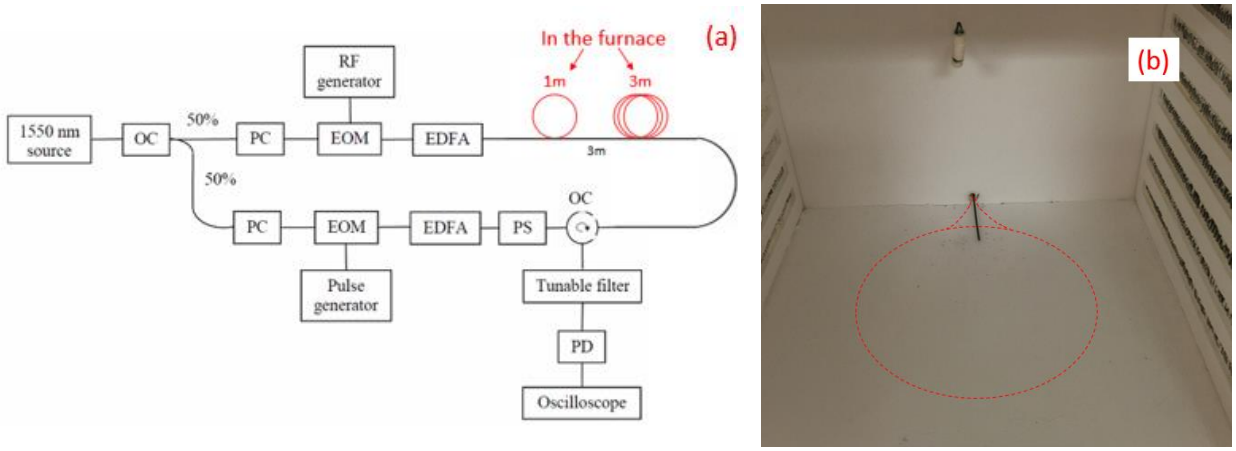

Figure 7-33. System setup for the temperature accuracy and repeatability test. (a) System diagram; (b) fiber and thermocouple placement in the box furnace.

The first thermal cycle was conducted up to 1000 ℃ to remove the fiber coating. The Brillouin signal response during the heat up process was recorded as shown in Figure 7-34. Below 900 ℃, the Brillouin signal response was quite smooth. When the fiber was heated above 900 ℃, abnormal change of the response was observed. It is believed to be a result of the coating being burnt off form the fiber, and the stress applied by the coating was gradually released. When the curve is compared with the response of a bare fiber (obtained in the second thermal cycle), significant differences can be observed.

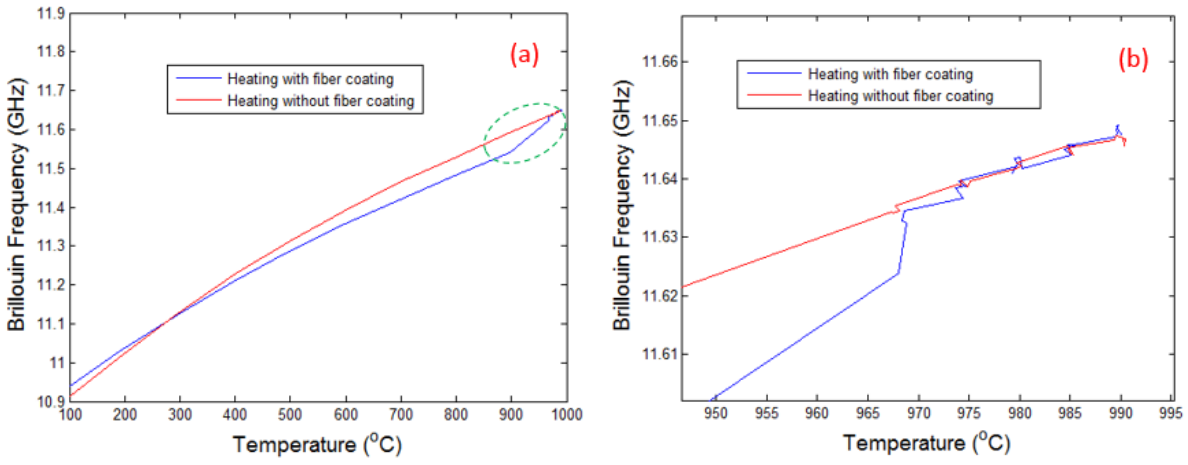

Figure 7-34. Brillouin frequency response to temperature of a SMF-28 sensing fiber with and without coating.

After the coating was burnt off, two additional thermal cycles were conducted on the same fiber up to 1000 ℃. Measurements were taken every 100 ℃ from 100 ℃ to 900 ℃, and every 5 ℃ from 965 ℃ to 990 ℃. In every thermal cycle, the fiber was annealed for 4 hours above 950 ℃. As shown in Figure 7-35, no obvious drift was observed between the two curves, which indicates the high repeatability of the system.

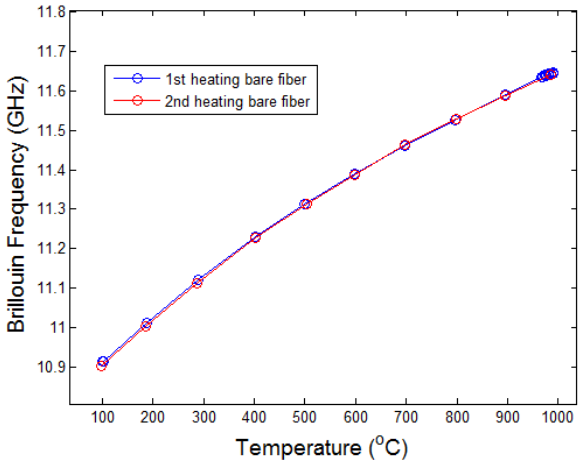

Figure 7-35. Brillouin frequency response of a bare sensing fiber recorded during two thermal cycles up to 1000 ℃.

A system calibration was conducted based on the data. Using a second order polynomial fitting, we obtained an expression of

$$\nu_b = -3.477 \times 10^{-7} \times T^2 + 0.0012013 \times T + 10.7981 \qquad \text{Eq. 7.15}$$

where ν_b is the Brillouin Frequency (in GHz) and T is the temperature (in ℃). According to the result of the fitting, at lower temperatures, the absolute value of the slope is larger, indicating a relatively higher temperature response.

To evaluate the temperature resolution of the system, 5 measurements were taken every 5 ℃ from 965 ℃ to 990 ℃. Lorentzian functions were used to fit the raw data, and the center positions of the best fittings were adopted as the Brillouin frequencies of the data sets. A typical fitting is shown in Figure 7-36.

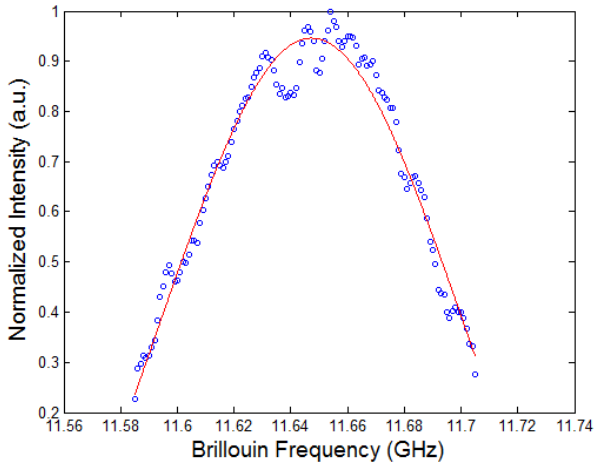

Figure 7-36. Lorentzian curve fitting of the Brillouin Spectrum obtained at 990 ℃.

The Lorentzian fittings of the Brillouin spectra obtained at temperatures from 965 ℃ to 990 ℃ are plotted in Figure 7-37. The peak positions of the fitting curves are marked with vertical lines. The fluctuation of the peak intensity is introduced by the EOM and the EDFA in the optical system, which does not affect the accuracy of the peak position demodulation.

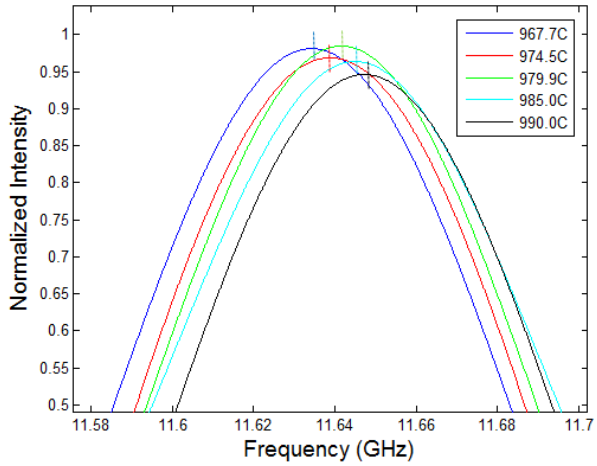

Figure 7-37. Best Lorentzian fittings of the Brillouin spectra at temperatures from 965 ℃ to 990 ℃.

Five measurements were taken at each temperature point. With these results, the standard deviations of the demodulated temperatures were calculated. As shown in Figure 7-38, the standard deviations at all the temperatures are within the range of 0.49 MHz to 0.65 MHz. Based on the calibration data of the sensor (Eq. 7.15), the slope of the frequency response is 0.51 MHz/ ℃ within this temperature range. Therefore, the standard deviation of the temperature measurement can be calculated using the following equation:

$$\sigma(T) = \frac{\sigma(\nu)}{k} \qquad \text{Eq. 7.16}$$

where $\sigma(\nu)$ is the standard deviation of the Brillouin frequency and *k* is the slope of the calibration function at the temperature *T*. Therefore, the temperature resolution of the system, which is defined as $2\sigma(T)$, can be calculated to be 2.5 ℃ within this temperature range.

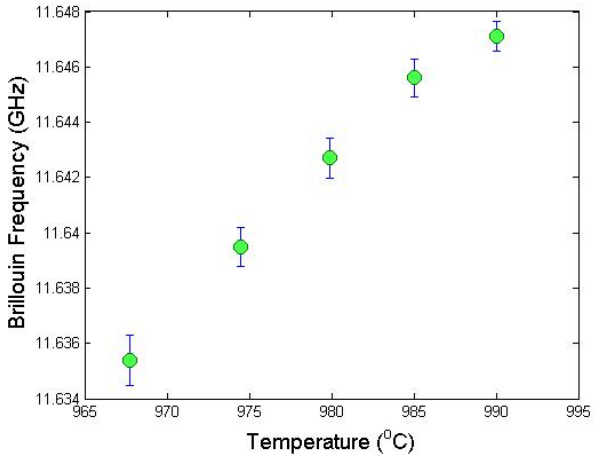

Figure 7-38. Temperature resolution of the sensing system within the temperature range of 965 ℃ to 990 ℃.

7.6.2 Spatial resolution

In these tests, 10 ns pump pulses were used to achieve 1 m spatial resolution. Based on the signal quality, 200 averages were applied in each measurement. Frequency scanning was performed from 10.7 GHz to 11.8 GHz with intervals of 2 MHz to cover the temperature range from room temperature up to 1000 ℃, taking 9 minutes for each measurement. In real applications, the response speed can be improved by reducing the frequency scanning range according to the temperature range in the sensing area.

The measured Brillouin frequency and temperature distribution along the entire 45 m long sensing fiber are plotted in Figure 7-39. A spatial resolution of 1m was well demonstrated.

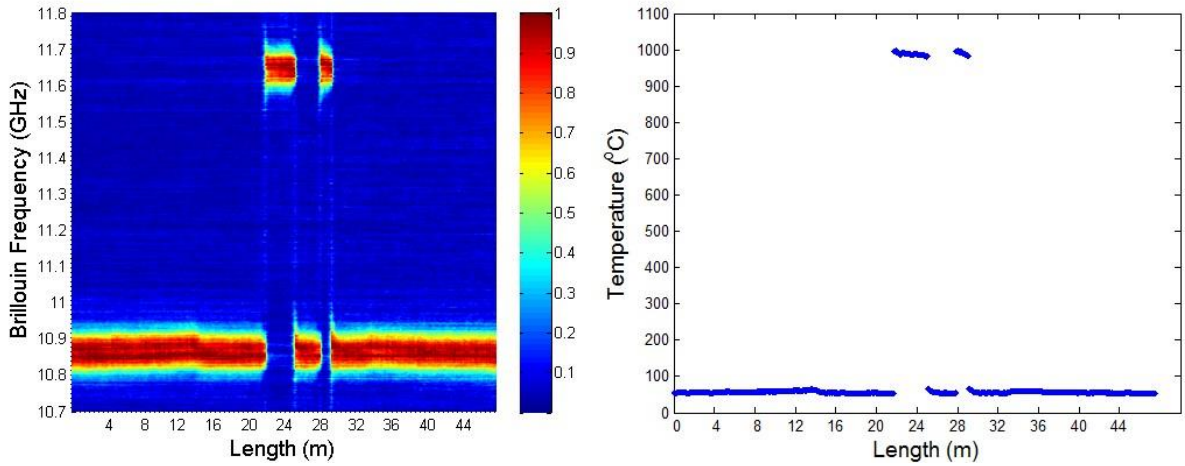

(a) (b)

Figure 7-39. Brillouin spectra (a) and demodulated temperature distribution (b) measured along the entire 45m long fiber sensor.

7.6.3 Temperature measurement repeatability test

The system setup for the temperature repeatability test is illustrated in Figure 7-40.Two segments of a single mode silica fiber were coiled inside a high temperature furnace. The length of each segment was 1 m. The length of the fiber between the two heated segments was 2 m, which was kept in room temperature. With such a setup, two hot spots with the size of 1 m each were simulated on the sensing fiber simultaneously.

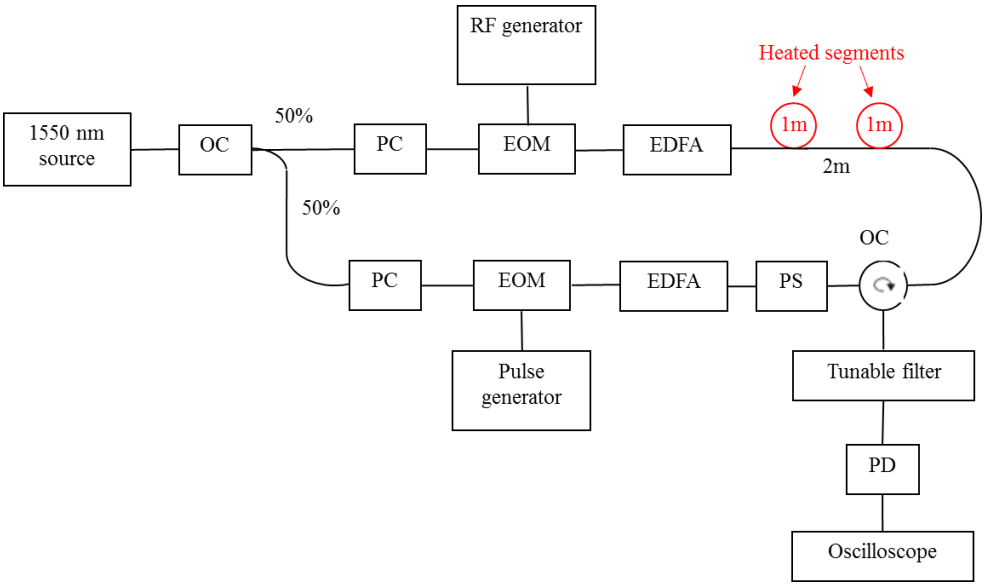

Figure 7-40. Setup diagram for the system repeatability test.

In the last section, we reported that the significant impact of fiber coating residue has on the Brillouin frequency measurement. Therefore, in this test, the fiber was pre-treated at 800 ℃ for two hours to completely remove the coating before starting the measurement heating cycles. Then, the fiber was cooled down, and heated up from 100 ℃ to 1000 ℃ with 100 ℃ step intervals for two complete thermal cycles. In this test, we focused on the repeatability of the sensor in short-term annealing processes.

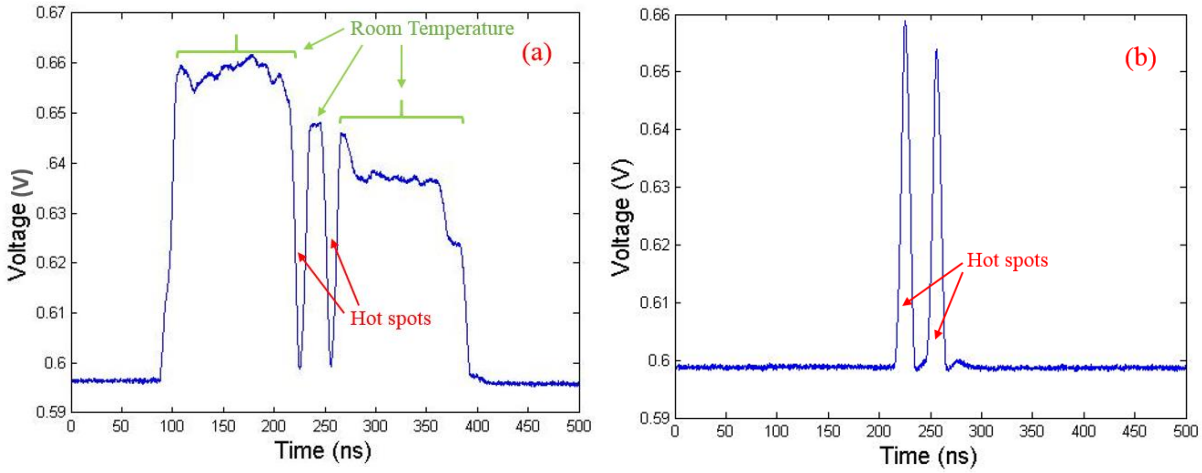

Figure 7-41. Brillouin signal obtained in time domain when the frequency difference between the pump and probe light was set at (a) 10.872 GHz and (b) 11.622 GHz.

A typical Brillouin signal recorded in time domain is shown in Figure 7-41. Figure 7-41 (a) illustrates the obtained Brillouin signal when the frequency difference between the probe and pump light was set at 10.872 GHz. This frequency difference corresponds to the Brillouin signal peak for the fiber kept at room temperature. As a comparison, Figure 7-41 (b) shows the signal curve when the frequency difference was set at 11.622 GHz. In this case, the hot segments at 1000 ℃ present the strongest Brillouin signal. The two peaks clearly separate and stand out of the background, indicating sufficient spatial resolving capability of the system. An obvious signal intensity decay on the signal can be observed after heated sections, which is a result of the relatively sharp bending of the heated fiber due to the limited space in the furnace.

By demodulating the Brillouin frequency peaks, the calibration curve of the Brillouin frequency versus temperature is plotted in Figure 7-42. It is clearly shown that no obvious drift between the data acquired in the two thermal cycles could be seen, indicating good repeatability of the sensor within the entire sensing range.

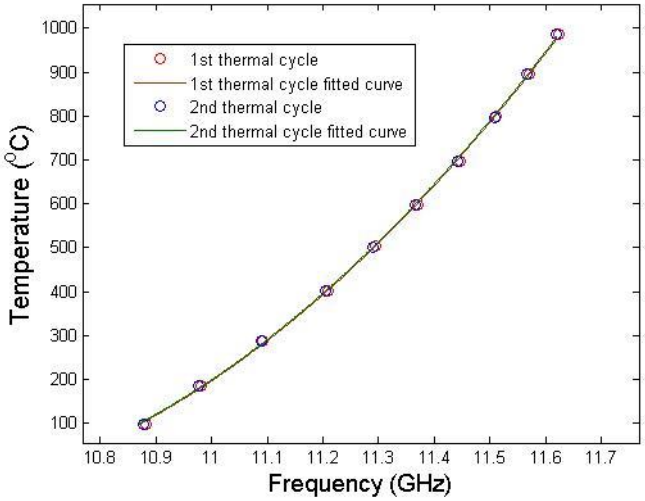

Figure 7-42. Measured Brillouin frequency vs. temperature calibration data obtained in the two thermal cycles, and a polynomial fitting of the data from the second annealing cycle.

By fitting the calibration curve in the second thermal cycle with a second-order polynomial function, we have

$$T = 6.60328\times10^{2}\nu_B^{\,2} - 1.36763\times10^{4}\nu_B + 7.07395\times10^{4} \qquad \text{Eq. 7.17}$$

where T is the temperature, and ν_B indicates the Brillouin frequency.

7.6.4 Temperature resolution evaluation

Since the system relies on frequency scanning to find the position of the Brillouin peaks, the temperature resolution of the system highly depends on the interval of the frequency scanning step. In this test, the temperature resolution of the system was evaluated with the Brillouin frequency scanning step set at 0.5MHz, 1MHz, and 2MHz respectively. Five scans were conducted under each step setting. The temperature resolution of the system was calculated through the standard deviation of the demodulated temperatures. To obtain high temperature stability, the tests were conducted at the temperature of 500 ℃.

Given the Brillouin frequency vs. temperature calibration equation (Eq. 7.17), the standard deviation of temperature (δ_T) can be calculated as

$$\delta_T = \frac{\partial T}{\partial \nu_B}\delta_B \qquad \text{Eq. 7.18}$$

where $\frac{\partial T}{\partial \nu_B}$ is the slope of the calibration curve, which represents the responsivity of temperature. At 500 ℃, its value was calculated to be 1.23 ℃/MHz.

Table 7-1, Table 7-2 and Table 7-3 list the Brillouin frequency demodulated at the center of the two heated fiber segments with frequency scanning steps of 0.5MHz, 1MHz and 2MHz

respectively. The Brillouin frequency was calculated via Lorentz fittings in the range of ±60MHz around the Brillouin peak position.

Table 7-1. Demodulated Brillouin frequency at 500 ℃ with 0.5MHz frequency step.

	1st segment	2nd segment
1st measurement	11.29027 GHz	11.29089 GHz
2nd measurement	11.29033 GHz	11.29097 GHz
3rd measurement	11.29039 GHz	11.29114 GHz
4th measurement	11.29042 GHz	11.29102 GHz
5th measurement	11.29031 GHz	11.29102 GHz
Standard deviation	0.061 MHz	0.091 MHz

Table 7-2. Demodulated Brillouin frequency at 500 ℃ with 1MHz frequency step.

	1st segment	2nd segment
1st measurement	11.29074 GHz	11.29136 GHz
2nd measurement	11.29077 GHz	11.29145 GHz
3rd measurement	11.29046 GHz	11.29126 GHz
4th measurement	11.29068 GHz	11.29133 GHz
5th measurement	11.29060 GHz	11.29138 GHz
Standard deviation	0.124 MHz	0.152 MHz

Table 7-3. Demodulated Brillouin frequency at 500 ℃ with 2MHz frequency step.

	1st segment	2nd segment
1st measurement	11.29087 GHz	11.29153 GHz
2nd measurement	11.29085 GHz	11.29156 GHz
3rd measurement	11.29143 GHz	11.29182 GHz
4th measurement	11.29184 GHz	11.29253 GHz
5th measurement	11.29118 GHz	11.29160 GHz
Standard deviation	0.415 MHz	0.419 MHz

Considering both data sets shown above, the temperature resolution was calculated to be 0.09 ℃, 0.17 ℃, and 0.52 ℃ respectively for the frequency scanning step settings of 0.5 MHz, 1 MHz, and 2 MHz. Even at 2 MHz frequency step, the temperature resolution of 0.52 ℃ is still significantly better than thermocouples. Although it is clear that a finer scan step setting could result in a

better temperature resolution, this improvement is achieved at the sacrifice of system response speed. Take the case of using 0.5 MHz step as an example, a complete scan from 10.700 GHz to 11.800 GHz with 50 ms measurement time in each step takes about two minutes. While the frequency scanning step is set to 2 MHz, only 30 s is needed for each scan. In real applications, optimizations can be performed between the temperature resolution and the system response time according to the requirements of the user.

7.7 Brillouin frequency drift in annealed fibers

7.7.1 Experiments

During a long-term two-cycle annealing test, a slow frequency drift of the Brillouin peak was observed. As shown in Figure 7-43, the Brillouin peak of the heated fiber section drifted to lower frequency after 1-day annealing at 1000 ℃ in both thermal cycles.

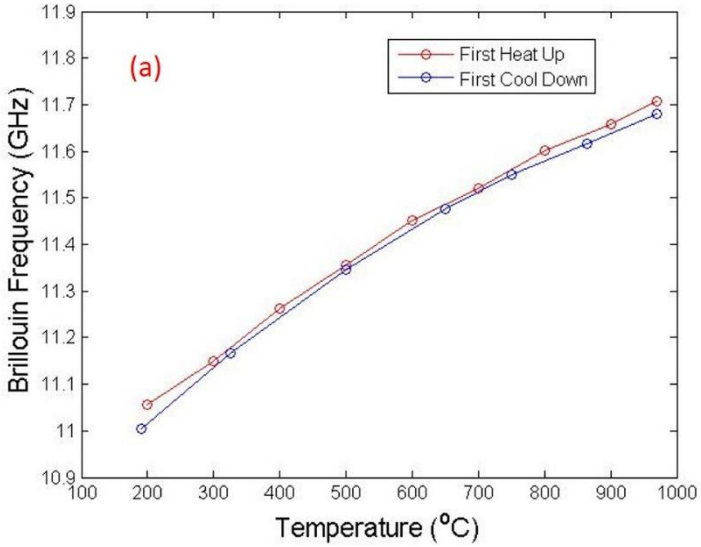

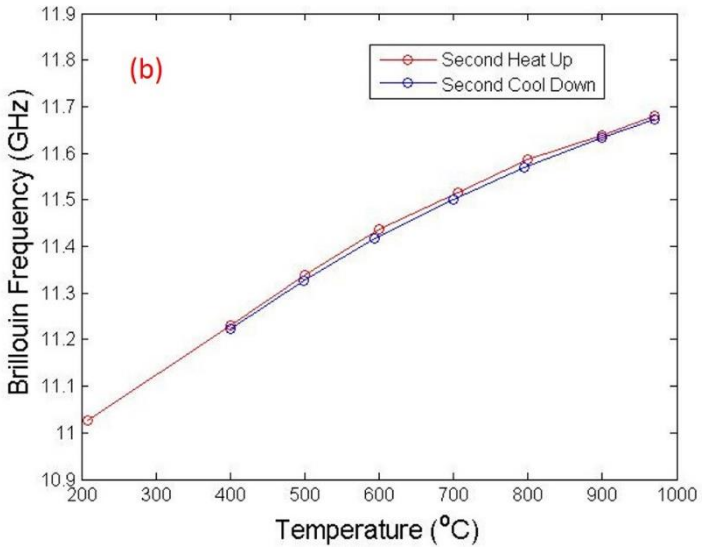

Figure 7-43. Brillouin frequency measured at the center of the hot spot during (a) the first annealing cycle; (b) the second annealing cycle. Fiber was annealed for 24 hours at 1000 ℃ between the ramp-up and ramp-down of each cycle.

By looking closely at the data, it was found that the Brillouin frequency drift during the first 1-day annealing was 26MHz, corresponding to 31 ℃ in temperature, and 8MHz during the second annealing, corresponding to 10 ℃ in temperature.

To further characterize the drift, another test was conducted with a 10m-long SMF-28 fiber coiled in a 12”×12”×12” box furnace. With a big chamber, the box furnace was able to hold a larger fiber coil and offer high temperature stability. The temperature stability is essential for the Brillouin frequency drift measurement since the amount of drifting is estimated to be only a few degrees per day. During the tests, a K-type thermocouple was installed near the fiber coil to monitor the temperature. The temperature stability of the furnace was measured to be within ±0.8 ℃ when the furnace stabilizes at the set temperature.

On the other hand, the Brillouin measurement system was also adjusted to perform finer scans for a better temperature resolution. In former Brillouin measurements, 5 MHz scanning step and 1 GHz scanning range were used to cover the temperature measurement range from room temperature to 1000 ℃. In the new test, the scanning step was set to 0.1 MHz, corresponding to 0.15 ℃ in temperature; and the scanning range was set to 30 MHz to cover only the width of the Brillouin peak. With the finer scanning step, the Brillouin drift could be measured with high accuracy. At the same time, to obtain higher signal quality, the pulse width of the pump pulse was set to 50 ns, corresponding to a spatial resolution of 5 m.

A temporal Brillouin signal recorded during the test is shown in Figure 7-44. The Brillouin gain signal was measured to be over 200 mV above the background. Given the high signal quality, averaging was not performed during the measurement.

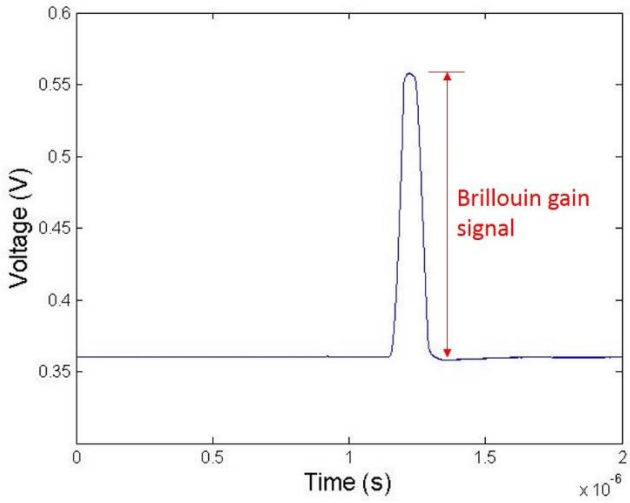

Figure 7-44. Temporal Brillouin gain signal acquired with a 50 ns pump pulse.

In the first test, the furnace was set at 900 ℃, while the temperature read by the thermocouple was 884 ℃. The transmission change of the fiber recorded during the 48-hour test is shown in Figure 7-45. It can be seen that the change of the fiber transmission is within the measurement error, indicating the long-term stability of the fiber at this temperature.

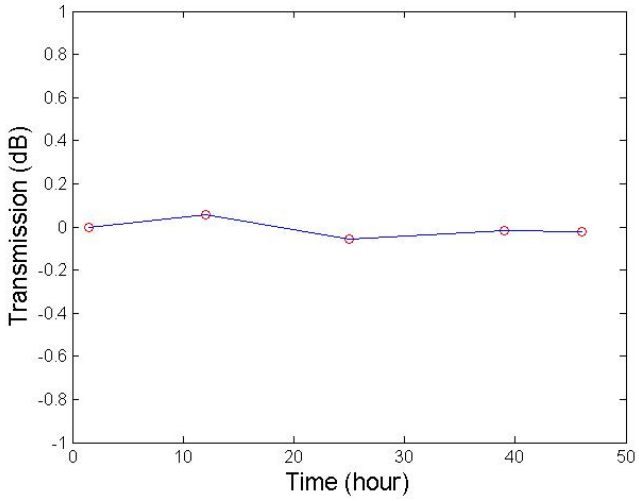

Figure 7-45. Recorded transmission of a 10 m long SMF-28 fiber during the 48-hour annealing test at 884 ℃.

The Brillouin frequency recorded during the 48-hour test at 884 ℃ is shown in Figure 7-46. According to the data, the Brillouin frequency variation during the test is within 0.3 MHz, corresponding to a temperature of 0.35 ℃. Given the ±0.8 ℃ temperature stability of the furnace, the Brillouin frequency can be considered unchanged during this test.

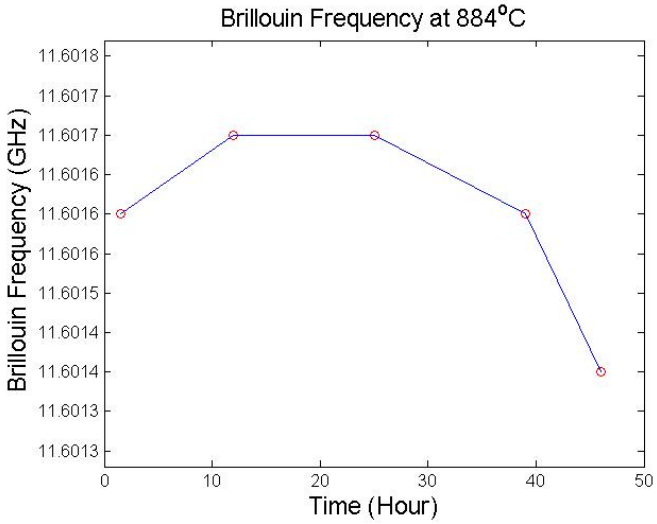

Figure 7-46. Brillouin Frequency drift of the 10 m long SMF-28 fiber during the 48-hour annealing test at 884 ℃.

In the second test, the furnace was set to 960 ℃, while the thermocouple read 945 ℃ at the fiber. The fiber transmission recorded during the 132-hour test is shown in Figure 7-47. The loss increased quickly in the first 50 hours of the test, and slowed down afterwards. A fitting with the exponential decay model shows a lifetime of 22.4 hours and a final loss of 1.74dB. For Brillouin systems with long sensing fibers, the loss of 0.174dB/m will significantly attenuate the Brillouin signal and thus severely degrade the signal quality.

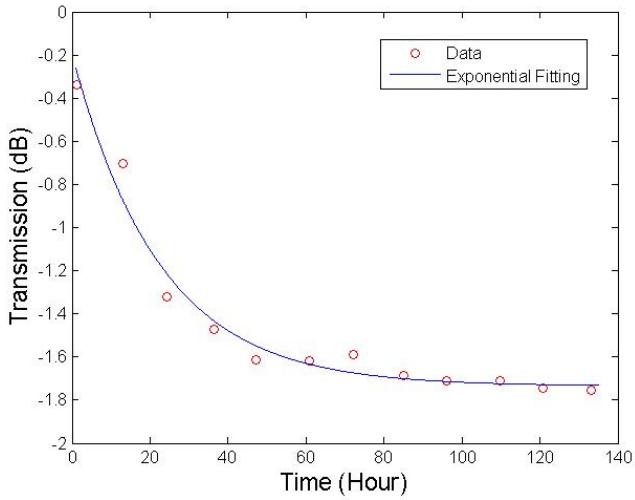

Figure 7-47. Recorded and fitted transmission of a 10m-long SMF-28 fiber during the 132-hour annealing test at 945 ℃.

The Brillouin frequency drift recorded during the annealing test is shown in Figure 7-48. An exponential decay fitting shows a lifetime of 43.5 hours. The disagreement in the lifetimes of the Brillouin frequency drift and the transmission decay indicates that they might have different mechanisms behind them.

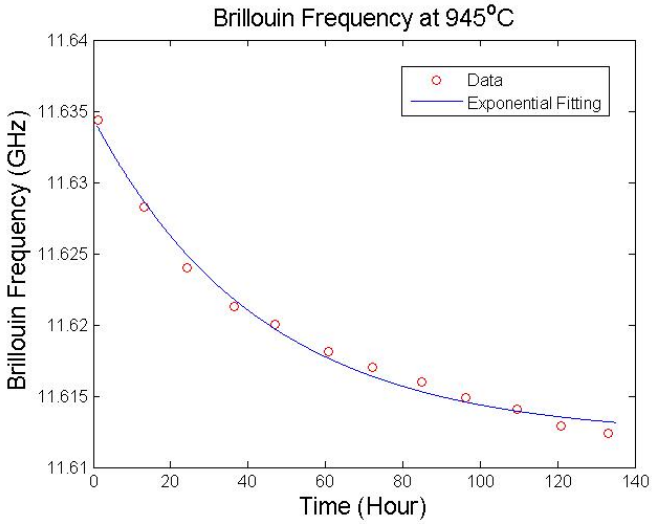

Figure 7-48. Recorded and fitted Brillouin Frequency drift of the 10m-long SMF-28 fiber during the 132-hour annealing test at 945 ℃.

7.7.2 Mechanism of Brillouin drift

Since Brillouin scattering is an interaction between photons and phonons in the fiber, the Brillouin frequency v_b is related to both the refractive index n and acoustic speed V_a of the fiber:

$$v_b = \frac{2n}{\lambda} V_a \qquad \text{Eq. 7.19}$$

where v_b is the Brillouin frequency, n is the refractive index of the fiber, V_a is the acoustic velocity in the fiber, and λ is the wavelength of the light in vacuum. By calculating the differential on both sides of the equation, the change of Brillouin frequency can be written as:

$$dv_b = \frac{2V_a}{\lambda} dn + \frac{2n}{\lambda} dV_a \qquad \text{Eq. 7.20}$$

For the convenience of calculation, the equation can be written in changing ratio of each parameter:

$$\frac{dv_b}{v_b} = \frac{dn}{n} + \frac{dV_a}{V_a} \qquad \text{Eq. 7.21}$$

From the 945 ℃ data shown in the former section, it can be calculated that the overall changing ratio of the Brillouin frequency was 0.185%. To investigate the mechanism of this change, the two components, the refractive index change and the acoustic velocity change, need to be characterized separately.

7.7.3 Refractive index change

The fiber refractive index change during annealing has also been observed to result in drifting of other fiber sensors. Juergens et al. annealed a regenerated fiber Bragg grating at 1000 ℃ for 4 days, and observed a Bragg wavelength drift of ~200 pm towards longer wavelength. [11] The corresponding refractive index change is calculated to be +0.013%.

One of the effects that causes the refractive index increase is the releasing of the frozen-in thermal stress. During the fiber drawing, the temperature of the fiber cools extremely fast, which could freeze a thermal stress between the fiber core and cladding. Due to the opto-elastic effect in fused silica, the stress slightly reduces the refractive index in the core. [59] When annealed, the fused silica softens, allowing the thermal stress frozen in the fiber to be gradually released, which appears to be a refractive index increase when measured.

Besides the thermal stress, viscoelastic stress can also be frozen in fibers and affect their refractive indices. [60] When the preform is heated and soften, the core and cladding can have different viscosity due to the non-uniform temperature, leaving a longitudinal stress along the drawn fiber. When such a fiber is annealed, the releasing of the frozen-in viscoelastic stress can lead to an increase of the refractive index as well.

Yablon et al. [60] investigated the refractive index restoring during the stress releasing. Shown in Figure 7-49, the increase of refractive index is within the range of 0.0002 ~ 0.0014 depending on the original fiber drawing tension, corresponding to an increase ratio of 0.014% ~ 0.097%. Our experimental result of 0.052% falls well in the middle of this range.

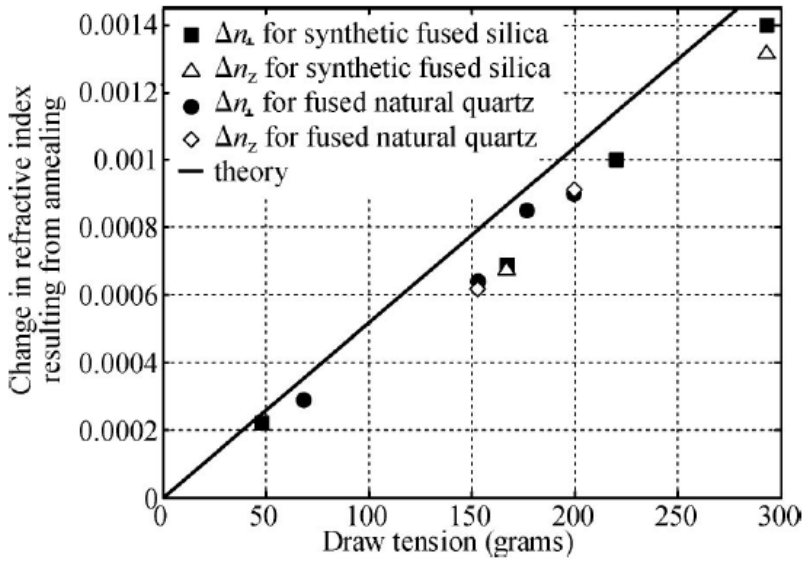

Figure 7-49. Refractive index change of fibers drawn under different tensions after thermal stress releasing. [60]

To measure the minor change of the refractive index, a special intrinsic Fabry–Perot interferometer (IFPI) was fabricated. As one of the Fabry-Perot based sensing technique, IFPI has a very high sensitivity to the effective optical path length change of the fiber segment within the cavity. In this test, an IFPI was fabricated with SMF-28 fiber. The unit was annealed at high temperature and the refractive index change of the fiber segment in the cavity was monitored during the test.

The structure of the IFPI is shown in Figure 7-50. Two tiny air bubbles were made within the core of the SMF-28 fiber using the etching-splicing technique. The air bubbles served as the two reflectors of the cavity.

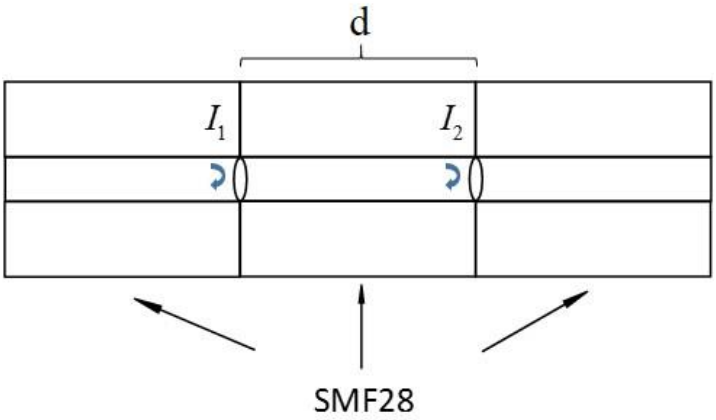

Figure 7-50. Structure of the air bubble IFPI sensor made with SMF-28 fibers.

For a low-finesse IFPI, the interference spectra can be expressed as

$$I(k) = |I_1(k)|^2 + |I_2(k)|^2 + 2\sqrt{I_1(k)I_2(k)}\cos[k \cdot 2nd + \phi] \qquad \text{Eq. 7.22}$$

where $I(k)$ is the interference spectral intensity, k is the wavenumber, $I_1(k)$ and $I_2(k)$ are the spectral intensity of the reflections from the two reflectors, n represents the effective refractive index of the fiber segment between the two reflectors, d is the physical length of fiber segment and ϕ is the initial phase. The term $2nd$ in the equation represents the OPD of the IFPI.

When the IFPI is at a constant temperature, the physical length d of the fiber segment in the cavity is considered to remain unchanged. Thus, any change of the OPD is induced by the change of the refractive index of the fiber segment:

$$\frac{dOPD}{OPD_0} = 2d \cdot \frac{dn}{n} \qquad \text{Eq. 7.23}$$

By measuring the OPD changing ratio of the fiber segment, the refractive index changing ratio of the fiber can be obtained.

The interference fringe acquired with the fabricated IFPI unit in room temperature is shown in Figure 7-51. The fringe contrast of the IFPI is measured to be over 30 dB.

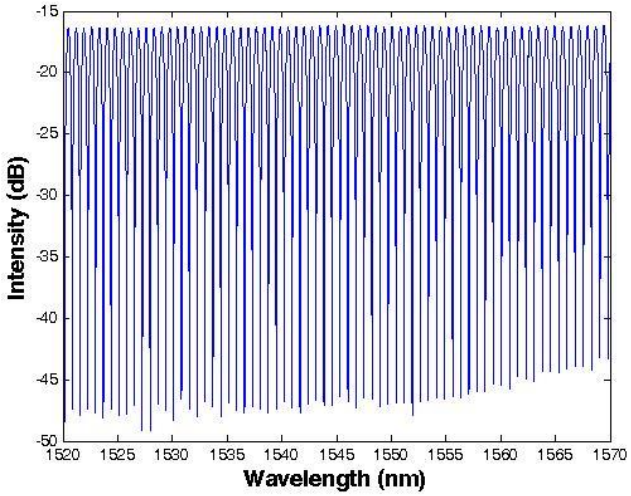

Figure 7-51. An interference spectrum of the air bubble IFPI measured at room temperature.

During the heating up process, unexpected jumping behavior was recorded in the demodulated OPD of the IFPI sensor, as shown in Figure 7-52.

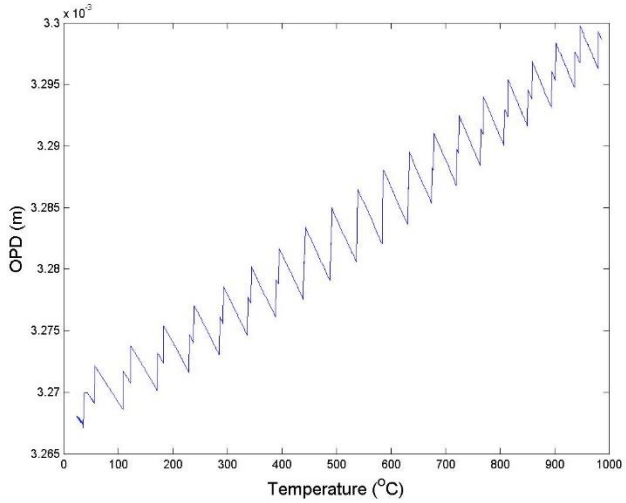

Figure 7-52. Demodulated OPD of the air bubble IFPI during the heating up process.

The jumping behavior of the demodulated OPD clearly indicates that the F-P demodulation algorithm was confused by the spectra generated by multiple cavities with similar lengths. By looking closer at the Fourier transform of an interference spectrum, two peaks can be identified overlapping with each other, as shown in Figure 7-53. The multi-cavity interference is believed to be introduced by the additional surfaces of the two bubbles: the size of the bubbles were not big enough for the algorithm to separate the two frequency components, and not small enough to be ignored. While assuming only one peak existing, the algorithm could not correctly demodulate the OPD of the cavity, generating a sawtooth curve. The actual length of the cavity should be continuously increasing as the temperature rose.

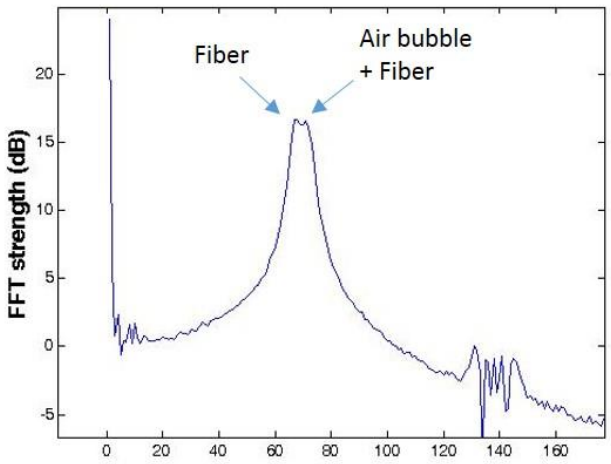

Figure 7-53. Fourier Transform of an interference spectrum generated by the air bubble IFPI.

Although the absolute value of the demodulated OPD was not correct, given our understanding on the algorithm and the consistency of the curve, the change of the refractive index can still be retrieved qualitatively. During the one-day annealing test at 1000 ℃, the OPD change of the IFPI unit was continuously demodulated and recorded, as shown in Figure 7-54. Given the relationship between the demodulated OPD vs temperature in Figure 7-52, the continuously decreasing curve indicates an increase of the actual OPD, corresponding to an increasing refractive index of the tested fiber.

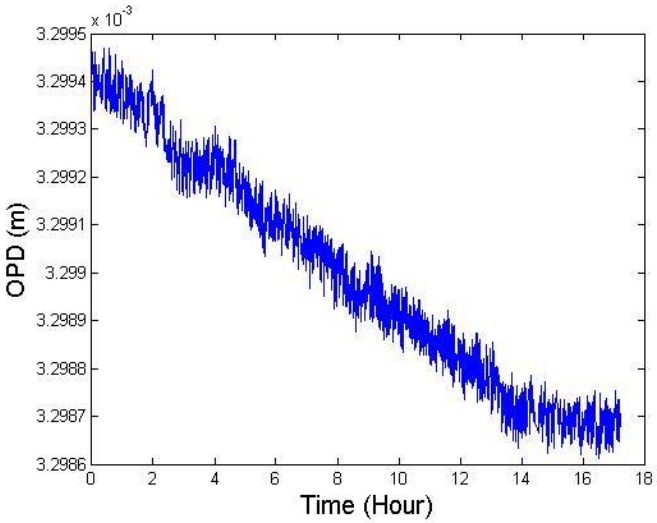

Figure 7-54. Demodulated OPD of the bubble IFPI during the continuous annealing test at 1000 ℃.

It is worth noting that the Brillouin frequency drift observed in the former experiments were negative, which is opposite to the refractive index change observed in this test. To confirm the conclusion, another fiber refractive index drift measurement was conducted.

In this test, a fiber Michelson interferometer was built to monitor the change of the fiber optical path length during a long-term annealing. The experimental setup is illustrated in Figure 7-55.

The two fiber arms were fabricated with similar length, while one of them goes through a tube furnace. A CTS serves as the light source and the detector, recording the interfering spectra formed by the reflection lights from the two fiber ends. The optical path length change on one arm will be reflected in the OPD between the two arms. Without any microstructure in the heated region, the measurement is expected to be less affected by unexpected effects.

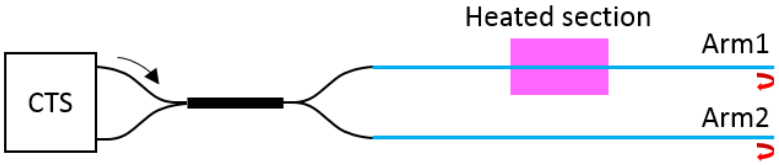

Figure 7-55. Fiber Michelson interferometer for the fiber refractive index drift test

The length of the heated fiber segment in the furnace was 8.25 inches. The heated length was over 60 times longer than in the IFPI test, which made the OPD more sensitive to the fiber refractive index change. As shown in Figure 7-56, during the 60-hour continuous annealing at 950 ℃, the optical path length of the heated arm was recorded to increase by 0.287mm, corresponding to a refractive index increase of 0.047%. The minor refractive index increase during the annealing agrees with the observation in the former test using IFPI.

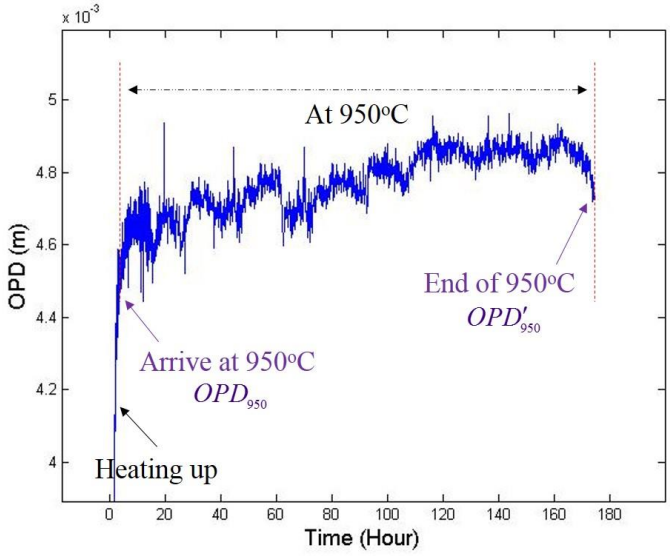

Figure 7-56. Demodulated fiber OPD change at 950°C during the 60-hour annealing measured with a fiber Michelson interferometer.

Before annealing, the initial optical path difference (OPD_{T0}) was measured with both fibers settled at room temperature (T_0). Determined by the physical length difference L_{T0} and the refractive index n_0 at room temperature, OPD_{T0} can be written as

$$OPD_{T0} = 2n_0 L_{T0} \qquad \text{Eq. 7.24}$$

The OPD change of the SMF-28 fiber during the 7-day annealing is shown in Figure 7-56. It can be clearly seen that the effective OPD gradually increased over the long-term annealing at the

constant temperature of 950℃. By assuming the physical length of the annealed silica fiber remained unchanged during the annealing, its refractive index change ratio can be calculated by

$$\frac{\Delta n}{n} = \frac{\Delta OPD}{2L} \qquad \text{Eq. 7.25}$$

According to the data, a ΔOPD of 0.315mm was measured at the end of the 7-day annealing. Given L = 8.25", $\Delta n / n$ is calculated to be +0.052%.

7.7.4 Young's modulus measurement of an annealed fiber

A Brillouin frequency shift can be resulted from both the refractive index and the acoustic velocity change in the fiber:

$$v_b = \frac{2n}{\lambda} V_a \Rightarrow \frac{dv_b}{v_b} = \frac{dn}{n} + \frac{dV_a}{V_a} \qquad \text{Eq. 7.26}$$

The acoustic wave generated by Brillouin effect is the longitudinal mode wave. Its acoustic velocity V_a depends on the Young's modulus (E) and density (ρ) of the fiber:

$$V_a = \sqrt{\frac{E}{\rho}} \Rightarrow \frac{dV_a}{V_a} = \frac{dE}{2E} - \frac{d\rho}{2\rho} \qquad \text{Eq. 7.27}$$

Young's modulus is defined as

$$E = \frac{F}{\sigma S} \qquad \text{Eq. 7.28}$$

where F is the applied force, σ is the strain in the fiber, and S is the cross-sectional area.

According to our former results, the Brillouin frequency drift is on the level of 0.2%, which means the measurement of the fiber's Young's modulus need to be highly accurate to correctly reflect the change. The scale (METTLER TOLEDO, AB54-S) used to measure the force applied on the fibers has a precision of 0.1 mg, corresponding to a force resolution of 1 mN. As a strain sensor, a fiber-based IFPI was fabricated by splicing a short segment of graded index fiber (GIF, Draka inc.) in an SMF-28 fiber (Figure 7-57). The length of the GIF is made equal to its self-focusing length (760 μm) for best light transmitting efficiency. A fringe visibility of 10 dB is obtained with the sensor, as shown in Figure 7-58.

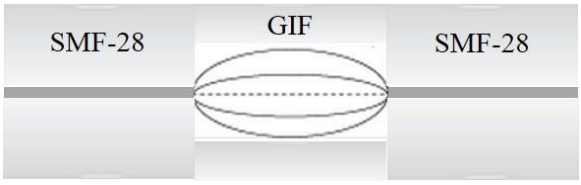

Figure 7-57. IFPI strain sensor structure.

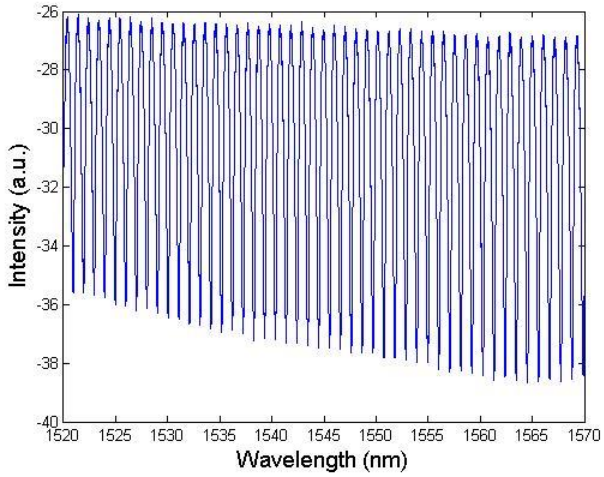

Figure 7-58. An interferometric spectrum obtained with the IFPI strain sensor.

A three-step procedure was followed in the Young's modulus measurement, as shown in Figure 7-59. First, the Young's modulus of the IFPI strain sensor was measured. Then a new SMF-28 fiber was bound onto the sensing fiber and the total equivalent Young's modulus was measured. With these two steps, the property of the sensor was characterized. Finally, the annealed SMF-28 fiber was bound onto the sensing fiber for the third Young's modulus measurement, from which the Young's modulus of the annealed fiber can be obtained.

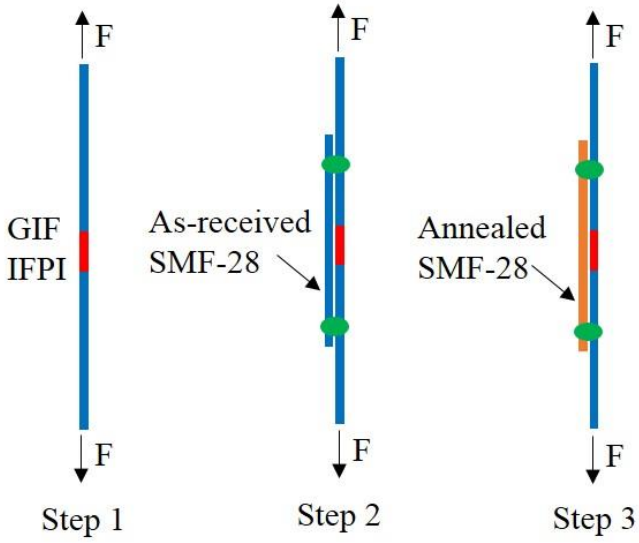

Figure 7-59. Three-step procedure of the Young's modulus measurement of the annealed fiber.

A bonded fiber bundle is shown in Figure 7-60. The two fibers are placed parallel and as close as possible during the bonding to minimize the sliding in the epoxy.

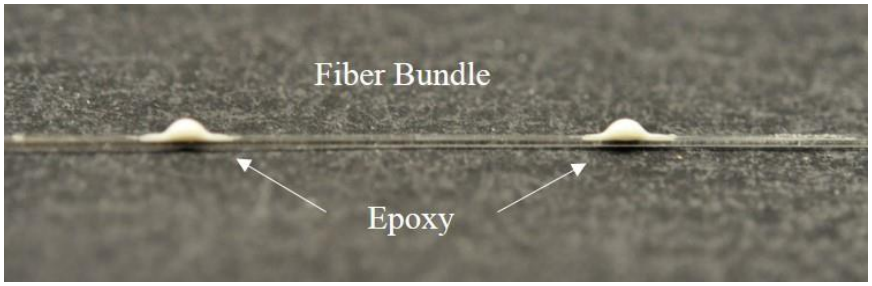

Figure 7-60. Bonded fiber bundle.

The measured data of OPD change versus applied force is plotted in Figure 7-61, in which all three sets of data show good linearity.

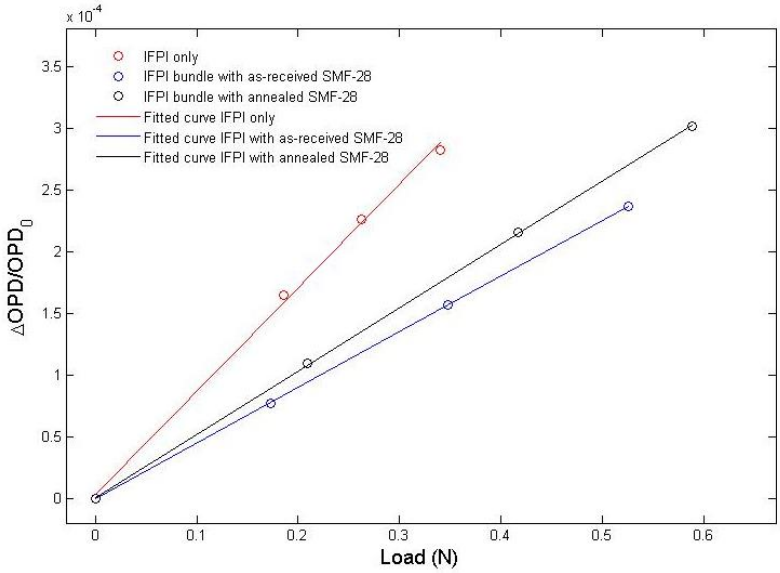

Figure 7-61. OPD change with respect to the applied force measured in the three steps of the test.

When strain is applied on the IFPI, the OPD change of the cavity is a combined result of two effects: the opto-elastic effect leads to a change of reflective index, and the physical length of the fiber is extended due to the deformation:

$$\begin{aligned} OPD' &= 2n_0(1+\Delta n)L_0(1+\Delta L) \\ &= 2n_0(1+C\frac{F}{S})L_0(1+\frac{F}{E_G S}) \\ &= OPD_0(1+C\frac{F}{S}+\frac{F}{E_G S}+\frac{CL_0}{E_G S}F^2); \end{aligned} \qquad \text{Eq. 7.29}$$

$$\Delta n = C\frac{F}{S};$$

$$\Delta L = \frac{F}{E_G S};$$

where *OPD*' and OPD_0 represent the OPD under force (F) and the initial OPD, respectively. S represents the cross-sectional area of the fiber. The refractive index change introduced by the

opto-elastic effect is proportional to the force on unit area, which is $\Delta n = CF / S$. E_G represents the Young's modulus of the GIF segment in the IFPI sensor. The change of physical length ΔL is written as $\Delta L = \frac{F}{E_G S} L_0$ according to the definition of Young's modulus. The OPD changing ratio is then expressed as

$$\begin{aligned} \frac{\Delta OPD}{OPD_0} &= \frac{C}{S} F + \frac{L_0}{E_G S} F + \frac{C L_0}{E_G S} F^2 \\ &\approx (\frac{C}{S} + \frac{L_0}{E_G S}) F \end{aligned} \qquad \text{Eq. 7.30}$$

where $\Delta OPD = OPD' - OPD_0$, and the higher order term $\frac{CL_0}{E_G S} F^2$ is ignored based on the high linearity shown in Figure 7-61. Therefore, the slope of the IFPI only line is

$$k_0 = \frac{C}{S} + \frac{L_0}{E_G S} \qquad \text{Eq. 7.31}$$

which corresponds to the red line in Figure 7-61.

The initial physical length of the IFPI (L_0) can be calculated from OPD_0, which is the original optical path difference of the IFPI when it is free of stress:

$$L_0 = \frac{OPD_0}{2n_0} \qquad \text{Eq. 7.32}$$

In the second test, when the IFPI is bundled with a new, de-coated SMF-28 fiber, the total effective Young's modulus (E_e) of the bundle is $E_e = \frac{E_G + E_s}{2}$. E_s represents the Young's modulus of the de-coated SMF-28 fiber with a known value of 69.22 GPa. The changing ratio of the combined OPD can be written as,

$$\begin{aligned} \frac{\Delta OPD}{OPD_0} &= \frac{C}{2S} \cdot F + \frac{L_{01}}{E_e \cdot 2S} F + \frac{C}{2S} \cdot \frac{L_{01}}{E_e \cdot 2S} F^2 \\ &\approx [\frac{C}{2S} + \frac{L_{01}}{(E_s + E_G) S}] F \end{aligned} \qquad \text{Eq. 7.33}$$

where L_{01} is the initial length of the IFPI in the second test. Thus the slope of the line is

$$k_1 = \frac{C}{2S} + \frac{L_{01}}{(E_s + E_G) S} \qquad \text{Eq. 7.34}$$

which corresponds to the black line in Figure 7-61.

With all the equations above, the Young's modulus of the Draka GIF fiber used in the IFPI cavity can be deduced from the equation

$$S(k_0 - 2k_1)E_G^{\,2} + [E_s S(k_0 - 2k_1) + (2L_{01} - L_0)]E_G - L_0 E_s = 0 \qquad \text{Eq. 7.35}$$

By solving this equation, E_G, the effective Young's modulus of the GIF, can be calculated to be 70.52GPa. The coefficient C is also deduced to be 1.03×10^{-11}.

Similarly, the slope of the line acquired in the third test can be expressed as

$$k_2 = \frac{C}{S} \cdot \frac{E_G}{E_s' + E_G} + \frac{L_{02}}{(E_s' + E_G)S} \qquad \text{Eq. 7.36}$$

where E_s' denotes the Young's modulus of the annealed SMF-28. Using the data in Figure 7-61, E_s' is calculated to be 68.551 GPa. Compared to the Young's modulus of the new SMF-28 fiber (69.22 GPa), this value has reduced by 0.966%.

7.7.5 Conclusion

Deduced from Eq. 7.26 and Eq. 7.27, the relative Brillouin frequency change can be expressed as

$$\frac{dv_b}{v_b} = \frac{dn}{n} + \frac{dE}{2E} - \frac{d\rho}{2\rho} \qquad \text{Eq. 7.37}$$

According to the results, the refractive index change of a fiber annealed at 950 ℃ for 7 days corresponds to a Brillouin frequency drift of +0.05%, while the Young's modulus change of a fiber annealed at 1000 ℃ for 7 days corresponds to a Brillouin frequency drift of -0.5%. The total Brillouin drift measured in a fiber annealed at 944 ℃ for 5 days is -0.187%. Although these results still cannot match quantitatively due to the different annealing temperature and time, we can still conclude that the change of the fiber's Young's modulus is the major cause of the Brillouin drift.

According to the test results, this drifting effect only occurs at temperatures over 900 ℃. For a normal operation condition in a coal gasifier, the working temperature of the sensor is around 800 ℃, and the high temperature close to 1000 ℃ will only be generated when the gasifier wall is severely corroded. The Brillouin drift, in this case, could potentially lead to a temperature reading error of up to 25 ℃ over a long period of time, but will not affect the capability of the system in indicating the position of the hot spots. In fact, given the exponential change of the Brillouin frequency as shown in Figure 7-48, it is possible to correct the drift in the demodulation algorithm. Even before the drift occurs, there will be enough information given by the sensing system that warns the operator that the refractory wall needs a maintenance very soon, and the drift will be reset as a new fiber sensor installed with the re-bricked gasifier wall.

8 Simulation of gasifier refractory with COMSOL

In this chapter, a computational thermal simulation of a running coal-gasifier was conducted using the finite element analysis (FEA) software COMSOL. The results are important for the

understanding of the working condition of the sensor and the designing of the sensor deployment strategy.

8.1 Modeling procedure

According to J. McDaniel and M. Hornick [61], a gasifier usually includes three layers, two layers of bricks and one layer of steel. Typically, there is a 1 inch air gap between the two 12 inches thick brick layers. The ¼ inch steel layer is outside of the second brick layer (as shown in Figure 8-1).

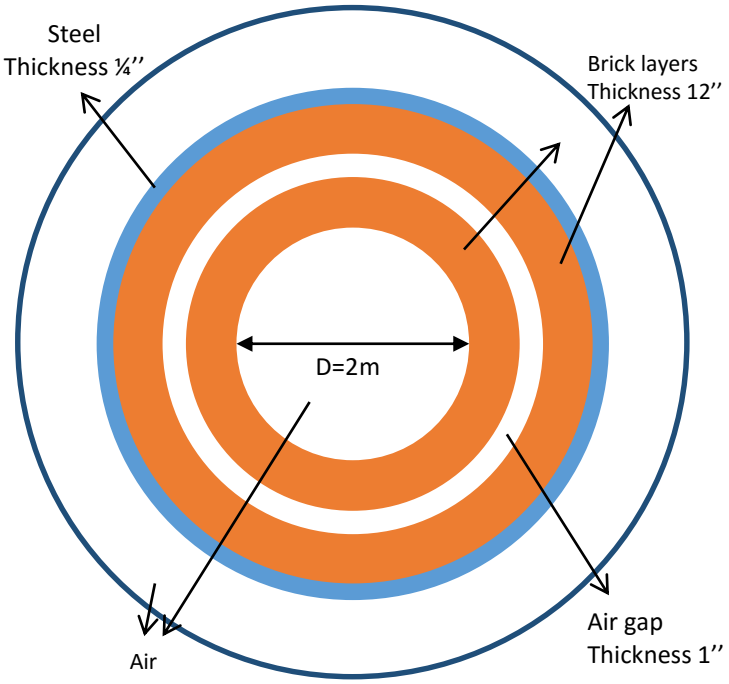

Figure 8-1. The cross-sectional illustration of a typical gasifier.

In COMSOL, the first step is to draw the geometry of the upper gasifier prototype. A crack is introduced to simulate the effect of erosion. Then, define the material for every subdomain. Some research has been made about the material properties, especially for the brick layer. More than 75% component of the brick powder is Cr_2O_3 [62]. So the thermal conductivity of this material is assumed to be 10 W/(m K), the density is about 5000 kg/m^3 and the heat capacity is about 122 J/(kg K). For the boundary conditions, however, the surface emissivity for Cr_2O_3 was not found. Based on the knowledge of the surface emissivity for chromium which is 0.08, the emissivity for Cr_2O_3 was set to 0.1 as an approximation.

8.2 Simulation result and analysis

In order to investigate the influence of the crack on the temperature distribution in the air gap between the brick layers (where the sensor are to be installed), two sets of simulations were conducted. First, the width of the crack was fixed to be 0.1 m, and the depth of the crack was varied from 0.05 m to 0.3 m with a 0.05 m step. Second, the depth of the crack was fixed to be

0.1 m, and the width of the crack was varied from 0.05 m to 0.3 m with a 0.05 m step. The geometry of the crack is shown in Figure 8-2.

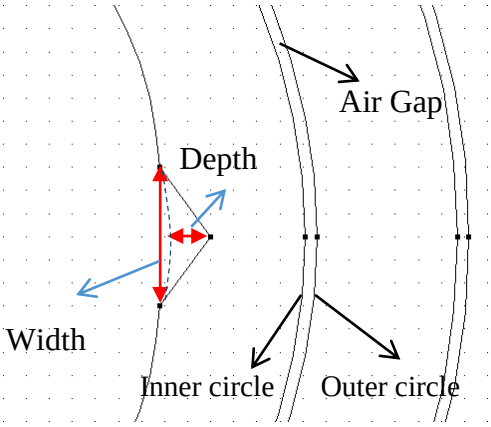

Figure 8-2. The geometry of the crack.

Simulation results of different crack geometries are shown in Figure 8-3. It is obvious to see the location (azimuth angle) of the crack-induced temperature increase in all the figures. With the fixed crack depth and changing crack width (a and b), the 'shoulders' of the main peak changed a lot for the inner circle of the air gap, while the temperature profile of the outer air gap simply increased without significant distortion. When the width was fixed and the depth was changed (c and d), the maximum temperature along the inner circle of the air gap varied dramatically.

These profiles can be used to estimate the spatial and temperature resolution of the sensor. In terms of spatial resolution, in order to measure the temperature difference for different crack width, the sensor should be able to sense the 'shoulders' in (a) (~0.4π rad) and the narrowest FWHM in (c) (~0.1π rad). Since the radius of the inner air gap is 1.305 m, the spatial resolution should be 0.1π ×1.305 m=0.4 m. (b) and (d) show that if the sensor is on the outer circle of the air gap, the temperature resolution should be as high as 0.3 ℃ to sense the 0.05 m change in width. Even though the temperature profile for the outer circle is wider, which relaxes the spatial resolution requirements, the reduced temperature sensitivity puts increases the requirement for the sensor temperature resolution.

In terms of temperature resolution, from Figure 8-4, it is clear that the maximum temperature shows a quadratic relation with crack width and exponential relation with its depth. Obviously, the width variation requires high temperature resolution. The temperature difference with 0.25 m and 0.3 m width is 2 ℃. Due to the limited spatial resolution of the sensing system, usually it is the FWHM temperature rather than the maximum temperature that could be resolved (the integration effect due to limited spatial resolution).

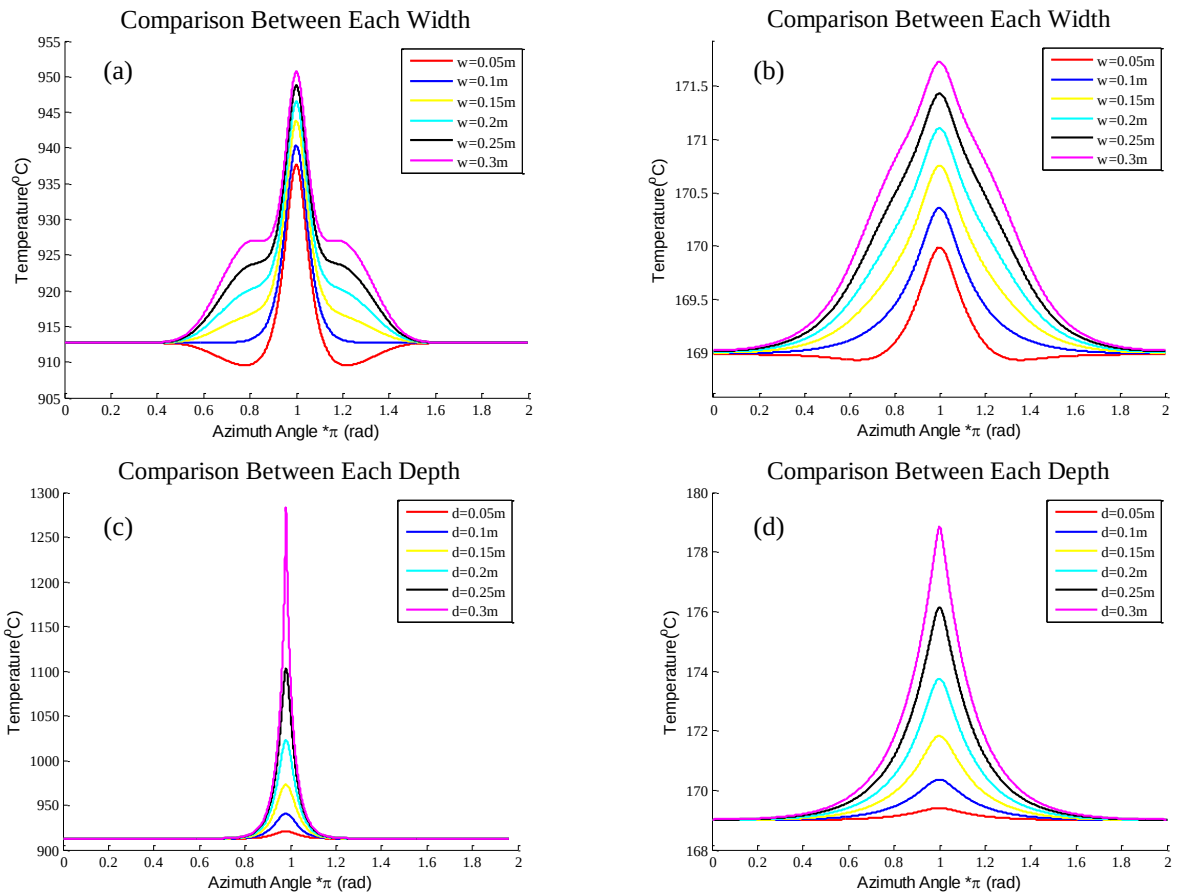

Figure 8-3. Temperature profile for the inner circle of air gap with (a) fixed depth and (c) fixed width; the temperature profile for the outer circle of air gap with (b) fixed depth and (d) fixed width.

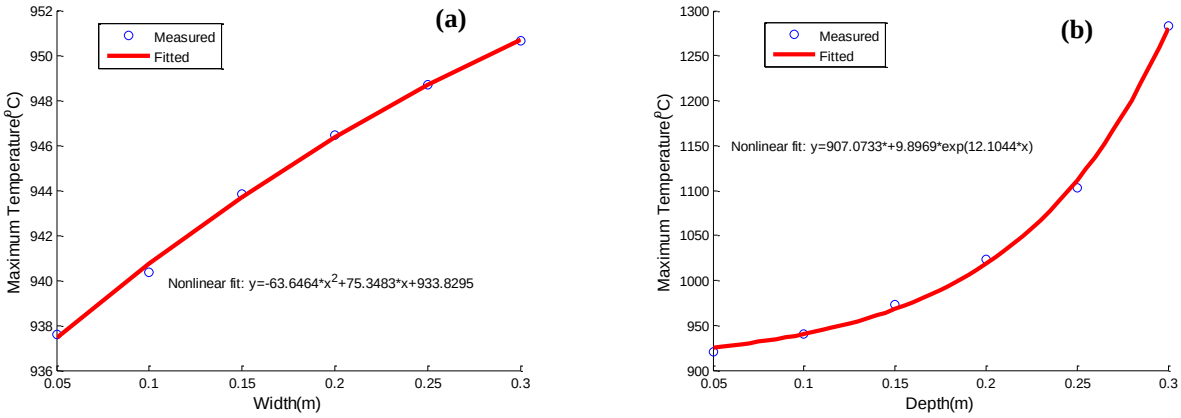

Figure 8-4. The measured and fitted maximum temperature result for the crack with (a) various widths and (b) various depths at the inner circle.

9 High temperature performance of fiber optic sensors

As mentioned in Chapter 6 and Chapter 7, it is observed that the loss of optical fibers increases as they are annealed at high temperature, which could potentially become an issue for the sensing technology. In this chapter, the study on the mechanism of this phenomenon will be introduced. The results will be crucial for the development of a successful packaging technology for the sensing fibers.

9.1 Mechanism of Optical fiber loss at high temperature

For the standard single mode fiber (Corning SMF28), there are two potential factors contributing to the loss when the fiber is heated up to high temperature. 1) Dopant diffusion which potentially decreases the refractive index (RI) difference between the core and the cladding. As the RI contrast decreases, the light confinement of the fiber degrades to induce transmission loss. 2) Micro-cracks. The defects frozen in the fiber during the drawing process will grow to from cracks if the fiber is heated to high temperature. The cracks lead to considerable attenuation due to light scattering. In the following sections, experimental tests will be conducted to investigate the major cause of the fiber loss increase during annealing.

9.2 SMF28 fiber annealing tests

In this section, a series of experiments have been conducted to test the fiber performance when annealed at high temperature.

a. Fiber looped, 10 cm diameter, 10 m heated, lead-in unprotected

A 10 m long SMF28 fiber was wrapped to loops (10 cm diameter) and put in the furnace. The lead-in fibers went through the hole on the front door and was connected to a CTS (Micron Optics Inc., Si-720), which was employed to measure the transmission of the fiber. The fiber was heated from room temperature to 1000 ℃. The transmission dropped from ~0 dB at room temperature to -46 dB at 1000 ℃. Upon opening the furnace's front door, the fiber broke at the lead-in section and the signal dropped to <-60 dB.

b. Fiber looped, 10 cm diameter, 10 m heated, lead-in protected

Two ceramic tubes were employed to hold the lead-in fiber. The fiber was then heated from room temperature to 1000 ℃ in several steps: 23, 400, 600, 846, 929, 953, 965, 1000 ℃. As shown in Figure 9-1, the transmission remained constant under 900 ℃. However it dropped dramatically beyond that temperature. At the same time, the thermal radiation was measured to be -45.35 dB at 1000 ℃, which contributed to the majority of the received signal.

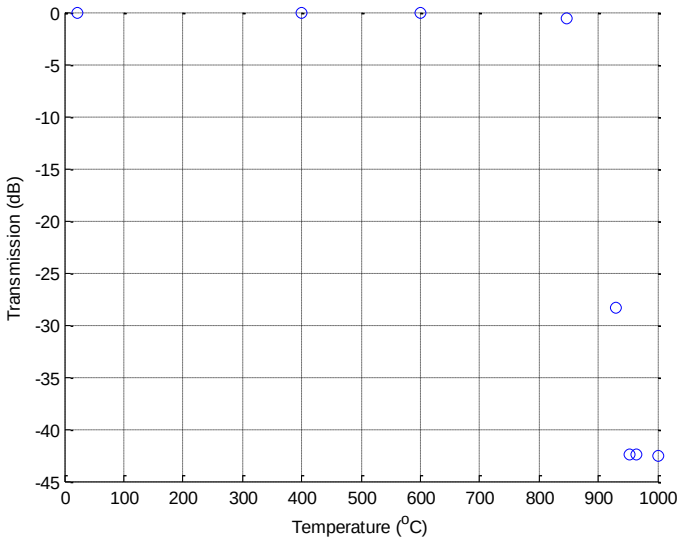

Figure 9-1. Transmission of the fiber under test at various temperatures.

c. Fiber straight, 1 m heated

A long ceramic tube was placed through the box furnace, forming a tube furnace. A 1 m long fiber was decoated and inserted into the ceramic tube. The heated fiber was kept straight and mechanically supported along the whole length using this configuration. The central part of the fiber (around 10 cm) was heated to 1000 ℃ and thermally stabilized for two days. The Fiber transmission was measured every 6 minutes during the process. The result shown in Figure 9-2 indicates that the transmission loss only increased by 0.08 dB. The conclusion is that when the fiber is kept straight, no significant loss is induced at 1000 ℃ in the fiber transmission, as instrument instability (e.g., laser power instability of the CTS) could lead to this measured degradation.

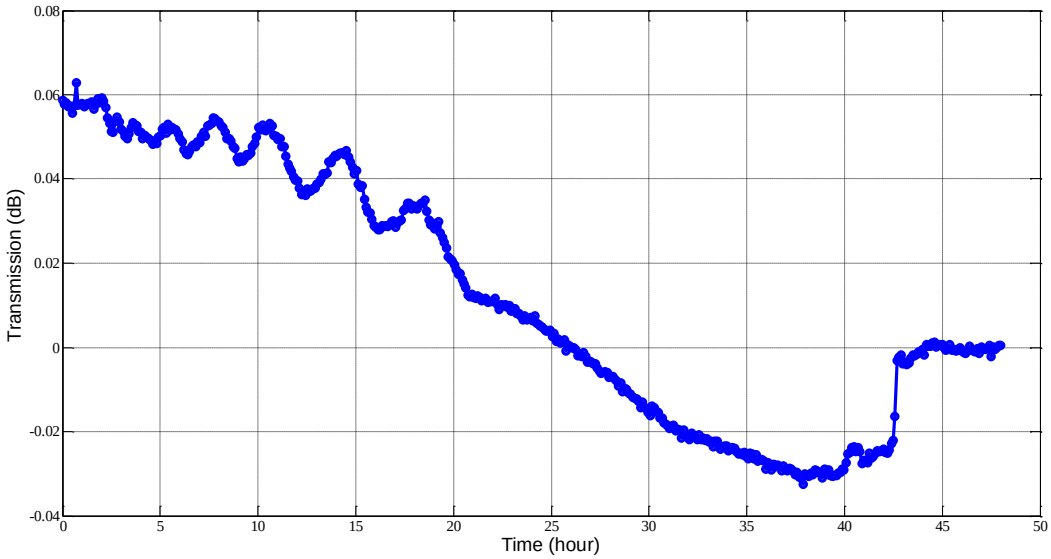

Figure 9-2. Transmission evolution of a 10 cm straight fiber within two days at 1000 ℃.

d. Fiber looped, 10 cm diameter, 100 m heated, lead-in unprotected

Two packs of 100 m long fiber were tested in the furnace using the CTS at the same time. A coupler was employed to provide the laser source for both packs and two channels on the CTS were used for detection. Since the CTS may be turned off during the test, a jumper was employed as a loss reference to calibrate the CTS rather than using the testing fiber at room temperature as the reference. The fiber was heated from room temperature to 1000 ℃, while measuring the transmission at the following temperatures, shown in Figure 9-3. These fibers did not experience much degradation at temperature below 850 ℃, but the transmission loss dropped dramatically when the temperature was beyond 1000 ℃. The time intervals between each data were also recorded and shown in Figure 9-3.

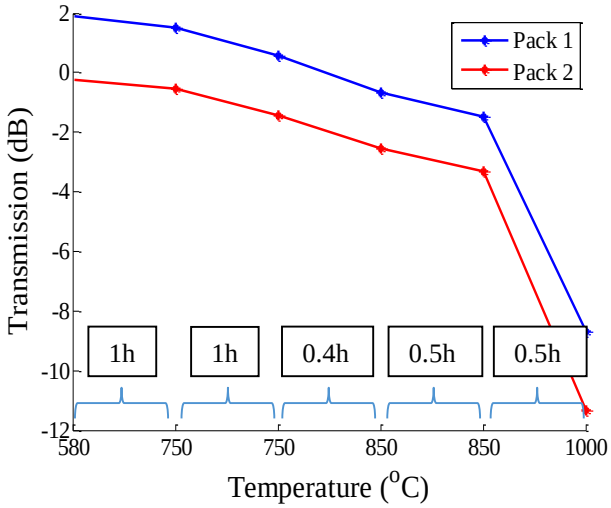

Figure 9-3. Transmission degradation during the heating process. Time intervals between each data are labeled.

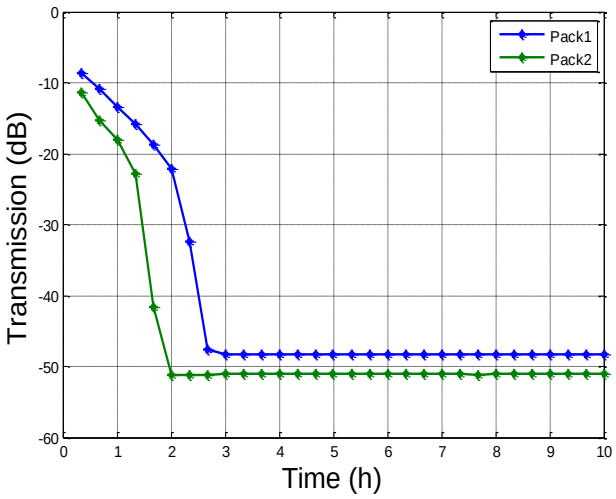

Figure 9-4. Transmission degradation at 1000 ℃.

Then, the fibers were kept at 1000℃ for 10 hours. The transmission degradation is illustrated in Figure 9-4. Both fibers show huge loss after being heated for more than 3 hours (the fiber was basically opaque to light at that point). This result was consistent with the previous experiment result *b*. It was found that both packs of fiber were intact upon inspection; however a breakage was observed at the lead-in section (Figure 9-5). This was caused by the stress induced by melted fiber coating.

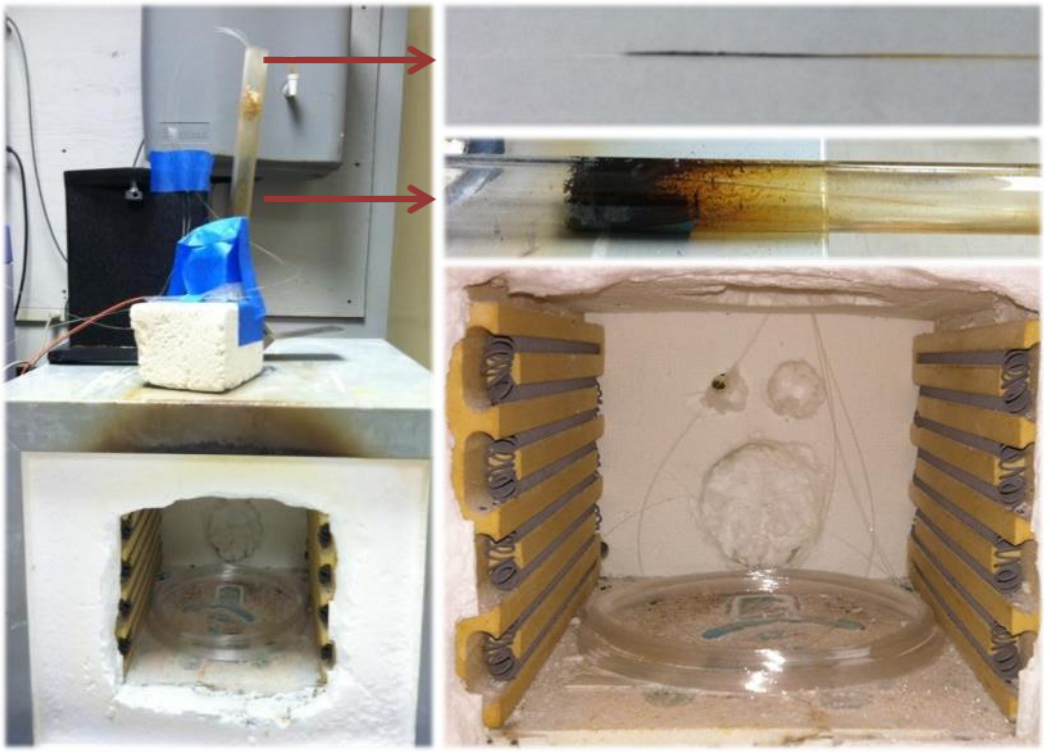

Figure 9-5. The two fiber loops were in good shape but the lead-in section was burnt and stuck together (causing fiber breakage).

e. Fiber looped, 10 cm diameter, 100 m heated, lead-in decoated

A 100m-long fiber wrapped with a radius about 12cm in the box furnace. The two ends of the fiber went through the hole on the top of the furnace, and was connected to the CTS, as shown in Figure 9-6. The CTS was calibrated with a jumper. The lead-in part of the fiber was decoated to prevent adherence.

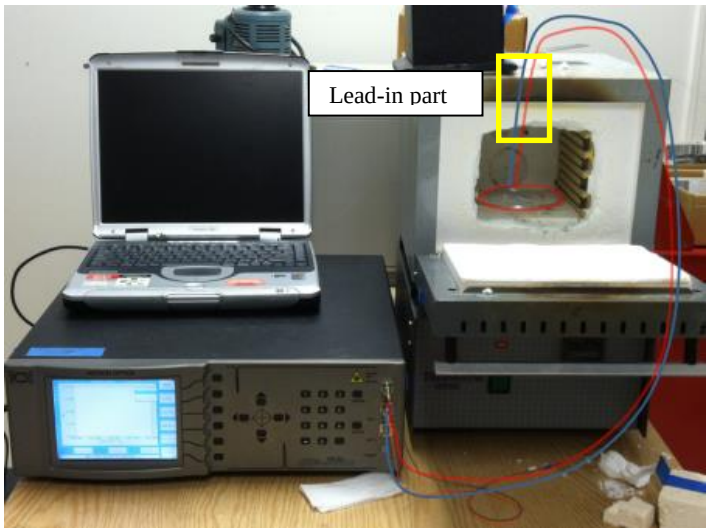

Figure 9-6. Experiment setup for heating 100m fiber to 1000 ℃.

The fiber was kept at 1000 ℃ for 35 hours and the transmission degradation is shown in Figure 9-7. The result shows that the fiber became opaque after being heated at 1000 ℃ for more than 20 hours (the transmission dropped below -25 dB).

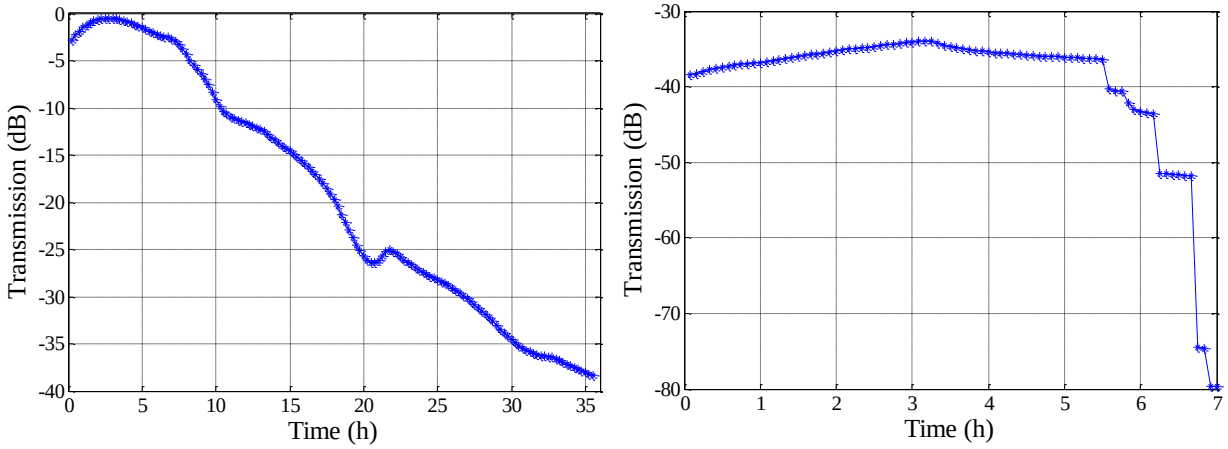

Figure 9-7. Transmission degradation of the 100m SMF28 at 1000 ℃ (left) and cooling down to room temperature (right).

A He-Ne laser was employed in the diagnosis of the fiber after the cooling procedure. The visible light from the He-Ne laser was injected into the fiber from two ends respectively (Figure 9-8). The red color in both figures helps locating the breakage positions along the fiber. There are two possible reasons for the light scattering: (1) the cracks scatter the light to large angles so the fiber cannot confine the light anymore; (2) the light is scattered by the break points in the fiber.

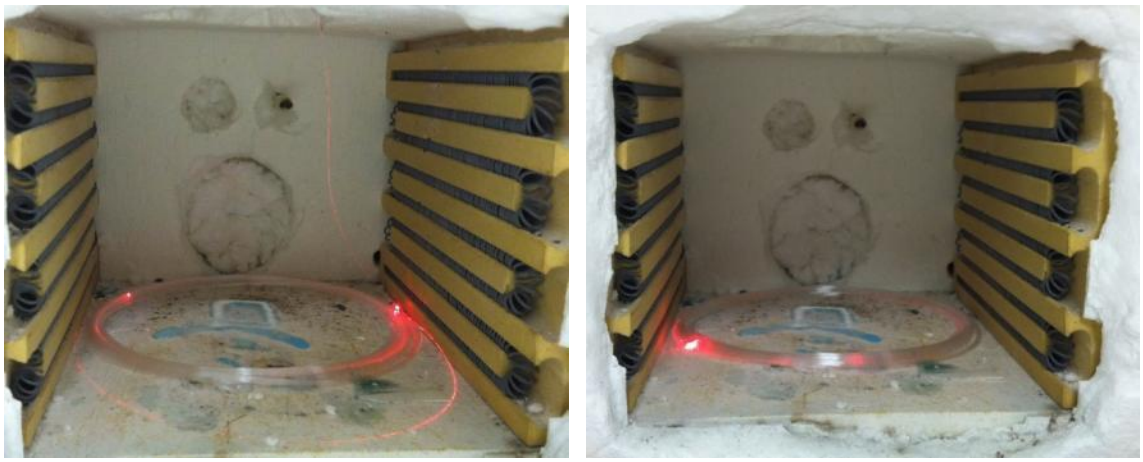

Figure 9-8. Visible light was injected into the fiber from one end (left) and then from the other end (right). The red color visible along the fiber indicates the locations where loss is induced.

f. Fiber straight, 10 m heated

A 100m long fiber was routed into 50 loops and put in the tube furnace to keep the heating part straight (Figure 9-9). A CTS was employed to measure the transmission of the fiber. According to the instruction of the furnace, only a 10cm section in the middle is uniform in temperature, based on which we can estimate the heating length on the fiber in this setup was around 10 m in total.

Figure 9-9. Experiment setup to measure the transmission degradation of SMF28 at 1000 ℃.

The result is shown in Figure 9-10. No significant degradation could be observed during the process. In conclusion, as long as the heated section is kept straight, no stress would build up to facilitate crack propagation at high temperature, resulting in minimum transmission loss during the long-term test.

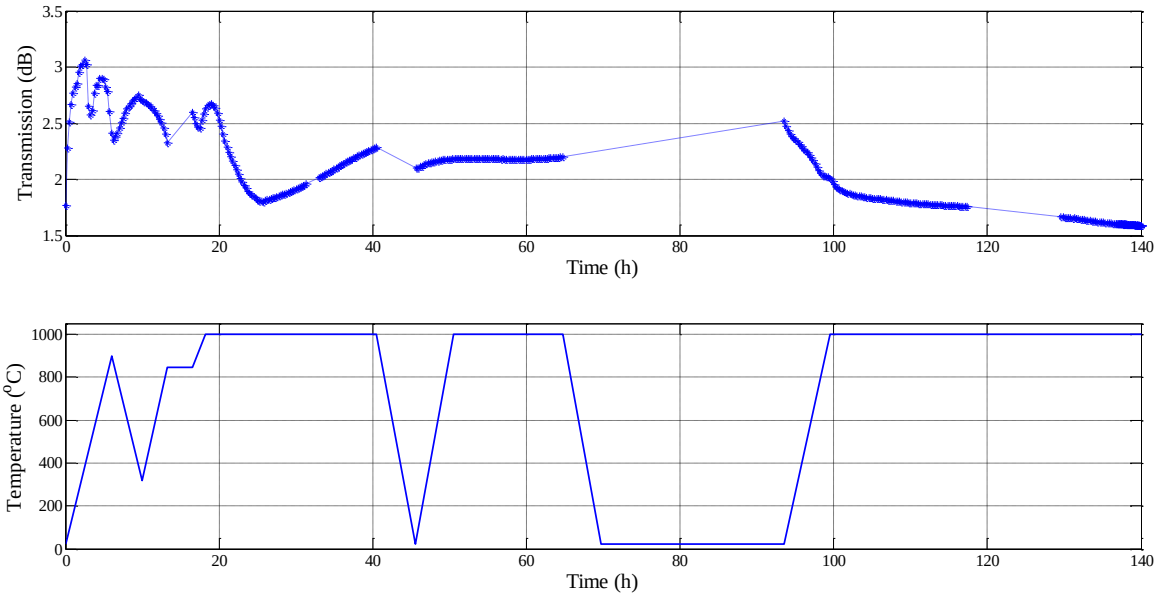

Figure 9-10. Transmission degradation (upper picture) of the SMF28 and its corresponding setting temperature of the furnace (lower picture).

g. Fiber looped, 15 cm diameter, 10 m heated, decoated.

A 10m long SMF28 fiber decoated by acetone was routed in loops of 15 cm diameter and put in a furnace. Lead-in and -out fibers ran through a hole in the side wall of the furnace and were connected to a Micron-Optics CTS, which was employed to monitor the transmission of the fiber in real time. The transmission loss was recorded after the fiber was heated to 1000 ℃. Based on the speculation that bending is one of the key factors that leads to a loss increase, this fiber should survive longer than fibers loops in the former test, which had a fiber bending diameter of 10 cm. However, as shown in Figure 9-11, the transmission drops to -45 dB within only 50 minutes, indicating a factor other than fiber bending could have greater impact on fiber breakage.

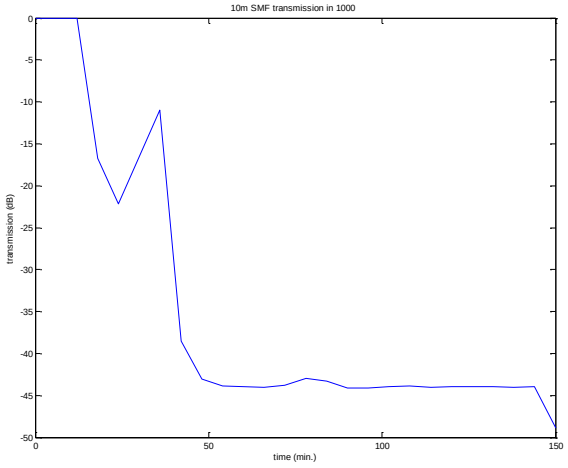

Figure 9-11. Transmission decay of 10m decoated SMF-28 single mode fiber looped at 1000 ℃.

h. Fiber looped, 15 cm diameter, 10 m heated, coated

Similar experiment was conducted but without fiber pre-decoating. As shown in Figure 9-12, at the beginning the curve, the transmission is higher than 0db due to thermal radiation, and gradually drops to below -25 dB after 110 hours.

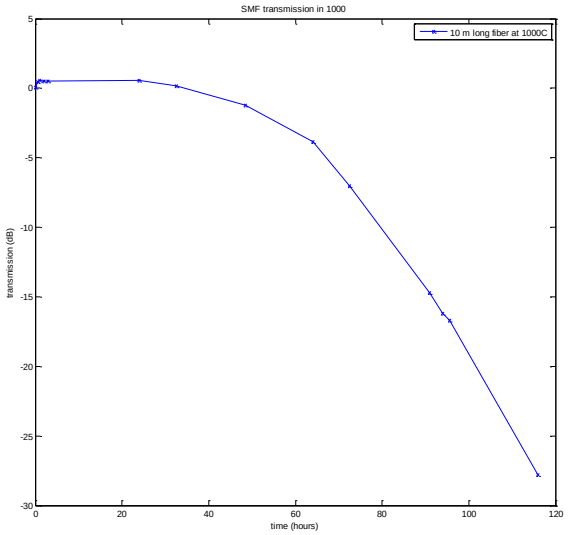

Figure 9-12. Transmission decay of 10m coated SMF-28 single mode fiber looped in 1000 ℃.

By comparing to the results with the decoated fiber, it is clear that the fiber coating improves the fiber performance under severe bending at high temperature. As the coating evaporate, the silica fiber loses the force holding its stress, and starts to break from the weakest points (as shown in Figure 9-13). In conclusion, stress is still the key factor in fiber failure at high temperature, which can be possibly solved by removing stress or providing external support with coating. This provides a basic guideline for future system setup.

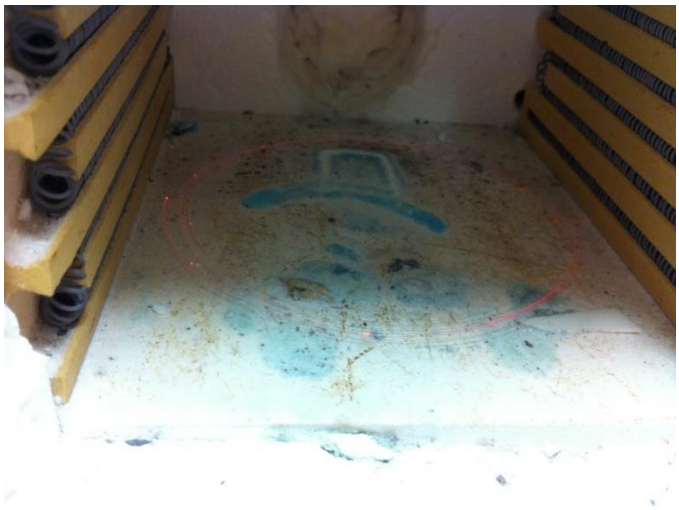

Figure 9-13. Visible light leaking from the fiber after heated.

i. Fiber looped, 10 cm diameter, 10 m long, twisted

In real application, bending of the sensing fiber can be expected to be minor, according to the large scale of the coal gasifier. However, twisting of the sensing fiber is independent to bending, and remains in the fiber during de-coiling and re-coiling. The twisting stress can be observed by the status of the fiber coil. As shown in Figure 9-14, the leading parts of the coil without stress releasing wrapped unnaturally (left), comparing with the loosely hanging ends in the stress released coil (right). In a twisted fiber coil, the force that holds against the internal twist comes from the fiber coating. When the coating burnt off at high temperature, the twisting force was resisted only by the softened silica fiber. In this case, breaking and cracking can happen at the weakest point within the most force-concentrated section. This explains why the breakage of the former experiments always occurred at the leading part of the fiber coil.

Figure 9-14. Photos of 10 cm diameter coil of 10 m long SMF28 fibers with (left) and without (right) internal twisting stress.

Transmissions in heating tests of two 10 cm diameter coils of 10 m long SMF28 fibers with artificial twist are shown in Figure 9-15. One coil (red line) broke before the temperature rose to 1000 ℃, while the other one dropped to ~-43 dB and broke within 2 hours.

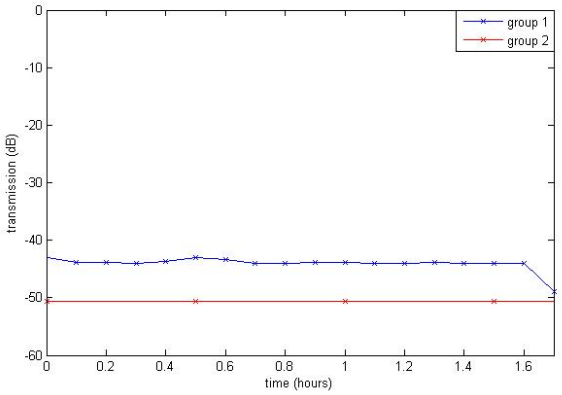

Figure 9-15. Transmission of two 5cm radius coils of SMF28 fiber with length of 10m with artificial twisting stress at 1000 ℃.

j. Fiber looped, large diameter, 50 m heated, twisting released

In order to find the condition that could eliminate fiber breakage, both bending and twisting stresses were relieved in this test. The fiber was coiled with large radius and run in and out of the furnace 250 times from two holes in the wall. The sections within the furnace hung into a curve with a bending radius of ~1 m, and the total heated length was ~50 m. The transmission during the 48 hour test at 1000 ℃ is shown in Figure 9-16.

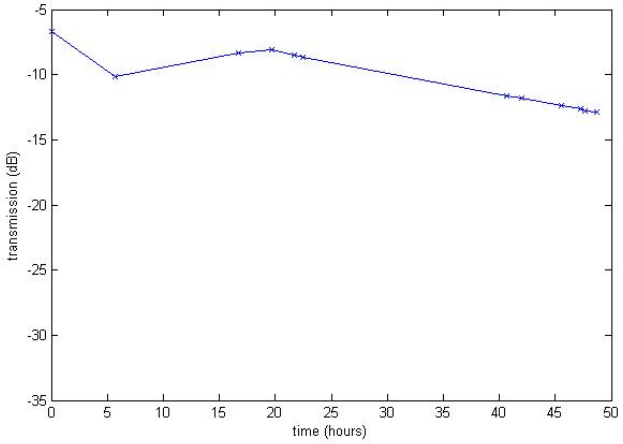

Figure 9-16. Transmission of a 50 m long, twist released SMF28 fiber with 1m bending radius at 1000 ℃.

Within the 48 hour test, the transmission dropped by ~-13 dB. The minor transmission drop might come from the multiple sections bearing high temperature gradient at the hot-cold interface near the furnace wall. No obvious breakage or crack was observed after annealing.

k. Fiber looped, 10 cm diameter, 10 m heated, twisting released

To remove the high temperature gradient sections and test the influence of bending, two sets of 10 m long SMF28 fibers were cut and manually coiled into 5cm radii with twisting stress released. A 48 hour durability test at 1000 ℃ was performed on both coils with transmissions monitored. The results are shown in Figure 9-17.

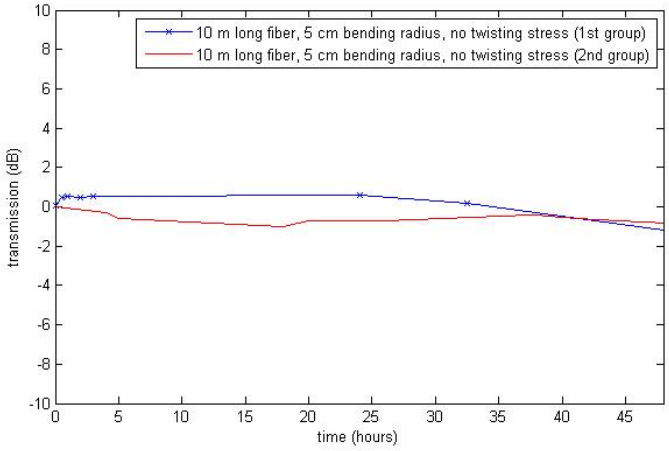

Figure 9-17. Transmissions of two groups of twist free 10 m long SMF28 fibers with 5cm bending radius at a temperature of 1000 ℃.

The results show that both coils survived the long term test with a transmission decrease within 1dB. Such results from highly bent fibers proved that bending does not necessarily lead to fiber breakage or cracking. The key of the fiber survivability at high temperature lies in the removal of the internal stress within the fiber, which could lead to fiber breakage as the fiber loses its flexibility when annealed. By properly removing the twisting-induced internal stress, long-term stability could be achieved. It is worth noting that the introduction of other stress by the environment will also lead to fiber failure, which need to be carefully avoided during packaging development.

9.3 Conclusion

In this chapter, the SMF28 single mode fiber has been tested in experiments for its survivability at 1000 ℃. It is found that the high loss in the fiber is caused by the breakage developed from the micro-cracks in the fiber. By properly removing the internal stress, especially twisting, in the fiber, breakage can be avoided. It is also found that the bending will not lead to breakage as long as the twisting force is properly handled. This will be provide basic guidelines for the design of the packaging technique.

10 Packaging of sensing fibers

As discussed in the former chapter, the sensing fiber is extremely sensitive to stress when annealed at high temperature. At the same time, the fiber will also be very fragile and requires gentle support. Therefore, the packaging of the sensor need to provide support to the sensing fiber, while not applying force on it. Moreover, to gain more versatility during installation, the packaging also need to be flexible and miniature. In this chapter, the investigation on several different packaging strategies through experimental tests will be introduced.

10.1 Stainless steel capillary tubing

In the first attempt, we used a thin stainless steel tubing to protect and support the fiber in the furnace. Figure 10-1 shows the stainless steel tubing from Vita Needle.

Figure 10-1. Small diameter tubing from Vita Needle.

A high temperature test was conducted on a micro stainless steel tubing from Vita Needle. A 10 cm long tubing with an outer diameter of ~500 μm and an inner diameter of ~300 μm was polished on both ends and heated to 1000 ℃ in a furnace for 20 hours to test its ability for

continuous use at high temperatures. The microscope pictures of the tube before and after the annealing are shown in Figure 10-2, in which the distortion was not obvious. However, the surface of the tube was roughened due to oxidation.

Figure 10-2. Microscope picture of stainless steel tubing before (left) and after (right) annealing.

Figure 10-3 shows the cross section of the tube after annealing. The shape of the tube is well preserved and no crack or breakage was generated during the annealing.

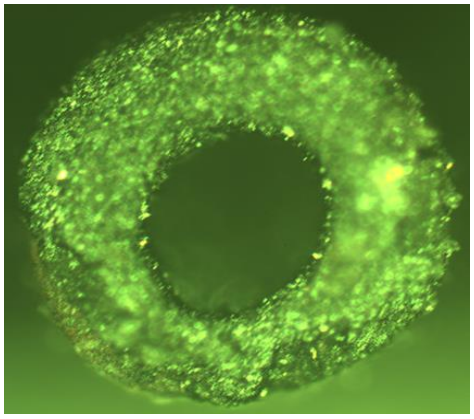

Figure 10-3. Cross-section of the tube after annealing.

Then, the tube was tested at high temperature as the fiber packaging. In the first test, an SMF-28 fiber was inserted into a thin 316 stainless steel tube, whose ID is barely larger than the diameter of the fiber with coating. The protected fiber ran straight through a box furnace, with a heated length of ~20 cm and guiding length of ~12 cm on both sides out of the furnace, as shown in Figure 10-4.

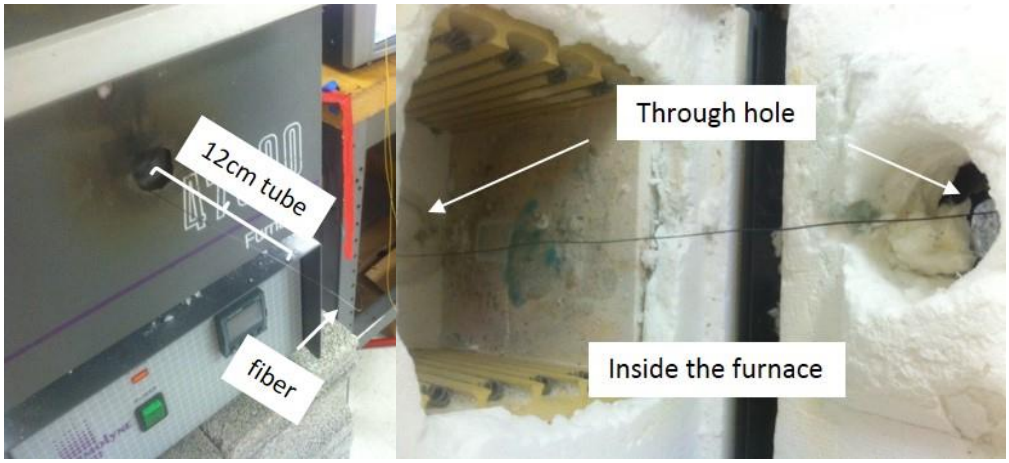

Figure 10-4. Experimental setup for the 1st fiber protection thermal stability test.

The temperature of the furnace was set to 1000 ℃ to test the thermal stability of the protected fiber. The light transmission of the fiber was recorded during the heating. As shown in Figure 10-5, the recorded light intensity goes up within the first hour due to the thermal radiation, and dropped quickly to -50dB in the following hour. A -50dB loss at the end of the test meant that the fiber was basically opaque and no longer useful.

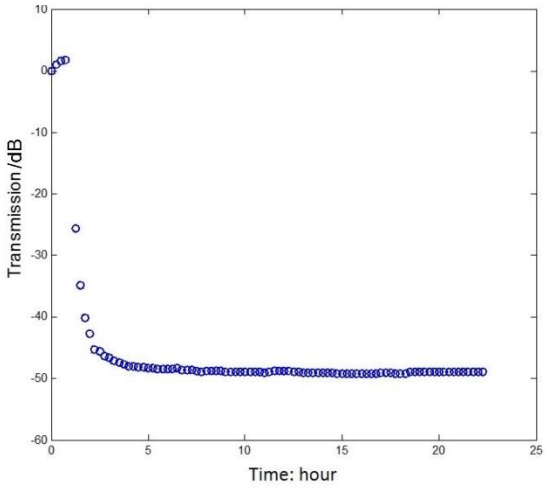

Figure 10-5. Transmission data of a coated SMF-28 fiber protected by a thin 316 stainless steel tube heated at 1000 ℃ for 23 hours.

Black residues were observed on the fiber near both outlets of the tube at the end of the test, as shown in Figure 10-6. These residues were confirmed to be the carbonized and evaporized polymer coating of the SMF-28 fiber, which led to external stress and contamination on the fiber.

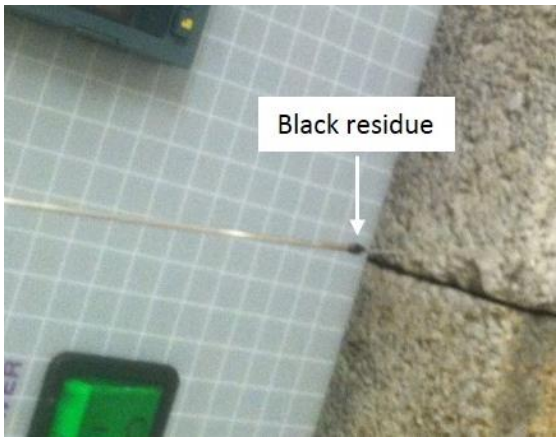

Figure 10-6. Black residue observed on the fiber near one of the tube outlets.

In the second test, the SMF-28 fiber was decoated before running through the stainless steel tube to eliminate the unwanted influence of the burnt coating residue. The rest of the setup was identical with the 1st test. The recorded transmission data of the fiber is shown in Figure 10-7. In the first 9 hours, only slight transmission reduction was observed. However, after that, the transmission of the fiber started a quick drop, indicating that severe damages occurred in the fiber. Compared to the 1st test, improvement of stability was clear but the performance still failed to match the expectation.

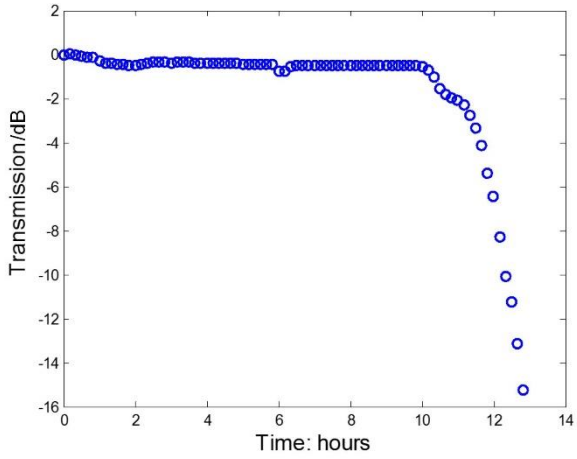

Figure 10-7. Transmission test of a bare fiber protected in a thin stainless steel tube at 1000 ℃ for 13 hours.

One potential cause of the fiber failure is the short length of the applied protecting tube. Given the high thermal conductivity of stainless steel, the 12 cm lead-in and lead-out tube length might not be enough to smooth the temperature distribution all the way to room temperature at the ends of the tube. In the third test, a longer stainless steel tube with ~33 cm lead-in and lead-out lengths was used in the same setup. The result of the 15-hour transmission test at 1000 ℃ is shown in Figure 10-8. At the end of the test, a transmission loss of 1.4 dB was recorded, indicating that no severe breakage occurred in the fiber during the test. However, the result also shows room for

further improvement. A loss of 7 dB/m could notably lower the signal when it occurs in a distributed sensing fiber.

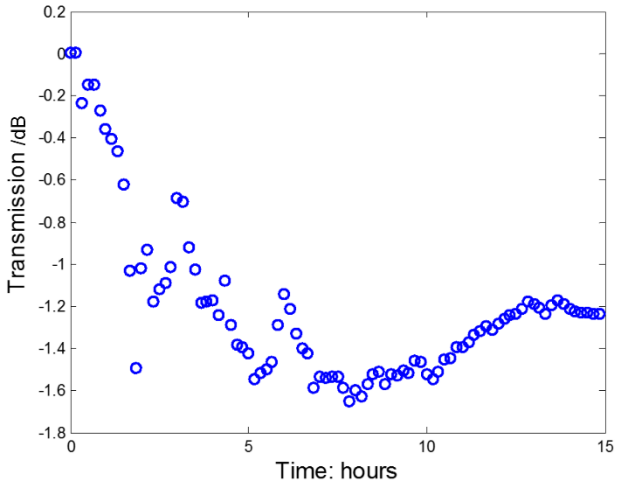

Figure 10-8. Transmission test of an SMF-28 fiber protected by a stainless steel tube with 33 cm lead-in and lead-out lengths at 1000 ℃.

10.2 Gold-coated fiber

To provide additional protection to the fragile fiber, another trial was conducted with gold-coated fiber instead of decoated SMF-28 fiber. Gold coatings has a high working temperature, providing better support to the fiber than polymer coatings at high temperature. At the same time, a bigger tube with 1 mm inner and 1.3 mm outer diameter was used to reduce the friction force between the tube and the fiber during the tube stretching caused by (coefficient of thermal expansion) CTE mismatch between the tube and the fiber. Since the gold coated fiber used in the test was a multimode fiber, an LED and a spectrometer (Ocean Optics) were used to measure the transmission of the fiber. The transmission data of the fiber heated at 1000 ℃ is shown in Figure 10-9. During the 4.5 h test, the fiber transmission kept dropping, indicating a continuous stretching on the fiber.

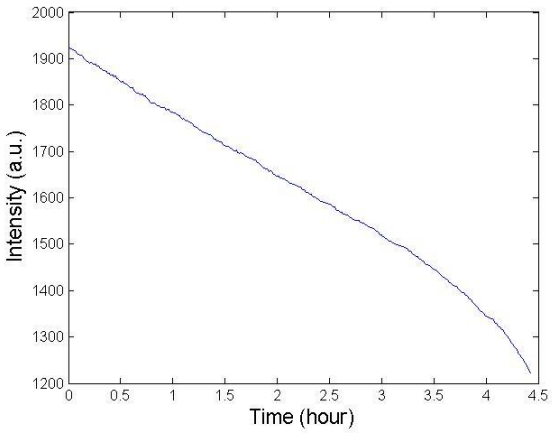

Figure 10-9. Transmission test of a gold coated fiber protected by a bigger stainless steel tube at 1000 ℃.

After cooled down, the tube and the fiber were taken out for failure analysis. A red laser was launched into the fiber, and relatively weak light was observed on the other end, which means the fiber was not physically broken after the test. The protecting stainless steel tube was severely oxidized and curved after the heating, which was also observed on thinner tubes in the former tests. A picture of the tube is shown in Figure 10-10.

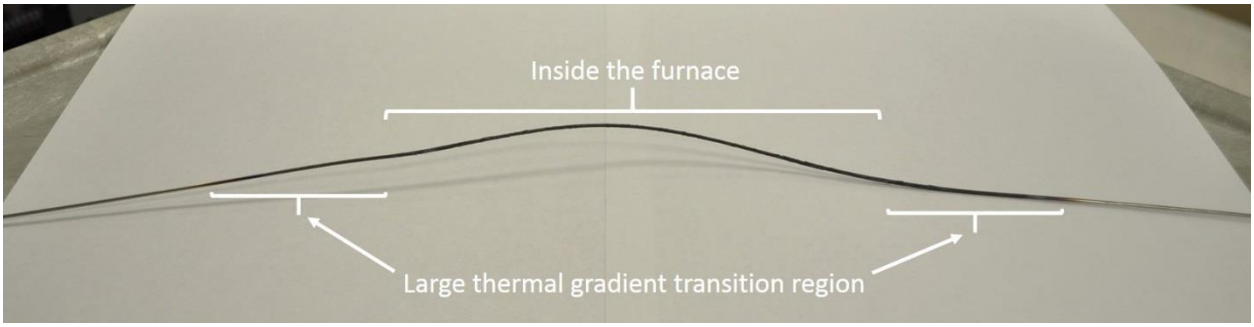

Figure 10-10. Rusted and curved stainless steel tube after heated at 1000 ℃.

The gold-coated fiber was taken out of the tube in one whole piece, as shown in Figure 10-11 (a). Due to the curving of the tube, the fiber was bended into a similar shape. The heated region of the gold coated fiber is shown in three segments (Figure 10-11 (b), (c), (d)). In region 1, which corresponds to the part heated at 1000 ℃, the gold coating on the fiber only had slight contamination (Figure 10-11 (b)). On the other hand, in region 2 and 3, the gold coating was severely contaminated by the rust from the tube (Figure 8 (c), (d)). The formation of the regional contamination indicated the distribution of the oxidization on the inner tube surface. Due to the small inner diameter, the oxygen exchange could not reach the center region before it burnt out with the tube in the outer region.

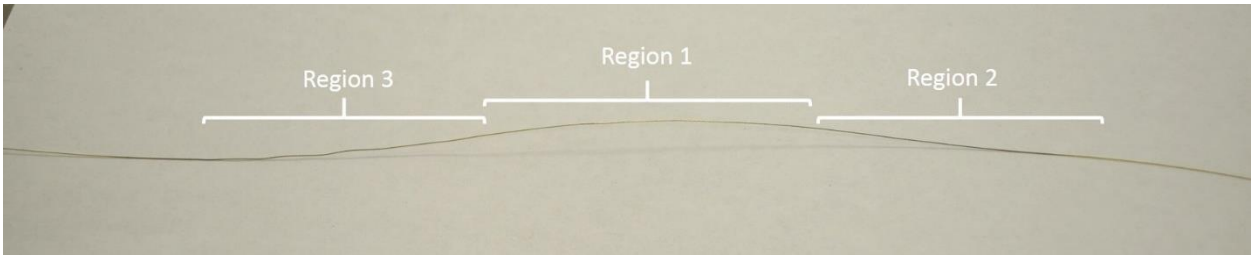

(a) Fiber after heating

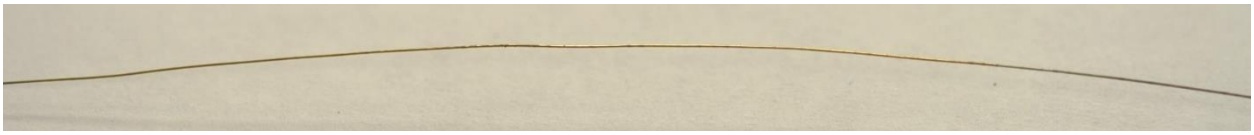

(b) Region 1

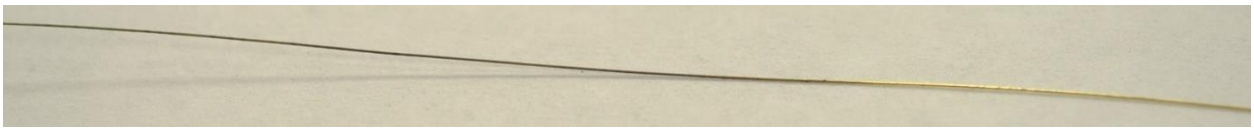

(c) Region 2

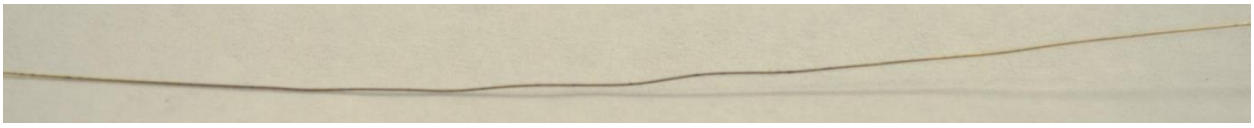

(d) Region 3

Figure 10-11. Pictures of protected gold coated fiber after heated at 1000 ℃.

According to the analysis, the failure of the stainless steel tube is the major cause of the fiber damage. At 1000 ℃, the 316 stainless steel tube was observed to oxidize and deform, which could lead to contamination and stress on the fiber. To avoid theses issues, special stainless steel tubes was used which could keep its physical and chemical properties at high tempearture.

10.3 Inconel 600 tubing

To eliminate the issues caused by tube oxidation, a new tube made of high temperature alloy Inconel 600 was tested as the packaging material. A 105/125 gold-coated MMF was installed into the straight Inconel tube, and heated in a tube furnace up to 1000 ℃. Figure 10-12 shows the monitored intensity of the reflected light from the fiber end. The transmission intensity started to drop after 4 hours of annealing at 1000 ℃, and kept deceasing at a high rate. After cooled down to room temperature, the data showed ~10dB loss comparing to the original intensity before annealing.

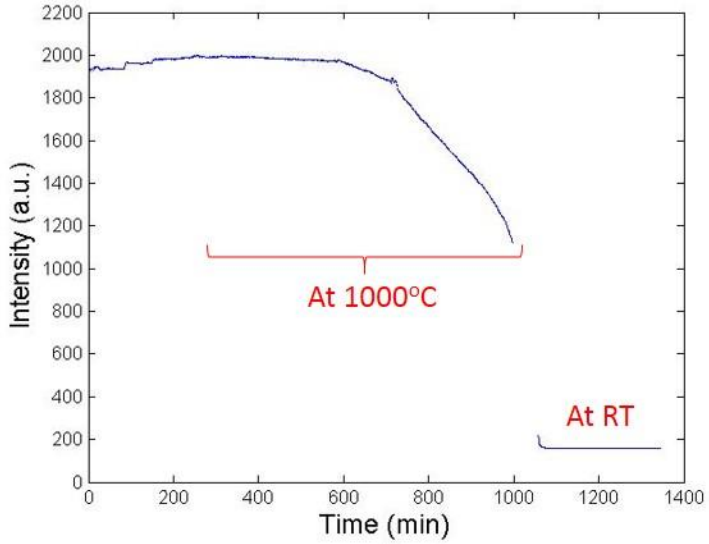

Figure 10-12. Monitored intensity decay of a gold coated fiber annealed in an Inconel 600 alloy tube.

As expected, the Inconel alloy tube performed well at high temperature and showed no deformation after the annealing, and the oxidization only occurs on the surface of the tube. However, the gold-coated fiber broke during the retrieval, and color change was observed on the coating on a ~4" long region, as shown in Figure 10-13 (a). When observed under microscope, the gold coating in the darkened region showed severe defect (Figure 10-13 (c)). When compared with the gold coating before annealing (Figure 10-13 (b)), obvious non-uniformity, cracks and even peel off could be observed.

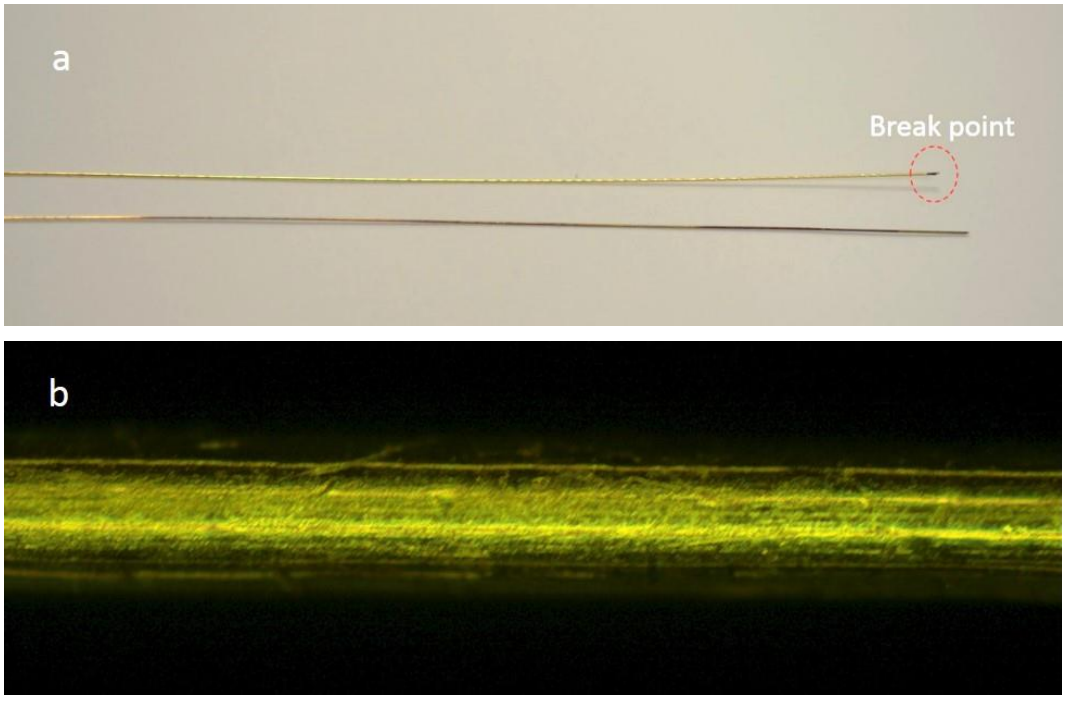

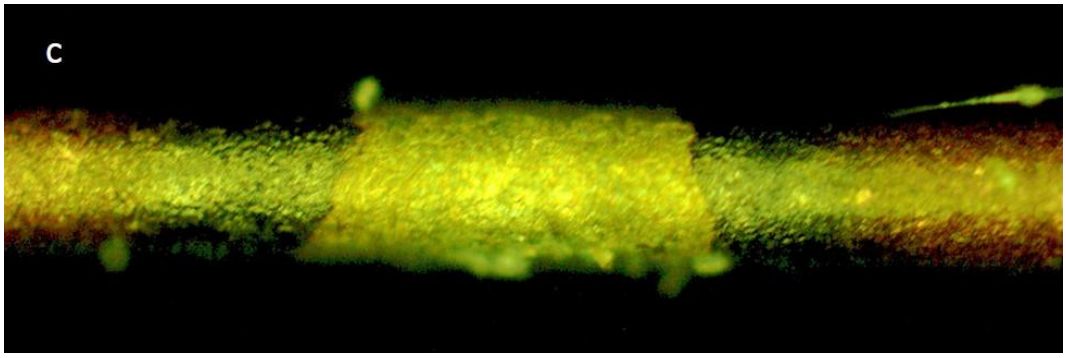

Figure 10-13. Gold coated fiber after the 1000 ℃ annealing in an Inconel alloy tube. (a) Photo of the fiber breaking point and the darkened segment on the fiber. (b) Microscope image of the gold coated fiber before annealing. (c) Microscope image of the darkened segment of the gold coated fiber after annealing.

This phenomena could be a result of both the softening of the gold coating and the CTE mismatch between the gold coating and the silica fiber. The degrading of the coating could introduce non-uniform stress within the weakened fiber, which leaded to fiber failure. The original goal of using gold-coated fiber was to provide additional support to the silica fiber; however, the results indicated that the gold coating could only cause more issues.

To avoid these issues, we turned back to bare silica fibers. A SMF-28 silica fiber was tested with the Inconel 600 tubing. Single-pass fiber loss was monitored by a CTS. The fiber was heated up and kept at 600 ℃ and 800 ℃ for 2 hours each, then 1000 ℃ for 24 hours. The recorded fiber transmission loss during the test is shown in Figure 10-14.

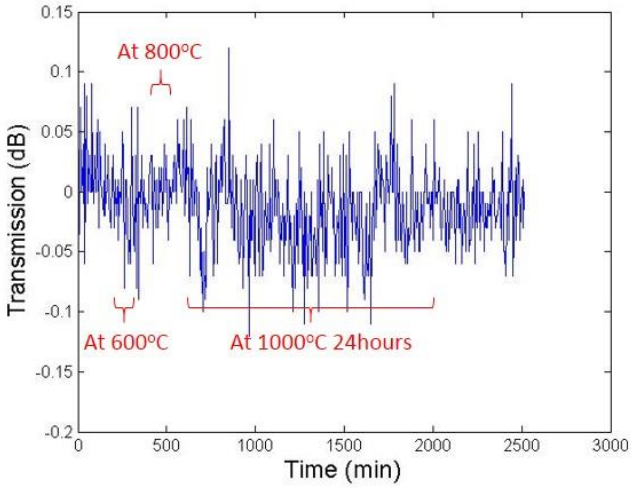

Figure 10-14. Transmission of a bare SMF-28 fiber protected in an Inconel alloy tube in a long term annealing test up to 1000 ℃.

The result showed highly stable performance of the bare fiber protected by Inconel 600 tubing. No obvious loss was observed during the heat-up, annealing and cool-down processes. Similar result was acquired in a second test with the same setup, which confirmed the feasibility of applying this packaging scheme up to 1000 ℃.

10.4 BOTDA test of packaged sensing fibers

Dual side band BOTDA system described in Section 7.4 was used for the packaged sensor test. With 10 ns pulse width, 1 m spatial resolution was achieved. Figure 10-15 shows the Brillouin signal of the resolved 1m heated fiber over 600 m span. The distance between the dashed lines in Figure 10-15 (b) represents a spatial length of 1 m.

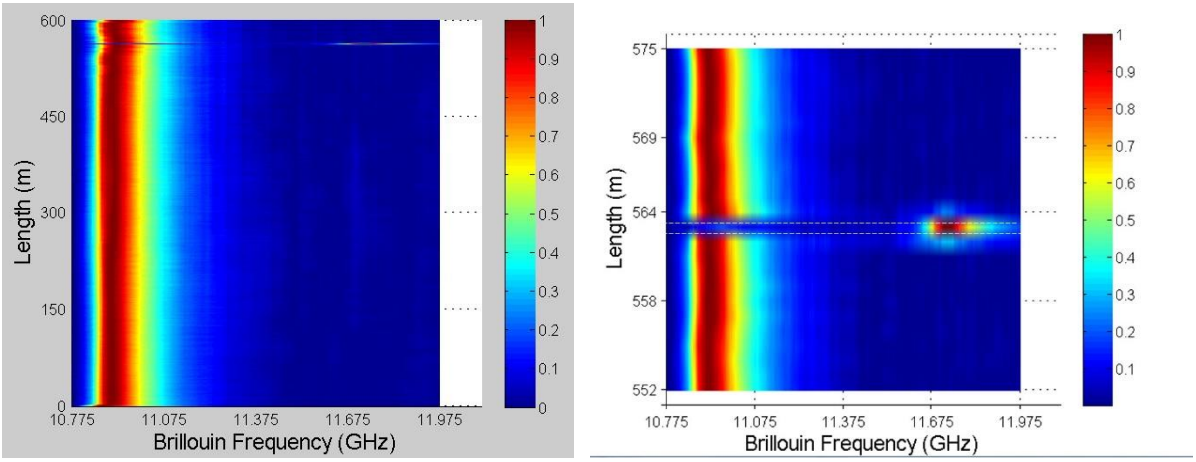

(a) (b)

Figure 10-15. Brillouin signal of 1m fiber heated at 1000 ℃ over a 600 m sensing span: (a) signal over the entire span; (b) zoomed in signal near the heated section.

A temperature calibration from 100 ℃ to 1000 ℃ was performed as the furnace heated up. As shown in Figure 10-16, the Brillouin frequency data did not show very good linearity vs temperature.

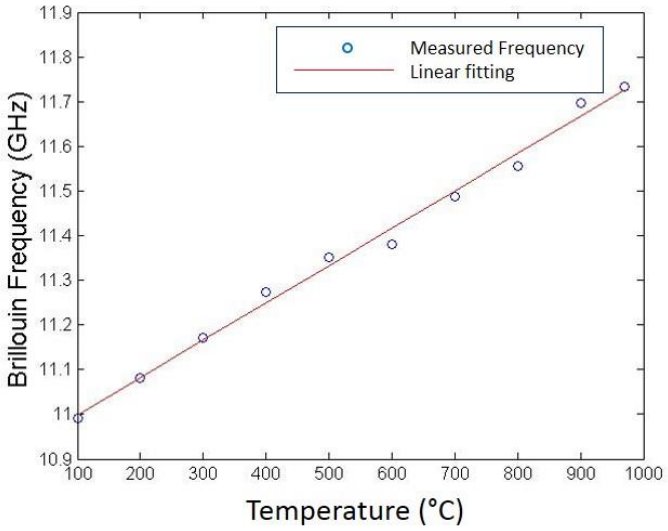

Figure 10-16. Brillouin frequency calibration of packaged fiber heated from 100 ℃ to 1000 ℃ in the testing environment.

One possible cause of the nonlinearity at higher temperature is the short heating length comparing to the system spatial resolution. In this test, the sensing fiber had one 70 cm section in the highest temperature region, and two 15 cm lead-in and lead-out sections in lower temperature region. As shown in Section 11.7, the higher the furnace temperature is, the larger the temperature difference between the higher and lower temperature region will become. With all the three sections within the system spatial resolution of 1m, the temperature difference will show up as a broadening in the Brillouin spectrum.

Figure 10-17 shows the Brillouin spectrum measured (a) at, (b) 1 m away and (c) 2 m away from the center of the high temperature region. Spectral crosstalk between the high and low temperature regions clearly show up in the signals acquired within the 1 m range from the heating center.

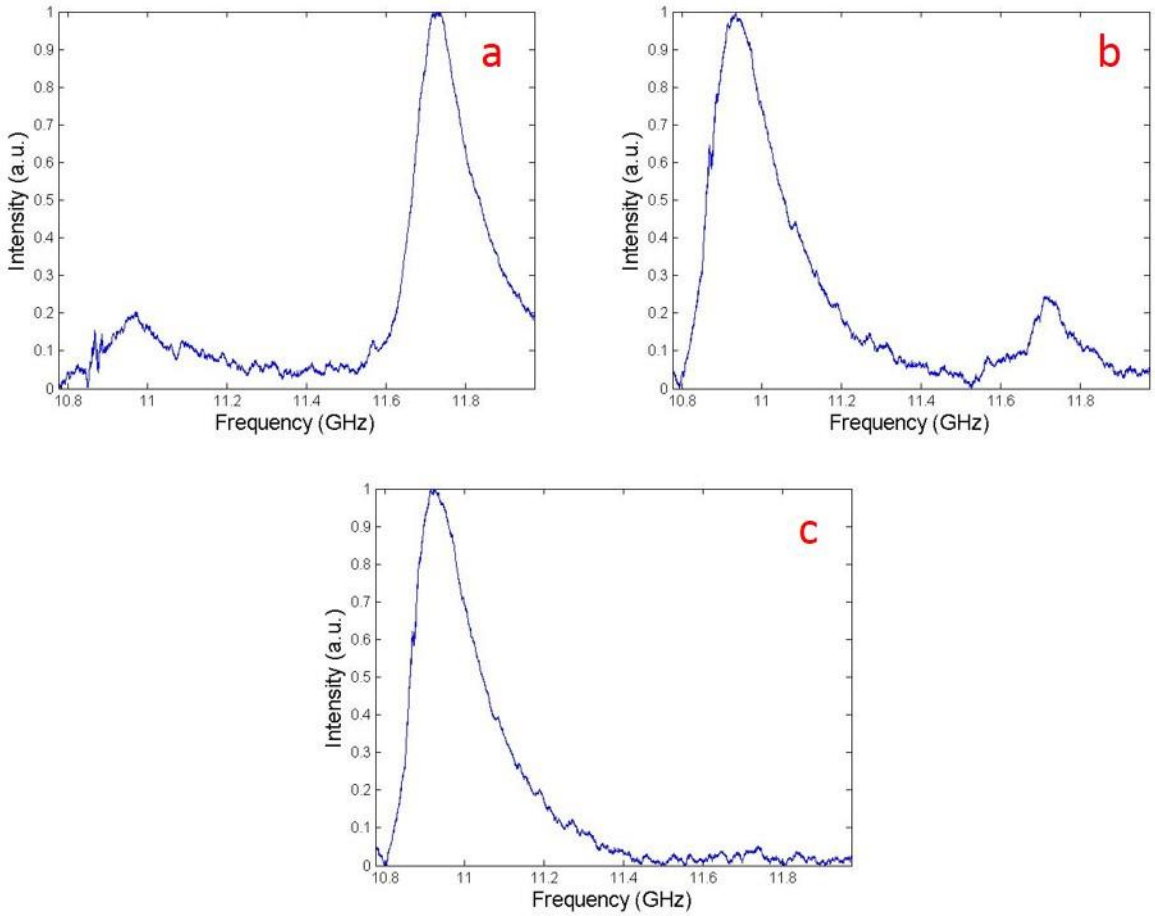

Figure 10-17. Brillouin Spectrum recorded (a) at, (b) 1 m from and (c) 2 m from the 1000 ℃ heating center.

Although the overlapped signal can cause shifts in the demodulated temperature, it could only happen in the case that the hot spot feature is smaller than the system spatial resolution (1 m). Even in this case, the system can still correctly indicate the position of the hot spot and estimate the temperature within a reasonable error level.

10.5 Conclusion

In this chapter, several different packaging methods were tested for the sensing fiber at high temperature. Inconel 600 alloy tubing was found to offer the best stability and performance over all tested materials. A sensing fiber packaged in an Inconel 600 tube was tested with the interrogation system up to 1000 ℃, demonstrating good high-temperature stability and expected sensing performance.

11 Lab-scale gasifier simulation system

To demonstrate the potential of the proposed distributed fiber high temperature sensor for refractory wear monitoring in an operating coal gasifier, a testing environment simulating the working condition in a gasifier was proposed. As a laboratory instrument, the testing environment is basically a miniature double-layer furnace. The sensing fiber will be placed in the testing chamber, which is the gap between the two layers. The furnace will work at temperatures up to 1000 ℃, and will have the ability to simulate various conditions in a coal-gasifier, including hot regions and gradient temperature distributions.

11.1 Conceptual design

The designed furnace is conceptually shown in Figure 11-1. The conceptual design of the double layer furnace was cylindrical to minimize fiber bending. To isolate the furnace from the floor, a base made of stainless steel plate and refractory bricks will be built. The whole structure will be raised from the floor for safety.

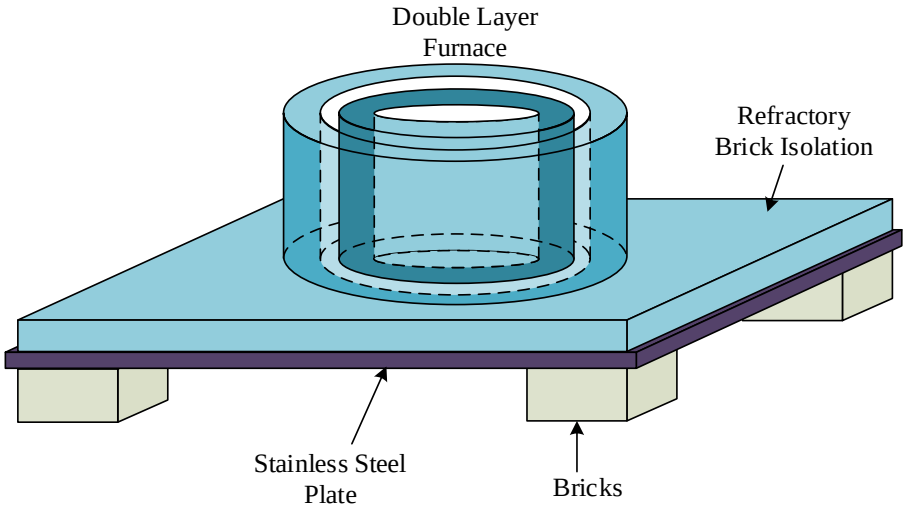

Figure 11-1. Overall furnace structure concept.

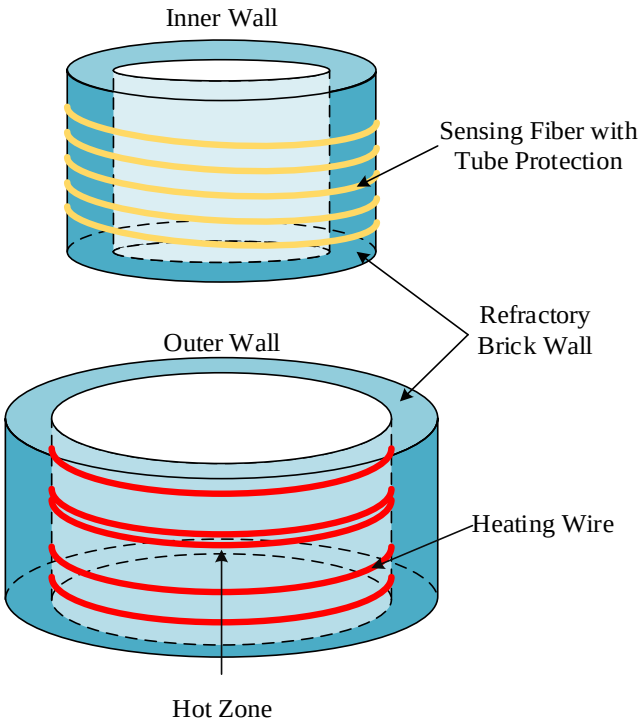

Figure 11-2. Fiber sensor and heat wire deployment concept.

To simulate the condition in the gap between the inner and outer walls of a working coal gasifier, the fiber sensor will be deployed uniformly on the outer surface of the inner layer of the furnace. The heating wire will be distributed on the inner surface of the outer layer instead of in the center of the furnace. The consideration behind this design is mainly on the high temperature. In a design with the heating element in the center cell, to achieve a temperature up to 1000 ℃ in the gap, the temperature within the center of the furnace have to be much higher than 1000 ℃ due to the heat insulation of the inner layer. This temperature will require special refractory bricks and heating wire, as most commercial available products have a maximum working temperature not much higher than 1000 ℃. Another benefit of deploying the heating wires between the walls is the higher temperature gradient that could be achieved in the gap, which will compensate for the difference in the vertical dimension of the furnace from a real coal gasifier. With the help of computational simulation, the position and intensity of heat wire will be carefully designed to simulate hot spots, hot zones and temperature gradients. The deployment strategy is illustrated in Figure 11-2.

11.2 First design

In this first design, normal refractory bricks were considered to be used to build the furnace. To realize the cylindrical geometry, the bricks need to be modified according to the design.

11.2.1 Geometry

The dimensions of common refractory bricks are 9×4.5×2.5 inches. According to these dimensions, a nonagon shaped furnace was designed as a compromise between the shape distortion and construction complexity. The 3D model of the furnace is shown in Figure 11-3.

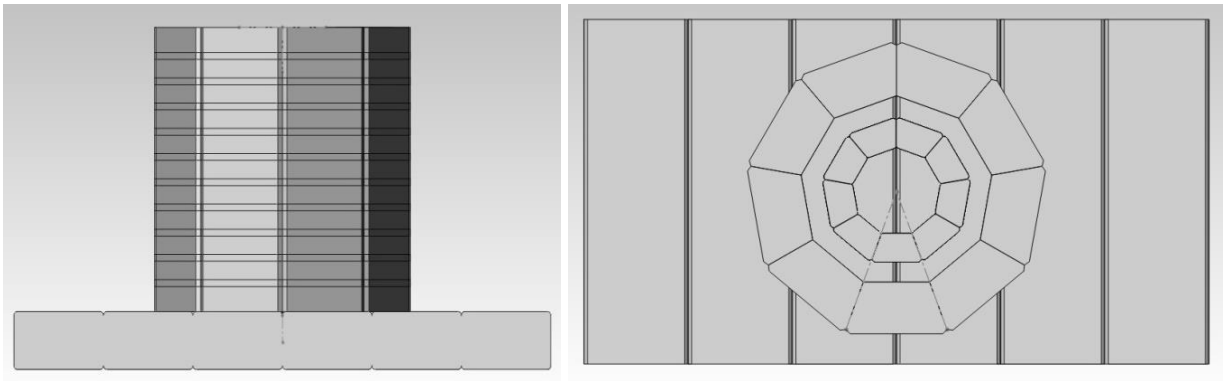

Figure 11-3. Model of the double-layered furnace.

Figure 11-4 and Figure 11-5 show the geometries and dimensions of the bricks for the inner and outer walls of the furnace. Both types of bricks will be fabricated from commercially available bricks. As shown in Figure 11-5, grooves will be engraved on the outer layer bricks for heating wire embedment.

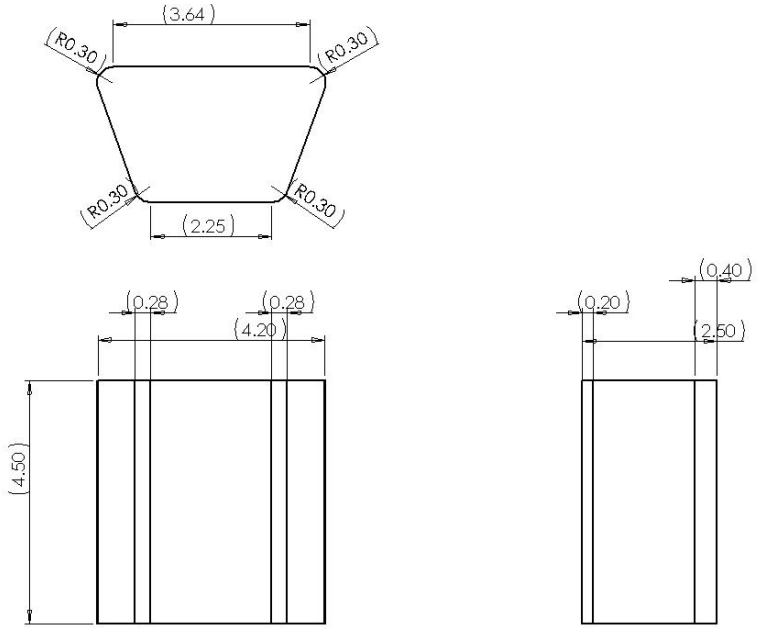

Figure 11-4. A refractory brick for the inner wall of the furnace.

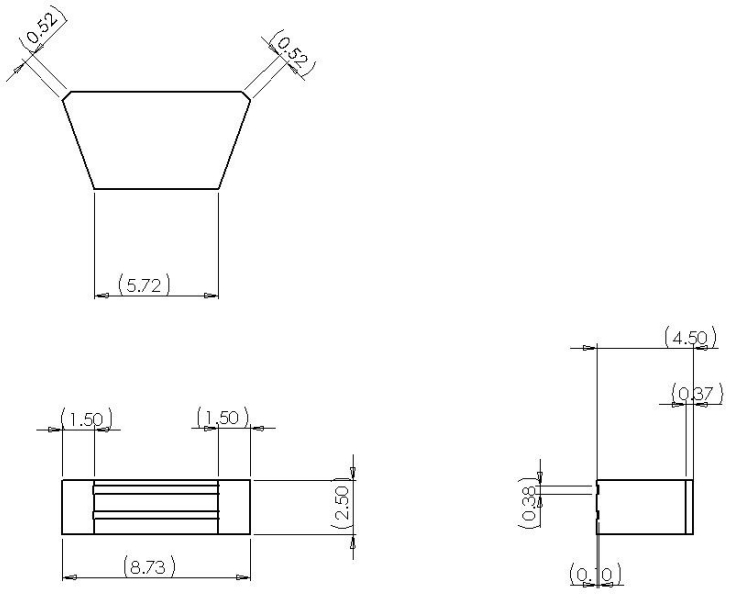

Figure 11-5. A refractory brick for the outer wall of the furnace.

Figure 11-6 illustrates the detailed dimensions of the assembled furnace. The gap between the inner and outer walls is set to ~2.5 inches for the deployment of the heating element, the fiber sensor and the other insulation materials. The total height of the furnace is ~22.5 inches, while the perimeter of the gap is ~1 m, which is designed to match the sensor's spatial resolution. A lid will be built with light insulating materials to seal the furnace.

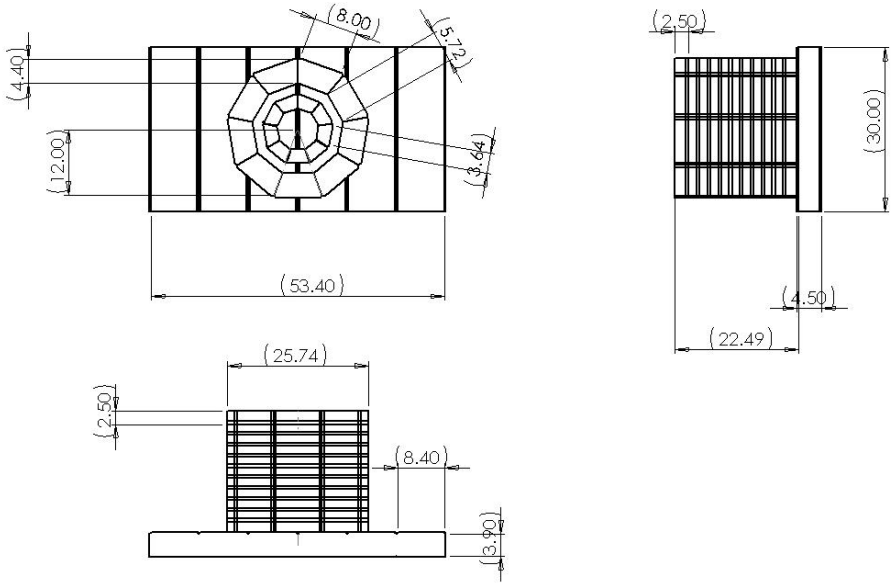

Figure 11-6. Dimensions of the assembled furnace.

Given the relatively small gap between the two walls, installing and replacing the fiber sensor will be difficult if the outer wall is not removed. To solve this problem, a removable inner liner is designed to wrap around the inner wall and hold the fiber sensor. By removing the liner,

replacements and examinations of the sensor can be performed without disassembling the furnace.

11.2.2 Refractory bricks

As stated above, commercially available standard refractory bricks with dimensions of 9x4.5x2.5" will be used in our design. The bricks will be first cut according to the designed dimensions (Figure 11-4 and Figure 11-5), and then milled for heat wire embedment (Figure 11-7).

Figure 11-7. Refractory bricks milling. [63]

11.2.3 Heating wire

NI 60-040 heating wire from Omega was chosen as the heating element of the furnace. With a maximum working temperature of 1000 ℃, the wire has a low resistance of 0.3219 Ω/feet and is easy to wind (as shown in Figure 11-8). By applying different winding intensities, the temperature distribution in the furnace can be controlled as designed.

Figure 11-8. Heating wire winding. [63, 64]

11.2.4 Insulation blanket

Thermal ceramic blanket SuperWool 607 is a non-hazardous material that possesses low bio-persistence and low thermal conductivity (0.8 W/m (℃)); the material comes between 1/8-2 inches thick, which can withstand a temperature up to 1300 ℃. The blanket will be used as the

liner around the inner wall to help fix the fiber sensor. It will also be part of the furnace lid to provide effective, lightweight insulation.

11.2.5 Hot spot and temperature gradient simulation design

The detailed design of the fiber sensor deployment is shown in Figure 11-9.

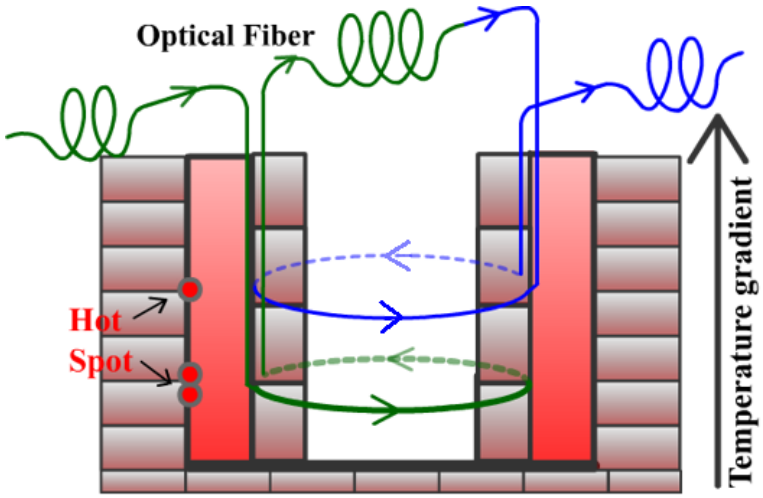

Figure 11-9. Details of fiber sensor deployment and environment simulation.

As presented above, the perimeter of the fiber sensor loop is designed to be ~1m, matching the spatial resolution of the system. However, the scale of a real coal gasifier could be tens of times larger than this simulation furnace. To better simulate the situation in a real coal gasifier, the sensing fiber will be led out of the furnace after each loop. A separate fiber coil of 10-20 m will be placed between two loops. In Figure 11-9, only two of the sensing fiber loops are shown for simplicity. This design will also reduce the length of the protection tubing, and thus relax the difficulty of leading the sensing fiber through the thin tubing. Inhomogeneous distribution of the heat wires along the vertical direction will be set to simulate different conditions in the coal gasifier, including hot spots and temperature gradient.

11.3 Outer wall thermal simulation

In the furnace design, the most important parameters that need careful optimization are the power of the heating element and the arrangement of the refractory materials. To estimate the power needed to heat the furnace, a computational model was designed to simulate the thermal distribution of the furnace outer wall.

Figure 11-10 shows the half cross-sectional view of the model. The thick layer on the left corresponded to the refractory brick layer, while the thin layer on the right stood for the refractory blanket. The model was simplified to be cylindrical to relieve the computational complexity. As the boundary conditions, the inner, upper and lower surface of the wall was set to be thermal insulated, the outer surface was set at fixed temperature of 50 ℃, and three small sections on the inner surface were set to emit constant heat flux of 2000 W to simulate the heating elements. The different boundary conditions are indicated by the blue lines in Figure 11-10.

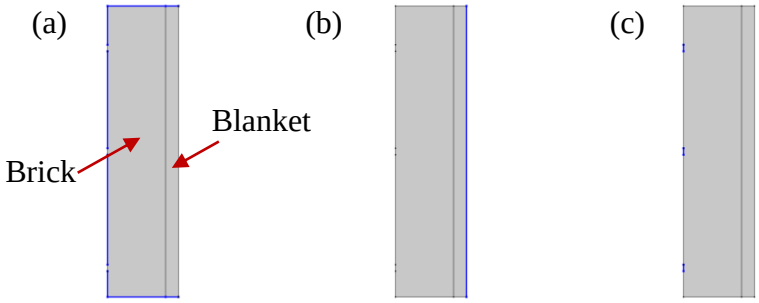

Figure 11-10 Boundary condition setup in the simplified outer wall model (half cross-sectional view): (a) thermal insulation; (b) fixed temperature (50 ℃); (c) heat flux (2000 W).

The simulated steady-state temperature distribution of the model is shown in Figure 11-11. The maximum temperature acquired in the model is 871 ℃ in the heating element region, which is lower than the target of 1000 ℃.

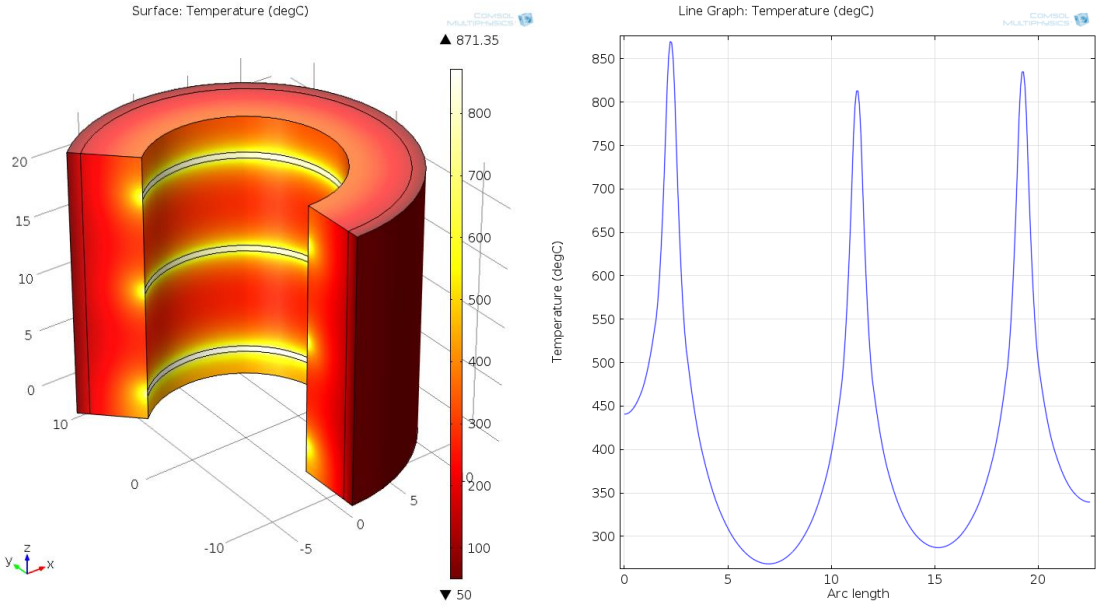

(a) (b)

Figure 11-11. Simulation result of the simplified outer wall model with 3 heating elements working at 2000W total. (a) Steady state temperature distribution; (b) vertical temperature profile along the inner surface.

On the inner surface temperature profile (Figure 11-11 (b)), it is shown that the temperature varies dramatically from the lowest ~250 ℃ up to the highest ~870 ℃. To achieve a uniform temperature distribution, the number of heating elements was increased to 5 in the second test. The total heating flux remained the same. The simulation result is shown in Figure 11-12.

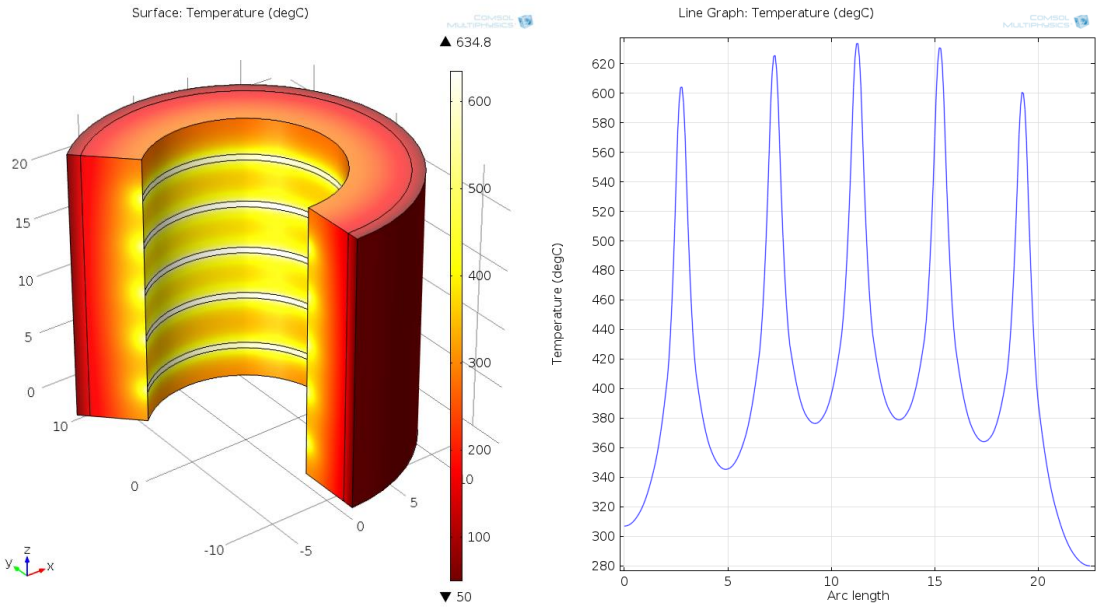

(a) (b)

Figure 11-12. Simulation result of the simplified model with 5 heating elements working at 2000 W total. (a) Steady state temperature distribution; (b) vertical temperature profile along the inner surface.

The temperature profile shown in Figure 11-12 (b) was more uniform as expected comparing to the former result, but the peak temperature dropped to 634 ℃ at the same time. The low inner surface temperature indicated that the insulation needed to be enhanced.

Since the refractory blankets have a notably higher thermal insulating capability than the bricks, attempts are made by adding additional layers of blanket on the inside and outside of the brick wall. The temperature distributions calculated under these conditions are shown in Figure 11-13. By placing a blanket on the inside, both the peak temperature and the peak-to-valley temperature difference on the inside surface increased (Figure 11-13 (b)). By adding blankets on the outside, the average temperature on the inner surface increased (Figure 12 (c) and (d)). With three blanket layers applied, one on the inside and two on the outside, the temperature on the inner surface was greatly increased, with the peak temperature of 1125 ℃ and an average temperature of above 800 ℃ (Figure 12 (d)).

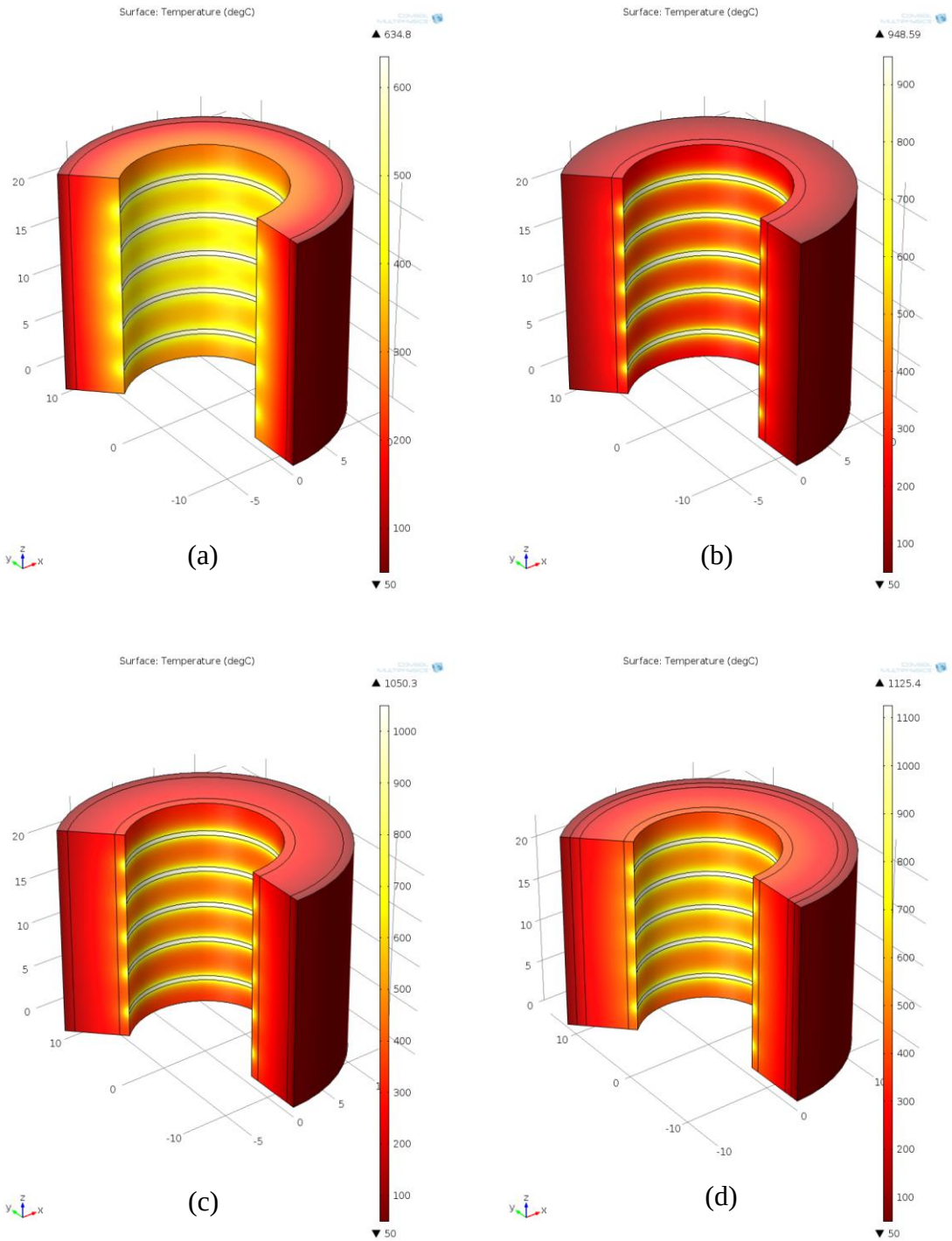

Figure 11-13. Simulated temperature distributions of different thermal blanket deploying strategies: (a) one layer on the outside; (b) one layer on the inside; (c) one layer on the inside and one on the outside; (d) one layer on the inside and two on the outside.

The simple simulation shown above provided us some basic pictures in the thermal property of the outer layer of the furnace. However, given the structure of the furnace, the temperature profile of the whole system could be much more complex to simulate. In this section, a comprehensive thermal model was made including more components taken in to consideration:

center air region, inner brick wall, inside blanket, heating chamber, heat source, outer brick wall, top blanket and base brick. Though the comprehensive model was much more time consuming due to its complexity (over 30 hours), it provided a much better picture of the furnace temperature distribution.

In the simulation, some parameters are set differently since a different model was used to simulate the radiation and dynamic of the system. The surface to surface radiation was set to occur on all inner surfaces, while all the outside surfaces were set to be emitting ambient radiation to the environment. Unlike the former model that directly offers the steady-state result, this model calculates the time based evolution of the temperature distribution. In the simulation, a 6000 second evolution was calculated with the three heating elements running at 6600 W total. The near-stabilized thermal distribution of the system is shown in Figure 11-14.

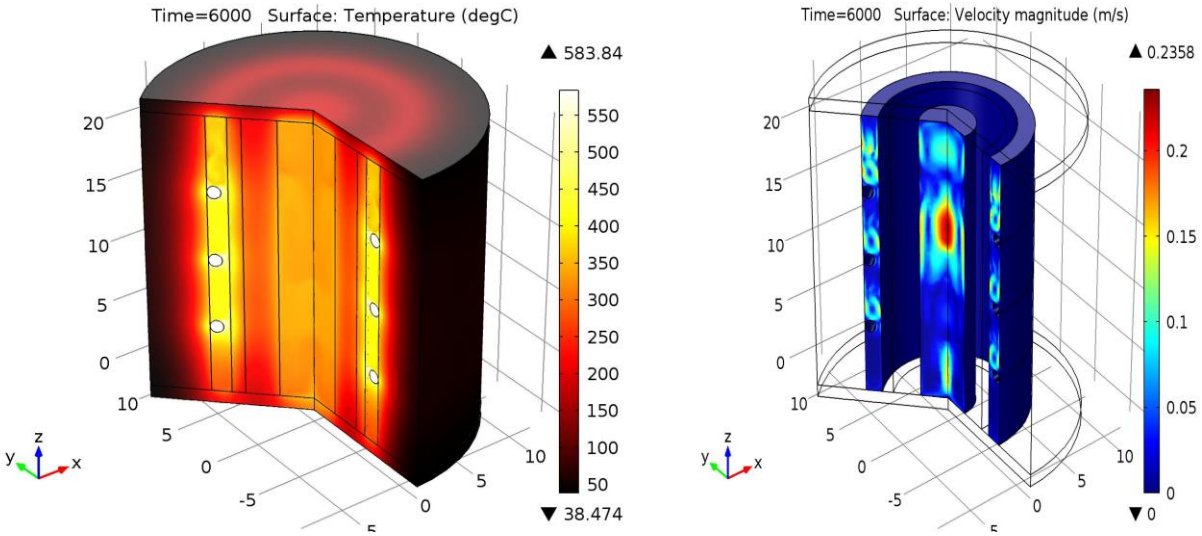

Figure 11-14. Near-stabilized results of the comprehensive simulation. (a) Temperature distribution; (b) air velocity distribution in the air cavities.

The temperature distribution of the system shown in Figure 11-14 (a) carries a lot of information that could help us better understand the behavior of the system:

- The maximum temperature in the whole system only reached 584 ℃. Comparing to the temperature distribution in the outer wall simulation, the maximum temperature was much lower due to the higher thermo loss on the surfaces.
- The temperature distribution in the heated chamber was more uniform than the inner surface temperature profile in the outer wall simulation. The temperature was basically uniform between the heating elements, slightly lower above the top heating element and much lower below the bottom heating element. This effect was a result of the air convection within the heated chamber (Figure 11-14 (b)).
- The center region, where no heating element was deployed, was also very hot. With only the top and bottom surface to emit energy, the center region was able to accumulate heat and reach as high as 350 ℃. The high temperature made the center area on the top and bottom surface a major source of energy emission.

- The high temperature in the air chambers greatly challenges the top and bottom insulating layer. Applying additional layers of heat insulation on the top and bottom surface could greatly reduce the heat leaking on these surfaces.

Based on the simulation results, it is challenging to achieve 1000 ℃ maximum temperature using the brick based design. Ceramic based design is under consideration due to its high thermal insulation capability, and materials will be filled into the center chamber to slow down the heat exchange in this region.

11.4 Final design

As discussed in the former section, the brick-based design proposes several challenges including poor thermal insulation and complicated heating wire installation. To meet our special needs for sensor testing, including the maximum operating temperature of 1000 ℃ and capability of generating specific temperature gradient, we turned to a commercial vendor to build a fully customized furnace with a real cylinder shape.

The final design of the double layer furnace is shown in Figure 11-15. The furnace contains three components: the inner insulation layer, the heating element layer and the outer insulation layer. The testing chamber locates between the inner insulation layer and the heating element layer. Two 6" high heating zones are arranged vertically in the chamber, which can be controlled independently to achieve designated temperature gradient. By design, the furnace should be capable of maintaining 1000 ℃ maximum temperature in the hot zone. According to the simulation results presented in the last report, by heating the upper zone only, maximum temperature gradient can be achieved in the vertical direction. In the final sensor test, the packaged sensing fiber will be deployed on the outer wall of the inner insulation layer with 13.5" OD, which corresponds to a 108 cm length in one loop.

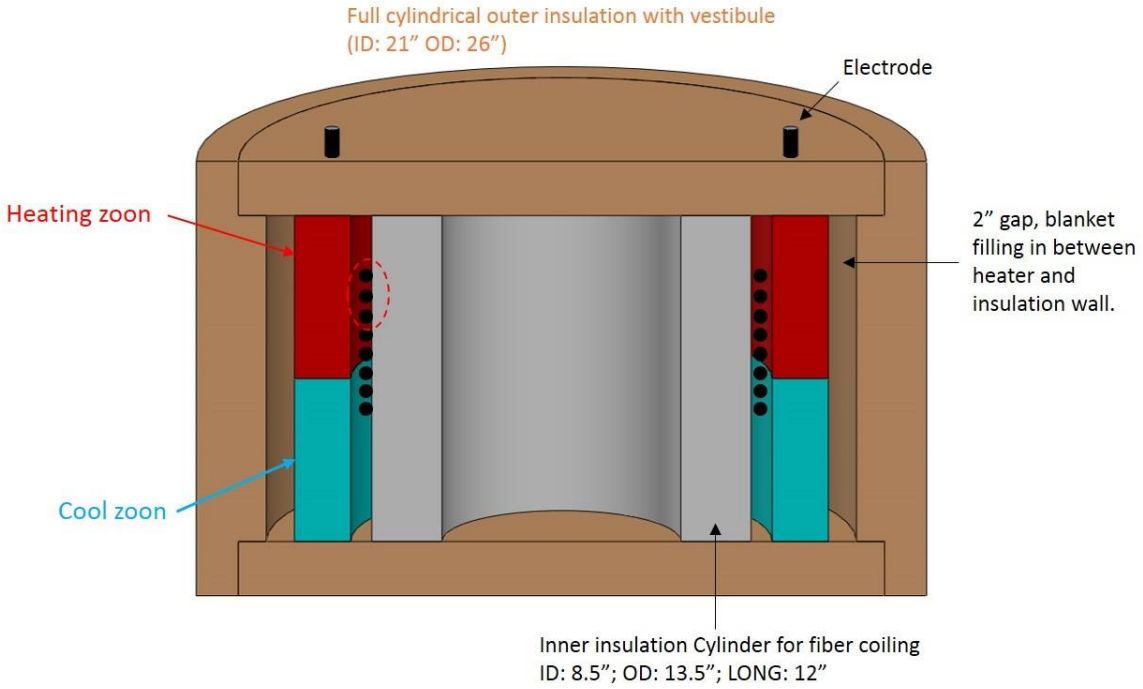

(a)

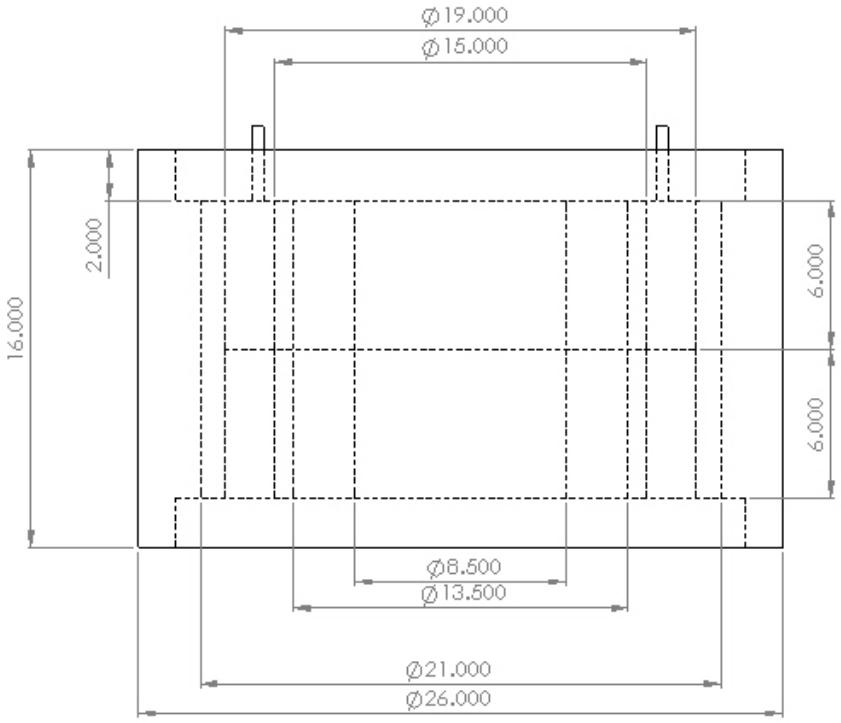

(b)

Figure 11-15. Final design of the double-layer furnace.

11.5 Completed assembly and temperature test

Photos of the assembled furnace are shown in Figure 11-16. The main body of the furnace (manufactured by Thermcraft Inc.) was supported and isolated from floor by a layer of hollow fire bricks. A temperature controller (WK518P by MTI Corp) was used to drive the furnace and control the temperature.

Figure 11-16. Assembled double-layer furnace.

After the furnace was assembled, 8 holes were drilled on the top vestibule, 4 for electrodes connecting to the heating wires, and the other 4 for thermocouples, as shown in Figure 11-17(a). By design, the sensing fiber will run through holes on the bottom of the furnace, and coil at different heights in the furnace to simulate a specific temperature distribution along the sensor, as shown in Figure 11-17(b).

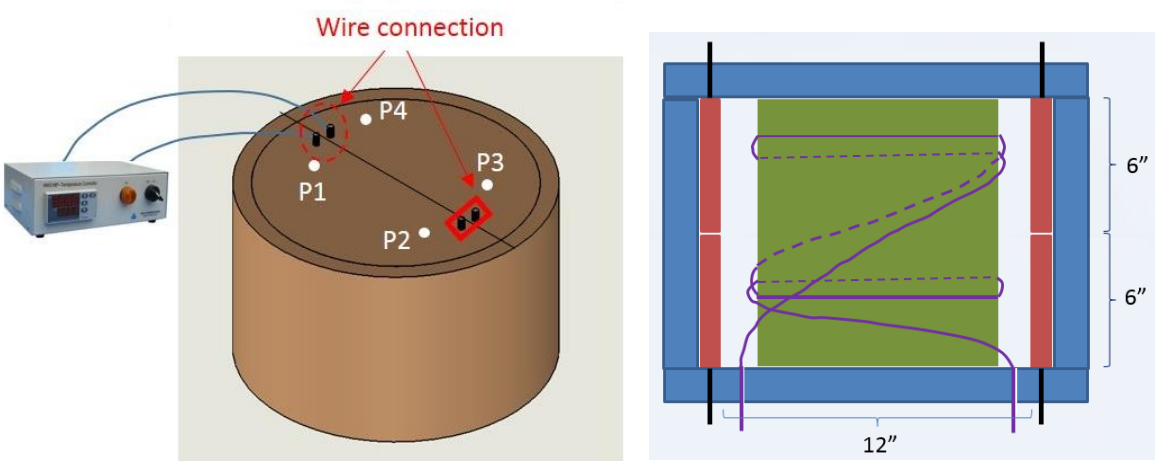

(a) (b)

Figure 11-17. (a)Wiring of the double layer furnace; (b) fiber installation route.

After the assembling was completed, the furnace was heated up for a test run. During the heat-up, the monitoring thermocouple connected to the controller was installed at P4 (as shown in Figure 11-17(a)), and another thermocouple was inserted into P1-P3 for an evaluation of thermo-uniformity at the same depth of the furnace. As shown in Table 11-1, the temperature variation at the three monitored points was generally within 6 ℃, which is good enough for such a big double-layer furnace. The difference between the reading of the test probe and the set temperature was caused by the vertical thermal gradient, which was expected.

Table 11-1. Temperature reading at P1-P3 at the same depth in the furnace.

Measurement	P1	P2	P3
Set at 600 ℃	584 ℃	582 ℃	578 ℃
Set at 800 ℃	782 ℃	780 ℃	777 ℃

11.6 Fiber installation

To fit in the 10’ long Inconel tube, the sensing fiber inserted was de-coated by ~9.5’ long, leaving 0.25’ coated sections on both ends to provide additional mechanical support. Both ends were left free to allow fiber sliding due to CTE mismatch between the tubing and the fiber.

Figure 11-18 shows a horizontal groove carved around the outer wall of the inner furnace layer to help positioning the packaged sensing fiber at the designed location, where the temperature is monitored by the controller. According to the heating element design of the furnace, the temperature distribution along the groove should be nearly identical.

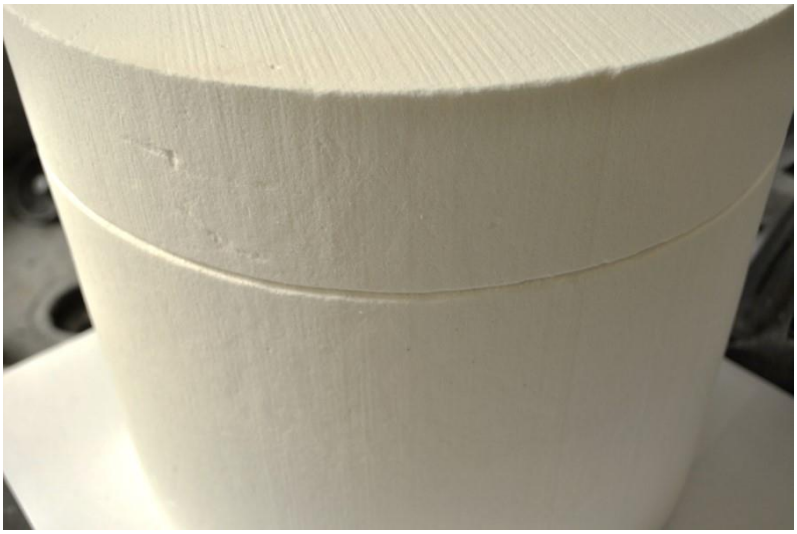

Figure 11-18. Sensor positioning groove carved on the inner insulation layer.

Due to the CTE mismatch between the Inconel alloy and the insulation ceramic, the packaging tube need to be fixed on in the groove to avoid movement as the furnace heats up. In the first attempt, ceramic adhesive was used to bond the tube to the insulation layer. However, due to the porous structure and weak mechanical strength of the insulation material, the adhesive peeled off from the insulation wall after air dry (Figure 11-19).

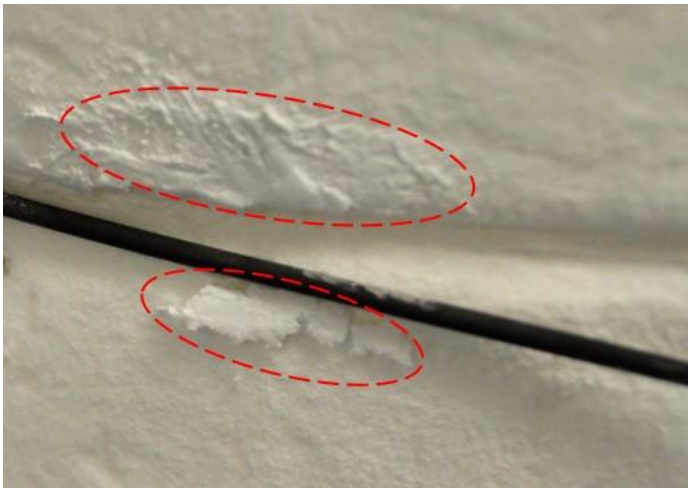

Figure 11-19. Ceramic adhesive peeled off when attempting to bond the Inconel tube onto the thermal insulation wall.

To hold the tube firmly on the furnace wall, holes were drilled on the insulation layer for staple shaped fixtures. Thermal wires were used to make the fixtures, assuring strength at high temperature. Ceramic tubes were inserted as sleeves to avoid collapsing at the contact point of the metal wire and the insulation layer, as shown in Figure 11-20 (a). With this method, the Inconel tube could be tightly mounted in the groove (Figure 11-20 (b)).

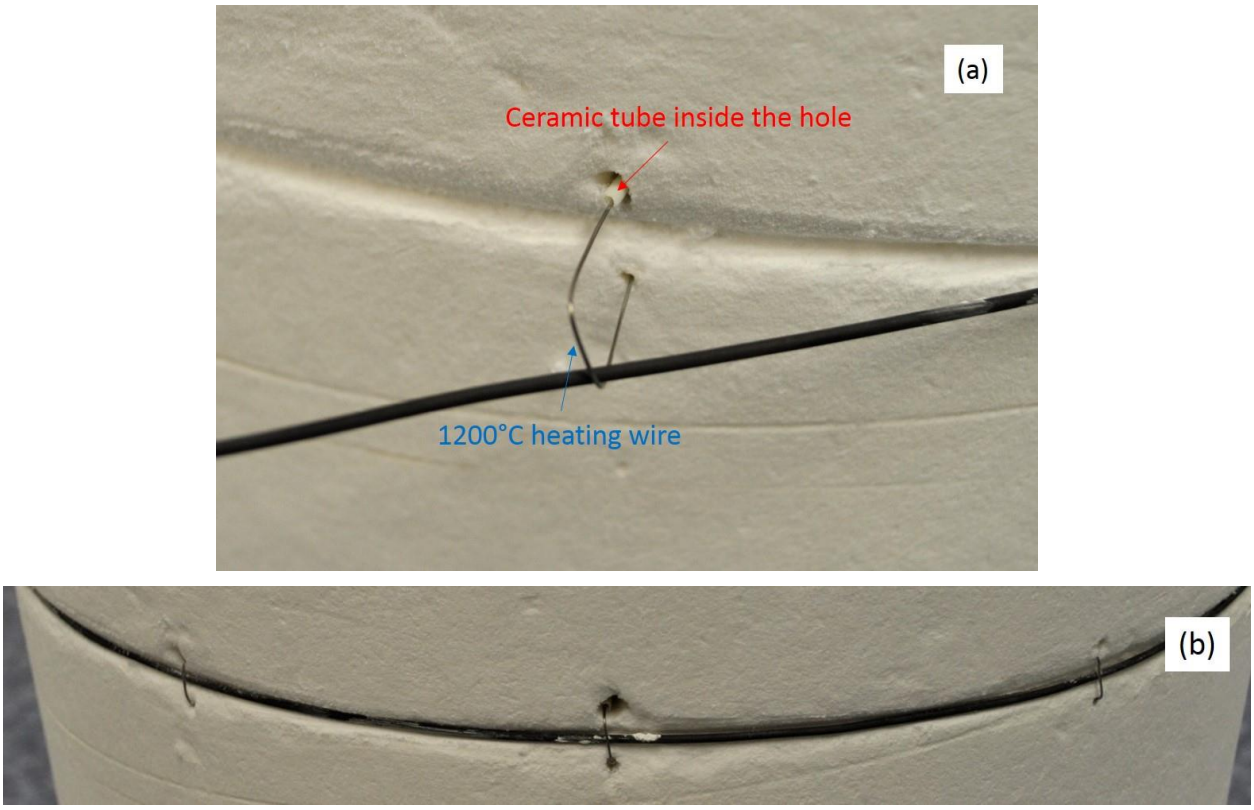

Figure 11-20. Inconel tube mounting on the thermal insulation layer.

In the first thermal test, the 1.125mm ID Inconel tube was pre-coiled before installation in the furnace. As shown in Figure 11-21, the tube was coiled into two full loops with the same diameter with the OD of the inner insulation layer for easy installation.

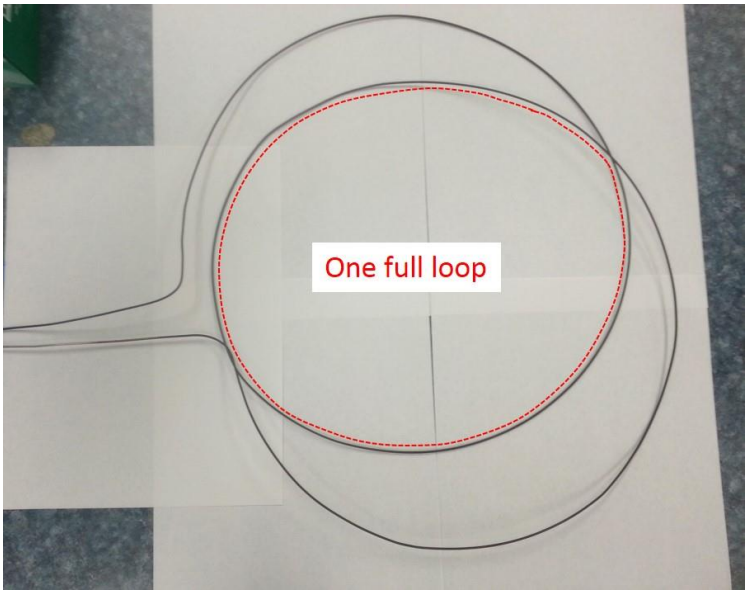

Figure 11-21. Pre-coiled Inconel tube.

Three thermocouple installing holes were drilled on the furnace cover at two diagonal positions (Figure 11-22 (a)): one for the temperature controller, the other two for temperature monitoring and thermal profile measurement respectively. The controlling sensor located at the same height with the sensing fiber to assure precise temperature reading for sensor calibration, while the other two sensors could move vertically to map the vertical thermal profile of the furnace (Figure 11-22 (b) and (c)). A preliminary heating test without fiber showed that when the controller stabilized the furnace at 1000 °, the monitoring thermocouple located at the same height at the diagonal position read a temperature of 994 ℃, indicating good thermal uniformity for such a large furnace with a narrow heating chamber. The green circles in Figure 11-22 shows the position where the Inconel tube run into the furnace.

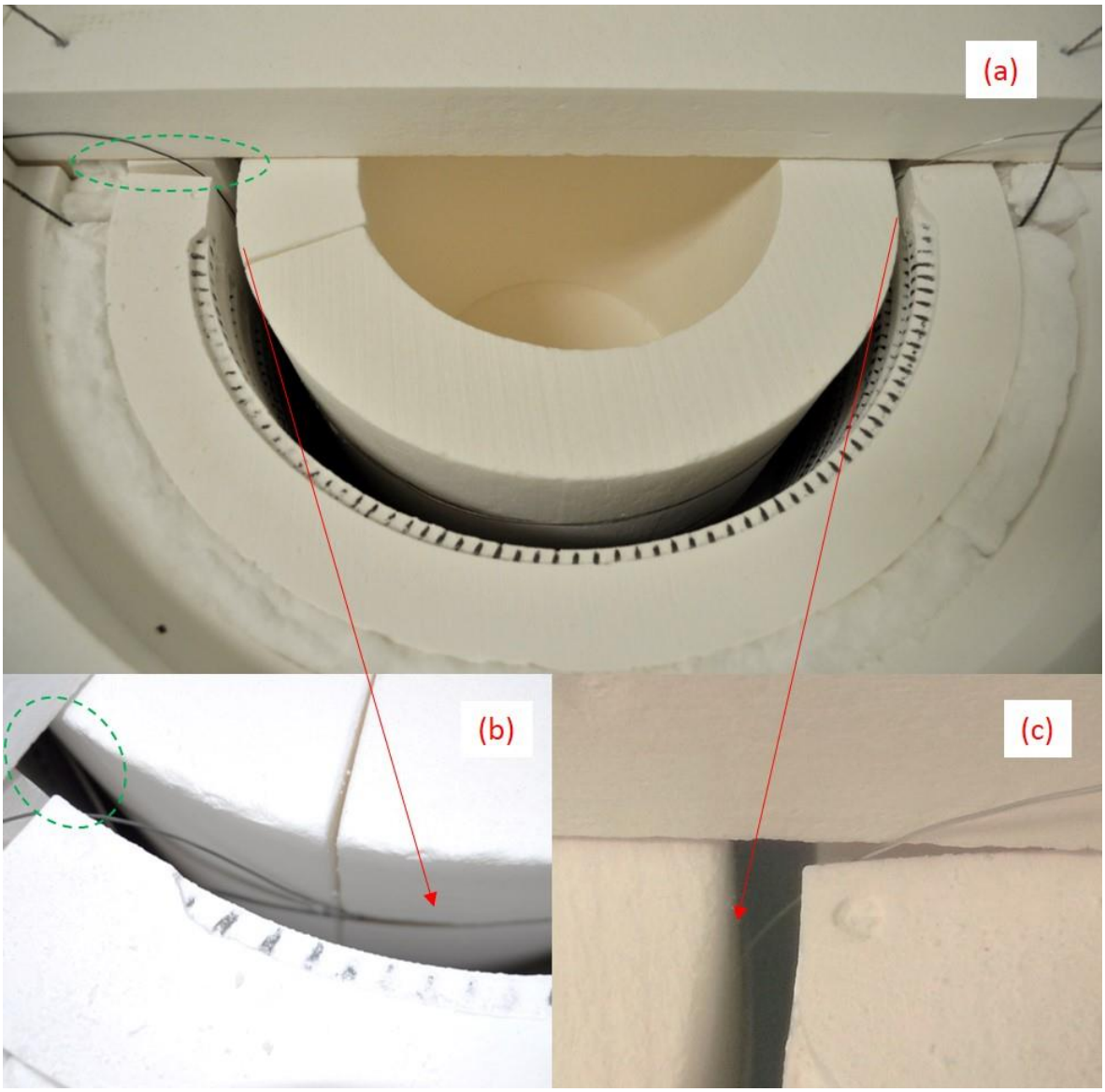

Figure 11-22. (a) Thermal couple installation overview; (b) controlling thermal couple; (c) monitoring thermal couple.

11.7 Furnace thermal profile mapping

A measurement of the furnace thermal profile was conducted during the 4.25 mm ID protecting tube annealing test. Since the tube runs through the joint of the two half-circle heating plates, a small gap was left on the furnace wall, forming a low temperature region in the heating chamber. Two sets of temperature measurements were conducted at diagonal locations with seven depths each, as shown in Figure 11-23. Probe 1 and Probe 2 correspond to the thermocouple inserting holes near and away from the gap on the insulation layer. The temperature shown in Figure 11-23 were measured when the controller stabilized the furnace at 970 ℃.

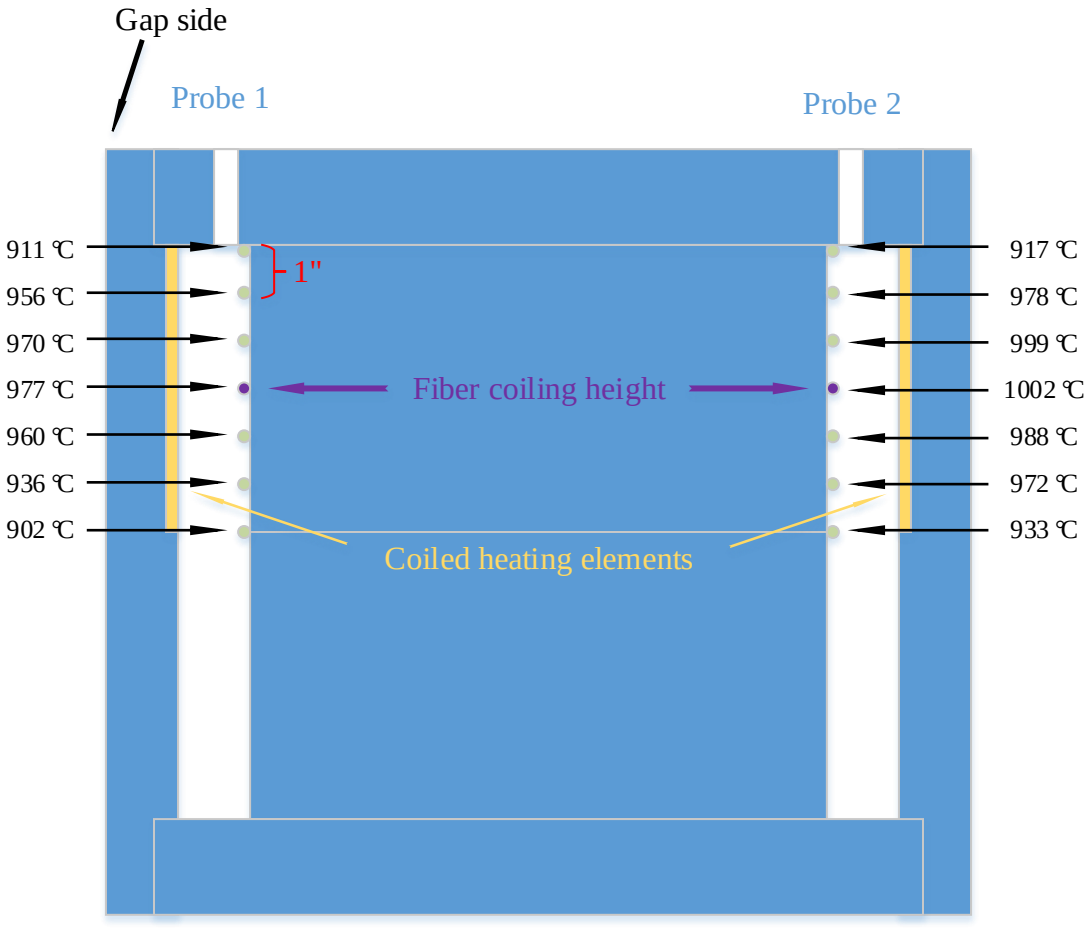

Figure 11-23. Furnace vertical thermal profile measurement.

The complete temperature distribution data during the furnace heating up is shown in Table 11-2 and Table 11-3. Since the controller thermal couple was installed near the gap, the readings on Probe 2 were ~30 ℃ higher than the set value when the temperature was above 900 ℃.

Table 11-2. Temperature distribution measured by Probe 1. Positions 1-7 corresponds to the vertical positions from high to low.

Controlling thermocouple \ Positions	1	2	3	4	5	6	7
100	90	98	99	100	95	87	77

200	177	196	200	199	188	165	131
300	265	294	301	299	287	257	209
400	362	397	403	401	384	352	308
500	458	493	505	504	485	451	411
600	548	591	605	604	588	555	511
700	641	687	703	705	688	655	619
800	732	789	804	805	789	760	725
900	846	884	902	906	890	863	833
970	911	956	970	977	960	936	902

Table 11-3. Temperature distribution measured by Probe 2. Positions 1-7 corresponds to the vertical positions from high to low.

Controlling thermocouple \ Positions	1	2	3	4	5	6	7
100	90	99	101	100	95	87	76
200	175	201	201	199	189	166	134
300	267	303	309	305	288	261	215
400	365	406	417	412	397	367	322
500	464	512	526	524	505	481	448
600	560	609	627	628	613	587	548
700	681	711	732	730	716	691	658
800	754	811	829	830	815	798	761
900	851	905	924	928	916	899	868
970	917	978	999	1002	988	972	933

At higher temperatures, a 20℃ temperature difference between the two monitored spots was observed due to the existence of the gap. Since the packaged fiber sensor was embedded on the inner layer of the furnace, which is hollow and thus allows the temperature to distribute more homogeneously, the temperature uniformity along the fiber coil is expected to be better than this measured result.

11.8 Conclusion

In this chapter, a customized instrument was designed and built to simulate the working condition in a coal-gasifier. Preliminary tests demonstrates the capability of the system of generating high temperature environment up to 1000℃ in the heating chamber. A temperature gradient could also be produced along vertical direction for the purpose of simulating the temperature feature of a hot spot. A fiber sensor installation technique in the furnace was also developed. This system will be used to evaluate the performance of the sensing system with packaged fiber sensors.

12 Sensing system test in gasifier simulation system

In this chapter, the sensing system was tested in the simulation system introduced in the former chapter.

12.1 High Temperature test with 1.125mm ID Inconel tube packaging

In the first test, the packaged sensing fiber was looped in the testing chamber for two full loops (as shown in Figure 11-21). The fiber survivability was tested with a power meter as the furnace heated up. Figure 12-1 shows the fiber transmission vs temperature as the temperature raised from 700 ℃ to 1000 ℃, while 50 ℃ steps were taken and on each step the temperature was held for 1 hour. After reaching 1000 ℃, the temperature was kept and the fiber was tested for 24 hours continuously. The loss recorded was negligible (less than 0.1dB) during the annealing procedure.

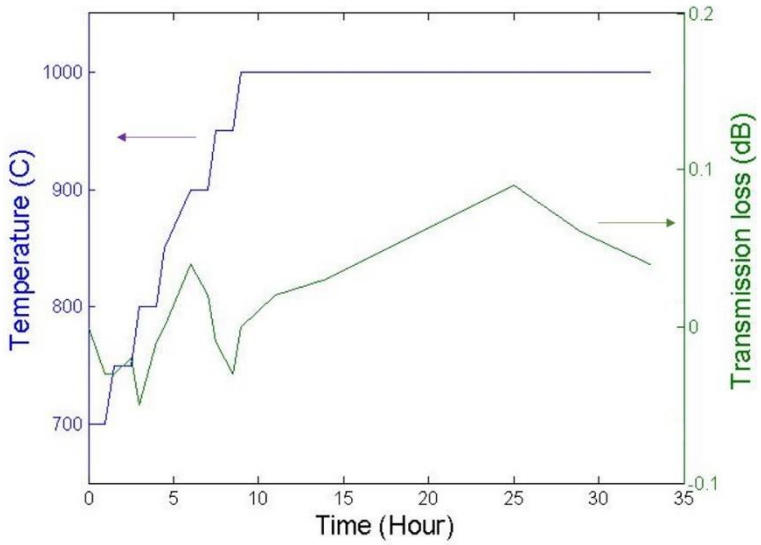

Figure 12-1. Recorded fiber transmission loss vs temperature with 1.125 mm ID Inconel tube packaging.

However, as the furnace begun to cool down, the transmission of the fiber dropped rapidly. When the temperature reached 900 ℃, the loss in the fiber increased to 41.8 dB, indicating that the fiber was practically broken.

The tube and the fiber was then disassembled from the furnace for failure analysis. During the retrieving of the fiber, it broke on both ends of the coiled section (Figure 12-2 (a)). At one of the breaking points, a curve was observed without any extrinsic stress (Figure 12-2 (b)). Considering the tube installation layout (Figure 12-3), it can be inferred that the curve and the breaking point corresponded to positions near the sharp bending of the tube, which are marked with red circles in Figure 12-3. Since this section is also the beginning of the high temperature region, it is possible that the breakage happens during the fiber retrieving due to the brittleness of the annealed fiber.

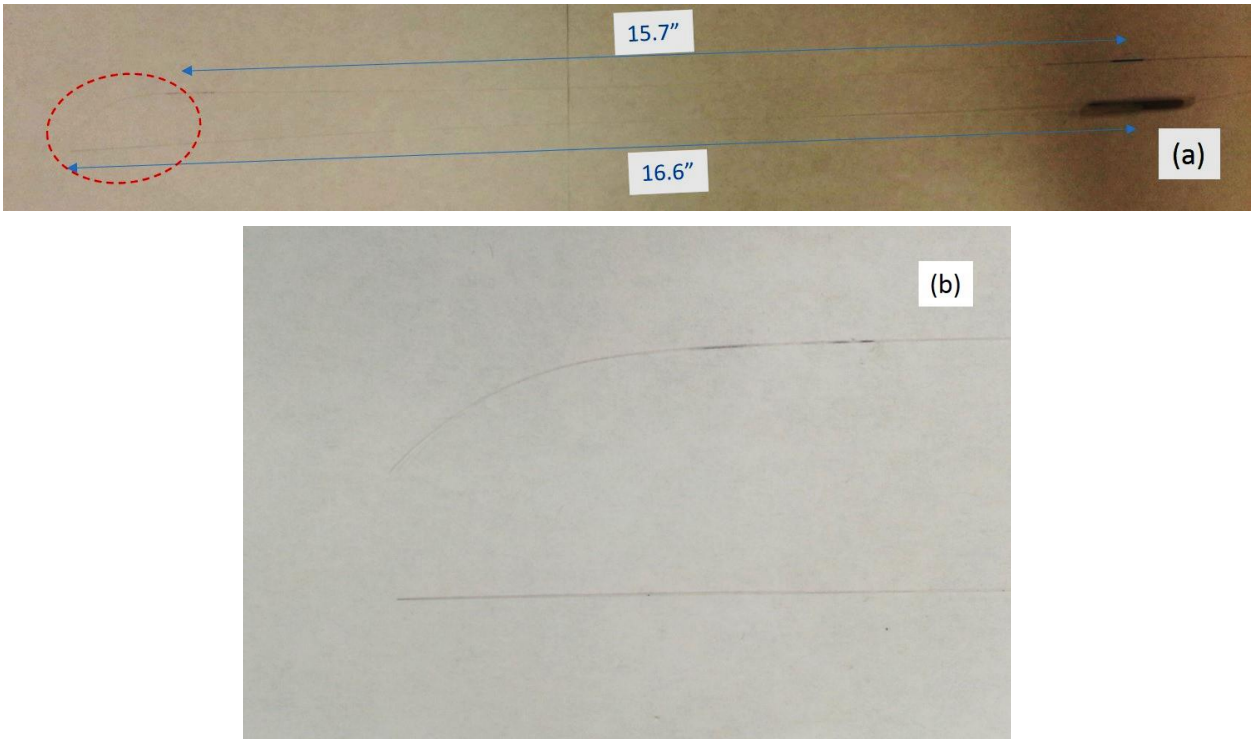

Figure 12-2. Retrieved broken fiber ends.

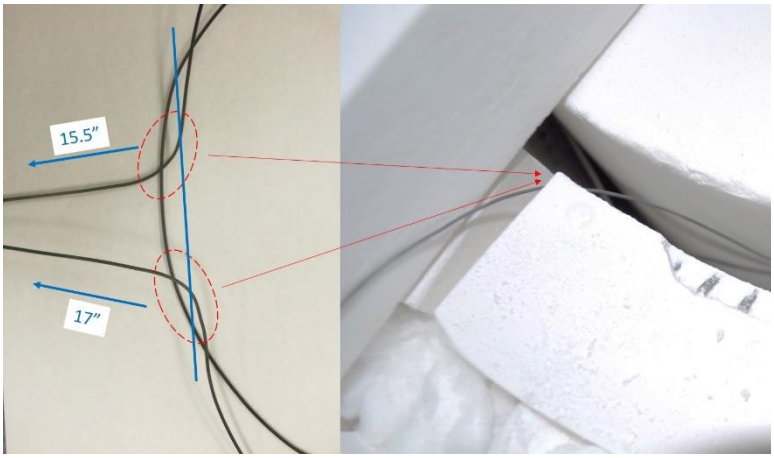

Figure 12-3. Inconel tube bending at the lead-in and lead-out sections.

12.2 Bending-relaxed Inconel tube mounting

To reduce the bending of the tube and the fiber, an improved coiling method was developed. As shown in Figure 12-4, the bending at the lead-in and lead-out sections was made into two relatively mild curves, leaving about 0.7 m of fiber in the high temperature section. The fiber was left loose in the tube and free at both ends to relax the stress caused by CTE mismatch.

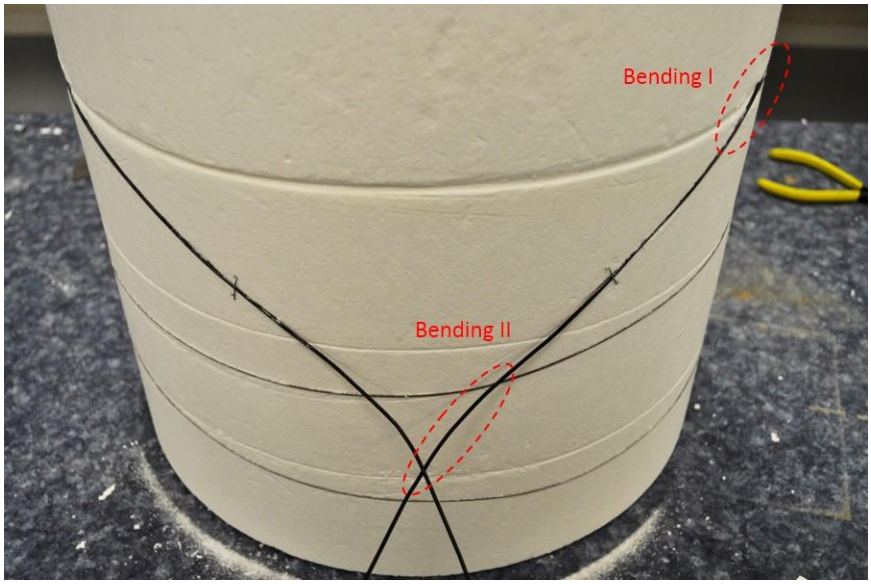

Figure 12-4. Bending-relaxed tube coiling method on the inner insulation wall

Another long-term stability test was conducted with the improved coiling method. The protected fiber was tested at 1000 ℃ for 24 hours and no additional loss was recorded. However, fiber failure occurred during the cooling down procedure again. The retrieved fiber shows a breakage at the position marked as Bending I in Figure 12-4, which is the beginning of the high temperature region.

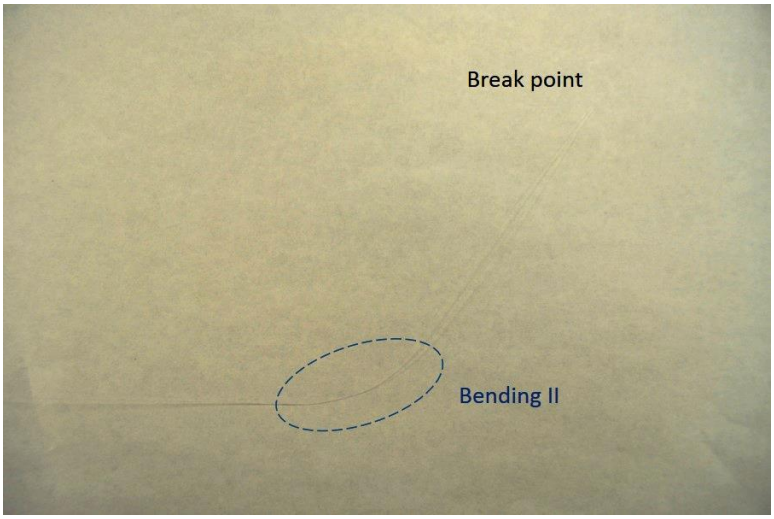

Figure 12-5. Fiber breaking position in modified coiling method.

The results of the two survivability tests indicate that the breakage of the fiber is more related to the temperature instead of fiber bending. It agreed with our former results that fiber coils with only 10 cm diameter can survive 1000 ℃ long term annealing tests without breaking. It was also demonstrated that silica fibers becomes so brittle after 1000 ℃ annealing that any additional internal or external force could easily break them. From the results shown above, the breakage is obviously a result of external force applied on the fiber in the cooling down process.

The major external force applied to the fiber during cooling down is from the packaging tube, caused by the large thermal expansion mismatch between Inconel alloy and silica fiber. When the packaged sensor was heated up, the tube expands much more than the fiber does. As shown in Figure 12-6, the simplified model of this procedure indicates that the fiber should be deployed along the outer ring in the tube at room temperature (Figure 12-6 (a)) to minimize the effect of the tube expansion. However, if the tube diameter *d* is not large enough to compensate the tube expansion, the fiber will still be stretched as the temperature raises. In this case, fiber will be pulled into the tube from both ends. During the temperature ramp up, the fiber still have enough flexibility and strength to adapt the shape change of the tube; however, in the cooling down process, after being annealed at 1000 ℃, the hardened brittle fiber does not have enough flexibility to follow the shrinking of the tube, and breaks as the tube touches and applies force on it.

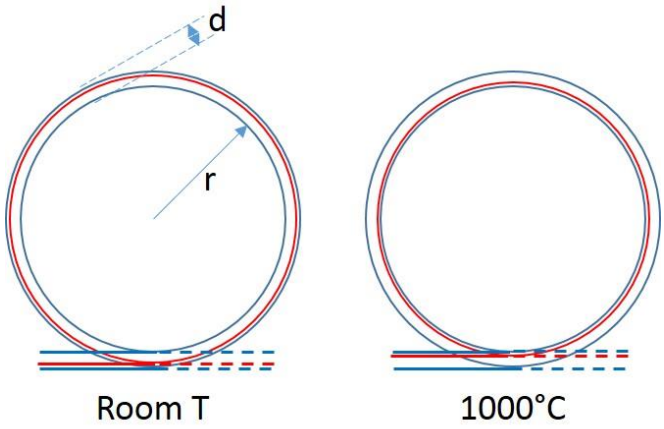

(a) (b)

Figure 12-6. Simplified thermal expansion model of the Inconel tube with fiber.

Based on the CTE data of Inconel alloy and silica fiber, it can be calculated that the tube will expand ~13 mm more than the fiber within one loop. Considering the circled shape of the loop, the tube ID (*d* in Figure 12-6 (a)) should be at least ~2 mm when the fiber is coiled along the outer circle (Figure 12-6 (a)) at room temperature to avoid stretching at high temperature (Figure 12-6 (b)).

12.3 Fiber test in 4.25mm ID tube

Based on the estimation in the former section, we used a new Inconel tube with 4.25 mm ID as the new packaging material. The additional margin of the tube ID was designed to compensate the space loss during the tube coiling, and the non-perfect fiber positioning in the tube. The tube coiling method was the same as shown in Figure 12-4.

The distributed sensing system was connected to the heated fiber during this test to monitor the temperature response. The furnace was kept at 1000 ℃ for 36 hours, and the Brillouin signal recorded is shown in Figure 12-7. The span of Brillouin frequency shift during the test corresponds to a temperature change of ~30 ℃. Since the actual temperature fluctuation of the furnace is much lower, this shift is recognized as a result the external stress applied on the fiber.

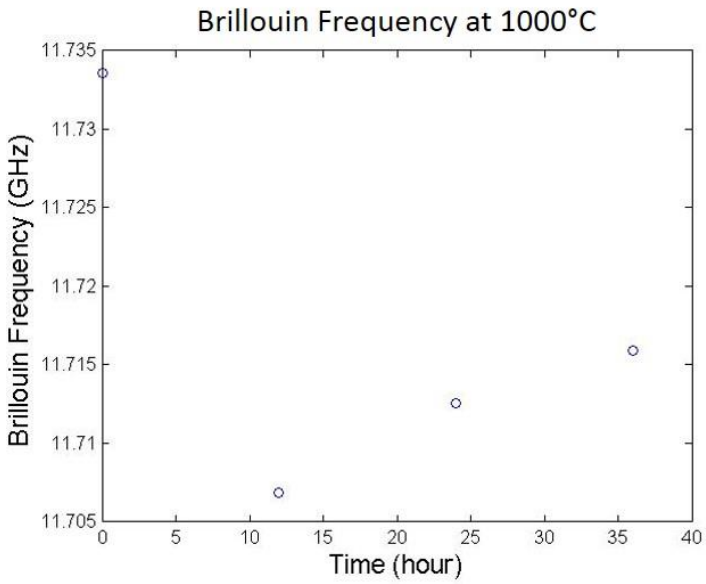

Figure 12-7. Brillouin frequency shift of a fiber protected in a 4.25mm ID Inconel tube kept at 1000 ℃.

During the cooling process, the fiber was recorded to break at the temperature of between 700 and 800 ℃. The inspection of the retrieved fiber showed breaking point positions identical with the former result shown in Figure 12-5. Comparing to the former record of breaking at 900 ℃, the new packaging showed limited improvement on fiber survivability.

In the second experiment, the SMF28 sensing fiber was loosely coiled in an Inconel tube with the ID of 4.25mm. Four thermal cycles were performed with all starting and ending temperatures set at 500 ℃, and kept at annealing temperatures of 750 ℃, 800 ℃, 850 ℃, and 900 ℃ respectively for 24 hours. The fiber transmission and the temperature were recorded through all thermal cycles, as shown in Figure 12-8.

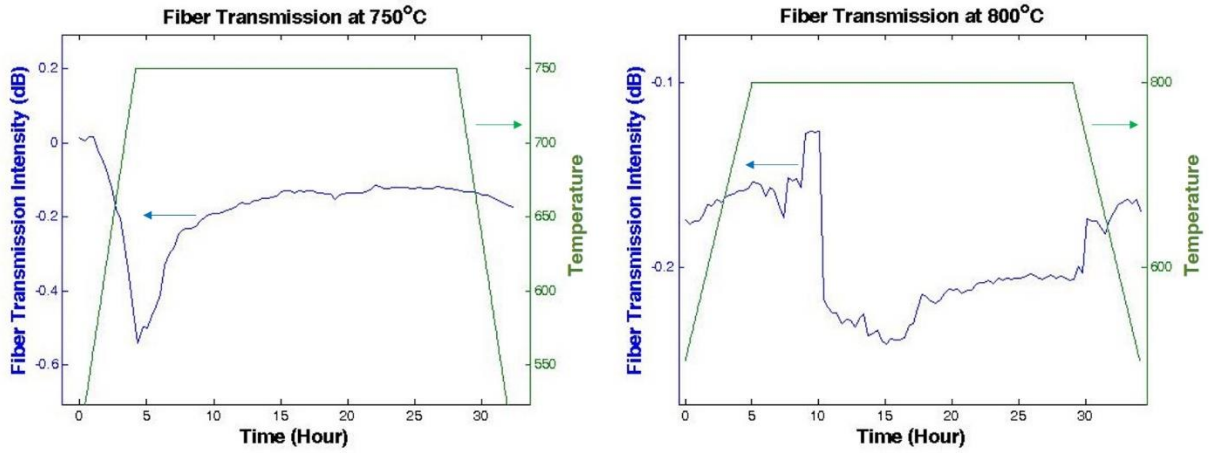

(a) (b)

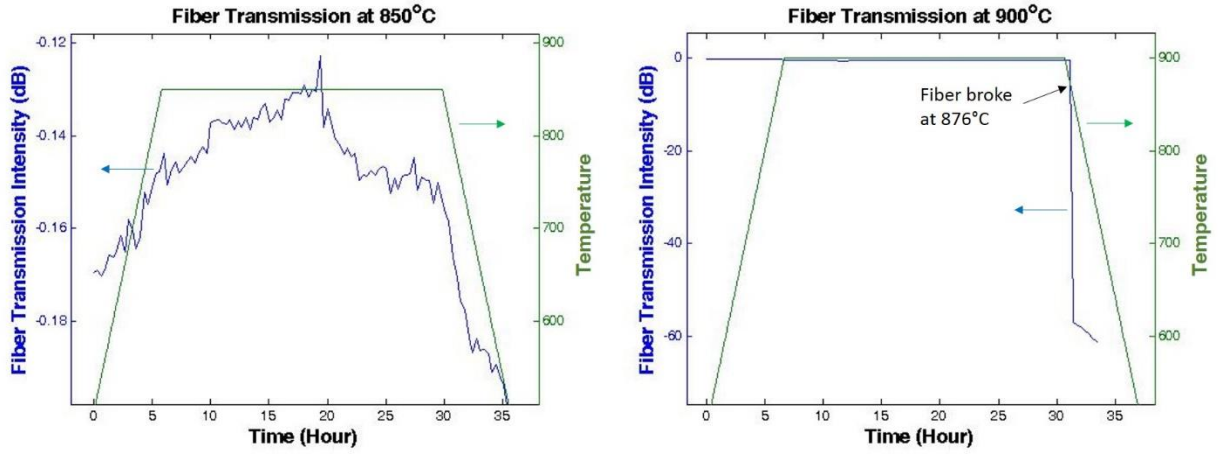

(c) (d)

Figure 12-8. Recorded transmission of the curved sensing fiber with Inconel tube packaging during 4 annealing cycles up to (a) 750 ℃, (b) 800 ℃, (c) 850 ℃ and (d) 900 ℃. Fiber failure was observed during the cooling process of the 900 ℃ annealing cycle

Minor loss change was observed during the first three annealing cycles. In the fourth test of 900 ℃, sudden fiber failure was observed at 876 ℃ on the cooling ramp, which agrees with our former test results. The temperature 900 ℃ is also where bare fiber becomes vulnerable to internal stress as presented in the former reports. Based on this result, it can be concluded that even with the coiled geometry and CTE mismatch presenting, the packaged sensing fiber could still be repeatedly used up to 850 ℃.

12.4 Fiber survivability without protection

In order to prove our speculation that the thermal expansion of the Inconel tubes was the cause of the fiber failures, another set of experiments were conducted using a bare sensing fiber without alloy tube packaging. As shown in Figure 12-9, the bare silica fiber was carefully installed in the v-groove machined on the outer surface of the furnace inner layer. Metal staples made of heating wire was used to fix the fiber on the refractory material.

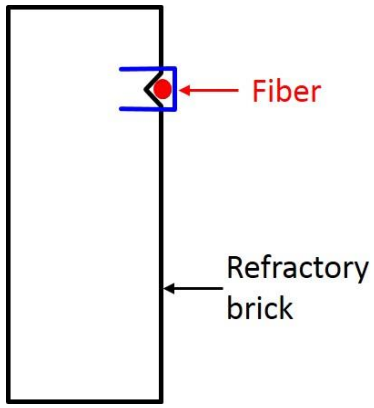

Figure 12-9. Bare sensing fiber mounting on the inner refractory wall.

To simulate the thermal profile of a hot spot on the coal-gasifier wall, the sensing fiber was coiled in a special pattern in the heated chamber. As shown in Figure 12-10, one loop of sensing fiber (112 cm) was coiled in the hot zone, while two loops were installed in the cool zone. Between the hot and cool segments, a transition region of about half loop (60 cm) were coiled on each side. A monitoring thermocouple that could move between the hot zone and the cool zone fiber was used to record the actual temperatures at these positions. The total length of the sensing fiber was 550 m, with the rest of the sensing fiber spooled in room temperature.

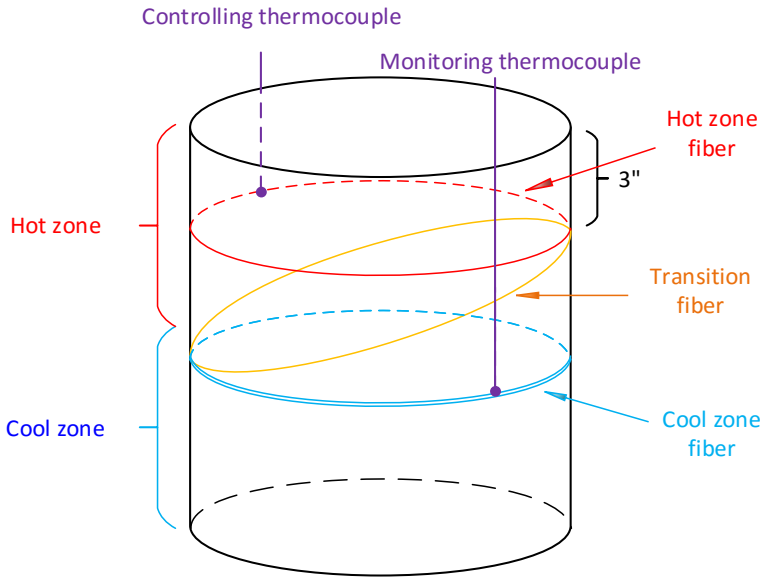

Figure 12-10. Sensing fiber installation geometry in the hot spot simulation test.

When the furnace stabilizes at 1000 ℃, the temperature measured in the hot and cool zones were 1000 ℃ and 938 ℃ respectively. As shown in the recorded Brillouin signal (Figure 12-11), the unheated sections of the sensing fiber presents as a clean and flat background, while the heated section stands out as a sharp peak. By zooming in at the heated section, the pattern of the hot spot is clearly shown. All five of the hot, cool and transition sections can be easily distinguished, as marked on Figure 12-11 (b).

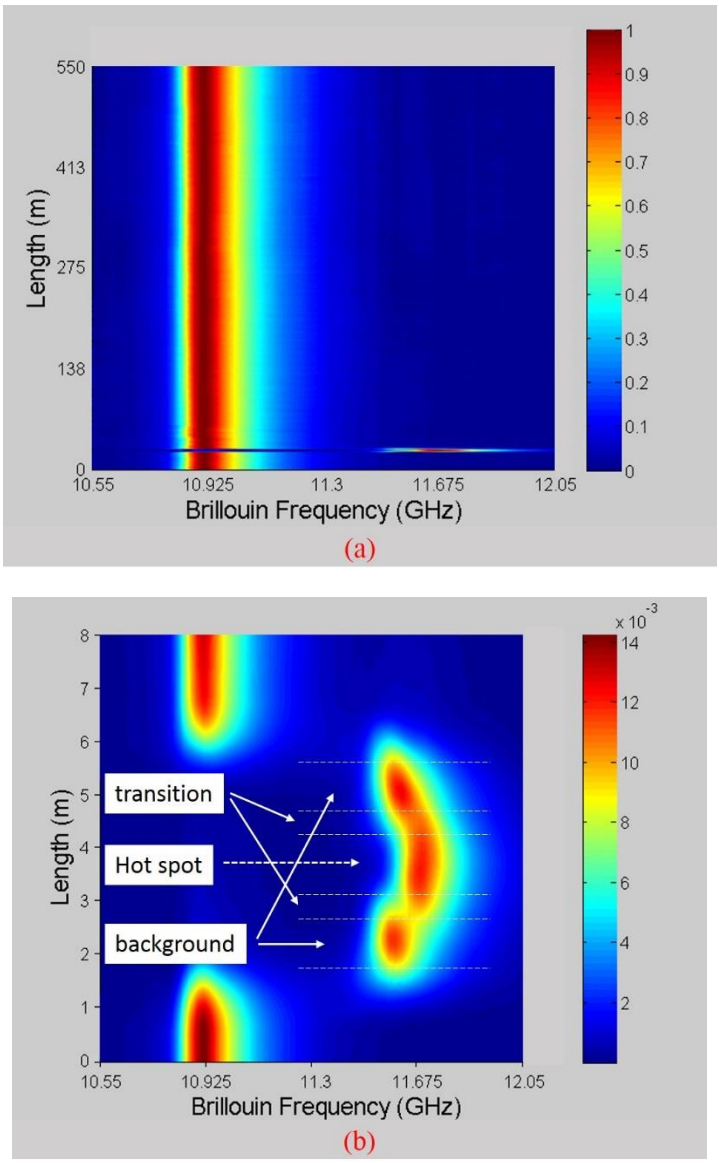

Figure 12-11. (a) Recorded Brillouin signal along the entire 550 m silica fiber with a ~3 m section heated in the furnace; (b) zoomed in view at the heated section, showing the temperature pattern of the simulated hot spot

To test the survivability of the bare fiber, two annealing cycles up to 1000 ℃ were conducted. The loss curves of the annealed fiber section during these tests are shown in Figure 12-12. It can be seen that the fiber loss increased slightly (~0.6 dB) during the first annealing, and held stable through the second annealing, which is well acceptable considering the extreme testing conditions. After the two annealing cycles, a red laser inspection on the retrieved fiber showed no observable leakage within the heated section.

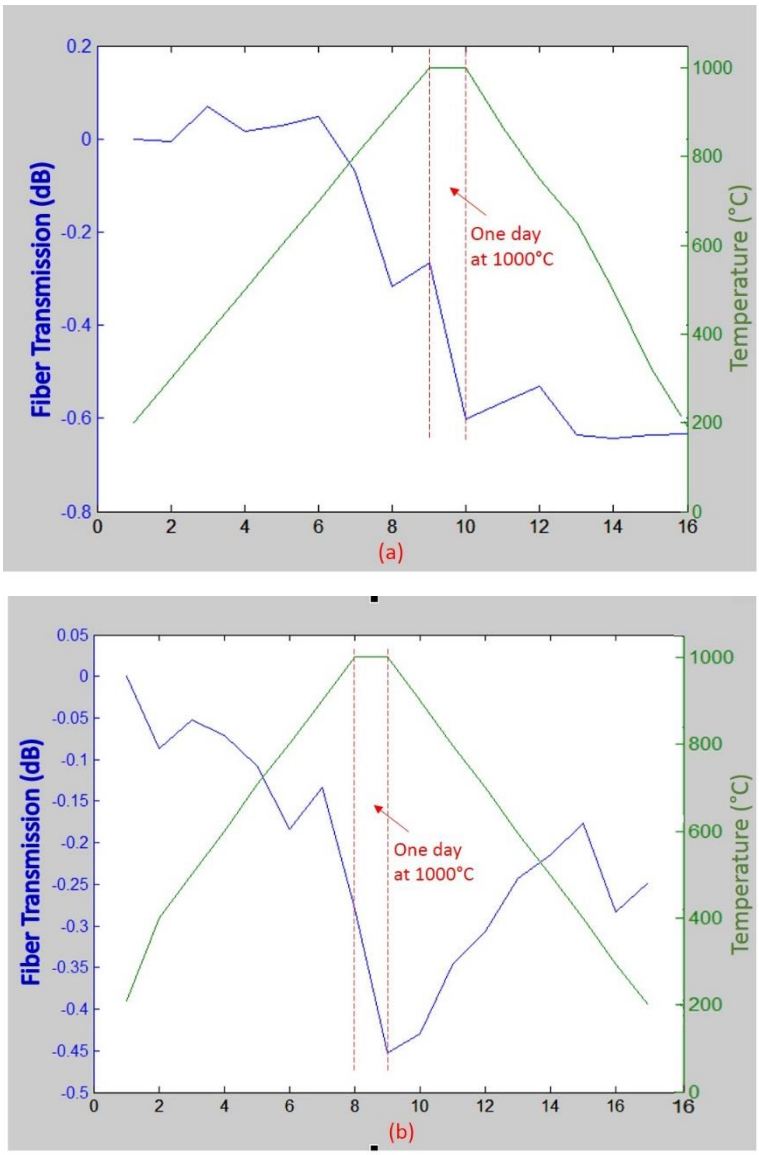

Figure 12-12. Transmission change of a bare sensing fiber during the (a) first and (b) second 1000 ℃ annealing cycle (data points along x-axis are not scaled to time).

The minor loss change agrees with our former results of the straight bare fiber annealing tests. From these data we conclude that the bare sensing fiber can be reused up to 1000 ℃ temperature, straight or curved. Based on these results, we believe that satisfying fiber survivability can be achieved in real coal-gasifier working environment by choosing proper packaging and deploying strategy.

12.5 Conclusion

The sensing system was tested with the gasifier simulation system. The results shows that packaged sensing fibers tend to break during the cooling-down process due to the fragility of the annealed fiber. A sensing demonstration with bare sensing fiber showed the capability of the

system in indicating the detailed features of a hot spot with the size of ~3 meters within a total range of 550m.

13 Potential sensor deploying strategy in coal-gasifiers

Figure 13-1 shows the original design of the sensing fiber deploying strategy on a coal gasifier inner wall, which is similar to the method used in simulation small-scale simulation furnace. Based on the experimental results and analysis in Chapter 12, we believe that the CTE mismatch between continuous Inconel packaging and the fiber is the major cause of fiber failure on the temperature ramp down from 1000 ℃. Besides, we found that the very long one-piece Inconel tubing could introduce more challenges in practice: the insertion and retrieving of sensing fiber into the tube could be difficult, and any repairing will require removing of the entire packaged fiber sensor. Moreover, since the sensing fiber is in one-piece, a breaking point at any position along the fiber will result in the failure of the entire sensing system.

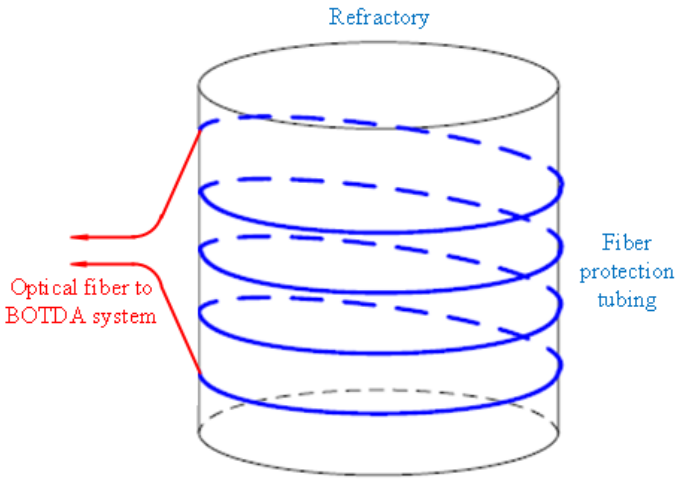

Figure 13-1. Original spiral fiber deploying strategy on a coal gasifier inner wall.

Accordingly, a new fiber deployment strategy was designed to avoid these potential issues. As shown in Figure 13-2, the sensing fiber was divided into segments connecting in the cool zone above and below the chamber, while these effective sensing segments packaged in straight Inconel tubes run vertically along the monitored refractory wall. With this new design, the issues in the original design could potentially be solved: the straight geometry of each tube will allow free slipping between the tube and the fiber, avoiding strain cross-talking during measurements and fiber failure during cooling down; by breaking the long sensor into shorter segments and connect them outside the chamber, the complexity of repairing and replacing of the sensing fiber will be greatly reduced. Although the fiber is placed vertically, according to our experience, they will be held by the friction with the tube wall, therefore the gravity of the fiber will not introduce additional strain in the sensing fiber. In this manner, a single breaking point can be fixed more easily by replacing the corresponding fiber section. The shorter and straight sections are also much easier to handle and install compared to the coiling design.

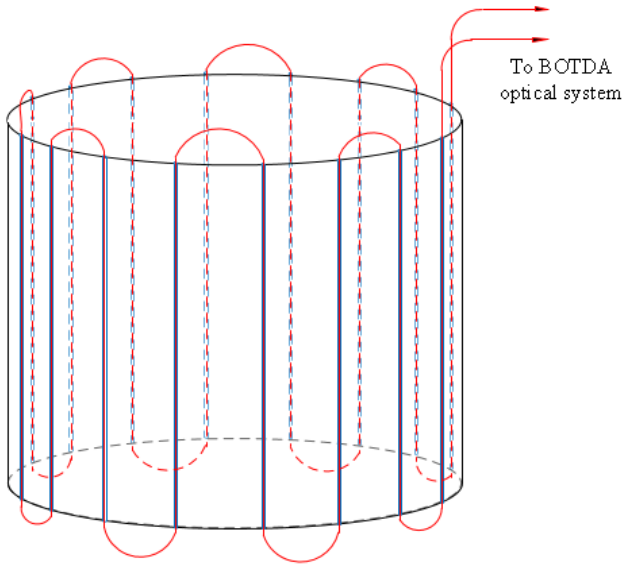

Figure 13-2. New vertical fiber deploying strategy.

To realize the design shown in Figure 13-2, the fiber sections need to be fusion spliced into one piece, which raises another potential issue of splicing loss. The loss of an average splicing point is on the level of 0.1 dB. For a sensor with 100 sections, there will be at least 100 splicing points along the sensing fiber, resulting in a total splicing loss of 10 dB, which is too high for the sensing system.

To solve this issue, an optical switch based scheme is proposed. As shown in Figure 13-3, the sensing fiber is divided into independent sections, and only one section is measured at a time, controlled by an optical switch. In this design, each section is much shorter compared to the fiber sensor in the two former designs, so the signal quality could be significantly higher due to lower fiber loss. In this case, one breaking point on the sensing fiber will affect only one single section, losing a small part of the entire monitored area instead of the entire sensor.

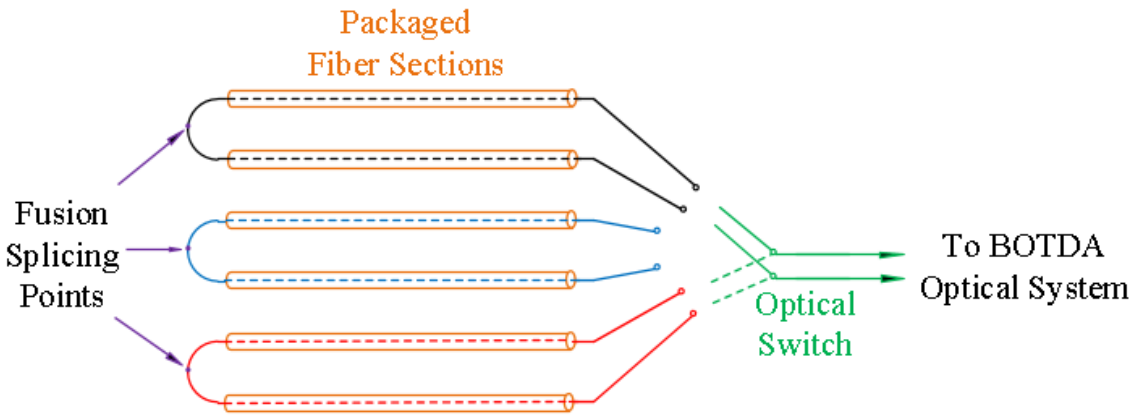

Figure 13-3. Schematic of optical switch based multi-section sensing scheme.

One drawback of the optical switch design is the reduced system response speed. Since the number of frequency scanning steps is defined by the temperature measurement range, the time

needed for a single temperature measurement of the system is basically the same for one section in the optical switch based design and in a single fiber sensor design. At the same time, given the higher signal quality, the number of average needed in the optical switch design can be fewer than the single-fiber schemes. Therefore, considering the switching time of the optical switch, the total measurement time will be roughly *n* times of the single fiber design, where *n* is the number of the fiber sections. Considering the low response speed requirement of this application, we believe this tradeoff of measurement speed for all the benefits discussed above is totally acceptable.

14 Conclusion

In this four-year project, we have developed and demonstrated a harsh environment distributed fiber sensing technology for coal gasifier refractory health monitoring. Several different sensing mechanisms were investigated, of which the Brillouin scattering based sensing scheme shows the best performance in laboratory tests. A complete bench-top sensing system based on the BOTDA technology was built, and the performance of the system was optimized for best spatial and temperature resolutions. In the high temperature tests, the SMF-28 single mode fiber sensors offered good performance and survivability under the temperature of 850 ℃, but showed significant mechanical strength weakening and slow Brillouin frequency drift when annealed at higher temperatures. Significant efforts were undertaken in overcoming these issues, including the development of a special fiber packaging technique and the study on the mechanism of the Brillouin frequency drift. To test and optimize the performance of the sensing system in the working condition of a coal-gasifier, a cylindrical furnace was designed and built to simulate coal gasifier high temperature environment. The sensing system was then tested with packaged and unpackaged sensing fibers installed in the testing environment. The spatial and temperature resolutions of the system were tested and determined, while the sensor failures were observed during the cooling down process after long-term high-temperature tests. Based on the observation, a sensor installation strategy in a coal-gasifier was proposed to achieve best sensor performance and survivability at high temperatures.

Bibliography

[1] M. R. Gary J. Stiegel, Howard G. McIlvried, "Integrated Coal Gasification Combined Cycle (IGCC)," in *The Gas Turbine Handbook*. vol. DOE/NETL-2006-1230, ed: U.S. Department of Energy, Office of Fossil Energy, National Energy Technology Laboratory, 2006.

[2] B. Chorpening, D. Tucker, and S. Maley, "Sensors applications in 21st century fossil-fuel based power generation," in *Sensors, 2004. Proceedings of IEEE*, 2004, pp. 1153-1156.

[3] S. J. Clayton, G. J. Stiegel, and J. G. Wimer, *Gasification technologies: Gasification markets and technologies-Present and future: An industry perspective*: US Department of Energy, 2002.

[4] K.-S. Kwong, J. Bennett, C. Powell, and R. Krabbe, "The improvement of slagging gasifier refractories," *Ceramic Transactions*, vol. 180, 2006.

[5] W. Bakker, "Materials guidelines for gasification plants," *EPRI, Palo Alto, CA*, 1998.

[6] S. Chakraborty, S. Sarkar, S. Gupta, and A. Ray, "Damage monitoring of refractory wall in a generic entrained-bed slagging gasification system," *Proceedings of the Institution of Mechanical Engineers, Part A: Journal of Power and Energy*, vol. 222, pp. 791-807, 2008.

[7] J. McDaniel and M. Hornick, "Tampa Electric Polk Power Station integrated gasification combined cycle project," *Prepared by Tampa Electric Company for The US Department of Energy*, 2002.

[8] K. L. Cooper, A. Wang, and G. R. Pickrell, "Optical Fiber High Temperature Sensor Instrumentation for Energy Intensive Industries," Virginia Polytechnic Institute and State University, Blacksburg, VA2006.

[9] Y. Zhu, Z. Huang, F. Shen, and A. Wang, "Sapphire-fiber-based white-light interferometric sensor for high-temperature measurements," *Optics letters*, vol. 30, pp. 711-713, 2005.

[10] R. Kashyap, *Fiber bragg gratings*: Academic press, 1999.

[11] J. Juergens, G. Adamovsky, R. Bhatt, G. Morscher, and B. Floyd, "Thermal evaluation of fiber Bragg gratings at extreme temperatures," in *43rd AIAA Aerospace Science Meeting and Exhibit, Reno, NV*, 2005.

[12] D. Grobnic, C. W. Smelser, S. J. Mihailov, and R. B. Walker, "Long-term thermal stability tests at 1000 C of silica fibre Bragg gratings made with ultrafast laser radiation," *Measurement Science and Technology*, vol. 17, p. 1009, 2006.

[13] C. M. Jewart, Q. Wang, J. Canning, D. Grobnic, S. J. Mihailov, and K. P. Chen, "Ultrafast femtosecond-laser-induced fiber Bragg gratings in air-hole microstructured fibers for high-temperature pressure sensing," *Optics letters*, vol. 35, pp. 1443-1445, 2010.

[14] W. W. Morey, G. Meltz, and J. M. Weiss, "High-temperature capabilities and limitations of fiber grating sensors," in *10th Optical Fibre Sensors Conference*, 1994, pp. 234-237.

[15] O. Frazao, J. L. Santos, F. M. Araújo, and L. A. Ferreira, "Optical sensing with photonic crystal fibers," *Laser & Photonics Reviews*, vol. 2, pp. 449-459, 2008.

[16] C. Martelli, J. Canning, N. Groothoff, and K. Lyytikainen, "Strain and temperature characterization of photonic crystal fiber Bragg gratings," *Optics letters*, vol. 30, pp. 1785-1787, 2005.

[17] M. A. Soto, A. Signorini, T. Nannipieri, S. Faralli, and G. Bolognini, "High-Performance Raman-Based Distributed Fiber-Optic Sensing Under a Loop Scheme Using Anti-Stokes Light Only," *Ieee Photonics Technology Letters*, vol. 23, pp. 534-536, May 1 2011.

[18] X.-H. Jia, Y.-J. Rao, K. Deng, Z.-X. Yang, L. Chang, C. Zhang, *et al.*, "Experimental Demonstration on 2.5-m Spatial Resolution and 1 degrees C Temperature Uncertainty Over Long-Distance BOTDA With Combined Raman Amplification and Optical Pulse Coding," *Ieee Photonics Technology Letters*, vol. 23, pp. 435-437, Apr 1 2011.

[19] Q. Cui, S. Pamukcu, A. Lin, W. Xiao, D. Herr, J. Toulouse, *et al.*, "Distributed Temperature Sensing System Based on Rayleigh Scattering BOTDA," *Ieee Sensors Journal*, vol. 11, pp. 399-403, Feb 2011.

[20] R. R. J. Maier, W. N. MacPherson, J. S. Barton, S. McCulloch, and B. J. S. Jones, "Distributed sensing using Rayleigh scatter in polarization-maintaining fibres for transverse load sensing," *Measurement Science & Technology*, vol. 21, Sep 2010.

[21] M. A. Soto, G. Bolognini, and F. Di Pasquale, "Optimization of long-range BOTDA sensors with high resolution using first-order bi-directional Raman amplification," *Opt. Express*, vol. 19, pp. 4444-4457, 2011.

[22] A. Guemes, A. Fernandez-Lopez, and B. Soller, "Optical Fiber Distributed Sensing - Physical Principles and Applications," *Structural Health Monitoring-an International Journal*, vol. 9, pp. 233-245, May 2010.

[23] A. K. Sang, M. E. Froggatt, D. K. Gifford, S. T. Kreger, and B. D. Dickerson, "One centimeter spatial resolution temperature measurements in a nuclear reactor using Rayleigh scatter in optical fiber," *Ieee Sensors Journal*, vol. 8, pp. 1375-1380, Jul-Aug 2008.

[24] J. P. Dakin, "Distributed optical fiber sensors," *Bellingham: SPIE*, pp. 284-311, 1995.

[25] X. Y. Bao, M. DeMerchant, A. Brown, and T. Bremner, "Tensile and compressive strain measurement in the lab and field with the distributed Brillouin scattering sensor," *Journal of Lightwave Technology*, vol. 19, pp. 1698-1704, Nov 2001.

[26] S. M. Maughan, H. H. Kee, and T. P. Newson, "Simultaneous distributed fibre temperature and strain sensor using microwave coherent detection of spontaneous Brillouin backscatter," *Measurement Science & Technology*, vol. 12, pp. 834-842, Jul 2001.

[27] H. Ohno, H. Naruse, M. Kihara, and A. Shimada, "Industrial applications of the BOTDR optical fiber strain sensor," *Optical Fiber Technology*, vol. 7, pp. 45-64, Jan 2001.

[28] J. Dakin, D. Pratt, C. Edge, M. Goodwin, and I. Bennion, "A distributed fibre temperature sensor using the optical Kerr effect," 1987, pp. 149-156.

[29] K. T. V. Grattan and B. T. Meggitt, "Optical Fiber Sensor Technology," pp. 260-261, 2000.

[30] D. Kumar, S. Sengupta, and S. K. Ghorai, "Distributed strain measurement using modal interference in a birefringent optical fiber," *Measurement Science & Technology*, vol. 19, Jun 2008.

[31] C. Crunelle, M. Legre, M. Wuilpart, P. Megret, and N. Gisin, "Distributed Temperature Sensor Interrogator Based on Polarization-Sensitive Reflectometry," *Ieee Sensors Journal*, vol. 9, pp. 1125-1129, Sep 2009.

[32] F. Parvaneh, M. Farhadiroushan, V. A. Handerek, and A. J. Rogers, "High-resolution optical-fibre distributed temperature sensor based on the frequency-derived technique," *Electronics Letters*, vol. 32, pp. 2263-2264, Nov 1996.

[33] G. S. Agarwal and W. Harshawardhan, "Inhibition and Enhancement of Two Photon Absorption," *Physical Review Letters,* vol. 77, pp. 1039-1042, 1996.
[34] V. Mizrahi, K. W. DeLong, G. I. Stegeman, M. A. Saifi, and M. J. Andrejco, "Two-photon absorption as a limitation to all-optical switching," *Opt. Lett.,* vol. 14, pp. 1140-1142, 1989.
[35] R. W. Boyd, *Nonlinear optics*: Academic Pr, 2003.
[36] A. Kudlinski, A. Mussot, R. Habert, and T. Sylvestre, "Widely tunable parametric amplification and pulse train generation by heating a photonic crystal fiber," *Quantum Electronics, IEEE Journal of,* pp. 1-1, 2011.
[37] L. Rapp and J. Ferreira, "Dynamics of Spectral Hole Burning in EDFAs: Dependence on Temperature," *Photonics Technology Letters, IEEE,* pp. 1-1, 2012.
[38] J. J. M. i Ponsoda, C. Ye, J. P. Koplow, M. J. Söderlund, J. J. Koponen, and S. Honkanen, "Analysis of temperature dependence of photodarkening in ytterbium-doped fibers," *Optical Engineering,* vol. 50, p. 111610, 2011.
[39] C. Dalzell, T. Han, I. Ruddock, and D. Hollis, "Two-photon excited fluorescence in rare-earth doped optical fibre for applications in distributed sensing of temperature," *Sensors Journal, IEEE,* pp. 1-1, 2010.
[40] G. P. A. . *Nonlinear Fiber Optics*, Third Edition ed.: Elsevier Science, USA. Chapter 10 Equation (10.2.2~5) 2001.
[41] K. Tajima, "Low-loss optical fibers realized by reduction of Rayleigh scattering loss," 1998, pp. 305-306.
[42] R. Ellis, "Explanation of Reflection Features in Optical Fiber as Sometimes Observed in OTDR Measurement Traces," 2007.
[43] I. Perkin Elmer, "Avalanche Photodiodes: A User's Guide."
[44] X. Y. Bao and L. A. Chen, "Recent Progress in Brillouin Scattering Based Fiber Sensors," *Sensors,* vol. 11, pp. 4152-4187, Apr 2011.
[45] T. K. T.Horiguchi, M.Tateda, "Tensile strain dependence of Brillouin frequency shift in silica optical fibers," *IEEE Photon Technol Lett,* vol. 1, May 1989.
[46] T. H. T. Kurashima, and M.Tateda, "Thermal effects on Brillouin frequency shift in jackedted optical silica fibers," *Appl.Opt,* vol. 29, 1990.
[47] F. F. D.Culverhouse, C.N.Pannel, D.A.Jackson, "Potential of stimulated Brillouin scattering as sensing mechanism for distributed temperature sensors," *Electron Lett,* vol. 25, 1989.
[48] F. F. D.Culverhouse, C.N.Pannel ,D.A.Jackson, "Stimulated Brillouin scattering: A means to realize tunable microwave generator or distributed temperature sensor," *Electron Lett,* vol. 25, 1989.
[49] R. W. Boyd, "Academic press: New York, NY, USA 2003," *Nonlinear Optics,* vol. chapter 9, 2003.
[50] T. Horiguchi, K. Shimizu, T. Kurashima, M. Tateda, and Y. Koyamada, "Development of a Distributed Sensing Technique Using Brillouin-Scattering," *Journal of Lightwave Technology,* vol. 13, pp. 1296-1302, Jul 1995.
[51] B. G. C. Anthony W.Brown, Kellie Brown, "Dark-Pulse Brillouin Optical Time-Domain Sensor with 20-mm Spatial Resolution," *jouranal of lightwave technology,* vol. 25, january 2007.

[52] D. J. W. V.Lecoeuche, C.N.Panell, D.A.Jackson, "Transient resopnse in high-resolution Brillouin-based distributed sensing using probe pulses shorter than the acoustic relaxation time," *Opt Lett,* vol. 25, 2000.
[53] X. Bao, J. Dhliwayo, N. Heron, D. J. Webb, and D. A. Jackson, "Experimental and theoretical studies on a distributed temperature sensor based on Brillouin scattering," *Lightwave Technology, Journal of,* vol. 13, pp. 1340-1348, 1995.
[54] S. Xie, L. Chen, and X. Bao, "Polarization averaged short-time Fourier transform technique for distributed fiber birefringence characterization using Brillouin gain," *Appl. Opt.*, vol. 51, pp. 4359-4369, 2012.
[55] K. S. Tsuneo Horiguchi, Toshio Kurashima, Mitsuhiro Tateda, Yahei Koyamada, "Advances in distributed sensing techniques using Brillouin scattering " *SPIE* vol. 2507.
[56] A. Minardo, R. Bernini, and L. Zeni, "A Simple Technique for Reducing Pump Depletion in Long-Range Distributed Brillouin Fiber Sensors," *Sensors Journal, IEEE,* vol. 9, pp. 633-634, 2009.
[57] C. C. Chow and A. Bers, "Chaotic stimulated Brillouin scattering in a finite-length medium," *Physical Review A,* vol. 47, pp. 5144-5150, 1993.
[58] A. E. Marble, K. A. Brown, and B. G. Colpitts, "Stimulated Brillouin scattering modeled through a finite difference time domain approach," pp. 404-415, 2004.
[59] J. Stone, "Stress-optic effects, birefringence, and reduction of birefringence by annealing in fiber Fabry-Perot interferometers," *Lightwave Technology, Journal of,* vol. 6, pp. 1245-1248, 1988.
[60] A. Yablon, M. Yan, P. Wisk, F. DiMarcello, J. Fleming, W. Reed, *et al.*, "Refractive index perturbations in optical fibers resulting from frozen-in viscoelasticity," *Applied physics letters,* vol. 84, pp. 19-21, 2004.
[61] M. Hornick and J. McDaniel, "Tampa Electric Polk Power Station Integrated Gasification Combined Cycle Project," Final Technical Report, DE-FC-21-91MC27363, prepared for the US Department of Energy, Office of Fossil Energy, National Energy Technology Laboratory (NETL): Morgantown, West Virginia2002.
[62] J. P. Bennett, "Refractory liner materials used in slagging gasifiers," *Refractories Applications and News,* vol. 9, 2004.
[63] TEMCo Industrial Power. *DIY: Build a Nichrome Wire electric aluminum melting furnace w/ fire brick*. Available: https://www.youtube.com/watch?v=en4yhzLuD9A
[64] OMEGA Engineering inc. *Resistance Heating Wire, Nickel-Chromium Alloy, 80% Nickel/ 20% Chromium*. Available: http://www.omega.com/pptst/NI80.html

List of Acronyms and Abbreviations

IGCC: Integrated coal-gasification combined cycle

PCF: Photonics crystal fiber

FWM: Four wave mixing

BOTDA: Brillouin optical time-domain analysis

LPG: Long period grating

NA: Numerical Aperture

OTDR: Optical time-domain reflectometer

SBS: Stimulated Brillouin scattering

FDTD: Finite-difference time-domain

ID: Inner diameter

TOC: Thermo-optic coefficients

DFB: Distributed feedback

SMF: Single-mode fiber

OSA: Optical spectrum analyzer

CW: Continuous wave

EOM: Electro-optical modulator

OTF: Optical tunable filter

GHz: Gigahertz

IFPI: Intrinsic Fabry–Perot interferometer

OPD: Optical-path difference

EMI: Electromagnetic interference

OFDR: Optical frequency domain reflectometry

SCFDR: Sub-carrier frequency domain reflectometry

PM: Polarization maintaining

FBG: Fiber Bragg grating

POTDR: Polarization Optical time-domain reflectometer

THz: Terahertz

TLPG: Travelling long period grating

XPM: Cross-phase modulation

EDFA: Erbium-doped fiber amplifiers

FWHM: Full width at half maximum

PD: Photodiode

SNR: Signal-to-noise ratio

COTDR: Coherent optical time-domain reflectometer

PIN: P-I-N photodiode

APD: Avalanche photodiode

PMT: Photomultiplier

NEP: Noise equivalent power

PC: Personal computer

DC: Direct current

MHz: Megahertz

KHz: Kilohertz

FUT: Fiber under test

CTS: Component test system

RF: Radio frequency

GIF: Graded index fiber

GPa: Gigapascal

FEA: finite element analysis

RI: Refractive index

CTE: Coefficient of thermal expansion

LED: Light emitting diode

MMF: Multimode fiber

OD: Outer diameter